Title
Analysis of Seismic Moment Tensors, In-Situ Stress, and Finite-Source Scaling of Earthquakes at The Geysers Geothermal Field, California

Author
Boyd, Olive Sierra

Publication Date
2018

Peer reviewed|Thesis/dissertation

Analysis of Seismic Moment Tensors, In-Situ Stress, and Finite-Source Scaling of Earthquakes at The Geysers Geothermal Field, California

by

Olive Sierra Boyd

A dissertation submitted in partial satisfaction of the
requirements for the degree of

Doctor of Philosophy

in

Earth and Planetary Science

in the

Graduate Division

of the

University of California, Berkeley

Committee in charge:

Professor Douglas S. Dreger, Chair
Professor Roland Bürgmann
Professor David Brillinger

Fall 2018

Analysis of Seismic Moment Tensors, In-Situ Stress, and Finite-Source Scaling of Earthquakes at The Geysers Geothermal Field, California

Abstract

Analysis of Seismic Moment Tensors, In-Situ Stress, and Finite-Source Scaling of Earthquakes at The Geysers Geothermal Field, California

by

Olive Sierra Boyd

Doctor of Philosophy in Earth and Planetary Science

University of California, Berkeley

Professor Douglas S. Dreger, Chair

The objective of this research was to develop methodologies of interest to the geothermal industry to estimate critical parameters needed to characterize the fracture network generated during Enhanced Geothermal System (EGS) development. This work was supported by the U.S. Department of Energy Geothermal Technologies Office (DOE GTO). The research focused on seismicity at The Geysers geothermal field located 120 km north of San Francisco, California. The Geysers geothermal field is the world's largest geothermal reservoir with approximately 1.6 GW installed electric capacity, 22 geothermal power plants with current average production of over 900 MW. Geothermal energy has been produced at The Geysers geothermal field since the early 1960s. Most of the earthquakes occur at shallow depths and are related to stress and hydrological perturbations due to geothermal energy operations including, on average, more than 57 million liters of treated wastewater injected daily. While the locations of earthquakes, as well as the timing and rates of their occurrence correlate with geothermal energy activities, greater understanding about the physical mechanisms is needed.

We developed and implemented a suite of methodologies to support the geothermal industry during EGS development. Our research focused on $1.0 < M_W < 5.0$ seismicity at The Geysers geothermal field, California to remotely estimate critical source parameters needed to characterize the fracture network generated during the EGS development. Initially 53 larger magnitude $M > 3$ earthquakes occurring throughout The Geysers geothermal field from 1992 to 2014 were investigated using an approach designed to assess resolution and uncertainty of seismic moment tensors. Deviatoric and full moment tensor solutions were computed, and statistical tests were implemented to assess solution stability, resolution and significance, particularly with respect to possible volumetric or tensile components. Several source models were examined including double-couple (DC), pure isotropic (ISO; volumetric change), and

volume-compensated linear vector dipole (CLVD) sources, as well as mixtures of these such as DC + CLVD, DC + ISO and shear-tensile sources. In general, it was found that The Geysers earthquakes as a population deviate significantly from northern California seismicity in terms of apparent volumetric source terms and complexity. The mean volumetric component of earthquake mechanisms at The Geysers is approximately 30% compared to essentially zero for earthquake mechanisms outside The Geysers geothermal field. The volumetric moment tensor components of The Geysers earthquakes could arise from the flashing of injected water to steam, or more likely from the tensile stress induced from rapid cooling of the hot rock through the introduction of water.

In another study, seismicity in the vicinity of an EGS demonstration project in the Northwest Geysers at the Prati 32 (P-32) injection well and the Prati State 31 (PS-31) production well is investigated to determine earthquake focal mechanisms, moment magnitudes, and in-situ stress of events that occur before and during reservoir stimulation starting October 6, 2011. We compiled a catalog of 167 waveform-based seismic moment tensors ranging in moment magnitude from 0.6 to 3.9. Owing to the large number of events a semi-automated approach was developed to align the data with the Green's functions used in the inversion. The automatic results were then reviewed to find the optimal shift for the inversion. The moment tensor catalog is subsequently used to invert for the stress tensor and to investigate possible temporal stress changes resulting from fluid injection. The relatively small uncertainties of the recovered stress tensors demonstrate the quality of the input mechanisms from the seismic moment tensor catalog. An approximate 15-degree counter-clockwise rotation of the least compressive stress σ_3 was found to occur during injection. More remarkable was a change in the orientation of the maximum compressive stress σ_1 from subhorizontal to vertical when injection operations temporarily halted. The orientation of σ_1 returned to subhorizontal when injection operations resumed. It is found that there was a systematic reduction in the stress shape factor, R, as the injected water volume increases, indicating an evolution toward a more transtensional stress state. This work shows that effective tracking of the evolution of the state of stress in a system due to the introduction of water may be accomplished utilizing a semi-automatic full waveform moment tensor method. In addition, the full waveform approach was found to provide more robust estimates of the magnitudes of the micro-earthquakes at The Geysers.

Finally, a finite-source inverse approach was used to estimate the rupture area for ten earthquakes ranging in magnitude from M_W 1.0 to 5.0. The slip models for these small earthquakes are complex with non-uniform distribution and in some cases with multiple asperities of slip release. They have complexity comparable to what is commonly found for larger earthquakes. We found the rupture area scaling with moment magnitude to be consistent with published relationships developed for globally distributed earthquakes with larger magnitudes ($M_W \geq 5.5$). This scaling relationship in conjunction with results from the stress inversion was subsequently applied to a set of earthquakes with high location accuracy to generate a statistical representation of the 3-D fracture network that was activated during the EGS demonstration project at Prati 32 injection well. We found the highest concentration of fractures located approximately 300 m to the north and 400 m below the bottom of the injection and production wells. Although this approach is approximate with respect to the actual orientation and dimension of the micro-earthquakes, it is a means to estimate a

representation of the stimulated fracture network and to evaluate fracture density which could be used to help industry target where to place steam recovery wells. Additionally, the detailed source analysis and scaling information together with characterizations of rates of earthquakes can help to inform on possible seismic hazard related to such operations. Finally, an objective of the research was the development of portable tools that may be applied to study seismicity in other geothermal systems which could help assess their energy and economic potential.

To my parents

Table of Contents

Abstract 1
Dedication Page i
Table of Contents ii
Acknowledgments iv

1. Introduction 1

2. A Systematic Analysis of Seismic Moment Tensor at The Geysers Geothermal Field, California 10
2.1 Chapter Abstract 10
2.2 Introduction 10
2.3 Methodology 13
2.4 Results 15
2.4.1 Catalog Statistics 15
2.4.2 Statistical Comparison of Northern California and The Geysers Full Moment Tensor Catalogs 16
2.4.3 Case Study of Selected End-Member Events 18
2.4.3.1 Example of a Dominant DC Event 18
2.4.3.2 Example of an Anomalous Large Isotropic Component Moment Tensor 20
2.4.3.3 Examples of Events with a Small Volumetric Component 26
2.4.3.4 Event 10: 12 October 1996 M_W 3.75, an Anomalous Moment Tensor? 33
2.5 Discussion and Conclusions 35
2.6 Data and Resources 37
2.7 Acknowledgments 37
2.8 Appendix 38
2.A.1 Table of Deviatoric Moment Tensor Solutions 39
2.A.2 Table of Full Moment Tensor Solutions 40

3. Analysis of Seismic Moment Tensors and *In Situ* Stress During Enhanced Geothermal System Development at The Geysers Geothermal Field, California 42
3.1 Chapter Abstract 42
3.2 Introduction 42
3.2.1 The Northwest Geysers EGS Demonstration Project 44
3.2.2 Waveform Data 46

3.3 Methods and Results 47
3.3.1 Moment Tensor Analysis 47
3.3.1.1 Case Studies of Selected Events 51
3.3.1.1.1 M_W 1.91 2012 March 27 51
3.3.1.1.2 M_W 2.44 2012 January 6 54
3.3.1.1.3 M_W 3.87 2014 January 21 57
3.3.1.2 Depth Distribution of Fault Mechanisms 57
3.3.2 *In Situ* Stress Analysis 59
3.3.2.1 Spatial-Temporal Trends in Seismicity 60
3.3.2.2 Temporal Trends in Stress 60
3.4 Discussion 64
3.4.1 Moment Tensor Analysis 64
3.4.2 Stress Analysis from Inversion of Focal Mechanisms 66
3.5 Conclusions 67
3.6 Acknowledgements 68
3.7 Appendix 68
3.A.1 Table of Studied Events 68
3.A.2 Derivation of Difference Between NCDED EGS Catalog M_W and M_W This Study 72

4. Stress Drop and Scaling of Earthquakes at The Geysers Geothermal Field, California 74
4.1 Chapter Abstract 74
4.2 Introduction 74
4.3 Data and Methodology 76
4.4 Results 79
4.4.1 Event 1 M_W 1.05 January 30, 2013 79
4.4.2 Event 2 M_W 1.48 January 30, 2013 89
4.4.3 Event 3 M_W 2.09 August 25, 2013 96
4.4.4 Event 4 M_W 2.87 February 6, 2013 103
4.4.5 Event 5 M_W 3.19 May 8, 2013 109
4.4.6 Event 6 M_W 3.73 January 21, 2014 116
4.4.7 Event 7 M_W 4.25 May 5, 2012 124
4.4.8 Event 8 M_W 4.27 January 4, 2009 128
4.4.9 Event 9 M_W 4.44 March 14, 2013 131
4.4.10 Event 10 M_W 4.53 January 12, 2014 134
4.5 Discussion 137
4.6 Conclusions 142
4.7 Acknowledgments 143

References 145

Acknowledgments

I would like to thank my advisor Douglas Dreger for his guidance, support, patience, and encouragement throughout this research. His passion and enthusiasm for geophysics compelled me to explore earthquake seismology, something I had purposely avoided until I sat down in his EPS 130 Strong Motion Seismology class. My qualifying exam committee members included Roland Bürgmann, David Brillinger, and George Brimhall who provided stimulating discussions and coursework that enhanced our seismological research objectives at The Geysers. It has been a privilege to be a student in Earth and Planetary Science at UC Berkeley and to be inspired by many professors including Bruce Buffett, Michael Manga, Raymond Jeanloz, Chi Wang, Barbara Romanowicz, Richard Allen and Rudy Wenk. I am very grateful to Roland Gritto, our main collaborator in this research at The Geysers geothermal field, one of the most enchanting places in northern California.

The Berkeley Seismological Laboratory is a gem of a place to collaborate with researchers from all over the world. Students in the Dreger group who paved the way with support and friendship include Sean Ford, Aurélie Guilhem, Shan Dou, Andrea Chiang, Avinash Nayak, Voon Hui Lai, Katie Wooddell, and Nate Lindsey along with postdoc Seung-Hoon Yoo and all the other visiting scholars from China, Italy, Australia, and beyond. What a pleasure it has been to work with all of you. Some of my best memories are when we would get together for a meal with Doug! It has been fun along the way with Mong-Han Huang, Sanne Cottaar, Pam Kaercher, Rob Porritt, Allen, Amanda, and Becky, Felipe Orellana, Qingkai Kong, Seth Saltiel, William Hawley, Luca Malagnini, Corinna Roy, Isabel Ryder, Ianire and Sergio, Dino Bellugi, Nestor Cuevas and more recently Nam, Sarina and Claire! I am very grateful for help in navigating the path from Margie Winn and Rachel Kowalik among many others here in EPS.

Special thanks go to Peggy Hellweg, Bob Uhrhammer, Doug Neuhauser, Charley Paffenbarger, Pete Lombard, Jennifer Taggart and the entire BSL staff who keep the data flowing. I am very grateful for the opportunity to collaborate with Taka'aki Taira, Craig Hartline and Julio Garcia, Calpine, and to Mike Floyd and Gareth Funning for giving me the opportunity to get my boots muddy at The Geysers, Larry Hutchings, Gisela Viegas, Pierre Jeanne, and Corinne Bachmann of Lawrence Berkeley National Laboratory (LBNL), Steve Jarpe, Ramsey Haught and many others for sharing their expertise and insights at The Geysers.

There is no way I could be here if it were not for the support and encouragement from many great teachers and students who are also friends and family. All my housemates who have worn down most of my rough edges, you have taught me a lot and more. My friends near and far, Margaret, Elizabeth, Shawn, Mitch, Richard and Edith, thank you for your good cheer. And to my family, especially my parents, brother Sandy, sister Monique, and all the relatives, you have been with me every step of the way. I am forever grateful for your love and support.

Chapter 1

Introduction

The objective of this dissertation is to develop methodologies of interest to the geothermal industry to estimate critical parameters needed to characterize the fracture network generated during Enhanced Geothermal System (EGS) development. This work was supported by the U.S. Department of Energy Geothermal Technologies Office (DOE GTO). My research focused on seismicity at The Geysers geothermal field located 120 km north of San Francisco, California. The Geysers geothermal field is the world's largest geothermal reservoir with approximately 1.6 GW installed electric capacity, 22 geothermal power plants with current average production of over 900 MW. Geothermal energy has been produced at The Geysers geothermal field since the early 1960s. Most of the earthquakes occur at shallow depths and are related to stress and hydrological perturbations due to geothermal energy operations, including on average more than 57 million liters of treated wastewater injected daily. While the locations of earthquakes, as well as the timing and rates of their occurrence correlate with geothermal energy activities, greater understanding about the physical mechanisms is needed.

Seismic source analysis including moment tensor solutions and finite-source modeling offer insight into the nature of equivalent forces causing the seismicity, the orientation of rupture planes, and the distribution of fault slip and stress release. Are source mechanisms predominantly double-couple (DC) in nature occurring on existing fractures and fault networks responding to stress perturbations resulting from geothermal production and injection activities, or do the earthquakes have sources that deviate from a pure double-couple that might be indicative of fluid involvement in the source process, such as tensile-cracks or shear-tensile mechanisms? In the past, a small number of Geysers earthquakes with $M > 4$ occurred with the microseismicity. More recently, however, there has been an increase in the number and rates of $M > 4$ events located within the microseismic cloud at The Geysers. Understanding the role of induced seismicity and the physical mechanisms of these events associated with geothermal energy operations is needed to evaluate seismic hazard associated with geothermal reservoir production.

To address this concern in Chapter 2 we investigated $M > 3$ seismicity that occurred from 1992−2014 throughout The Geysers geothermal field. We applied a variety of techniques to develop a catalog of deviatoric and full moment tensor solutions and to assess the resolution and uncertainty of non-double-couple components. Deviatoric and full moment tensor solutions were computed and statistical tests were employed to assess solution stability, resolution, and significance. We found from a systematic approach toward characterizing uncertainties in moment tensor solutions that The Geysers earthquakes, as a population, deviate significantly from northern California seismicity in terms of apparent volumetric source terms and complexity, and that for some events isotropic components indicate tensile

processes that could be the result of fluid mechanisms and/or of thermal stress from the reintroduction of fluids in the reservoir.

In Chapter 3 we investigated the seismicity associated with water injection at the EGS demonstration project in the Northwest Geysers. The results show that there was a marked increase in the rate of seismicity in the 1 x 2 km^2 study area centered on Prati 32 injection well as injection commenced on October 6, 2011. We developed a semi-automated approach to estimate seismic moment tensors of the micro-earthquakes utilizing three-component seismic waveforms which resulted in the compilation of a 167-event seismic moment tensor catalog for events ranging in moment magnitude from 0.6 to 3.9. The moment tensor catalog was subsequently utilized to invert for the stress tensor and to investigate possible temporal changes resulting from the fluid injection. The results of inverting for the stress tensor demonstrate the quality of the seismic moment tensor catalog through the relatively small uncertainties in the recovered stress tensors. An approximate 15-degree counter-clockwise rotation of the least compressive stress σ_3 was found to occur during injection. More remarkable was a change in the orientation of the maximum compressive stress σ_1 from subhorizontal to vertical when injection operations temporarily halted. The orientation of σ_1 returned to subhorizontal when injection operations resumed. The magnitude of these rotations is consistent with other nearby empirical observations (Martínez-Garzón *et al.*, 2013) and thermo-hydromechanical simulation results (Jeanne *et al.*, 2015). It is found that there was a systematic reduction in the stress shape factor, R, as the injected water volume increases, indicating an evolution toward a more transtensional stress state.

In Chapter 4 we estimated rupture area for ten earthquakes ranging in magnitude from M_W 1.0 to 5.0 using a finite-source inversion method and found that the scaling with moment magnitude is consistent with published relationships developed for globally distributed earthquakes with larger magnitudes ($M_W \geq 5.5$). This scaling relationship in conjunction with results from the stress inversion was subsequently applied to a set of earthquakes with high location accuracy to generate a statistical representation of the 3-D fracture network that was generated during the EGS demonstration project at Prati 32. We found that the highest concentration of fractures is located approximately 300 m to the north and 400 m below the bottom of the injection and production wells. The finite-source approach was found to be technically feasible although automated methods for the identification of possible empirical Green's function events, smaller earthquakes providing information about the wave propagation signature in the seismic data and verification of stable deconvolutions for moment rate functions, would be needed for routine application to seismicity in geothermal environments. Although this approach is approximate with respect to the actual orientation and dimension of the micro-earthquakes, it is a means to estimate a representation of the stimulated fracture network and to evaluate fracture density which could be used to help industry target where to place steam recovery wells. Additionally, the detailed source analysis and scaling information together with characterizations of rates of earthquakes can help to inform on possible seismic hazard related to such operations. Finally, an objective of the research was the development of portable tools that may be applied to study seismicity in other geothermal systems which could help assess their energy and economic potential.

In the following section, research methodologies and results from each of the investigations are summarized by chapter.

Chapter 2 entitled, A systematic analysis of seismic moment tensor at The Geysers geothermal field, California (published in the Bulletin of the Seismological Society of America, Boyd *et al.*, 2015), is focused on determining full waveform moment tensor solutions of $M > 3$ background and induced seismicity occurring throughout the geothermal field from 1992−2014. The seismic moment tensor may be interpreted in terms of the orientation of fault structures on which shear-dislocation occurs, as well as evidence of dilation. Three-component waveform data are inverted for the moment tensor resulting in a catalog of source parameters, as well as various moment tensor decompositions (double-couples, non-double-couple, tensile crack and isotropic dilational components).

Three-component, complete waveform data from broadband stations of the Berkeley Digital Seismic Network (BDSN), Northern California Seismic System (NCSS), and the Transportable Array (TA) deployment (2005-2007) of the National Science Foundation EarthScope experiment are inverted for deviatoric and full, six-element moment tensors, using the method outlined in Minson and Dreger (2008). The broadband velocity data from stations located at distances between 30 and 400 km are instrument corrected, integrated to displacement, and filtered with an acausal, four-pole, Butterworth bandpass filter with a 0.02 to 0.05 Hz or 0.02 to 0.10 Hz passband depending on station distance and signal-to-noise levels in the respective passbands. It was not possible to use one set of stations for all events because of changes in the seismic networks and changes in signal-to-noise levels. In each case we maximized the number of stations depending on signal-to-noise levels. Green's functions were computed for velocity models used in the routine monitoring of Northern California seismicity (e.g., Pasyanos *et al.*, 1996).

In addition to finding the best fitting least squares solutions we applied the *F*-test to test the significance of full moment tensor models with 6 degrees of freedom (DOF) over the simpler deviatoric (5-DOF) and pure double-couple (4-DOF) models. As non-double-couple components to the moment tensor can arise from complexity in the source, the approximate nature of the applied Green's functions (computed for 1-D seismic velocity models), and background noise, care is needed in assessing the recovery of those components and in their interpretation (e.g., Panning *et al.*, 2001; Templeton and Dreger, 2006). The jackknife test is used to assess the stability of solutions due to station configuration. A residuals bootstrap is used to characterize random aleatoric variability in the solutions, and finally the Network Sensitivity Solution (NSS; Ford *et al.*, 2010) or Source-Type-Inversion (Nayak and Dreger, 2015) are used to map the full moment tensor solution goodness of fit in the complete source-type space (Hudson *et al.*, 1989). All of these tests require significant computational effort and therefore a staged approach is taken where if a solution is largely double-couple no additional analysis is performed. If a solution has large non-double-couple components such as a compensated linear vector dipole (CLVD) (Knopoff and Randall, 1970) and/or a volumetric term, an *F*-test is first performed to assess significance of the more complex model. If the *F*-test indicates a significant improvement in fit with the non-double-couple

terms then the jackknife, bootstrap and NSS analyses are performed to assess the stability of the solution and the confidence in the recovery of the non-double-couple components.

In the course of our study we found that the depth sensitivity of data filtered from 0.02 to 0.05 Hz is fairly limited, and therefore we restrained our analysis to event depths determined from the NCSS catalog, which utilizes data recorded by local Lawrence Berkeley National Laboratory (LBNL) and United States Geological Survey (USGS) stations. In the future, with better-calibrated velocity models and/or seismic data recorded with local stations, we may be able to improve on moment tensor based source depth determination. However, for this work we assumed that the depths reported in the catalog are well determined and focused on the recovery of the seismic moment tensor source parameters.

The results of Chapter 2 show that deviatoric moment tensor solutions for the studied events have a predominantly E-ESE tensile axis varying from relatively rare strike-slip to more common normal faulting events. Large CLVD solutions can accommodate both of these DC types. In some of these events the combination of first-motion polarities jointly inverted with the long-period waveforms favors the full moment tensor solution, which have a small volume increase component. In the southeast Geysers the tensile axis is oriented north-south. One of the southeast Geysers events was found to have a large isotropic component with a very high measure of statistical significance. It occurred on October 12, 1996 in the southern end of the field. The deviatoric solution for this event and others nearby show an unusual east-west striking normal solution. We found from the systematic approach toward characterizing uncertainties in moment tensor solutions that The Geysers earthquakes, as a population, deviate significantly from northern California seismicity in terms of apparent volumetric source terms and complexity, and that for some events isotropic components indicate tensile processes that could be the result of fluid mechanisms and/or of thermal stress from the reintroduction of fluids in the reservoir. The results of this work have been published (Boyd *et al.*, 2015).

In Chapter 3 entitled, Analysis of seismic moment tensors and in-situ stress during Enhanced Geothermal System (EGS) development at The Geysers geothermal field, California, (published in Geophysical Journal International, Boyd *et al.*, 2018) $M < 3.7$ seismicity associated with the Prati 32 injection well in the Northwest Geysers is studied. Identifying, creating, and managing fractures and flow paths are essential tasks during EGS resource development. The successful generation of a fracture network requires a priori knowledge of in-situ stress and natural fracture orientation and spacing. However, because the orientation and magnitude of in-situ stress may not be reliably available and injecting fluids at high rates and volume may disturb the natural stress state, it is advantageous to monitor in-situ stress during the injection process. Knowing the stress evolution and nature of the rupture process, as well as the spatial distribution of fluid flow, are essential to understanding and characterizing the generation of the fracture network during EGS development.

In this study three-component short-period (4.5 Hz) data sampled at 500 Hz recorded by the LBNL 34-station permanent geophone network was used during the injection phase of the DOE GTO funded EGS demonstration project at Prati 32 to study seismicity within a 1 x 2 km^2 area centered on the Prati 32 injection well. A subset of seismic stations less than 6 km

from Prati 32 injection well were used in this study. Earthquakes with magnitude $M \geq 1$ (DOE Enhanced Geothermal System Earthquake Catalog) were chosen for deviatoric moment tensor investigation. A first step for both inverting for in-situ stress and for developing a source-area scaling relationship is the development of a robust seismic moment tensor catalog. Using waveform data from the LBNL short-period network we have refined a semi-automated approach for estimating the seismic moment tensor and have compiled a 167-event seismic moment tensor catalog for events ranging in moment magnitude from 0.6 to 3.9.

Seismic moment tensors are computed utilizing the methods described in Minson and Dreger (2008), Ford *et al.* (2010) and Boyd *et al.*, (2015). For the largest earthquake, M_W 3.74, the moment tensor solution was determined using the Berkeley Seismological Laboratory (BSL) moment tensor interface and broadband data from the Berkeley Digital Seismic Network (BDSN). Data for the $1.0 \leq M \leq 3.7$ events are obtained from the local LBNL short-period seismic network. The seismic waveform data are processed by removing the instrument response to ground velocity followed by bandpass filtering of the waveforms with a causal 4th-order Butterworth filter with corners at 0.7 and 1.7 Hz (0.6 to 1.4 s period) for $1 \leq M < 2.8$ events and 0.2 and 1.0 Hz for $M \geq 2.8$ events. The data are subsequently resampled at 0.1 s. Green's functions for the inversion are computed using a 1-D velocity model, derived from a 3-D velocity model for the Northwest Geysers developed by Julian *et al.* (1996). This model was shown to perform well for moment tensor inversion (e.g., Guilhem *et al.*, 2014).

Moment tensor analysis requires the alignment of the observed waveforms to the computed Green's functions. With a well-calibrated velocity model it is sometimes possible to invert the waveform data without timing shifts, however in our analysis data time shifting is necessary, and the shifts represent departures from the assumed velocity model with the actual velocity structure along the paths. Typically the time shifts are estimated by trial and error, however due to the large number of events investigated we employed a grid search to find the best time alignment shifts automatically. The results indicate a systematic shift to negative values with the mean at approximately −3 samples or −0.3 seconds. This indicates that the data need to be shifted to a later time indicating that the model is slower on average than the actual Earth structure. The magnitude of the shifts on average is approximately one-third of the central period of the utilized passband. The mean shift value does not appear to change during injection.

An effort was made to have as many stations in common as possible for all of the studied events. Initially seismic data from as many as 10 stations within 6 km of the studied events were considered for preliminary moment tensor analysis. Depending on these initial fits of the observed data with the Green's functions, 5 to 6 stations were then selected for moment tensor processing using a grid-search algorithm to automatically find the optimal alignment of the observed data with the synthetic Green's functions. This method is applied to all of the studied events for automated moment tensor computation. These results are then checked and if necessary minor adjustments are applied to shift the data for optimal fit. In the final processing stage, data with poor fits are removed.

Most of the mechanisms in our catalog of events are strike-slip, followed by normal with a few reverse fault mechanisms. The strike-slip events are found to occur at all depths, whereas the normal and reverse events tend to occur above and within the reservoir. There is also a suggestion that the variety in focal mechanisms is greater prior to and during the first ten months of injection. Subsequent focal mechanisms following multiple shut-in periods become more uniform and consistent with the tensile stress direction inferred from previous studies (Ross *et al.*, 1996; Guilhem *et al.*, 2014; Boyd *et al.*, 2015).

There was an initial discrepancy between the waveform inversion M_W and that reported in the LBNL catalog. LBNL computes M_W by averaging the instrument corrected *P*-wave displacement spectrum from 1 Hz to the corner frequency for $M < 3.5$ events, applying the whole space Green's function equation for direct *P*-waves. Thus, even though both measures are effectively M_W one is computed using the complete waveform including P, S and surface waves (this study) and the other only the *P*-wave displacement spectrum. Through discussion with colleagues at LBNL errors in the formula used to estimate the spectral M_W were discovered. These have subsequently been corrected. Using the moment tensor based M_W estimates an empirical correction for the LBNL spectral M_W estimates was found.

The moment tensor catalog was used to invert for the in-situ state of stress within the study region, employing the STRESSINVERSE software package developed by Vavryčuk (2014). Sliding windows containing 30 events for each time period with a 10-event overlap was used in the stress inversion. Because it is not known which of the two possible nodal planes is the actual earthquake rupture plane, the STRESSINVERSE code uses an iterative method to find the nodal planes most consistent with the stress field given fault frictional properties. The results show an interesting, systematic change in the orientation and magnitude of the stress environment. First, there is an approximately 15-degree counter-clockwise rotation of σ_3, the least compressive stress during the study period and a marked rotation in the orientation of the maximum compressive stress σ_1 from subhorizontal to vertical when injection operations temporarily cease. The orientation of σ_1 returns to subhorizontal when injection operations resume.

The results in Chapter 3 show that there was a marked increase in the rate of seismicity in a 1 x 2 km^2 region around the Prati 32 injection well as injection commenced on October 6, 2011. In fact, comparing the monthly averaged injection rate with monthly averaged seismicity reveals a very strong correlation, in which the low pre-injection rate of seismicity is markedly increased with the initiation of injection. After the injection rate stabilizes the rate of earthquakes is seen to reach a steady level. Short-term fluctuations in the injection rate seem to also be marked by short-term fluctuations in the rate of earthquakes. The magnitudes of these events tend to be very small although a number of *M* 3+ events have occurred. Using the semi-automated waveform approach developed for this study a 167-event, waveform-based, seismic moment tensor catalog for events ranging in moment magnitude from 0.6 to 3.9 was compiled. This waveform-based catalog was used to empirically correct the LBNL M_W catalog for the Prati 32 stimulation experiment. Stress tensor inversion results have small uncertainties indicating the quality of the moment tensor catalog. The stress inversion results show the state of stress was affected by the injection of water, where there is an approximate 15-degree counter-clockwise rotation of σ_3. More remarkable is a change in

the orientation of the maximum compressive stress σ_1 from subhorizontal to vertical when injection operations temporarily halted. The orientation of σ_1 returned to subhorizontal when injection operations resumed. The magnitude of these rotations is consistent with other nearby empirical observations (Martínez-Garzón *et al.*, 2013) and thermo-hydromechanical simulation results (Jeanne *et al.*, 2015; Ziegler *et al.*, 2017). It is found that there was a systematic reduction in the stress shape factor, *R* (Gephart and Forsyth, 1984), as the injected water volume increases, indicating an evolution toward a more transtensional stress state.

Chapter 4 entitled, Stress Drop and Scaling of Earthquakes at The Geysers Geothermal Field, California, investigates relationships between moment magnitude, M_W, and rupture area. This chapter builds on Chapter 3 with the goal of defining an approach for mapping the M_W of the micro-earthquakes to fault dimension for use in mapping a statistical representation of the fracture network activated by fluid injection. The approach taken is the estimation of finite-source parameters (rupture area, rupture dimension, slip distribution, and stress-change) using the empirical Green's function (eGf) approach of Mori and Hartzell (1990). This method inverts the seismic moment rate functions obtained from empirical Green's function deconvolution, in which the waveform of a smaller, collocated earthquake is deconvolved by effectively removing the wave propagation component from the records. The deconvolution is carried out in the frequency domain.

The determination of finite-source parameters first requires a moment tensor solution of the larger target event to define the orientation of the fault plane. Events analyzed in Chapter 3 were identified as potential target events for the analysis, and catalogs were searched to find nearby smaller earthquakes (eGf events), typically one magnitude unit smaller, with a relatively large correlation coefficient with respect to the target event. The empirical Green's function approach assumes that the target and eGf pair are co-located events having a similar source mechanism with a difference in magnitude of at least one unit. Suitable eGf events horizontally located within 200 m from larger target events were found in the high-resolution double-difference earthquake catalog from Waldhauser and Schaff (2008). For smaller magnitude target events, the DOE Enhanced Geothermal System Earthquake Catalog was searched for possible eGf events. The eGf waveforms were then deconvolved from the target waveforms to identify those that produced pulse-like moment rate functions (MRFs) with the highest signal to noise ratio.

The raw 500 Hz geophone data were corrected for instrument response, high-pass filtered, and decimated to facilitate deconvolution. The eGf events were spectrally deconvolved from the target events using 15 s of data (-2 to +13 s from the onset of the *P*-wave) with a 1% water level to minimize instabilities caused by division of small values in the eGf spectra (Dreger *et al.*, 2007). The resulting moment rate functions at each station were stacked and inspected to determine the best eGf events with high-quality, high signal-to-noise ratio moment rate functions at nearby stations less than 5 km away. Following Dreger (1997) and Dreger *et al.* (2007) the MRFs are interpreted by cutting the pulses at the zero crossing. When the necessary conditions that the target-eGf pair is collocated and with the same or very similar mechanism are satisfied the deconvolution of the eGf with the target event results in pulse-like moment rate functions (e.g., Mori and Hartzell, 1990; Dreger *et al.*, 1996). The MRF may then be inverted for the slip distribution assuming the orientation of the rupture

plane from the seismic moment tensor results (e.g., Mori and Hartzell, 1990; Dreger *et al.*, 1996). From the slip distribution models it is possible to map the stress change during the rupture using the method of Ripperger and Mai (2004).

We have obtained finite-source models for ten earthquakes at The Geysers spanning the magnitude range from M_W 1.0 to 5.0. All of the events show complexity in rupture with spatially variable slip and stress drop. Some of the larger events show considerable complexity in the slip distribution with multiple asperities or slip patches. The rupture planes are consistent with the orientation of nearby major fault systems while the average stress drops range from 1.6 to more than 10 MPa indicating large variation in the state of stress and the strength of reservoir rock. Due to the non-uniform slip and stress distributions of the events some of the slip patches have very high stress drop indicating local-scale high strength patches (e.g., Dreger *et al.*, 2007). The rupture area and average slip in the ten models was estimated and compared to the scaling laws of Wells and Coppersmith (1994) and Leonard (2010). These scaling laws are based on global earthquake catalogs of events with M_W larger than 5.5, with the great majority of events being larger than M_W 6.0. The results for The Geysers earthquakes show that the finite-source rupture models are consistent with the two global scaling laws, displaying self-similar scaling, although The Geysers earthquakes may be on average slightly more compact, or exhibit higher stress drop than the average of the events in Wells and Coppersmith (1994) and Leonard (2010). The Geysers events are found to lie within the 2-sigma curves for rupture area from the Leonard (2010) relationship and within the 0.1 and 100 MPa Brune stress drop range.

In summary we developed a suite of methodologies to support the geothermal industry during enhanced geothermal system development. Our research focused on $1.0 < M_W < 5.0$ seismicity at The Geysers geothermal field, California to remotely estimate critical parameters needed to characterize the fracture network generated during the EGS development. We initially investigated larger magnitude $M > 3$ events occurring throughout the geothermal field from 1992−2014 using a systematic approach to develop a catalog of deviatoric and full moment tensor solutions and an assessment of the resolution of non-double-couple components. Methods outlined in Chapter 2 (Boyd *et al.*, 2015) serve as a guide for how to address the very difficult problem of determining non-double-couple moment tensor solutions and evaluating their significance. We developed a semi-automated method to estimate seismic moment tensors of the micro-earthquakes associated with the EGS demonstration project in the Northwest Geysers. This work resulted in the compilation of a 167-event deviatoric seismic moment tensor catalog for events ranging in moment magnitude from 0.6 to 3.9. The moment tensor catalog was subsequently utilized to invert for the stress tensor and to investigate possible temporal changes resulting from the fluid injection. The results for inverting for the stress tensor demonstrate the quality of the seismic moment tensor catalog through the relatively small uncertainties in the recovered stress tensors and that fluid injection operations have a substantial impact on the state of stress and the fractures that become activated. The finite-source approach was used to estimate the rupture area for earthquakes ranging in magnitude from M_W 1.0 to 5.0. We found the scaling with moment magnitude to be consistent with published relationships developed for globally distributed earthquakes with larger magnitudes ($M_W \geq 5.5$). This scaling relationship in conjunction with results from the stress inversion was subsequently applied to a set of earthquakes with high

location accuracy to generate a statistical representation of the 3-D fracture network that was generated during the EGS demonstration project at Prati 32. We found that the highest concentration of fractures is located approximately 300 m to the north and 400 m below the bottom of the injection and production wells. The study is beneficial to the public in that the source methods improve the understanding of the nature of seismicity occurring in the geothermal field and could help to assess seismic hazards. It is beneficial to industry in that by monitoring seismicity and the developing fracture network more efficient stimulation and extraction of steam may be possible. Finally, the tools developed are portable and may be applied to study seismicity in other geothermal systems, which could help assess their energy and economic potential.

Chapter 2

A Systematic Analysis of Seismic Moment Tensor at The Geysers Geothermal Field, California

Published as:
Boyd, O.S., D.S. Dreger, V.H. Lai, and R. Gritto, 2015. A systematic analysis of seismic moment tensor at The Geysers geothermal field, California, *Bull. Seism. Soc. Am.*, **105** (6), 2969-2986, doi: 10.1785/0120140285.

2.1 Chapter Abstract

The Geysers geothermal field is one of the most seismically active regions in northern California. Most of the events occur at shallow depths and are related to stress and hydrological perturbations due to energy production operations. To better understand the relationships between seismicity and operations, better source mechanism information is needed. Seismic moment tensors offer insight into the nature of equivalent forces causing the seismicity. Fifty-three $M > 3$ events located at The Geysers geothermal field were selected from the University of California Berkeley Moment Tensor Catalog for analysis of seismic moment tensor solutions and associated uncertainties. Deviatoric and full moment tensor solutions were computed, and statistical tests were employed to assess solution stability, resolution, and significance. In this study, we examine several source models including double-couple (DC), pure isotropic (ISO; volumetric change), and volume compensated linear vector dipole (CLVD) sources, as well as compound sources such as DC + CLVD, DC + ISO, and shear-tensile sources. In general we find from a systematic approach toward characterizing uncertainties in moment tensor solutions that The Geysers earthquakes, as a population, deviate significantly from northern California seismicity in terms of apparent volumetric source terms and complexity.

2.2 Introduction

Geothermal energy has been produced at The Geysers geothermal field in northern California since the early 1960s. Seismic monitoring by Lange and Westphal (1969) showed the existence of earthquakes in The Geysers area predominantly along the Sulfur Creek fault zone and within the area of hydrothermal activity. With the initiation of fluid injection in

1969 (Enedy *et al.*, 1991), further seismic monitoring by Hamilton and Muffler (1972) characterized the increasing microseismicity. Marks *et al.*, (1978) determined that seismicity was induced by steam withdrawal and or reinjection of condensate.

It has been demonstrated that increased steam production and fluid injection correlates positively with changes in earthquake activity (Majer and McEvilly, 1979; Eberhart-Phillips and Oppenheimer, 1984; Oppenheimer, 1986; Stark, 1990; Enedy *et al.*, 1991; Greensfelder, 1993; Kirkpatrick *et al.*, 1999; Ross *et al.*, 1999; Smith *et al.*, 2000; Majer and Peterson, 2005), resulting in thousands of tiny earthquakes each year with events ranging in magnitude up to 4.5 (Majer *et al.*, 2007). Although the locations of earthquakes and the timing and rates of their occurrence correlate with production and injection activities, little is known about the physical mechanisms. Are they predominantly double-couple (DC) in nature occurring on existing fractures and fault networks responding to stress perturbations resulting from these activities, or do the events have sources that deviate from a pure DC, that might be indicative of fluid involvement in the source process, such as tensile-cracks or shear-tensile mechanisms? In the past a small number of Geysers events with $M > 4$ have occurred with the microseismicity. More recently, however, there has been an increase in the number and rates of $M > 4$ events located within the microseismic cloud at The Geysers. Understanding the role of induced seismicity and the physical mechanisms of these larger-magnitude events associated with geothermal energy operations is needed to evaluate seismic hazard associated with reservoir production.

Seismic moment tensor analysis can be used to determine the source mechanism and stress environment for larger events. Moment tensor analysis at The Geysers has evolved over the years beginning with a frequency domain approach developed by O'Connell and Johnson (1988). Subsequent investigations by Julian *et al.* (1993) and Kirkpatrick *et al.* (1996) found evidence of nonshear source mechanisms at The Geysers. Ross *et al.* (1999) used a method of inverting *P*-wave first motions and *P*/*S* amplitude ratios to study small events in The Geysers and found evidence for non-DC earthquakes, some of which were comprised of large compensated linear vector dipole (CLVD) solutions with cases of both volumetric expansion and compaction. Recent investigations (Guilhem *et al.*, 2014; Johnson, 2014a,b) show a range of source mechanisms including both shear and tensile processes.

In other geothermal and volcanic environments non-DC moment tensor solutions have been found. For example, Nettles and Ekstrom (1998) reported solutions for seismic events associated with the Bardarbunga volcanic eruption in Iceland that are characterized as vertically oriented, CLVD with major vector dipole in tension, which they interpret as evidence of ring faulting associated with caldera collapse. Tkalčić *et al.* (2009) and Fichtner and Tkalčić (2010) studied these events and found that there is no volumetric component to the moment tensor and demonstrated that the observed solution could also arise from spatially offset volume-increase sources (dikes and sills) and volume-decrease sources (supplying magma chamber). In 1997, a sequence of moderate earthquakes was observed during a heightened period of seismic activity, deformation, and degassing at the Long Valley Caldera of eastern California. Over 24,000 recorded events occurred between January 1997 and February 1998 (Barton *et al.*, 1999). Four of these had source solutions with statistically significant isotropic components (e.g., Dreger *et al.*, 2000; Minson and Dreger, 2008). A comprehensive study of Long Valley seismicity confirmed the four unusual solutions and

found one more event that had a resolvable isotropic component (Templeton and Dreger, 2006); however, most of the studied events were found to not deviate significantly from a pure DC solution. Minson *et al.* (2007) studied regional distance broadband waveforms of the June 2000 Miyakejima, Japan, earthquake swarm and found that many of these events had large isotropic solutions that could be indicative of tensile processes from fluids exsolving from magma along a 20-km-long propagating dike following caldera collapse at Miyakejima. Shimuzu *et al.* (1987) proposed a tensile crack coupled with a shear crack as the source mechanism of short-period earthquakes associated with the 1983 eruption of Miyakejima.

There has also been focus on determining moment tensor solutions for earthquakes induced by hydraulic fracture stimulation (Baig and Urbancic, 2010) and borehole injection in the reservoir at Soultz-sous-Forets, France, hot-dry-rock (HDR) geothermal site. Cuenot *et al.* (2006) analyzed data from the 2003 hydraulic stimulation experiment and observed a higher proportion of the non-DC component for earthquakes near the injection well. On the other hand, Horalek *et al.* (2010) studied 45 of the largest M 1.4–2.9 earthquakes from a 2003 borehole injection experiment and found that DC mechanisms dominated the sequence. Godano *et al.* (2011) studied four microearthquakes induced in the Soultz-sous-Forets HDR reservoir and obtained moment tensor solutions having high uncertainty associated with low isotropic and CLVD components. Deichmann and Giardini (2009) found that seismicity induced by the enhanced geothermal system of Basel, Switzerland generally have focal mechanisms that indicate shear failure on pre-existing faults, with some focal mechanisms showing signs of non-DC components with volume change.

In all studies of this type, the challenge lies in ascertaining the resolution of the various source components, their significance, and uncertainty. A systematic procedure for the evaluation of aleatoric and epistemic solution uncertainty for nuclear monitoring has been developed by Ford *et al.* (2008, 2009, 2010, and 2012). These studies introduced techniques for the assessment of solution stability with the objective of critically examining non-DC components of derived moment tensor solutions. The effects of velocity model, station configuration, random errors, and noise levels were all utilized to inform a level of confidence on possible non-DC moment tensor solutions for the purpose of identifying nuclear explosions from earthquake signals. This approach is extensible to other classes of seismic events, such as underground cavity collapses (Ford *et al.*, 2008), alpine glacier icequakes (Walter *et al.*, 2009, 2010), and seismicity in environments with high fluid and/or gas pressure (Nayak and Dreger, 2014).

Recent studies at The Geysers include Johnson (2014a,b), who investigated time-dependent moment tensors of $M < 3$ earthquakes from 2011 to 2012, and Guilhem *et al.* (2014) who obtained full moment tensor solutions of $M \sim 3$ earthquakes from 2009 to 2011 using waveform modeling and first-motion polarity. Both studies investigated earthquakes in the northern region of The Geysers using short-period seismic data from a local network and show a range of source mechanisms, including both shear and tensile processes. In the investigation presented here, broadband seismic data from regional networks are used to study moment tensors of $M > 3$ earthquakes throughout the geothermal field. We apply techniques described in the next section to develop a catalog of deviatoric and full moment tensor solutions and an assessment of the resolution of non-DC components of 53 earthquakes that

occurred at The Geysers from 1992 to 2014.

2.3 Methodology

We invert three-component, complete waveform data from broadband stations of the Berkeley Digital Seismic Network, Northern California Seismic System (NCSS), and the Transportable Array deployment (2005-2007) of the National Science Foundation EarthScope experiment (see Data and Resources) for deviatoric and full, six-element moment tensors, using the method outlined in Minson and Dreger (2008). The broadband velocity data from stations located at distances between 30 and 400 km are instrument corrected with reported pole-zero response functions, integrated to displacement, and filtered with an acausal, four-pole, Butterworth band-pass filter with a 0.02−0.05 Hz or 0.02−0.10 Hz passband, depending on station distance and signal-to-noise levels in the respective passbands. It was not possible to use one set of stations for all events because of changes in the seismic networks and changes in signal-to-noise levels. In each case we maximized the number of stations depending on signal-to-noise levels. The station locations are shown in the inset of Figure 2.1.

Green's functions for the inversion were computed for the GIL7 and SOCAL 1D velocity models, which are derived from broadband waveform modeling and routinely used by the Berkeley Seismological Laboratory (BSL) to monitor California seismicity (e.g., Pasyanos *et al.*, 1996). The Green's functions, including near-, intermediate-, and far-field terms for body and surfaces waves, were computed with FKRPROG written by Chandan Saikia, which is based on the method of Wang and Herrmann (1980).

The processed seismic waveform data are inverted for deviatoric and full moment tensor solutions following the methods outlined in Minson and Dreger (2008) and Ford *et al.* (2008, 2009, 2010). In addition to finding best-fitting solutions, we apply the *F*-test to test the significance of models with higher degrees of freedom, jackknife tests to assess the stability of solutions due to station configuration, a residuals bootstrap to characterize random aleatoric variability in the solutions, and finally the Network Sensitivity Solution (NSS; Ford *et al.*, 2010) to map the full moment tensor solution goodness of fit in the complete source-type space (Hudson *et al.*, 1989). Further discussion of these statistical tests is provided in later sections. All of these tests require significant computational effort; therefore, a staged approach is taken in which no additional analysis is performed if a solution is largely DC. If a solution has large non-DC components such as a CLVD (Knopoff and Randall, 1970) and/or a volumetric term, an *F*-test is first performed to assess significance of the more complex model. If the *F*-test indicates a significant improvement in fit with the non-DC terms then the jackknife, bootstrap, and NSS analyses are performed to assess the stability of the solution and the confidence in the recovery of the non-DC components.

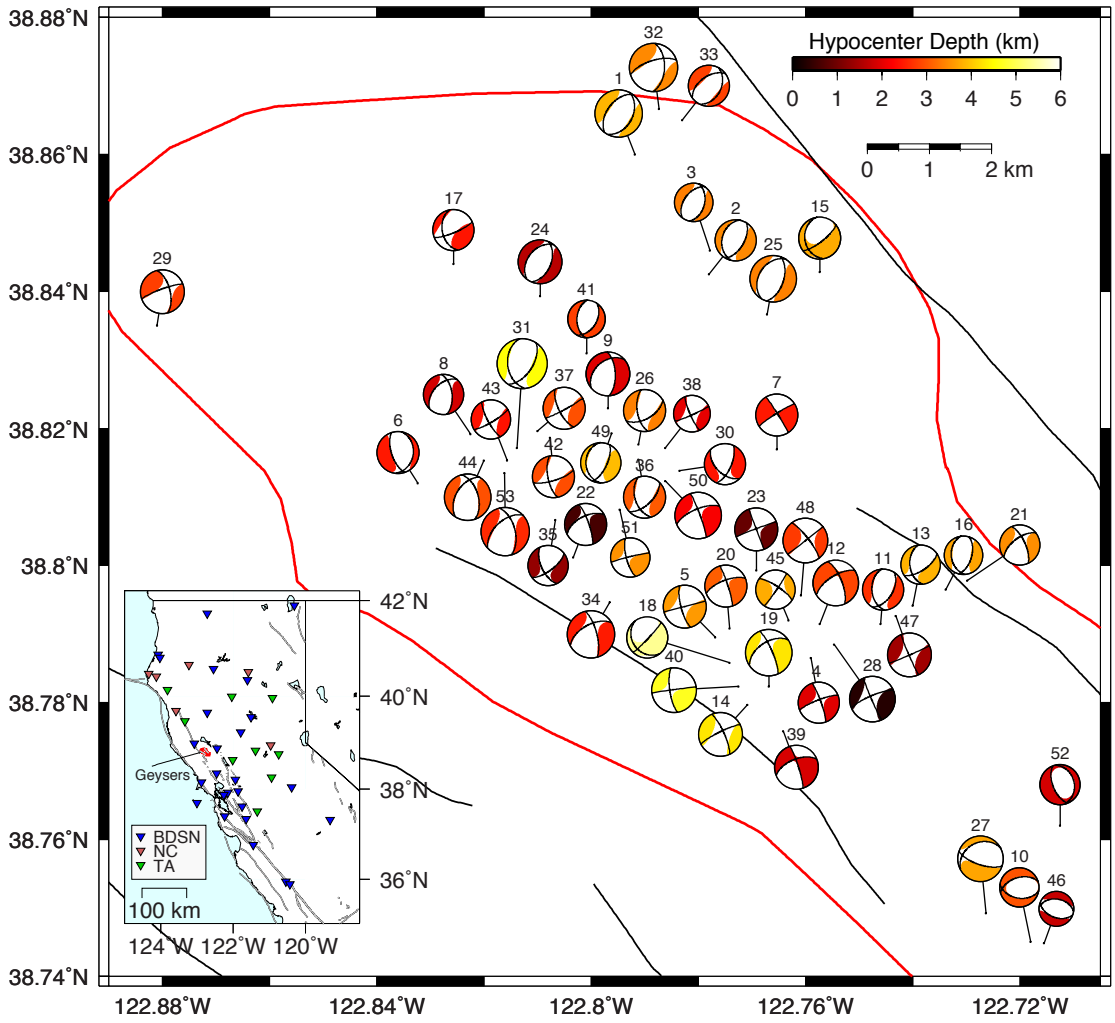

Figure 2.1. Deviatoric moment tensor solutions, shaded by hypocenter depth determined by NCSS, of numbered events listed in Table 2.A.1 in Section 2.8 Appendix. The red line shows the extent of the geothermal steam field (C. Hartline, Calpine, personal comm., 2012), and black lines indicate the surface traces of known faults. The inset shows the locations of broadband stations used in the analysis.

In the course of our study, we found that the depth sensitivity of data filtered between 0.02 and 0.05 Hz is fairly limited. We therefore restrain our analysis to event depths determined from the NCSS catalog, which utilizes data recorded by local Lawrence Berkeley National Laboratory (LBNL) and U.S. Geological Survey (USGS) stations. In the future, with better-calibrated velocity models and/or seismic data recorded with local stations, we may be able to improve on moment-tensor-based source depth determination. However, for now we assume that the depths reported in the catalog are well determined and focus on the recovery of the seismic moment tensor source parameters.

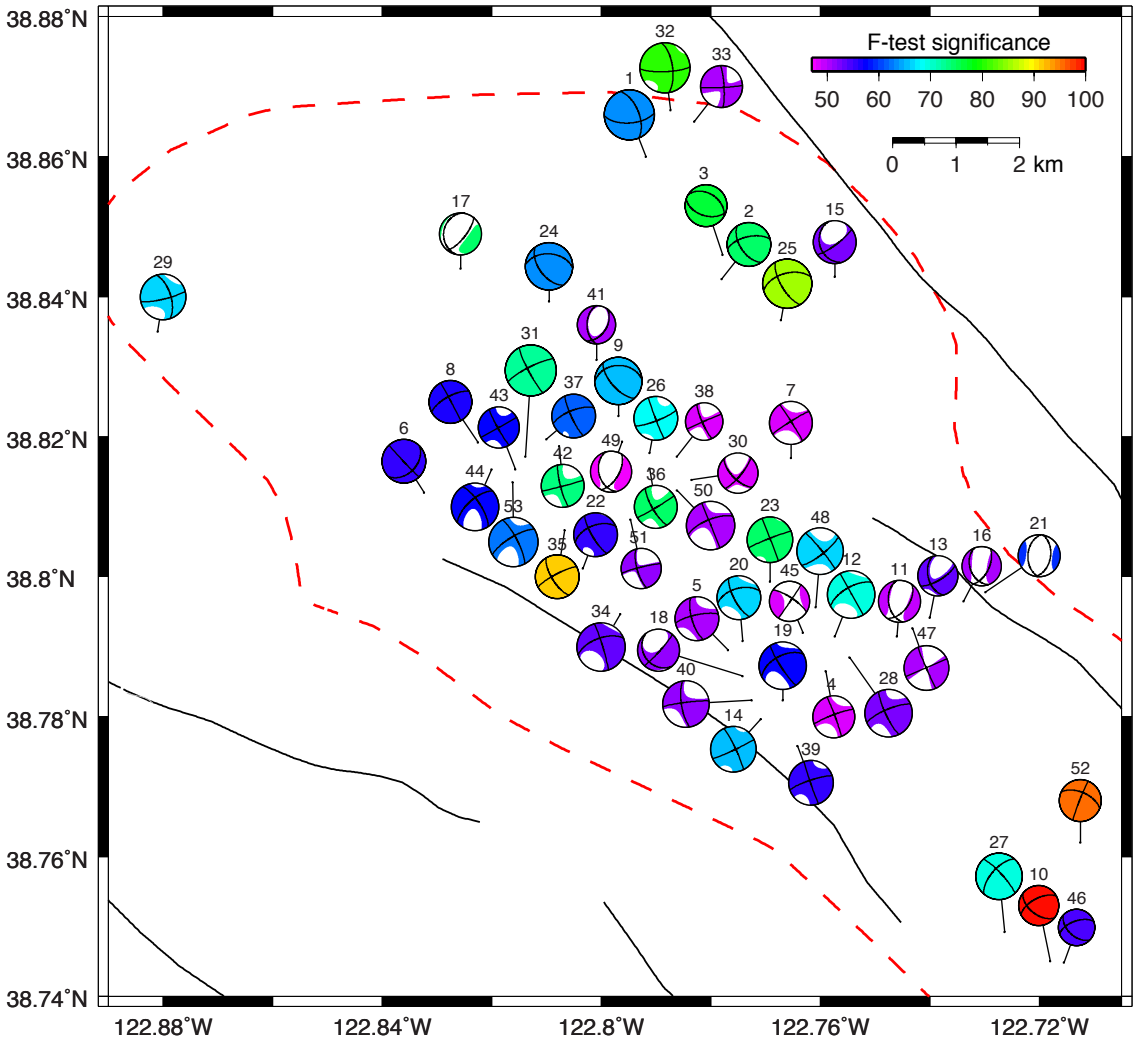

Figure 2.2. Full moment tensor (FMT) solutions, shaded by the statistical significance of the isotropic component as determined by the *F*-test, of numbered events listed in Table 2.A.2 in Section 2.8 Appendix. The red dashed line shows the extent of the geothermal steam field (C. Hartline, Calpine, personal comm., 2012), and black lines indicate the surface traces of known faults.

2.4 Results

2.4.1 Catalog Statistics

In Figure 2.1 deviatoric moment tensors solutions are shown for the studied events. These solutions show a predominantly east-southeast tensile axis varying from relatively rare strike-slip to more common normal-faulting events. Large CLVD solutions can accompany both of these DC types. One important exception is in the southeast Geysers, where the tensile

axis is oriented north-south. For comparison, the full moment tensor solutions are shown in Figure 2.2. Here, the moment tensors are shaded by the statistical significance of the isotropic component recovered from the full moment tensor inversion, as determined by the *F*-test. There are several solutions in which the statistical significance is relatively high. It is interesting to note that the DC component of these solutions is more consistent with the strike-slip mechanisms shown in Figure 2.1. Most of the deviatoric and full moment tensor solutions show an orientation of east-southeast for the tensile axes that is consistent with recent moment tensor investigations of Johnson (2014a,b) and Guilhem *et al.* (2014) and recent stress studies using focal mechanisms by Martínez-Garzón *et al.* (2013) and Boyle and Zoback (2014). However, for the few earthquakes in the southeast Geysers, the orientation of the tensile axes is rotated north-northeast and is consistent with Kirkpatrick *et al.* (1996) who investigated earthquakes in the southeast Geysers. They found the orientation of principal axes of moment tensors with positive volumetric components to be consistent with a normal-faulting mechanism and rotated from the regional tectonic stress.

One event (event 10) has a large isotropic component with a very high measure of statistical significance. It occurred on 12 October 1996 in the southern end of the field. The deviatoric solution for this event and others nearby show an unusual east-west striking normal solution. The deviatoric and full moment tensor solutions for all studied events are given in Tables 2.A.1 and 2.A.2, respectively, in Section 2.8 Appendix. Full moment tensor solutions having greater confidence as determined by the *F*-test and other statistical and sensitivity analyses described below are indicated by asterisks. These events are more fully investigated in a later section.

2.4.2 Statistical Comparison of Northern California and The Geysers Full Moment Tensor Catalogs

Because the decomposition of the seismic moment tensor is nonunique, it is useful to consider full moment tensor solutions in the Hudson *et al.* (1989) source-type space. This representation plots the ratio of the largest and smallest deviatoric eigenvalues (*T*) on the x axis, and the ratio of the isotropic moment and total moment (*K*; Bowers and Hudson, (1999)) on the y axis. *T* and *K* are defined below. The eigenvalues of the full moment tensor are m_1, m_2, and m_3.

$$T = \frac{2m_1^{dev}}{\left|m_3^{dev}\right|}, \qquad in\ which \quad \left|m_3^{dev}\right| \geq \left|m_2^{dev}\right| \geq \left|m_1^{dev}\right| \tag{2.1}$$

and

$$K = \frac{M_o^{iso}}{\left|M_o^{iso}\right| + \left|m_3^{dev}\right|}, \qquad in\ which \qquad M_o^{iso} = (m_3 + m_2 + m_1)/3. \tag{2.2}$$

T and *K* range from -1 to 1. Hudson *et al.* (1989) introduced a mapping that results in a uniform distribution of *T* and *K* presented in a Cartesian coordinate system with two

parameters *u* and *v*, which can range from -1 to 1, that represent the deviatoric and volumetric components of the moment tensor in the same manner as *T* and *K*.

Full moment tensor solutions from the 1992−2012 BSL catalog consisting of 828 events and excluding The Geysers events in this study, were computed from the Northern California Earthquake Data Center database. Figure 2.3a shows the source-type plot for these 828 events distributed throughout northern California and The Geysers, denoted by plusses and circles, respectively.

Dreger *et al.* (2000) and Templeton and Dreger (2006) use the *F*-test to assess the statistical significance of the higher-degree-of-freedom full moment tensor solution compared with the lower-degree-of-freedom deviatoric solution. This test is based on the ratio of the model fit variance for the two cases normalized by the number of uncorrelated data. As in Dreger *et al.* (2000) we use the temporal width of the applied Butterworth filters to assess the degree of correlation of samples in the data time histories. For example, we are commonly inverting 120 s of 1 sample/s data for a three-component station, resulting in 360 independent data points. For a 20 s Butterworth filter, we consider only 18 independent data points in computing the *F*-test significance. With this conservative approach, Figure 2.3a shows that the vast majority of northern California events have *F*-test significance less than 50% (549 out of 828 events), and only five events have significance above 90%.

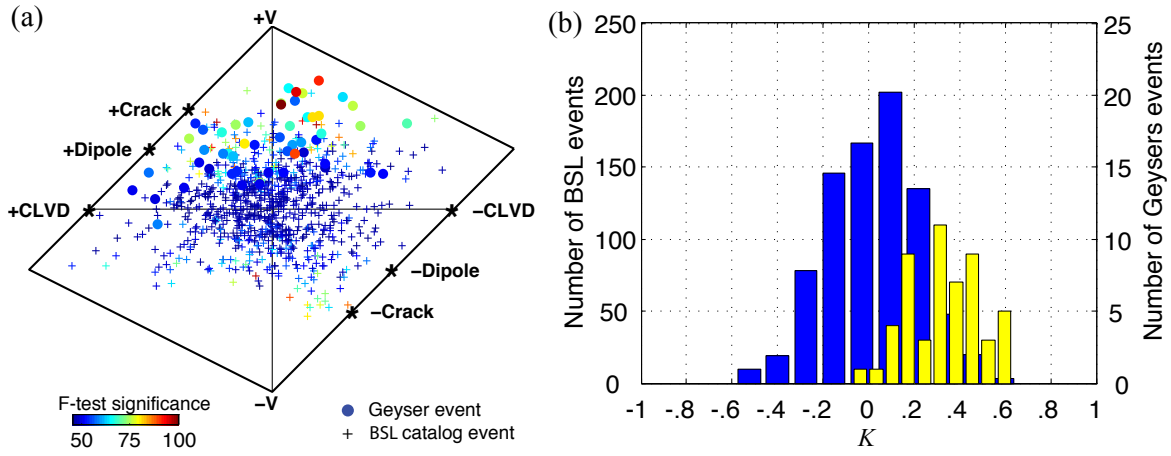

Figure 2.3. (a) Source-type plot of 828 events from the Berkeley Seismological Laboratory (BSL) catalog (plusses) and 53 events from The Geysers (circles), shaded by statistical significance as determined by the *F*-test. (b) Histogram of the isotropic parameter, *K*, for BSL catalog (blue, background distribution), number of BSL events along the left axis, and Geysers (yellow, foreground) with number of events along the right axis.

Of these, three occurred in Long Valley between 1995 and 1998 (Dreger *et al.*, 2000; Templeton and Dreger, 2006), one occurred 102 km north of The Geysers, and one occurred offshore of Arcata, California. These latter two may be due to poor station coverage. When Geysers solutions are evaluated with this test, 6 events are above 80%, 3 events are above

90%, and only 1 event meets the very stringent criteria of better than 99% significance. Thus, The Geysers is unusual with a high number of possibly statistically significant volumetric moment tensor solutions. It is interesting that, for all of the Geysers events with relatively high statistical significance, their solutions have components of volume increase, in contrast to Ross *et al.* (1999), who showed both volume-increase and volume-decrease source mechanisms from their first-motion and body-wave amplitude ratio analysis.

Fitting a multivariate normal distribution to the northern California data reveals that the mean in *T*, *K* space is -0.0132 and 0.0182, essentially indicating that the distribution is centered on DC mechanisms for these events. On the other hand, the 53 Geysers events (Fig. 2.3b) are shifted substantially away from the DC origin, and the mean of the distribution in *T* and *K* space is -0.0177 and 0.3331. The Geysers events stand out as a population with the largest *K* values in the volume-increase region (upper half) of Figure 2.3a. The *K* parameter of both the BSL and Geysers catalogs is normally distributed with unequal sample variance of 0.04 and 0.03, respectively. The separation of the means in the two populations is 0.32, a 99.9% statistically significant shift that corresponds to greater than 2σ of the northern California event distribution as computed by the two-sample *t*-test of unequal sample sizes, (Bock *et al.*, 2010).

2.4.3 Case Study of Selected End-Member Events

2.4.3.1 Example of a Dominant DC Event

First, we consider event 41, M_W 3.6 on 30 January 2010, with a dominant DC solution. Figure 2.4 shows the waveform fits, *P*-wave radiation pattern, and the NSS (Ford *et al.*, 2010) of the full moment tensor.

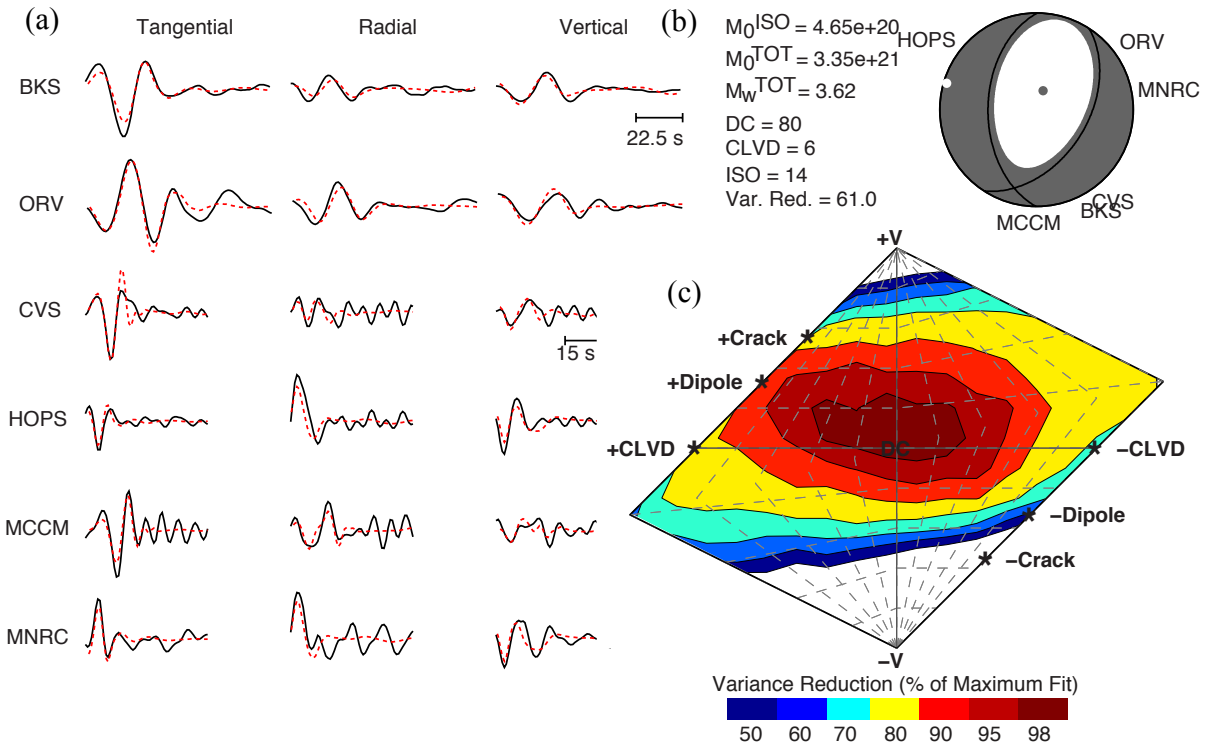

Figure 2.4. Event 41, 30 January 2010 M_W 3.6: (a) Observed (solid) and synthetic (dotted) waveforms from the FMT solution with 80% DC, 6% CLVD, and 14% ISO components. (b) The FMT inversion yields a mostly normal focal mechanism. (c) The network sensitivity solution (NSS) plot shows a maximum fit surface in source-type space. The fit is scaled to maximum fit found from 200 million uniformly distributed moment tensor solutions. The central region is within 98% of the maximum fit. It is notable that the deviatoric line along the horizontal axis has solutions that are above 80% of the maximum fit.

For six three-component stations, the deviatoric solution fits at 60.4%, measured by the variance reduction (VR) shown as equation (2.3), in which d, and s are data and synthetic seismograms, respectively:

$$VR = \left(1 - \frac{\sum(d-s)^2}{\sum d^2}\right) \times 100. \qquad (2.3)$$

This event features an 80% DC component with the full moment tensor solution showing a low level of statistical significance of only 50.84%. The NSS maps the maximum fit surface by considering as many as 200 million moment tensor solutions uniformly distributed in source-type space and has been shown to be a useful tool in event source-type discrimination (e.g., Ford *et al.*, 2012; Chiang *et al.*, 2014). For event 41, we find that the best-fit region is centered near the DC solution. The 98% fit contour indicates uncertainty in the solution, showing that good levels of fit can also be obtained with mixtures of approximately 20% volume increase and ±40% CLVD. As mentioned before, the improved fit afforded by the extra degree of freedom of the volumetric component is not statistically significant compared

to the deviatoric solution. The restrained deviatoric moment tensor inversion results in a DC component of 96% of the total seismic moment, and thus the interpretation for this event is that it has a DC mechanism.

2.4.3.2 Example of an Anomalous Large Isotropic Component Moment Tensor

Next we compare the result for event 10, M_W 3.75 on 12 October 1996 in the southeast region of the geothermal field, which has a large non-DC moment tensor solution (Fig. 2.2). The *F*-test for a solution utilizing 10 three-component stations results in a statistical significance of 99%, indicating this event is anomalous compared to both the northern California catalog and the 53 Geysers events considered in this study.

Recorded data and synthetic waveforms for event 10 are shown in Figures 2.5a and 2.5b for the deviatoric and full moment tensor solutions, respectively. Using waveforms from 10 stations, the deviatoric solution yields a VR of 65.3%, as measured by equation (2.3). However, the full moment tensor solution results in a substantially better VR of 77.6%. Given the number of stations, components, the corresponding data samples, and consideration of the degree to which individual samples are correlated through the applied low-pass filter (e.g., as defined in Dreger *et al.*, 2000), as described above, the full moment tensor solution represents an improvement in fit above the 99% level, and has a larger 57% volume-increase component.

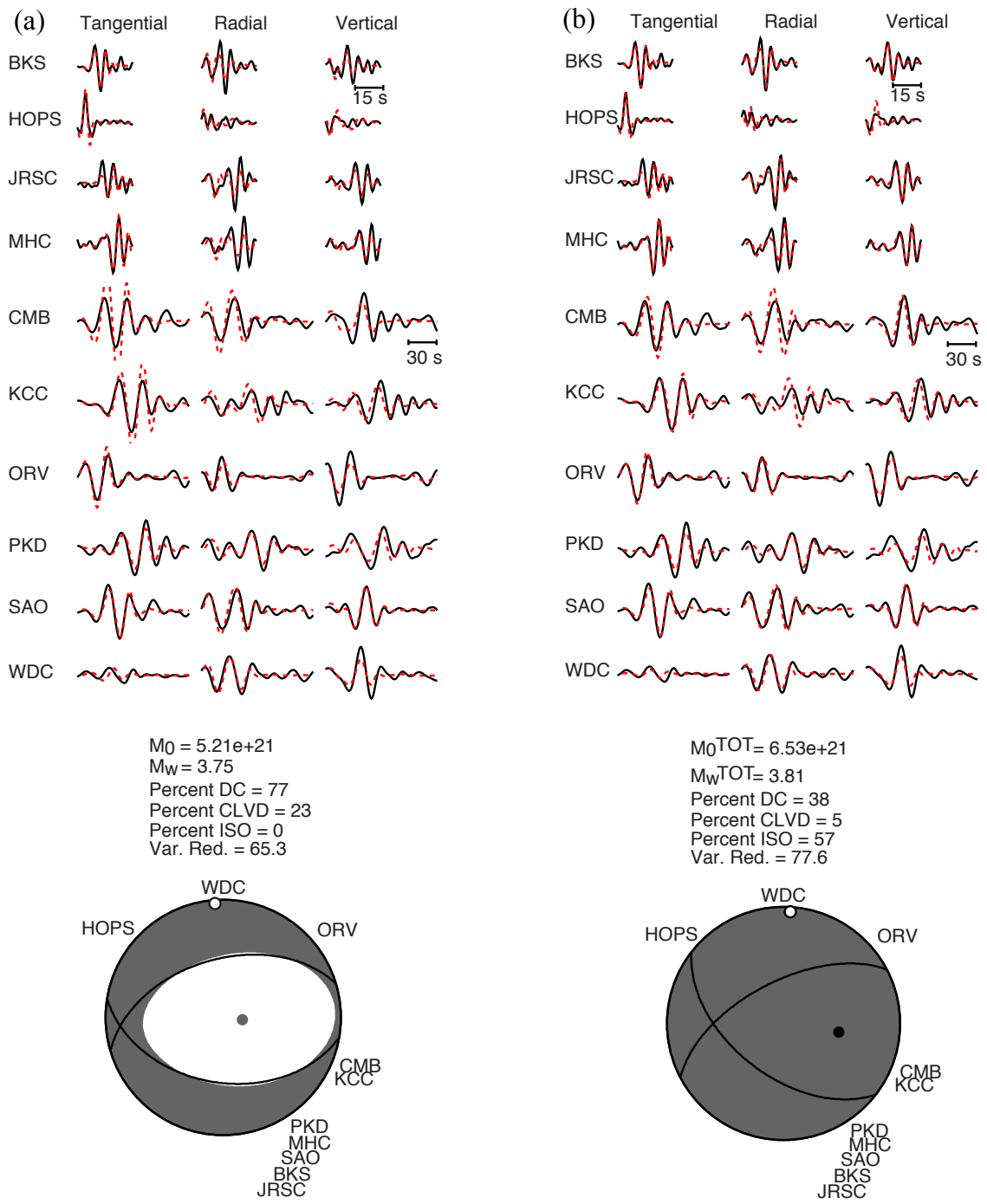

Figure 2.5. Event 10, 12 October 1996: (a) Observed (solid) and synthetic (dashed) waveforms and deviatoric moment tensor solution. (b) Observed (solid) and synthetic (dashed) waveforms and FMT solution. The improvement in fit of the FMT solution is statistically significant at 99% as determined by the *F*-test.

To examine the stability of the full moment tensor solution, we apply a jackknife test on station subsets. The jackknife test is performed by inverting all combinations of 9, 8, 7, and 6 stations from the full 10-station set and plotting the *T* and *K* parameters on a source-type plot (Fig. 2.6). The best 10-station solution is shown with a star, and the 9-, 8-, 7-, and 6-station solutions are indicated with circles. The majority of the groups that have a smaller isotropic component are composed of six stations and have one station in common, HOPS. These tests show that no single station or particular azimuth is biasing results toward a non-DC solution, and that the solution is very stable.

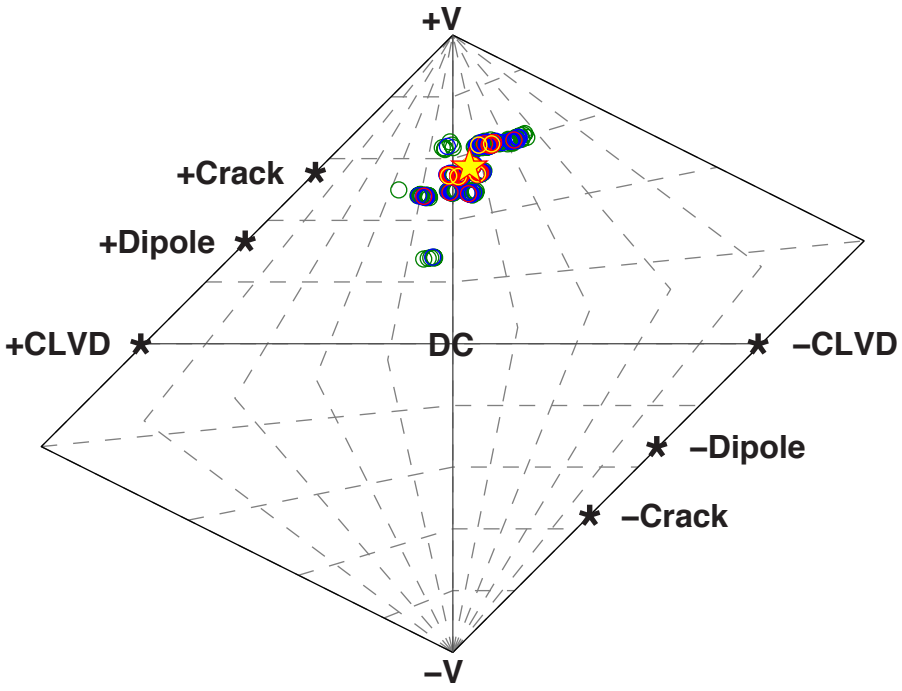

Figure 2.6. Event 10, 12 October 1996: jackknife tests with subsets of 9, 8, 7, and 6 stations (circles) from a total of 10 stations. The star indicates the best 10-station moment tensor solution.

Random errors in the solution are found by bootstrapping residuals from which the residuals between observed and synthetic waveforms from the best-fitting solution are then randomly applied to the data. The data are then re-inverted. We test 10,000 realizations. Although random noise could be used, actual signal-to-noise levels are low, and thus the estimated uncertainty would be quite low. Application of residuals assigns errors at a level that the applied model (velocity model Green's functions and moment tensor solution) fails to fit the data. Using the residuals instead of an *a priori* estimate of noise is both more conservative and meaningful. Figure 2.7 shows that the aleatoric uncertainty in the non-DC solution is very small.

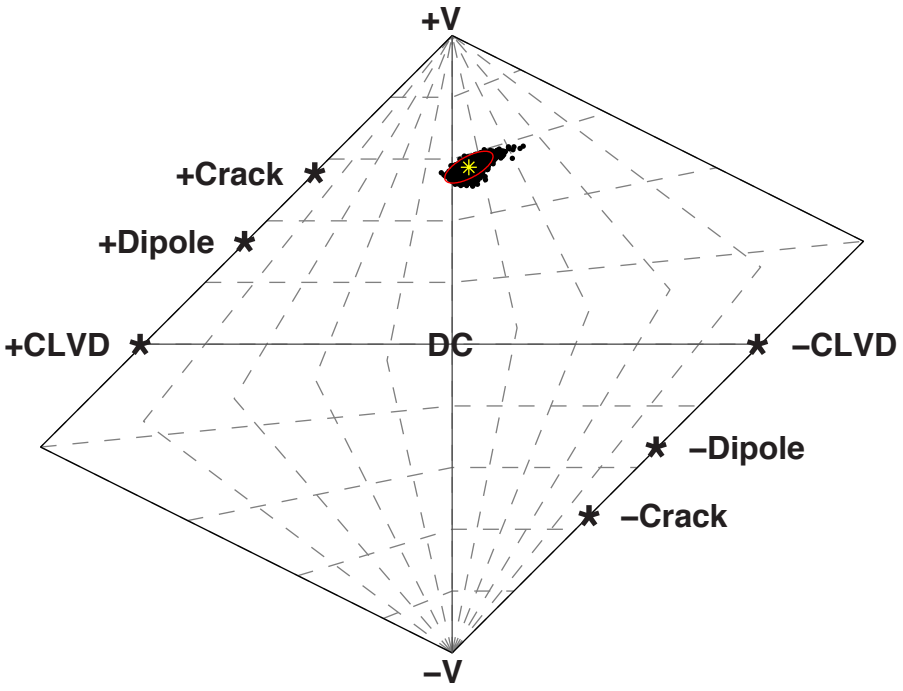

Figure 2.7. Event 10, 12 October 1996: results of 10,000 bootstrap simulations of residuals from the best moment tensor solution, shown with the asterisk. The 99% confidence ellipse of the distribution of moment tensor solutions is computed by bootstrapping the residuals.

It is interesting to examine the decomposition of the full moment tensor solution for the different tested source depths. Figure 2.8a shows the source depth is shallow with the best-fitting depth of 3.5 km, which is consistent with the catalog depth of 2.98. Figure 2.8b shows all of the solutions have relatively small DC components (generally less than 45%). As the source depth gets deeper, the solution becomes dominantly isotropic, and there are no solutions that result in a large DC or a small isotropic solution over the range of depths. The *F*-test level of significance at depth 1.5 km is 50.6% and increases to over 99% at greater depths. It is important to note that, in general, The Geysers events tend to be shallow (less than 5 km) as shown in Figure 2.1.

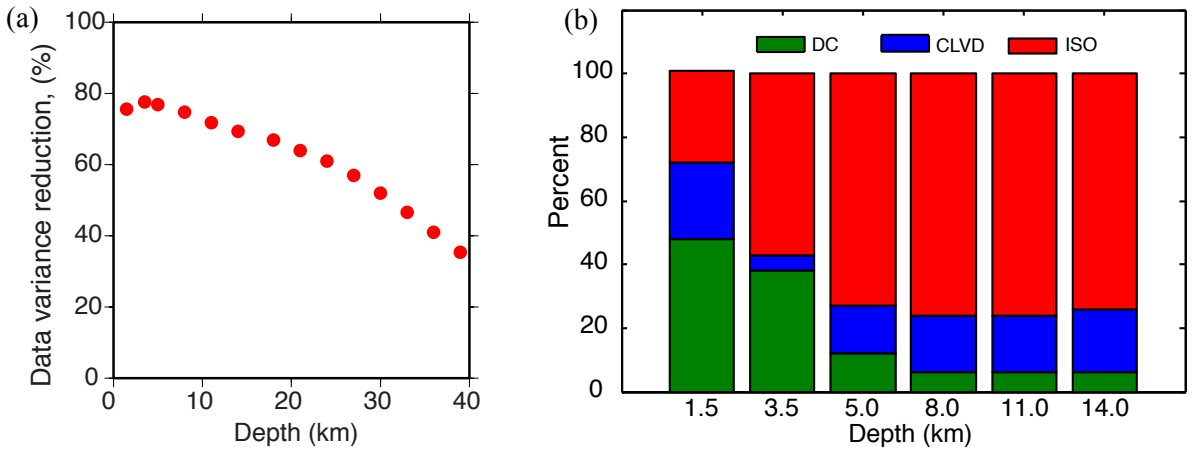

Figure 2.8. Event 10, 12 October 1996: (a) Goodness-of-fit, expressed as variance reduction of the full moment tensor solutions, as a function of source depth. (b) Relative percentages of DC, CLVD, and ISO (volume-increase) components of the FMT solutions as a function of source depth.

In Figure 2.9 we show the NSS maximum fit surface considering 200 million uniformly distributed moment tensors, testing the solutions against the 10 three-component waveforms shown in Figure 2.5. The upper fields are showing 90%, 95%, and 98% of the best-fit solution. The DCs and deviatoric solutions fit, at best, only 80% of the best-fit solution. A striking observation is the considerably different goodness-of-fit surface compared to the previous DC case, which demonstrates the anomalous nature of the seismic radiation in event 10 compared to event 41. A similar difference in NSS was found for the 2009 Democratic People's Republic of Korea nuclear explosion and a nearby Chinese earthquake (Ford *et al.*, 2010) and formed the basis for discriminating the explosion from an earthquake using regional moment tensor analysis.

Finally, we compare the goodness of fit of several other solution types in Table 2.1. The pure DC and explosion cases, as well as the DC + explosion and tensile-crack + DC are best-fit solutions determined by grid search. A pure explosion fails to fit the data because such a model does not generate *SH* and Love waves, which are very strong in the long-period records (Fig. 2.5). The range of solutions on the deviatoric line fits the data substantially worse than any of the solutions that include an isotropic component. This suggests that an isotropic component is indeed needed to provide a good level of fit to the data, although there is uncertainty in terms of what the underlying mechanism may be.

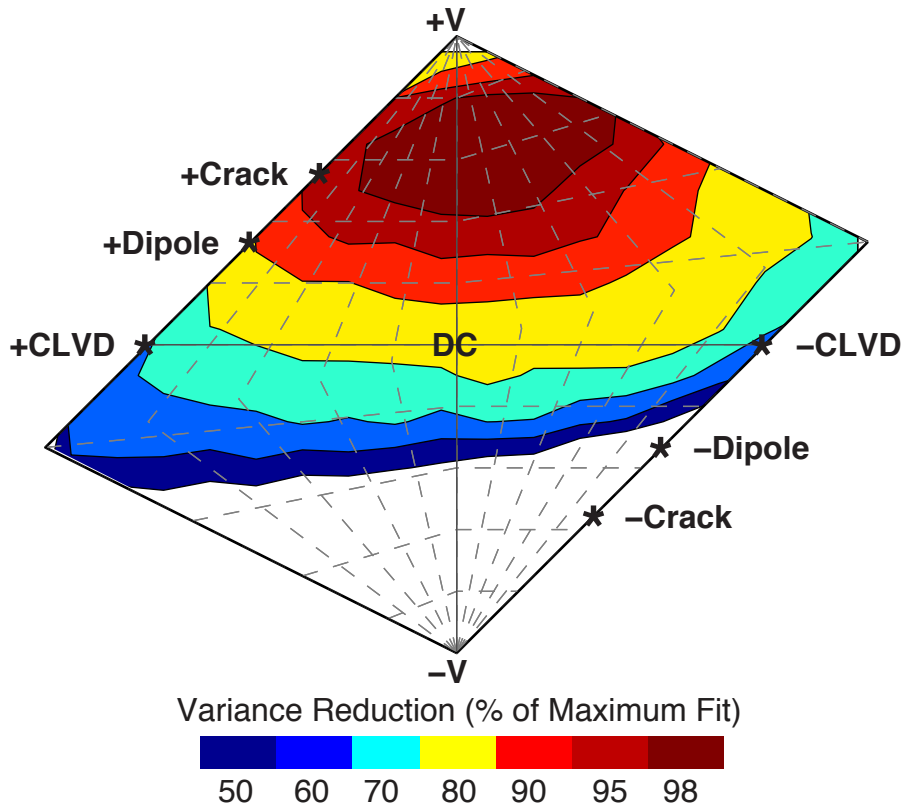

Figure 2.9. NSS for event 10, 12 October 1996: This plot shows a maximum fit surface in source-type space. The fit is scaled to a maximum fit found from 200 million uniformly distributed moment tensor solutions. The dark shaded region in the upper half is within 98% of the maximum fit. It is notable that the deviatoric line along the horizontal axis lies in a region where the variance reduction ranges from 70-80% of the maximum fit.

Table 2.1
Model Fits of Event 10, 12 October 1996

Solution Type	VR	Percent of maximum VR
Full Moment Tensor	78	100.0
DC + explosion	73	93.5
Tensile-crack + DC	72	92.3
Deviatoric	65	83.3
Double-couple	64	82.1
Explosion	18	23.1

Variance reduction (VR) as defined by equation (2.3), and percent of maximum VR of different moment tensor decompositions for event 10.

In summary, the evidence for event 10 indicates a substantial and significant departure from a DC mechanism. The NSS distribution and the locations of the best solutions and uncertainty in source-type space, together with the results of the DC + explosion grid search results, indicate that the best mechanism for this event is likely a combination of a DC and a spherically symmetric volume-increase source. Examination of first motions, however, indicates a dilatational component at some stations suggesting that the large volumetric component may not have been the initiating process, but rather followed the DC component. Alternatively, the proportion of volume-increase moment release may have initiated relatively weakly and then developed into the dominant term as the source process evolved. There are several complex source mechanisms that could explain these data including the following: (1) thermally induced tensile weakening could initiate a shear dislocation that leads to larger tensile failure. The addition of cool injectate into the system could lead to these strong tensile stress conditions (Stark, 2003; Beall *et al*., 2010). (2) Strain from an initial shear dislocation could cause elevated pore pressures in a sealed region around the dislocation. If pore pressure could exceed the minimum local stress, the pore fluids could subsequently dilate pathways opened up from faulting damage (Ashby and Sammis, 1990; Lyakhovsky *et al*., 1997; Johnson and Sammis, 2001; Hamiel *et al*., 2004; Ben-Zion and Ampuero, 2009).

2.4.3.3 Examples of Events with a Small Volumetric Component

Event 44, with M_W 4.43 occurred on 1 March 2011. The deviatoric moment tensor solution is a north-northwest-striking normal DC with a moderate 47% CLVD component (Fig. 2.1). Comparing the VR of the deviatoric solution (79.3%) with that of the full moment tensor result (80%), we find that the best solution indicates a northwest-striking, strike-slip DC (Fig. 2.2) with a small (32%) component of volume increase. However, the fit of the full moment tensor solution is only marginally better, and this is consistent with the *F*-test, which indicates the improvement in fit with the extra degree of freedom rises to a significance level of only 58%. It should be noted that, for an event with a small volumetric component, the fit will be dominated by the nonvolumetric term. Therefore, the improvement in fit afforded by the volumetric term will be small, resulting in a low level of statistical significance as measured by the *F*-test. An interesting observation for this event, however, is that the full moment tensor inversion is more consistent with the first-motion observations (Fig. 2.10f).

Following the approach in Ford *et al*. (2012) and Chiang *et al*. (2014), in which both long-period waveforms and first motions are combined in an NSS (Ford *et al*., 2010) analysis, we find a best solution that satisfies both data sets. In this two-step method, the NSS is first evaluated for a large number of uniformly distributed sources. In this case, 200 million moment tensor solutions were considered (Fig. 2.10b). This NSS distribution is different than the two shown in Figures 2.4c and 2.9, for events 41 and 10, respectively. The solution of event 44 clearly does not have either the signature seen for the DC event 41 discussed previously (Fig. 2.4c) or for other DC events (Ford *et al*., 2010; Chiang *et al*., 2014). It also does not have a peaked or focused fit distribution for a large volume-increase component such as is seen for event 10 in Figure 2.9. Instead, the NSS fit distribution shows that both deviatoric (large non-DC) and solutions with varying degrees of isotropic radiation satisfy the data through a trade-off. The second step in the methodology is to evaluate the solutions found from the NSS analysis against the first-motion observations. This is accomplished by

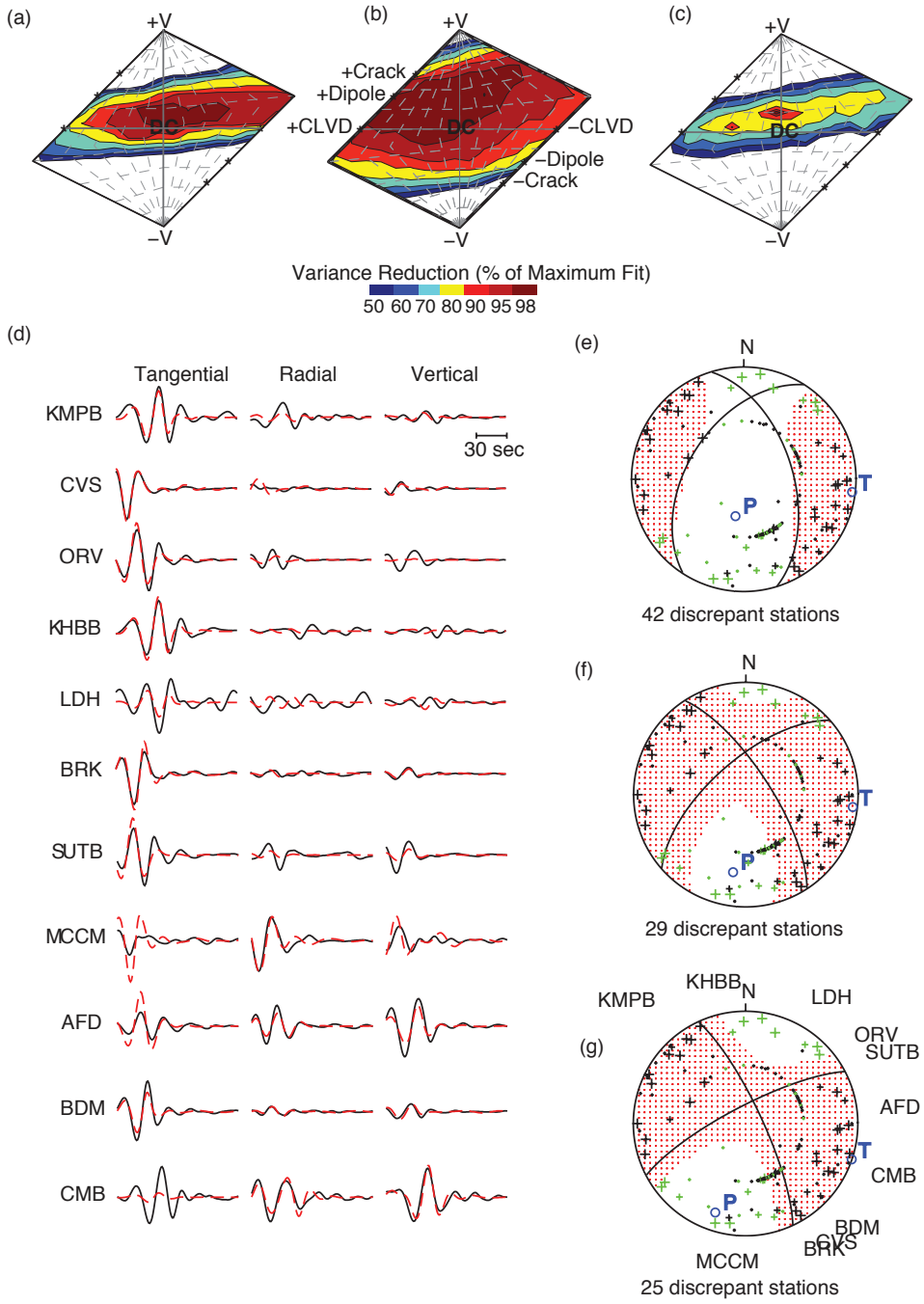

Figure 2.10. Event 44, 1 March 2011 M_W 4.43: (a) NSS for first motions. (b) NSS for FMT waveform analysis. (c) Constrained NSS obtained by testing the output of the waveform NSS against first-motion observations. (d) Observed (solid) and synthetic (dashed) waveforms for the FMT inversion. (e) Deviatoric solution and first motions. Compressional and dilatational first motions are shown with black and green plusses, respectively. (f) FMT solution and first motions. (g) Constrained FMT (CFMT) solution and first motions. The fit to the first motions in each case is given by the number of stations with first motions inconsistent with the various moment tensor solutions. A high number of stations with discrepant first-motion observations indicates a poor fit.

computing the polarity of the first motions from the NSS solutions and comparing them to the observed first-motion data. The VR is calculated as

$$\mathrm{VR} = \left(1 - \frac{\sum\left(\mathrm{Pol}_{\mathrm{obs}} - \mathrm{Pol}_{\mathrm{synth}}\right)^2}{\sum \mathrm{Pol}_{\mathrm{obs}}^2}\right) \times 100. \tag{2.4}$$

The combined waveform and first-motion VR is then calculated as

$$\mathrm{VR} = \left(\mathrm{sVR}_{\mathrm{reg}} \times \mathrm{sVR}_{\mathrm{fm}}\right) \times 100 \tag{2.5}$$

in which $\mathrm{sVR}_{\mathrm{reg}}$ and $\mathrm{sVR}_{\mathrm{fm}}$ are normalized by the maximum waveform and first-motion VR, respectively. This process finds the best waveform-derived solutions that can also explain the first-motion observations.

As can be seen in Figure 2.10e, there is an inconsistency between the deviatoric solution and the first motions with 42 discrepant observations; the full moment tensor solution, having a low *F*-test significance of 58%, better satisfies the first-motion observations with fewer (29) discrepancies. As discussed above, the solution in Figure 2.10g is obtained by subjecting the NSS analysis to both waveform and first motions. This mechanism provides a reasonably good level of fit to the waveform data, resulting in a 70.2% VR in waveform fit; and, for the first-motion data, there are only 25 discrepant observations. The DC component is consistent with other DC mechanisms found in the deviatoric analysis Figure 2.1. The small (24%) isotropic component may be due to tensile failure following weakening caused by the shear dislocation. Tensile stresses are produced by the cooling influence of injectate. Alternatively, the strain associated with the shear dislocation could cause pore pressures to elevate, promoting additional tensile failure if the pore fluids cannot rapidly dissipate. The moment tensor solution (M_{xx}, M_{xy}, M_{xz}, M_{yy}, M_{yz}, M_{zz}) for the combined waveform and first-motion inversion is (−157.82, −243.08, 100.58, 476.52, 36.4, 68.36) in units of 1 x 10^{20} dyn·cm.

There are several other events that have the same type of behavior as event 44. For example, event 37, M_{W} 3.99 that occurred on 24 February 2008, has a deviatoric moment tensor solution with a low DC component of 17% (Figure 2.1). Following the analysis described above, the results for this event are shown in Figure 2.11. Compressional and dilatational first-motion observations, shown with black and green plusses, respectively, are displayed with the deviatoric solution in Figure 2.11e. A high number of stations (48) have discrepant first motions compared to the deviatoric solution. In other words, there is an inconsistency between the deviatoric solution and first-motion observations, whereas the full moment tensor solution, with a higher *F*-test significance (80%) than the previous example, better satisfies the first motions with fewer stations (23) that have discrepant observations (Fig. 2.11f). The next step is to subject the NSS analysis to both waveform and first motions, and the best-fit solution is shown in Figure 2.11g. This mechanism provides a reasonably good level of fit to the waveform data (69.5% VR) and results in a minimum of 21 stations that have discrepant first-motion observations. The DC component is consistent with other DC mechanisms found in the deviatoric analysis (Fig. 2.1). The moment tensor solution (M_{xx},

M_{xy}, M_{xz}, M_{yy}, M_{yz}, M_{zz}) for the combined waveform and first-motion inversion is (−0.2472, −95.648, −24.37, 158.45, 85.757, 124.45) in units of 1 x 10^{20} dyn·cm.

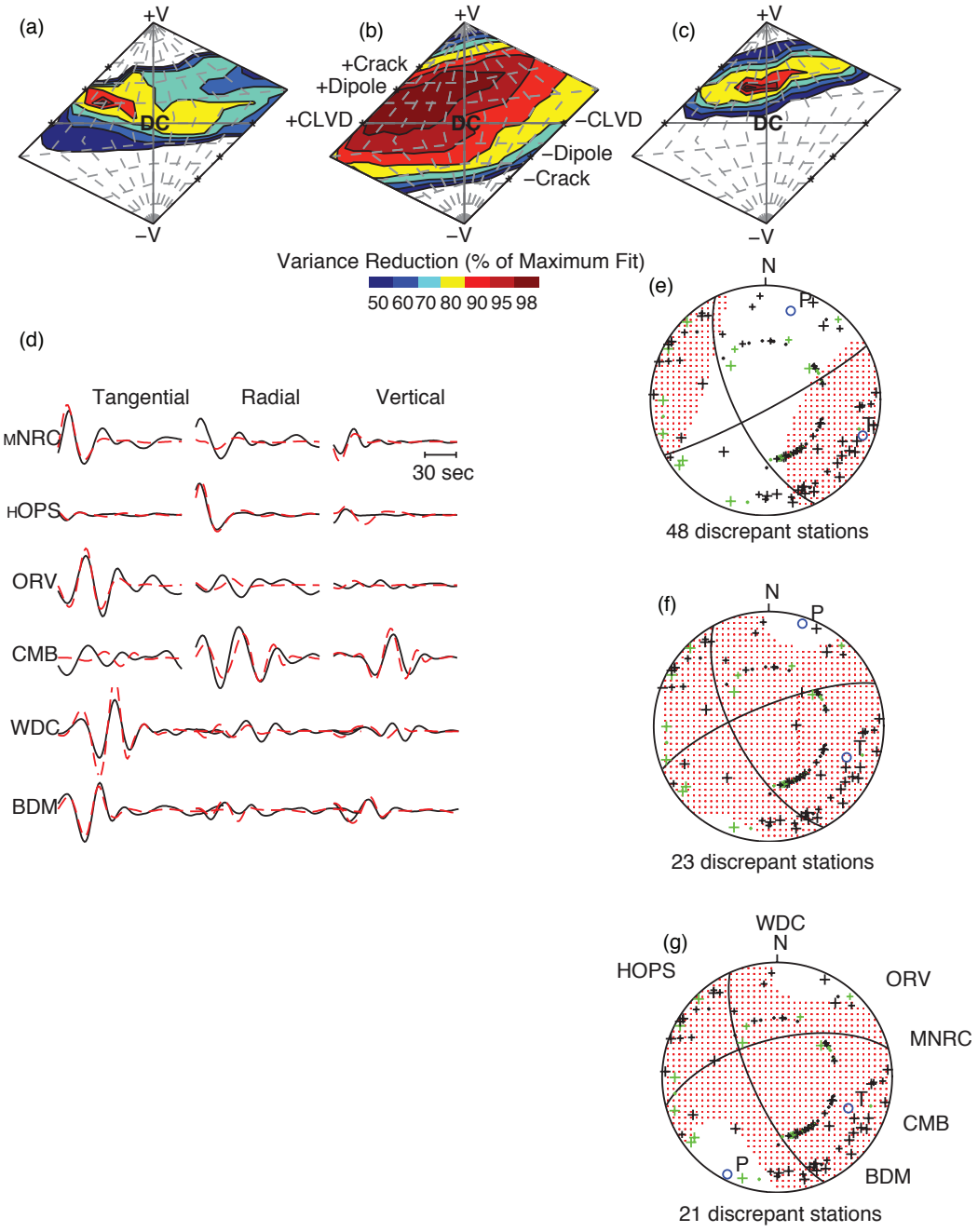

Figure 2.11. Event 37, 24 February 2008 M_W 3.99. (a) NSS for first motions. (b) NSS for FMT waveform analysis. (c) Constrained NSS obtained by testing the output of the waveform NSS against first-motion observations. (d) Observed (solid) and synthetic (dashed) waveforms for the FMT inversion. (e) Deviatoric solution and first motions. Compressional and dilatational first motions are shown with black and green plusses, respectively. (f) FMT solution and first motions. (g) Constrained FMT (CFMT) solution and first motions. The fit to

the first motions in each case is given by the number of stations with first motions inconsistent with the various moment tensor solutions. A high number of stations with discrepant first-motion observations indicates a poor fit.

Event 31, M_W 4.71 that occurred 12 May 2006, is the largest of the studied events with a relatively low DC component of 34%. Likewise, with the previous two events, a high number of stations (57) have discrepant first motions compared to the deviatoric solution shown in Figure 2.12e. Again, there is an inconsistency between the deviatoric solution and the first motions, with 57 discrepant observations, whereas the full moment tensor solution, with a relatively low *F*-test significance (59.56%) does not do much better with 56 discrepant observations, Figure 2.12f. As discussed above, by subjecting the NSS analysis to both waveform and first motions, the best-fit solution is shown in Figure 2.12g. This mechanism provides a relatively poor level of fit to the waveform data, (43.9% VR) and results in a minimum of 27 stations with discrepant observations. The DC component is consistent with other DC mechanisms found in the deviatoric analysis (Fig. 2.1). The moment tensor solution (M_{xx}, M_{xy}, M_{xz}, M_{yy}, M_{yz}, M_{zz}) for the combined waveform and first-motion inversion is (−604.4, 123.6, 443.4, 1235.0, 807.6, 339.9) in units of 1 x 10^{20} dyn·cm.

A final example is event 9, M_W 4.14 with a 99% DC component that occurred on 16 January 1995. The *F*-test evaluating the full moment tensor solution to the deviatoric solution shows an improvement in fit with a significance level of 65%. As seen in Figure 2.13g, the constrained waveform solution is most consistent with the first motion data, resulting with the fewest number of discrepant observations (23), compared with the deviatoric (Fig. 2.13e) and full moment tensor (Fig. 2.13f) solutions. As Figure 2.13e shows, there is an inconsistency between the deviatoric solution and the first motions with 38 discrepant observations. The fit of the first-motion data with the full moment tensor solution is slightly worse, with 40 discrepant observations (Figure 2.13f). However, the constrained mechanism provides a reasonably good level of fit to the waveform data, (57.4% VR) and results in a minimum of 23 discrepant observations. The DC component is consistent with other DC mechanisms found in the deviatoric analysis (Fig. 2.1). The moment tensor solution (M_{xx}, M_{xy}, M_{xz}, M_{yy}, M_{yz}, M_{zz}) for the combined waveform and first-motion inversion is (49.346, −45.078, −34.259, 172.62, 241.62, −127.21) in units of 1 x 10^{20} dyn·cm.

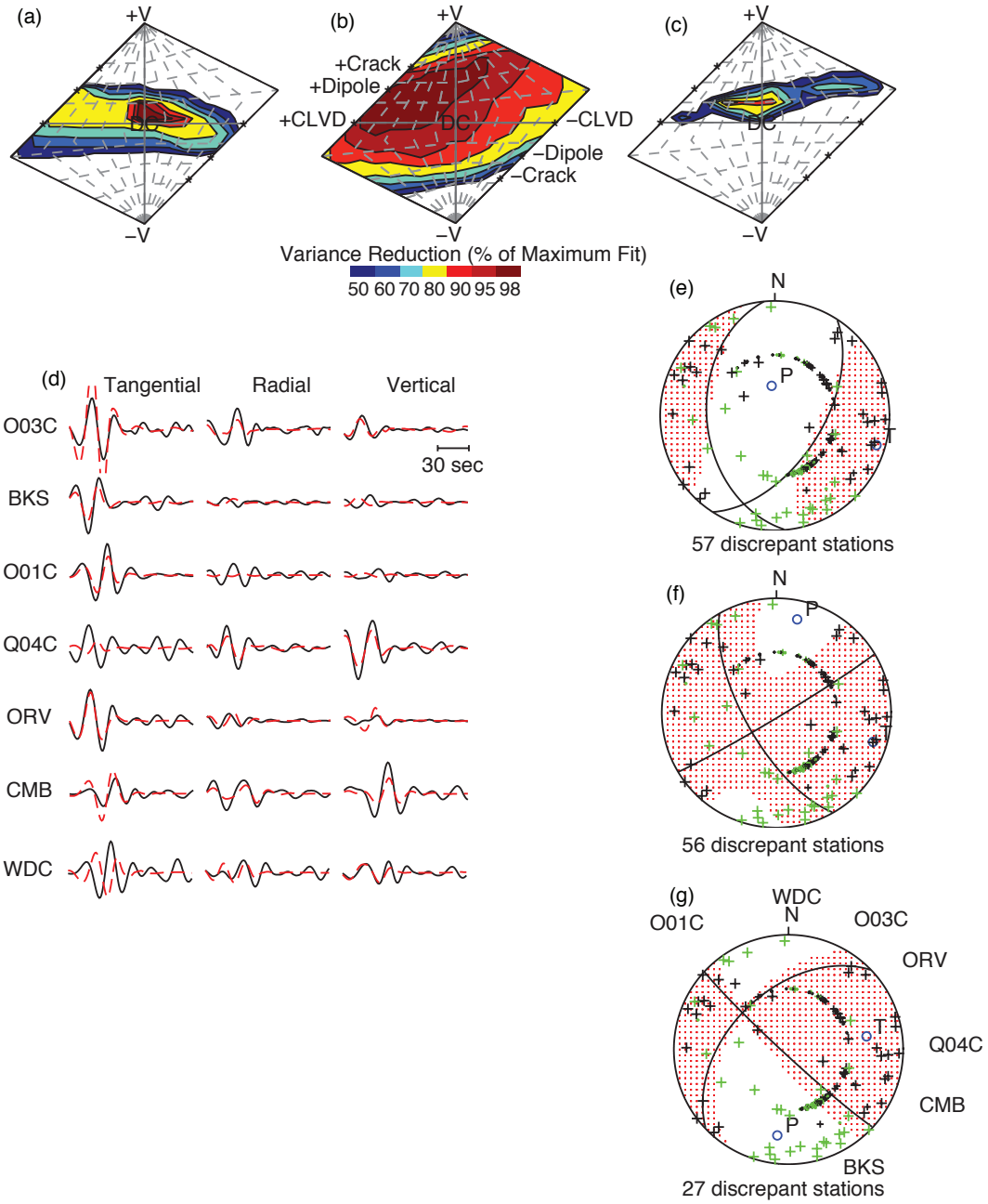

Figure 2.12. Event 31, 12 May 2006 M_W 4.71. (a) NSS for first motions. (b) NSS for FMT waveform analysis. (c) Constrained NSS obtained by testing the output of the waveform NSS against first-motion observations. (d) Observed (solid) and synthetic (dashed) waveforms for the FMT inversion. (e) Deviatoric solution and first motions. Compressional and dilatational first motions are shown with black and green plusses, respectively. (f) FMT solution and first motions. (g) Constrained FMT (CFMT) solution and first motions. The fit to the first motions in each case is given by the number of stations with first motions inconsistent with the various moment tensor solutions. A high number of stations with discrepant first-motion observations indicates a poor fit.

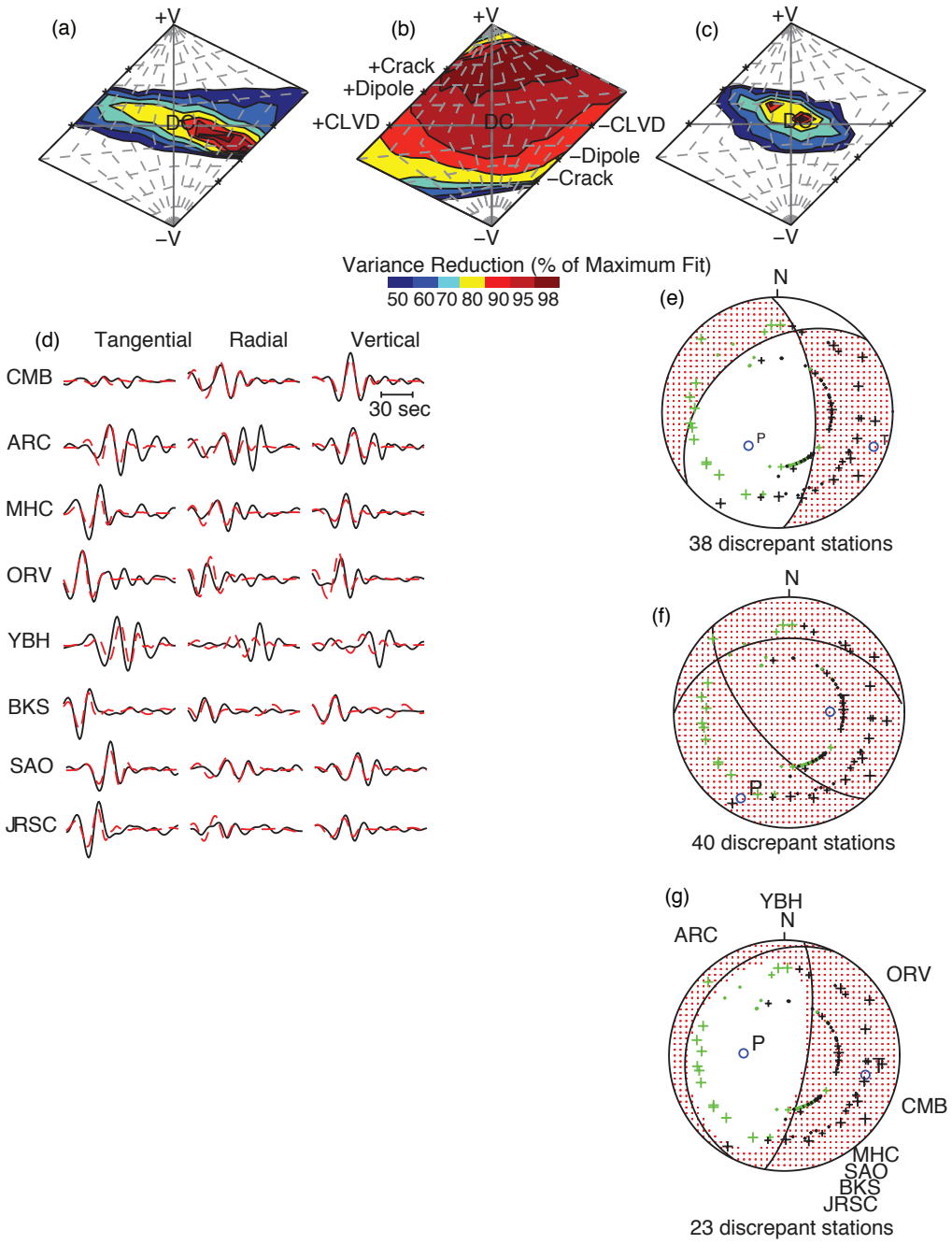

Figure 2.13. Event 9, 16 January 1995 M_W 4.14. (a) NSS for first motions. (b) NSS for FMT waveform analysis. (c) Constrained NSS obtained by testing the output of the waveform NSS against first-motion observations. (d) Observed (solid) and synthetic (dashed) waveforms for the FMT inversion. (e) Deviatoric solution and first motions. Compressional and dilatational first motions are shown with black and green plusses, respectively. (f) FMT solution and first motions. (g) Constrained FMT (CFMT) solution and first motions. The fit to the first motions in each case is given by the number of stations with first motions inconsistent with the various moment tensor solutions. A high number of stations with discrepant first-motion observations indicates a poor fit.

The results for these four events, listed in Table 2.2, suggest there may be a relatively small (10%-38%) volume-increase component in the constrained waveform mechanisms.

Table 2.2
Summary of First-Motion Fits

Date (yyyy/mm/dd)	Event Number	M_W	Dev Fit Disc. FM	FMT Fit Disc. FM	FMT VR DC/CLVD/ISO	CFMT Fit Disc. FM	CFMT VR DC/CLVD/ISO
2011/03/01	44	4.43	42	29	80.0 42/26/32	25	70.2 67/10/24
2008/02/24	37	3.99	48	23	78.7 33/19/48	21	69.5 43/19/38
2006/05/12	31	4.71	57	56	83.4 29/35/36	27	43.9 45/34/20
1995/01/16	9	4.14	38	40	68.9 27/8/65	23	57.4 86/4/10

Fits to deviatoric (Dev), full moment tensor (FMT), and constrained FMT (CFMT) solutions, as measured by the number of discrepant first-motion (Disc. FM) observations. A high number of discrepant observations indicates a poor fit. Also included are percent components of double-couple (DC), compensated linear vector dipole (CLVD), and volume-increase (isotropic, ISO) for FMT and CFMT solutions.

2.4.3.4 Event 10: 12 October 1996 M_W 3.75, an Anomalous Moment Tensor?

We applied the constrained FMT (CFMT) method to the 12 October 1996 M_W 3.75 event (event 10) to gain further insight into the unusually large and statistically significant isotropic component. The first-motion data have both up and down polarities and fit the deviatoric solution better than the full moment tensor solution with fewer discrepant stations (32 compared to 44), as shown in Figure 2.14d,e. Likewise, the constrained waveform solution, Figure 2.14f, has a large 65% DC component, 27% CLVD component, and 8% ISO component and is more consistent with the deviatoric solution, but it provides a very poor level of fit to the waveform data (VR = 43.2%). Clearly the high-frequency first-motion data appear to be inconsistent with the long-period moment tensor solution constrained at depth 3.5 km, the depth of our Green's functions closest to the USGS-determined depth of 2.98 km. Even though Figure 2.8a shows that we have relatively good source depth resolution, and the best depth of 3.5 km agrees well with the catalog depth of 2.98 km, we examined in detail the full moment tensor solution at depth 1.5 km with a 29% isotropic component, approximately half of that at depth 3.5 km (Fig. 2.8b). The first-motion data at depth 1.5 km fit the deviatoric solution better than the full moment tensor, as shown in Figure 2.14j and 2.14k, respectively, with 31 discrepant stations compared to 34. At the shallower depth, the high-frequency first-motion data are more consistent with the long-period moment tensor solutions and best fit the constrained full waveform solution (47% DC, 39% CLVD, and 14% ISO) with the fewest number (13) of discrepant stations (Fig. 2.14l). For the constrained waveform solution, the waveform fit is also relatively high (68.7%). The first-motion data are most consistent with the constrained waveform solutions at both depths, each having a relatively high DC component, moderate CLVD, and small ISO component compared with the full moment tensor solutions. However, both solutions produce an inferior fit to the waveform data with lower VRs. From this analysis, it seems that this event requires a volume-increase component, but its magnitude is complicated by the apparent inconsistency of first-motion and waveform

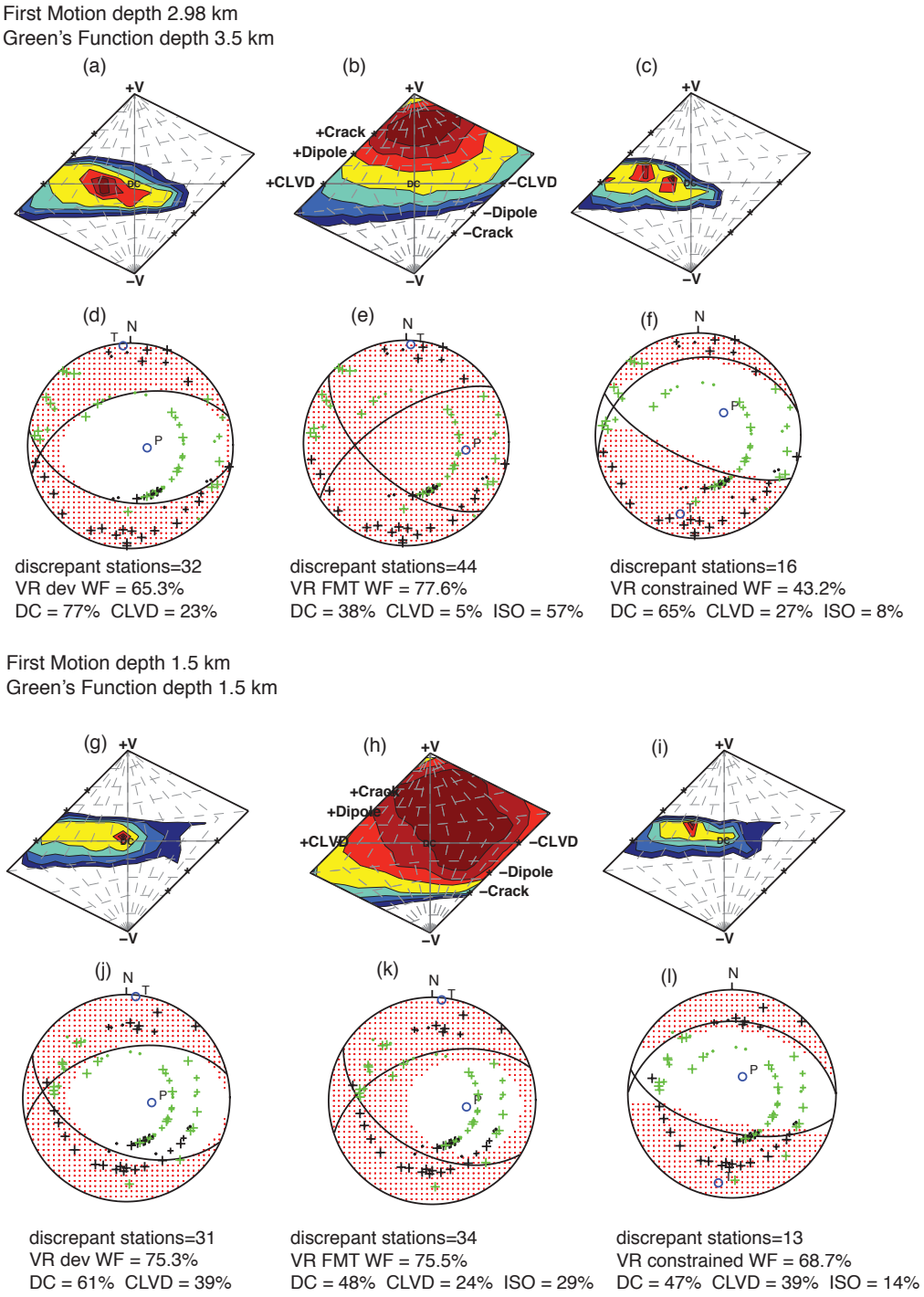

Figure 2.14. Event 10, 12 October 1996 M_W 3.57: (a-c) first-motion NSS, FMT waveform inversion NSS, and constrained waveform NSS at depth 3.5 km. (d-f) The deviatoric, FMT, and CFMT solutions at depth 3.5 km with first motions. Compressional and dilatational first motions are shown with black and green plusses, respectively. (g-i) Corresponding NSS solutions at depth 1.5 km. (j-l) Corresponding moment tensor solutions and first motions at depth 1.5 km.

results. The above analysis is predicated on the assumption that the first-motion and long-period waveforms are sensitive to the same source process, which is supported for the previous cases. However, it is also possible that the mechanism of this event could have transitioned from one that was initially shear dominated to one that was subsequently tensile dominated.

2.5 Discussion and Conclusions

Anomalous moment tensor solutions have been reported for past Geysers events (Julian *et al*., 1993; Ross *et al*., 1996, 1999). Over the past 22 years, the BSL has published analyst-reviewed seismic moment tensors that now comprise a catalog of 881 events in northern and central California. We found that the distribution of these events, excluding the studied Geysers events, has a mean consistent with a DC mechanism. As was shown in Figure 2.2, there are events that deviate from a DC, however, the vast majority of these do not have a level of statistical significance that indicates the isotropic components are resolved. We found that, as a population, the 53 studied events at The Geysers tend to have higher statistical significance of recovered isotropic components and that the mean of the distribution is significantly shifted to positive K, as defined in equation (2.2), indicating volume increase.

It has been shown that care is needed in evaluating the robustness and stability of non-DC and full moment tensor solutions (e.g., Dufumier and Rivera, 1997; Dreger *et al*., 2000; Vavryčuk, 2001, 2011; Templeton and Dreger, 2006; Minson *et al*., 2007; Ford *et al*., 2008, 2009, 2010). We applied a systematic procedure for the evaluation of aleatoric and epistemic solution uncertainty of seismic moment tensor solutions, using bootstrap, jackknife and NSS approaches to develop solutions that can be used to investigate the underlying mechanical and fluid-mechanical processes that result in the observed seismicity in The Geysers geothermal field.

This staged procedure first uses the *F*-test to evaluate the improvement in fit afforded by the extra degree of freedom of a full moment tensor inversion compared to a deviatoric moment tensor inversion. Based on this criteria, most of the 53 events may be characterized as deviatoric, however, there are 6 events with statistical significance above 80% and 3 above 90%. In cases in which events are found to have large positive isotropic components, we find from the additional sensitivity studies that the results are robust. We also found cases in which small isotropic components are likely, although based on the waveform data alone and the *F*-test, they are not resolved. Through the combination of long-period waveforms and first motions, we are able to obtain stronger constraints on the moment tensor solutions, finding that solutions that best satisfy both data sets are composed of a large strike-slip DC component with a relatively small, (10%−38%) volume increase. The use of first motions implies commonality of the source process from initiation (first-motions) to when the majority of moment release occurs (from the long-period waveforms), which of course may

not always be the case (Scott and Kanamori, 1985).

Event 10 in the southeast Geysers is such an example in which the very large isotropic component predicts compressional first motions at all azimuths and takeoff angles, which is not observed. As shown above, this could be due to source depth, where a shallower source depth reduced the isotropic component and provided a good level of agreement with first-motion polarities but very poor waveform fit. On the other hand, the waveform moment tensor inversion yields a best-fit depth of 3.5 km that is in agreement with the catalog depth of 2.98 km. Because of uncertainty in the depth from the moment tensor analysis due to imperfect velocity models and station coverage, we generally restrained our analysis to event depths determined from the NCSS catalog. When event 10 occurred in 1996, the LBNL and USGS seismic networks were smaller and errors in depth may have been greater than those today, especially for events located along the boundaries of the networks. However, it is also possible that as the source process evolved, beginning with a dominant shear mechanism with perhaps a small tensile component, it transitioned into a larger tensile component through a weakening process. The relatively small isotropic components found for other events based on a combined waveform and first-motion analysis indicates that this is a possibility. Tensile stresses in the geothermal field are produced by the cooling influence of injectate and could be a driving mechanism for some of these events.

As we have shown, there are some events that have strong evidence of positive isotropic moment tensor components that suggest a component of tensile failure. These observations are consistent with those of Guilhem *et al*. (2014) and Johnson (2014a). The extended crack model proposed by Johnson (2014b) accounts for volume increase through the opening of wing cracks at the ends of a shear crack. Not only does this model account for positive isotropic components, it also suggests that two modes of failure, including shear slip and tensile opening, may be sequential. Whether or not this could explain the discrepancy between high frequency first motions, indicative of a normal mechanism for event 10, and the long-period moment tensor solution with a 57% isotropic component would require further analysis. Another relevant point mentioned by Johnson (2014b) is the likelihood that cracks in close proximity may interact. Given the highly fractured subsurface with complex conjugate fault geometries and stress heterogeneity from nearby weakened fault zones, it may be possible that shear slip occurs such that critically stressed fractures, favorably oriented for failure, are reactivated, (Majer and McEvilly, 1979; Bufe *et al*., 1981; McLaughlin, 1981; Eberhart-Phillips and Oppenheimer, 1984; Oppenheimer, 1986; King *et al*., 1994; Cladouhos *et al*., 2009; Martínez-Garzón *et al*., 2013). Two other nearby events, event 27 (27 December 2004 M_W 4.31, depth 3.71 km) and event 46 (29 June 2011 M_W 3.26, depth 1.76 km) have large isotropic components of 49% and 52%, respectively. These events occur in the southern part of the reservoir, close to event 10 and have similar mechanisms composed of a north-south tensile stress axis and east-west normal DCs. This may be due to stress heterogeneity from the close proximity of the fractured and weakened east-west trending Big Sulfur Creek fault zone compared to the surrounding stress regime (Moore and Gunderson, 1995; Cladouhos *et al*., 2009).

Comparing moment tensor elements from different data sets with different frequency content (e.g., Guilhem *et al*., 2014) to see how well they agree or disagree may provide

insight into the stages of a time-dependent source mechanism, and broadband source analysis would be worthwhile to consider in a future study. The results presented here indicate that seismicity at The Geysers is complex. As a population, the studied events have more significant and larger volumetric components compared to the rest of California; however, based on our analysis, most of the events are likely the result of shear failure due to both tectonic shear stress and tensile stress induced by the injection of water and extraction of steam, but several of the studied earthquakes show evidence of tensile components that could be in response to tensile stress caused by thermal changes due to water injection.

2.6 Data and Resources

Data for this study come from the Berkeley Digital Seismic Network (BDSN; http://dx.doi.org/10.7932/BDSN, last accessed August 2014), operated by the University of California Berkeley Seismological Laboratory, which are archived at the Northern California Earthquake Data Center (NCEDC; http://dx.doi.org/10.7932/NCEDC, last accessed August 2014); Northern California Seismic Network; Lawrence Berkeley National Laboratory; and the Transportable Array. First-motion polarity data were acquired using FPFIT software (Reasenberg and Oppenheimer, 1985) with data from the NCEDC and reviewed using (1) the U.S. Geological Survey Jiggle software, a graphical earthquake analysis tool available for earthquake data processing centers and not intended for general public use, and (2) Seismic Analysis Code (Goldstein *et al*., 2003). Maps were made using Generic Mapping Tools v.4.5.9 (www.soest.hawaii.edu/gmt, last accessed August 2015; Wessel and Smith, 1998).

2.7 Acknowledgments

The authors thank Associate Editor Stephanie Prejean and three reviewers for their helpful comments and suggestions. We also thank the students, staff, and faculty of the University of California Berkeley Seismological Laboratory (BSL) for their contributions to the BSL moment tensor catalog, especially Peggy Hellweg, Taka‘aki Taira, Jennifer Taggart, and Tom Weldon; Sean Ford, Aurélie Guilhem, Seung-Hoon Yoo, Mong-Han Huang, Andrea Chiang, and Avinash Nayak for their codes and support; Harold Macbeth and David Oppenheimer, U.S. Geological Survey, and Pete Lombard, BSL, for help with first-motion data, and Craig Hartline, Calpine, for his support in this research. Data from this study come from the Berkeley Digital Seismic Network (BDSN), operated by the UC Berkeley Seismological Laboratory, which are archived at the Northern California Earthquake Data Center (NCEDC). Waveform data, metadata, or data products for this study were accessed through the NCEDC. This work is supported by the Assistant Secretary for Energy Efficiency and Renewable Energy, Office of Geothermal Technologies of the U.S. Department of Energy under Contract Number DE-EE0002756. This is Berkeley Seismological Laboratory

Contribution Number 2015-08.

2.8 Appendix

Table 2.A.1 Deviatoric Moment Tensor Solutions

No.	Date	Time	Mw	Mo	Mxx	Mxy	Mxz	Myy	Myz	Mzz	DC	CLVD	VR
1	19-Sep-92	23:04:47	4.47	6.25E+22	12.20	-475.91	71.09	457.67	-76.95	-469.86	25	75	66
2	18-Jan-93	23:27:11	3.92	9.42E+21	-5.06	-43.56	-21.66	79.03	32.00	-73.97	57	43	71
3	19-Jan-93	0:24:29	3.66	3.86E+21	0.30	-20.19	6.03	32.99	-0.30	-33.29	62	38	61
4	15-Feb-93	18:04:24	3.88	8.21E+21	-44.58	-60.90	11.26	60.55	8.35	-15.96	71	29	74
5	16-Mar-93	3:59:27	4.03	1.36E+22	-40.39	-115.11	-29.82	84.36	27.87	-43.97	38	62	70
6	23-Aug-93	15:03:27	3.99	1.18E+22	-23.08	16.10	-27.07	104.92	-64.95	-81.84	67	33	72
7	29-Nov-93	10:47:04	3.95	1.04E+22	-91.66	-45.44	10.40	94.41	4.85	-2.75	97	3	74
8	29-Aug-94	5:09:25	3.83	6.97E+21	-18.97	-29.98	14.10	68.51	15.78	-49.54	54	46	74
9	16-Jan-95	1:34:38	4.14	2.00E+22	-8.86	-86.36	53.30	145.65	97.97	-136.79	99	1	67
*10	12-Oct-96	4:25:47	3.75	5.21E+21	48.56	-2.66	3.59	3.38	-14.00	-51.94	77	23	65
11	18-Nov-96	6:56:53	3.89	8.40E+21	-25.27	-32.64	-13.95	89.64	8.68	-64.37	39	61	69
12	4-Dec-96	21:21:15	4.34	3.96E+22	-213.03	-199.91	171.01	323.54	82.38	-110.51	95	5	80
13	18-Jun-98	23:24:40	3.75	5.27E+21	-6.14	-29.86	-25.28	37.82	7.86	-31.68	70	30	67
14	18-Feb-99	8:58:42	4.15	2.08E+22	-99.85	-133.42	15.29	215.37	-13.83	-115.52	14	86	63
15	4-Apr-99	6:00:37	3.96	1.07E+22	-5.94	-15.52	-84.01	64.13	32.21	-58.19	52	48	50
16	29-Jul-99	4:52:27	3.66	3.83E+21	-16.43	-6.63	-3.75	43.90	12.00	-27.48	28	72	64
17	6-Jan-00	21:38:11	3.85	7.42E+21	-6.32	-58.14	-33.44	34.32	36.19	-28.01	12	88	69
18	5-Apr-00	2:20:31	3.88	8.36E+21	-24.09	10.37	-64.27	43.56	42.27	-19.47	48	52	62
19	8-Dec-00	7:41:11	4.37	4.48E+22	-268.99	-198.35	61.87	438.34	162.95	-169.35	45	55	86
20	18-Apr-02	11:35:41	3.98	1.17E+22	-51.01	-81.44	27.88	63.76	53.79	-12.75	98	2	79
21	9-May-02	11:07:56	3.78	5.82E+21	-32.07	-24.15	15.52	58.86	10.67	-26.79	56	44	79
22	20-May-03	16:50:42	4.05	1.50E+22	-60.68	-67.07	39.79	102.10	92.55	-41.43	82	18	80
23	3-Aug-03	12:00:53	4.09	1.70E+22	-102.59	-132.10	-3.38	108.47	-14.17	-5.88	93	7	81
24	3-Oct-03	16:56:35	4.13	1.94E+22	-17.74	-121.64	-115.97	99.74	36.28	-81.99	73	27	72
25	18-Feb-04	20:37:46	4.58	9.36E+22	114.45	-251.80	608.39	439.69	-432.57	-554.14	89	11	68
26	29-Oct-04	18:02:55	3.98	1.16E+22	-31.73	-80.80	-13.19	104.36	-15.59	-72.64	26	74	73
27	27-Dec-04	10:36:23	4.31	3.61E+22	296.96	-13.98	-224.28	-80.63	-102.88	-216.34	78	22	64
28	9-May-05	22:37:39	4.33	3.85E+22	-201.02	-250.35	-32.67	348.70	121.72	-147.68	27	73	81
29	19-Oct-05	0:05:12	4.14	2.03E+22	-67.32	-153.65	75.84	129.69	-33.07	-62.38	54	46	79
30	17-Nov-05	8:55:06	3.88	8.19E+21	-38.18	21.83	-24.79	83.72	23.52	-45.54	63	37	64
31	12-May-06	10:37:29	4.71	1.45E+23	-473.29	-598.33	-294.10	1512.30	343.24	-1039.00	34	66	83
32	20-Oct-06	17:00:08	4.56	8.70E+22	94.44	-757.22	263.03	405.55	-69.55	-499.99	30	70	80
33	20-Oct-06	23:31:40	3.86	7.70E+21	18.25	-71.44	12.75	33.68	-10.92	-51.93	9	91	73
34	24-Apr-07	21:08:29	4.46	6.03E+22	-233.54	-362.79	124.02	504.09	202.09	-270.55	58	42	81
35	20-Jul-07	17:50:20	3.79	5.98E+21	-32.92	-24.81	-22.04	58.14	1.56	-25.23	68	32	69
36	1-Dec-07	20:50:12	3.93	9.63E+21	-43.28	-44.70	-17.69	105.00	13.44	-61.73	23	77	75
37	24-Feb-08	5:32:10	3.99	1.21E+22	-60.17	-72.32	-21.66	118.89	35.94	-58.71	17	83	74
38	27-Mar-08	21:04:36	3.47	2.01E+21	-10.13	-13.42	-1.67	19.33	1.26	-9.21	26	74	75
39	30-May-08	4:48:36	4.14	2.04E+22	-98.88	-135.17	54.72	120.20	89.94	-21.31	94	6	80
40	4-Jan-09	17:27:10	4.27	3.20E+22	-66.16	-295.96	-87.39	97.32	34.70	-31.15	77	23	78
41	30-Jan-10	9:32:33	3.60	3.13E+21	1.49	-8.97	-7.08	28.21	-2.99	-29.70	96	4	60
42	15-Jul-10	15:31:44	3.95	1.06E+22	-17.75	-91.64	-18.20	74.54	7.21	-56.79	21	79	79
43	15-Jul-10	23:54:20	3.71	4.65E+21	-26.61	-23.85	-3.72	51.93	2.43	-25.33	17	83	78
44	1-Mar-11	2:19:47	4.43	5.44E+22	-200.52	-103.50	126.95	600.11	70.10	-399.59	53	47	79
45	28-May-11	22:55:25	3.73	4.87E+21	-38.15	17.22	0.77	49.01	-15.09	-10.87	51	49	66
46	29-Jun-11	11:13:31	3.26	9.68E+20	9.63	2.97	-0.89	-0.89	-1.02	-8.74	70	30	64
47	13-Feb-12	4:47:13	4.16	2.15E+22	-112.73	-147.06	-7.78	200.32	6.20	-87.59	32	68	73
48	5-May-12	9:23:23	4.25	2.99E+22	-249.21	-74.45	-31.49	316.44	-53.25	-67.23	60	40	74
49	9-Jul-12	0:01:18	3.83	6.85E+21	-27.54	-27.86	-15.09	62.09	41.27	-34.55	19	81	80
50	14-Mar-13	9:09:23	4.44	5.66E+22	-311.27	-380.99	76.59	416.98	183.69	-105.71	73	27	83
51	14-Jul-13	22:40:38	3.70	4.35E+21	-17.67	-36.47	-11.21	21.61	8.18	-3.94	73	27	84
52	28-Aug-13	4:43:06	3.76	5.62E+21	12.37	9.73	-13.19	40.93	-25.10	-53.30	68	32	70
53	12-Jan-14	20:24:47	4.53	7.76E+22	-313.08	-352.11	152.58	816.36	82.85	-503.28	38	62	88

No.: Studied event number; Date Time from NCSS catalog; Mw: moment magnitude; Mo: seismic moment in units of dyn·cm; M_{xx}, M_{xy}, M_{xz}, M_{yy}, M_{yz}, M_{zz}: Moment tensor values in Aki convention with units of 1 x 10^{20} dyn·cm; DC: percent double-couple; CLVD: percent compensated linear vector dipole; VR: percent deviatoric variance reduction.

* the full moment tensor solution should be used for this event.

Table 2.A.2 Full Moment Tensor Solutions

No.	Date	Time	MoD	MoI	MoT	MD	MT	Mxx	Mxy	Mxz	Myy	Myz	Mzz	D	C	I	V	F-sig
1	19-Sep-92	23:04:47	5.70E+22	7.35E+22	1.42E+23	4.44	4.71	334.52	-462.69	78.38	800.25	-81.97	1072.50	14	30	56	69	63.17
2	18-Jan-93	23:27:11	7.95E+21	1.06E+22	1.88E+22	3.87	4.12	41.94	-42.01	-20.02	128.26	30.83	148.98	38	5	57	75	74.45
3	19-Jan-93	0:24:29	3.92E+21	6.14E+21	1.05E+22	3.67	3.95	27.41	-19.60	6.65	61.15	-0.86	95.54	24	15	61	68	76.37
4	15-Feb-93	18:04:24	8.15E+21	3.40E+21	1.20E+22	3.88	3.99	-22.58	-60.83	11.32	82.58	8.27	42.06	54	16	29	74	48.50
5	16-Mar-93	3:59:27	1.39E+22	7.71E+21	2.29E+22	4.03	4.18	-6.58	-113.68	-28.48	119.83	26.89	118.17	43	21	36	70	52.02
6	23-Aug-93	15:03:27	9.04E+21	8.34E+21	1.92E+22	3.91	4.13	26.43	13.38	-27.23	152.51	-64.65	71.65	18	34	48	74	55.86
7	29-Nov-93	10:47:04	1.04E+22	2.83E+21	1.42E+22	3.95	4.04	-73.51	-45.37	10.41	112.73	4.81	45.53	53	25	21	74	48.17
8	29-Aug-94	5:09:25	5.71E+21	7.77E+21	1.39E+22	3.77	4.03	30.64	-29.76	14.16	118.68	15.64	83.36	31	11	58	75	56.25
9	16-Jan-95	1:34:38	1.95E+22	3.55E+22	5.62E+22	4.13	4.44	216.86	-90.93	53.98	365.28	96.87	482.75	27	8	65	69	65.26
*10	12-Oct-96	4:25:47	2.79E+21	3.65E+21	6.53E+21	3.57	3.81	63.02	3.42	4.21	26.15	-14.72	20.18	38	5	57	78	99.77
11	18-Nov-96	6:56:53	8.01E+21	5.27E+20	1.02E+22	3.87	3.94	-23.37	-32.22	-13.80	92.34	8.57	-53.07	31	63	6	69	49.56
12	4-Dec-96	21:21:15	3.69E+22	2.45E+22	7.10E+22	4.32	4.50	-98.42	-198.44	170.34	446.34	81.85	387.36	11	50	40	82	69.08
13	18-Jun-98	23:24:40	4.78E+21	1.34E+21	6.43E+21	3.72	3.81	-0.64	-26.24	-24.80	48.86	7.50	-8.06	59	19	22	68	53.42
14	18-Feb-99	8:58:42	2.09E+22	1.94E+22	4.22E+22	4.15	4.35	13.43	-132.08	15.40	333.88	-15.56	233.57	35	17	48	65	65.10
15	4-Apr-99	6:00:37	1.01E+22	2.16E+21	1.37E+22	3.94	4.03	3.75	-10.27	-83.54	80.35	31.70	-19.17	41	42	18	51	52.29
16	29-Jul-99	4:52:27	3.50E+21	5.17E+20	4.97E+21	3.63	3.73	-14.44	-5.84	-3.58	46.90	11.89	-17.03	13	75	13	65	50.17
17	6-Jan-00	21:38:11	8.18E+21	1.12E+22	1.95E+22	3.88	4.13	74.40	-59.92	-29.39	116.22	31.21	144.46	40	3	58	73	74.14
18	5-Apr-00	2:20:31	8.33E+21	1.69E+21	1.14E+22	3.88	3.97	-10.02	13.53	-64.17	59.42	42.23	1.43	37	46	17	63	51.46
19	8-Dec-00	7:41:11	4.45E+22	2.30E+22	6.93E+22	4.37	4.50	-164.42	-197.18	60.39	545.10	162.76	308.33	55	11	34	87	59.87
20	18-Apr-02	11:35:41	1.24E+22	8.46E+21	2.31E+22	4.00	4.18	-3.99	-83.67	33.55	111.99	50.30	146.01	23	37	41	82	73.48
21	9-May-02	11:07:56	5.55E+21	3.06E+21	8.94E+21	3.77	3.90	-16.32	-24.65	16.92	76.13	9.42	31.86	50	14	35	81	59.98
22	20-May-03	16:50:42	1.47E+22	9.38E+21	2.44E+22	4.05	4.19	-0.51	-68.89	39.35	158.58	92.14	122.70	57	4	39	81	56.11
23	3-Aug-03	12:00:53	1.70E+22	5.12E+21	2.36E+22	4.09	4.19	-70.12	-131.80	-2.02	140.72	-15.70	82.73	51	25	23	81	51.58
24	3-Oct-03	16:56:35	1.95E+22	3.23E+22	5.35E+22	4.13	4.42	211.85	-128.56	-103.00	334.58	21.46	422.07	26	12	62	81	94.37
25	18-Feb-04	20:37:46	7.77E+22	6.39E+22	1.52E+23	4.53	4.72	389.73	-242.69	592.20	722.53	-422.01	804.67	29	26	45	71	66.57
26	29-Oct-04	18:02:55	1.08E+22	8.70E+21	2.00E+22	3.96	4.14	12.00	-78.36	-13.82	154.74	-16.30	93.99	46	9	45	76	68.34
27	27-Dec-04	10:36:23	3.00E+22	2.90E+22	6.21E+22	4.26	4.47	464.04	-0.08	-211.30	94.88	-119.44	311.04	32	19	49	69	73.99
28	9-May-05	22:37:39	3.91E+22	2.19E+22	6.25E+22	4.33	4.47	-61.06	-248.68	-33.00	488.86	121.55	230.04	55	9	36	81	52.33
29	19-Oct-05	0:05:12	2.02E+22	1.28E+22	3.51E+22	4.14	4.30	-0.27	-152.49	77.84	199.47	-22.01	185.03	38	23	39	81	66.52
30	17-Nov-05	8:55:06	7.75E+21	2.00E+21	1.03E+21	3.86	3.95	-28.67	23.76	-24.41	94.72	24.77	-6.12	58	21	21	65	53.12
31	12-May-06	10:37:29	1.23E+23	6.88E+22	2.11E+23	4.66	4.82	-118.96	-599.05	-297.40	1852.20	341.51	333.74	29	35	36	83	59.56
32	20-Oct-06	17:00:08	8.44E+22	7.86E+22	1.73E+23	4.55	4.76	483.81	-761.82	263.63	803.64	-68.82	1068.10	30	22	48	83	80.31
33	20-Oct-06	23:31:40	7.32E+21	2.95E+21	1.14E+22	3.85	3.98	32.01	-71.40	13.02	47.33	-10.97	9.31	33	38	29	74	50.29
34	24-Apr-07	21:08:29	5.67E+22	2.59E+22	8.44E+22	4.44	4.55	-109.51	-360.97	132.25	624.01	202.09	261.98	60	8	31	82	55.41
35	20-Jul-07	17:50:20	5.14E+21	1.00E+22	1.61E+22	3.74	4.07	46.37	-22.65	-11.99	133.96	5.09	120.10	13	21	66	77	90.76
36	1-Dec-07	20:50:12	8.95E+21	4.38E+21	1.45E+22	3.90	4.04	-19.96	-43.14	-15.76	130.66	14.10	20.32	36	31	33	78	74.67
37	24-Feb-08	5:32:10	1.28E+22	1.18E+22	2.60E+22	4.01	4.21	3.92	-72.73	-31.59	188.20	28.31	161.60	33	19	48	79	80.30
38	27-Mar-08	21:04:36	2.00E+21	6.28E+20	2.87E+21	3.47	3.58	-5.94	-13.40	-1.63	23.42	1.26	1.39	43	33	24	75	49.27
39	30-May-08	4:48:36	2.05E+22	2.13E+22	4.61E+22	4.14	4.38	58.63	-139.40	64.66	277.44	76.30	303.82	16	33	51	83	75.58
40	4-Jan-09	17:27:10	3.22E+22	7.86E+21	4.07E+22	4.28	4.34	-19.07	-296.34	-87.28	148.20	33.20	107.11	74	7	20	79	51.46
41	30-Jan-10	9:32:33	2.84E+21	4.65E+20	3.35E+21	3.57	3.62	3.95	-8.79	-6.91	30.92	-2.91	-20.92	80	6	14	61	50.84
42	15-Jul-10	15:31:44	1.13E+22	5.34E+21	1.77E+22	3.97	4.10	7.93	-95.18	-23.76	118.73	12.22	33.43	45	23	32	80	66.46
43	15-Jul-10	23:54:20	5.23E+21	3.13E+21	8.69E+21	3.75	3.90	-10.56	-25.47	-5.10	79.74	4.26	24.89	48	15	38	81	79.59
44	1-Mar-11	2:19:47	4.56E+22	2.18E+22	7.22E+22	4.38	4.51	-94.48	-104.98	129.60	703.99	69.88	45.64	42	26	32	80	57.98
45	28-May-11	22:55:25	5.04E+21	4.57E+20	6.34E+21	3.74	3.80	-42.10	18.01	2.19	48.22	-14.74	-19.82	39	53	8	67	58.03
46	29-Jun-11	11:13:31	6.28E+20	6.82E+20	1.46E+21	3.14	3.38	13.65	3.00	-0.87	3.38	-1.05	3.39	11	37	52	65	53.47
47	13-Feb-12	4:47:13	2.19E+22	3.47E+21	2.88E+22	4.16	4.24	-91.79	-147.48	-13.08	230.12	11.72	-33.99	39	47	14	73	50.17
48	5-May-12	9:23:23	3.18E+22	1.32E+22	4.63E+22	4.27	4.38	-189.22	-63.44	-31.66	422.80	-45.71	161.99	59	12	29	78	88.87
49	9-Jul-12	0:01:18	6.47E+21	2.03E+21	1.02E+22	3.81	3.94	-13.65	-21.80	-16.54	78.25	42.24	-3.73	12	64	24	81	57.18
50	14-Mar-13	9:09:23	5.59E+22	1.43E+22	7.06E+22	4.44	4.50	-217.20	-379.09	71.87	511.43	178.43	135.86	78	2	20	83	50.27
51	14-Jul-13	22:40:38	4.24E+21	6.53E+20	5.10E+21	3.69	3.74	-12.17	-35.06	-11.50	26.57	8.23	5.19	70	16	13	84	50.34
52	28-Aug-13	4:43:06	3.91E+21	3.84E+21	8.02E+21	3.67	3.87	35.57	9.90	-12.89	65.14	-25.35	14.57	38	13	50	73	61.40
53	12-Jan-14	20:24:47	6.98E+22	3.12E+22	1.07E+23	4.50	4.62	-167.79	-347.72	158.05	965.73	80.44	137.99	49	20	31	89	62.10

No.: Studied event number; Date Time from NCSS catalog; MoD: Scalar moment using Dziewonski & Woodhouse (1983) definition, units dyn·cm; MoT: Scalar moment using total moment definition from Bowers and Hudson (1999), units dyn·cm; MD: moment magnitude using Dziewonski & Woodhouse (1983) definition for scalar moment; MT: moment magnitude using Bowers and Hudson (1999) definition for total scalar moment; M_{xx}, M_{xy}, M_{xz}, M_{yy}, M_{yz}, M_{zz}: Moment tensor values in Aki convention with units of 1 x 10^{20} dyn·cm; D: percent double-couple; C: percent compensated linear vector dipole; I: percent isotropic

component; V: percent full moment tensor variance reduction; *F*-sig: *F*-test statistical significance between the full and deviatoric moment tensor solutions.

* the full moment tensor solution should be used for this event.

Chapter 3

Analysis of Seismic Moment Tensors and *In Situ* Stress During Enhanced Geothermal System Development at The Geysers Geothermal Field, California

Published as:
Boyd, O.S., D.S. Dreger, R. Gritto, and J. Garcia, 2018. Analysis of seismic moment tensors and *in situ* stress during Enhanced Geothermal System development at The Geysers geothermal field, California, *Geophys. J. Int.*, **215**, 1483-1500, doi: 10.1093/gji/ggy326.

3.1 Chapter Abstract

Seismicity in the vicinity of an Enhanced Geothermal System (EGS) demonstration project in the Northwest Geysers at the Prati 32 (P-32) injection well and the Prati State 31 (PS-31) production well is investigated to determine earthquake focal mechanisms, moment magnitudes and *in situ* stress of events that occur before and during reservoir stimulation starting 2011 October 6. We present a catalog of 167 waveform-based seismic moment tensors ranging in moment magnitude from 0.6 to 3.9. The moment tensor catalog is subsequently used to invert for the stress tensor and to investigate possible temporal stress changes resulting from fluid injection. We find an approximate 15-degree counter-clockwise rotation of the least compressive stress σ_3 during injection. More remarkable is a change in orientation of the maximum compressive stress σ_1 from subhorizontal to vertical when injection operations temporarily cease. The orientation of σ_1 returns to subhorizontal when injection operations resume. It is found that there was a systematic reduction in the stress shape factor, *R*, as the injected water volume increases, indicating an evolution towards a more transtensional stress state.

3.2 Introduction

Creating, identifying, and managing fractures and flow paths are essential tasks during Enhanced Geothermal System resource development. Successful generation of a fracture network requires *a priori* knowledge of *in situ* stress and natural fracture orientation and

spacing. Because the orientation and magnitude of *in situ* stress may not be reliably available, and injecting fluids at high rates and volume may disturb the natural stress state, it is advantageous to monitor *in situ* stress during the injection process. The determination of *in situ* stress from earthquake focal mechanisms (Gephart & Forsyth 1984; Michael 1984) has been shown to provide stable and robust estimates of the orientation of the principal components of the stress ellipsoid at depth (Michael 1987), to enable regional characterization of tectonic stress (Hardebeck & Michael 2006), to document changes in stress state following large earthquakes (Hardebeck & Hauksson 2001), and to delineate ambient stress in applications of hydraulic fracturing (Baig & Urbancic 2010). Central to this approach is a reliable focal mechanism catalog with well-characterized uncertainties.

In The Geysers geothermal field Boyle & Zoback (2014) use a data set of over 6,000 well-constrained focal mechanisms in the Northwest Geysers from 2005 to 2012 to invert for stress within and below the reservoir. Their analysis shows that geothermal energy operations have not significantly influenced the stress field on average. However, Martínez-Garzón *et al*. (2013) find large changes in local stress fields due to heavy rates of seasonally modulated fluid injection. They investigate stress tensor changes related to fluid injection from 2007 to 2012 by inverting focal mechanisms of seismic events having 10 or more high-quality first-motion polarities, and apply a stress inversion method using first-motion polarities as input data to identify the best-fitting stress orientations and focal mechanisms. Using both field-wide seismic data and data associated with a particular cluster in the NW Geysers, they show significant temporal variations in stress, with rotations in the stress tensor (σ_1−σ_3) as fluid injection commences as well as during injection as injection rates fluctuate. In particular, they find that the plunge of σ_1 rotates from near-vertical pre-injection towards the horizontal during the heaviest periods of water injection. The thermo-hydromechanical modeling of Jeanne *et al*. (2015) and Ziegler *et al*. (2017) is consistent showing significant rotations of σ_1 from an initial prescribed vertical orientation to horizontal orientation as fluid is introduced into the system. Jeanne *et al*. (2015) argue that changes in stress tensor orientation can be caused by injection-induced cooling of the reservoir in addition to seasonal variations in injection rate. However, in the thermal-hydromechanical modeling of Ziegler *et al*. (2017) they find that thermal effects do not contribute to stress tensor rotations while other effects such as permeability, injection rate, and initial differential stress are controlling factors. The observations of Martínez-Garzón *et al*. (2013) are remarkable in that they demonstrate that the monitoring of stress changes from seismicity can be used to assess changes in conditions of a geothermal reservoir.

In another recent study, Martínez-Garzón *et al*. (2017) determine full moment tensor solutions using a hybrid moment tensor inversion (Kwiatek *et al*. 2016) at the Northwest Geysers. The 1 x 2 km^2 study area is near Prati 9 (P-9) and Prati State 29 (PS-29) injection wells where injection rates follow seasonal cycles with larger volumes injected during the winter. Their results show a relationship between faulting style and earthquake magnitude with normal faulting mechanisms dominating for $M_W < 2$ events at lower differential stresses and both strike-slip and reverse faulting mechanisms for larger events. Analysis of non-double-couple components indicates larger volumetric components are observed for events closer to injection wells and during periods of increased injection volumes. Other recent moment tensor studies at The Geysers include Johnson (2014a,b) who investigates time

dependent moment tensors of $M < 3$ earthquakes from 2011 to 2012 in the vicinity of EGS development, and Guilhem *et al*. (2014) who obtain full moment tensor solutions of $M \sim 3$ earthquakes located southeast of the EGS demonstration project from 2009 to 2011 using waveform modeling and first-motion polarity. These studies also investigate earthquakes in the northwestern region of The Geysers using short period seismic data from the local Lawrence Berkeley National Laboratory (LBNL) seismic network and show a range of source mechanisms including both shear and tensile processes. For $M > 3.5$ events, waveform data with good signal-to-noise ratios from regional networks can provide reasonable estimates of moment tensor solutions and detailed analysis of uncertainties for reliable determinations of seismic source type (Ford *et al*. 2009, 2010). Following this approach, Boyd *et al*. (2015) extend the full moment tensor analysis at The Geysers to include $M > 3.5$ events throughout the geothermal field from 1992 to 2012 using regional broadband data and find a range in source type including volumetric components. The study of smaller magnitude events limits the long-period end of the usable spectrum of the seismic waveform data because of decreasing signal-to-noise, and higher frequencies require the use of waveforms from closer stations. For example, Guilhem *et al*. (2014) invert data in the 0.7−1.7 Hz and 0.5−2.5 Hz passbands. For the purpose of evaluating stress changes related to the EGS demonstration project we were able to determine deviatoric focal mechanisms of $M_W > 0.6$ seismicity using complete waveform inversion of high quality short-period seismic data in the same passband.

3.2.1 The Northwest Geysers EGS Demonstration Project

The Geysers geothermal reservoir is the world's largest electricity generating operation with a current electricity generation of 825 MWe. The Geysers is located in northern California in the Mayacamas Mountains 150 km northwest of San Francisco. The reservoir is comprised of a vapor-dominated system with peak temperatures up to 400 °C. The top of the steam field is encountered at varying depth (0.6−1.5 km) within metagraywacke (metamorphosed sandstone), while the steam reservoir reaches into the basement (> 2.5 km depth), which is comprised of granitic felsite and is thought to be the heat source of the reservoir (Walters *et al*. 1992; Walters and Beall 2002; Garcia *et al*. 2016).

The EGS demonstration project is located in the Northwest Geysers geothermal field, within the felsite, where reservoir temperatures rise to 400 °C. High temperatures > 240 °C suggest a recent granitic intrusion under the EGS project area that may have started cooling 5−10 thousand years ago, (Williams *et al*. 1993). Investigations of $\delta^{18}O$ indicate that meteoric water in the normal temperature reservoir (NTR 240 °C) has weakly interacted with the steam in the high temperature reservoir (HTR) suggesting that the EGS reservoir is non-hydrothermal hot dry rock (Lutz *et al*. 2012). The EGS demonstration area is 1 x 2 km^2 and roughly centered on EGS wells that were previously abandoned (Fig. 3.1). In preparation for the EGS demonstration project, PS-31 was deepened to 3058 m in August 2010 and P-32 was deepened to 3396 m. While deepening the wells, P-32 encountered higher temperatures, greater permeability, and steam entries indicating that it would be a better injection well rather than PS-31, as initially planned. A slotted liner was installed in P-32 from 2590 m to 3398 m to allow water injection into the reservoir. The EGS wells intersect the HTR from 3.0 to 3.5 km depth with a separation distance of 0.5 km (Garcia *et al*. 2012). Interestingly, water

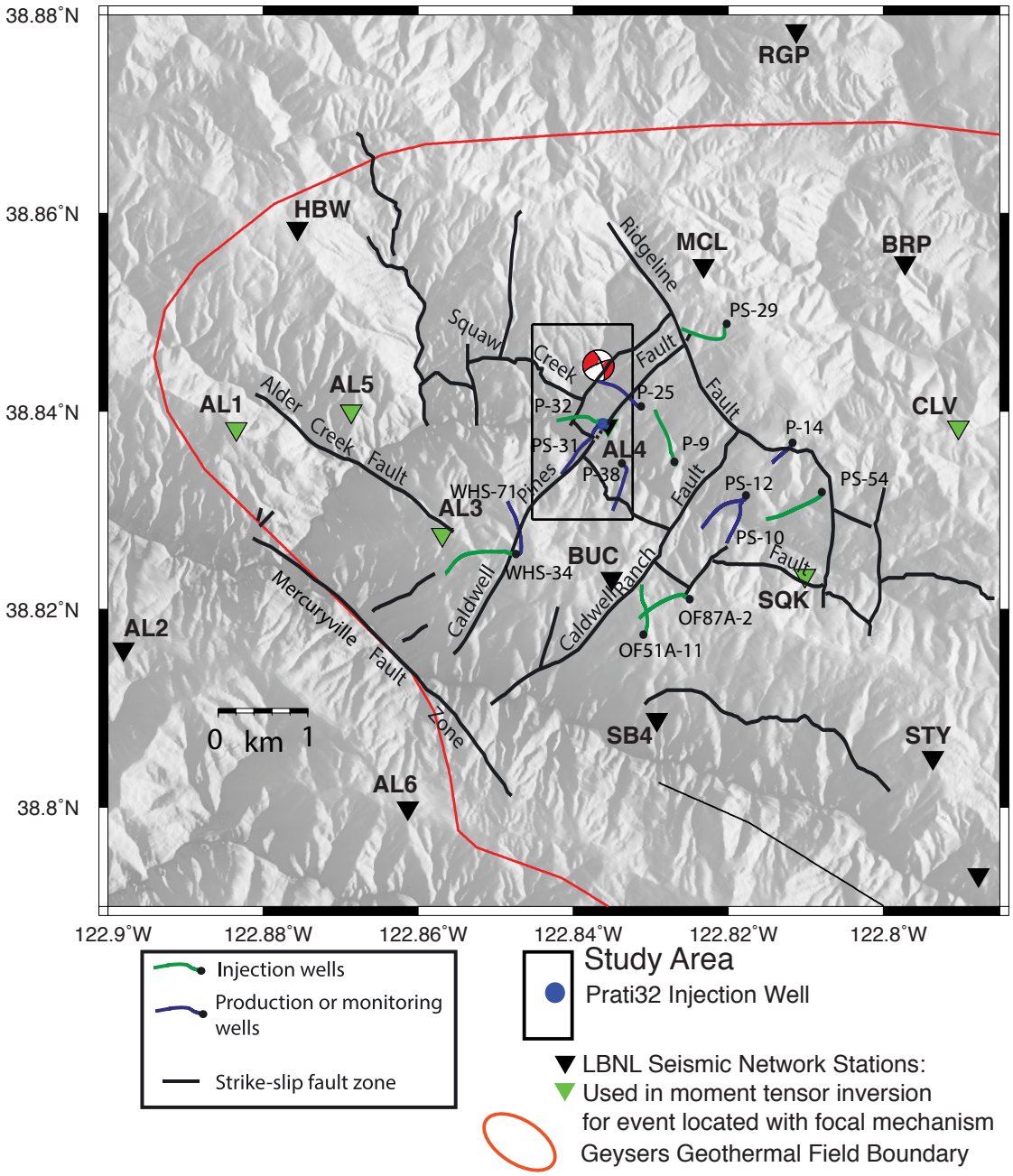

Figure 3.1. Map of the Northwest Geysers geothermal field. The EGS study area is a 1 x 2 km^2 rectangle centered on EGS production well Prati State 31 (PS-31) and EGS injection well Prati 32 (P-32), blue dot. Trajectories of injection wells (green lines) and production wells (blue lines) show additional production wells (P-25 and P-38) in the EGS study area and nearby associated injection well P-9 further east. The location of a M_W 2.17 2009 November 16 pre-injection event is shown with its focal mechanism. The locations of short-period seismic stations operated by LBNL used in this study are indicated by triangles (data from stations marked by green triangles were used to invert for the moment tensor of the event located with the focal mechanism). The approximate boundary of The Geysers steam field and selected faults are delineated with red and black lines, respectively. Fault and well trajectories adapted from Jeanne *et al*. (2015).

injection at The Geysers does not require pumping because vacuum conditions created in the wellbore and reservoir draw-in water as steam condenses (Garcia *et al*. 2016). Six Quaternary surface shear zones (Mercuryville, Alder Creek, Squaw Creek, Ridgeline, Caldwell Pines, and Caldwell Ranch, Fig. 3.1), have been identified and may possibly extend to depths of the HTR creating barriers to flow in adjacent regions of the reservoir (Garcia *et al*. 2016). One of these shear zones known as the Caldwell Pines Fault trends northeast (Nielson *et al*. 1991) and extends from the surface to the reservoir and may form a hydraulic discontinuity between the EGS wells PS-31 and P-32 and those to the south in the Caldwell Ranch Project (Prati 38 (P-38)) as evidenced by a differential pressure of 6.2 x 10^5 Pa (Garcia *et al*. 2016). Interestingly, our analysis includes fewer and larger events south of the Caldwell Pines Fault as injection progresses.

Comparing the monthly averaged injection rate (blue line) with monthly averaged seismicity (red asterisks) from the Northern California Earthquake Data Center, Enhanced Geothermal System (NCEDC EGS) catalog in Fig. 3.2 reveals a strong correlation coefficient of 0.77 (R^2 = 0.59) and from the *p*-value (3.2e-16) the correlation is significantly different than zero. The low pre-injection rate of seismicity markedly increases with the initiation of injection. Later as the injection rate stabilizes the rate of earthquakes is seen to reach a steady level as well. In fact, short-term fluctuations in the injection rate seem to also be marked by short-term fluctuations in the rate of earthquakes. The magnitude of completeness for seismicity observed in the study area after the start of injection is M_W = 1.2 (Garcia *et al*. 2016). Leptokaropoulos *et al*. (2018) performed extensive statistical tests between seismicity and injection rate in two nearby wells finding strong correlation in which changes in the seismicity rate lag changes in the injection rate by approximately 2 weeks.

3.2.2 Waveform Data

During the study period the LBNL seismic network consists of more than 30 three-component short-period (4.5 Hz) geophones sampled at 500 Hz. Data from seismic stations within 6 km of the study area (Fig. 3.1, triangles) were considered in this study. For example, data from a subset of seismic stations (Fig. 1, green triangles) were used to invert for moment tensor parameters of a M_W 2.17 2009 November 16 event located with its focal mechanism in Fig. 1. A list of earthquakes within the study area from 2011 October 6 through 2014 with magnitude $M \geq 2$ was compiled from the NCEDC EGS catalog for deviatoric moment tensor investigation. According to Majer & Peterson (2007), events are located to within 100 m accuracy in the southeast Geysers with the LBNL seismic network. The largest earthquake with moment magnitude M_W 3.87 is computed using the Berkeley Seismological Laboratory (BSL) moment tensor method and broadband data from the Berkeley Digital Seismic Network (BDSN) (e.g. Pasyanos *et al*. 1996; Boyd *et al*. 2015). Data for $M \leq 2.9$ events are obtained from the local LBNL short-period seismic network. All of the waveform data and associated metadata were acquired from the NCEDC (2014).

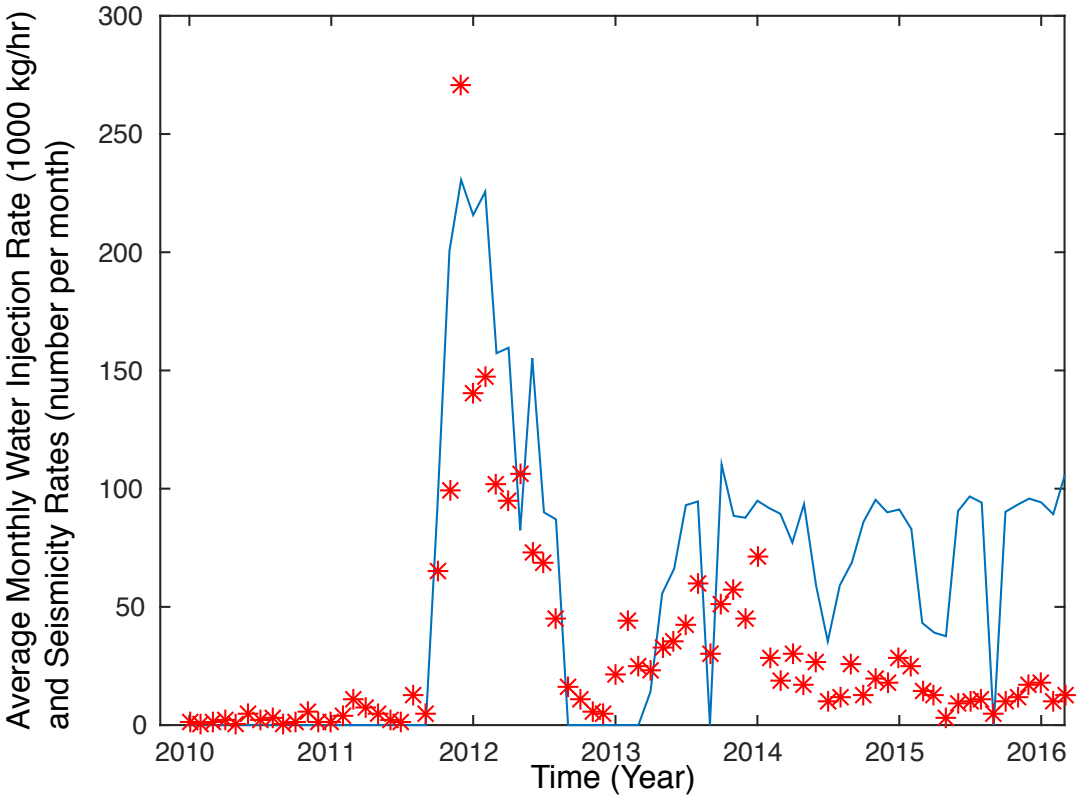

Figure 3.2. NCEDC EGS catalog monthly average seismicity (red asterisks) and Prati 32 monthly average injection rate (1000 kg hr^{-1}, blue line) prior to and during injection. The seismicity rate is highly correlated with the monthly injection rate. The correlation coefficient is 0.77 (R^2 = 0.59) and from the *p*-value (3.2e-16) the correlation is significantly different than zero.

3.3 Methods and Results

3.3.1 Moment Tensor Analysis

For seismic moment tensor inversions the seismic waveform data are processed by removing the instrument response to ground velocity followed by bandpass filtering of the waveforms with a causal 4th-order Butterworth filter with corners at 0.7 and 1.7 Hz (0.6−1.4 s period) for $M < 2.8$ events and 0.2 and 1.0 Hz for $M \geq 2.8$ events. The data are subsequently resampled at 0.1 s.

Synthetic Green's functions for the inversion are computed using a 1-D velocity model derived from a 3-D velocity model for the Northwest Geysers developed by Julian *et al*. (1996). This velocity model was also used by Guilhem *et al*. (2014) in their analysis of $M \sim 3$ seismicity. The synthetic Green's functions, including near-, intermediate- and far-field terms for body and surfaces waves, are computed using Computer Programs in Seismology

CPS Version 3.30 (Herrmann 2013). Our analysis is restrained to event depths reported in the NCEDC EGS catalog when available, or in the NCEDC Northern California Earthquake Catalog (NCSS). To compute the seismic moment tensors, we utilize the methods described in Minson & Dreger (2008), Ford *et al*. (2010), Nayak & Dreger (2015) and Boyd *et al*. (2015). Part of this analysis requires the alignment of the data with respect to the computed Green's functions. With a well-calibrated velocity model it is sometimes possible to invert the waveform data without time-shifts. In this analysis, however, time-shifts are necessary and represent departures of the assumed velocity model from the actual velocity structure along the paths, as well as accounting for uncertainty in the reported event locations. Usually in routine analysis by the Berkeley Seismological Laboratory the time-shifts between data and Green's functions for a given velocity model are estimated by trial and error to find the optimal alignment of the data with the Green's functions. In this study however, due to the large number of investigated events we employ a grid search to automatically find the best time alignment shifts. Analysis of the time-shifts indicates a systematic shift to negative values with the mean at approximately −three samples corresponding to −0.3 s. The magnitude of the shifts is relatively small and on average is approximately 1/3 of the central period of the utilized passband. While there is some variation in the time alignment shifts, possibly due to slight differences in the path to respective stations, they generally indicate that the actual average velocities between the source region to the nearby stations are faster than the 1-D average velocity model used to compute the synthetics.

It is not possible to use one set of stations to compute moment tensors during the initial injection phase starting 2011 October 6 due to variations in signal-to-noise levels. Initially seismic data from as many as 10 stations within 6 km of the studied events are considered for preliminary moment tensor analysis. Depending on these initial fits of the observed data with the synthetic Green's functions, up to six stations are subsequently selected for moment tensor processing using a grid-search algorithm to automatically find the optimal alignment of the observed data with the synthetic Green's functions. This method is applied to all of the studied events for automated moment tensor computation. These results are then appraised and, if necessary, minor adjustments are applied to shift the data for optimal fit. In the final processing stage, data with poor fits (variance reduction less than 20 per cent) are removed. Computed deviatoric focal mechanisms are displayed in Fig. 3.3 along with P-32 injection rate as a function of time starting 2009 November 15.

Deviatoric [double-couple (DC) + compensated linear vector dipole (CLVD)] and full [DC + CLVD + isotropic (ISO)] moment tensor solutions are computed for 167 events within the EGS study area. The deviatoric focal mechanisms shown in Fig. 3.3 are used in the subsequent stress analysis. Increasing percentage of the CLVD component is indicated with colors transitioning from cool (blue) to warm (red). The size of the focal mechanisms scales with computed moment magnitude. Event number, date, time, M_W (this study), moment, moment tensor components, per cent DC, per cent CLVD, and variance reduction (VR) are listed in Table 3.A.1, in Section 3.7 Appendix. The isotropic component of the full moment tensor solutions is plotted with plus symbols to give a sense of its percentage range. The median of the per cent isotropic component (thin black line) is plotted to investigate whether or not volume-increase or volume-decrease source processes correlate with injection rate. To adequately resolve the statistical significance of the isotropic component of the full moment

tensor solutions, however, requires more in-depth analysis as demonstrated in Boyd *et al*. (2015) and is beyond the scope of this analysis.

While the focal mechanisms are consistent with the tensile stress direction inferred from previous studies (Ross *et al*. 1996; Guilhem *et al*. 2014; Boyd *et al*. 2015), there are interesting patterns observed with this 167-event catalog of $M_W > 0.6$ events. Moment tensors of pre-injection events have a greater per cent double-couple (DC) component indicated by the cooler colors. Similarly, the three largest magnitude events have a higher percentage DC component. Larger magnitude events are more frequent during injection. Strike-slip events are most common prior to and during the initial injection phase and there appears to be more normal faulting mechanisms as injection continues. Bursts of increased earthquake rate occur from 2011 August 2 to 3, with five studied events. The most notable burst with 12 studied events during a 3-day interval occurs from 2013 January 30 to February 1 when injection resumes after an extended shut-in period lasting 160 days. These events exhibit strike-slip faulting mechanisms with higher percentages ~40 per cent CLVD component indicated by shades of green. The per cent isotropic component in the full moment tensor solutions ranges between ± 20 per cent, where positive indicates volume increase. However, in the following section we do show such analysis for a few selected events that indicates the small volumetric components are likely real, but a comprehensive study of possible volumetric components for the entire catalog is left as future work. Nevertheless, it is interesting that the per cent isotropic median line is observed to change during the stimulation experiment. Most notably, it changes to negative values at the cessation of injection in late 2012.

Reservoir stimulation in P-32 started 2011 October 6 with an initial injection rate of 70−76 kg s^{-1} (4164−4542 litres per minute (lpm) (1100−1200 gallons per minute (gpm))) for 24 hours and was subsequently reduced to 25.3 kg s^{-1} (1514 lpm (400 gpm)) for the next 55 days. Fig. 3.3 shows changes in injection rate (red curve) over the entire study period. The largest magnitude event in the 1 x 2 km^2 EGS study area (Fig. 3.1), M_W 3.87 (Md 3.48), occurred 2014 January 21 more than two years after injection began. Other $M > 3$ events in the EGS study area include Md 3.19 1994 June 6; M_W 3.0 2012 July 16 (M_W 2.74 this study) and M_W 3.09 2014 June 28 (M_W 2.76 this study). On 2016 December 16 a M_W 5.0 event occurred approximately 2 km SW of P-32.

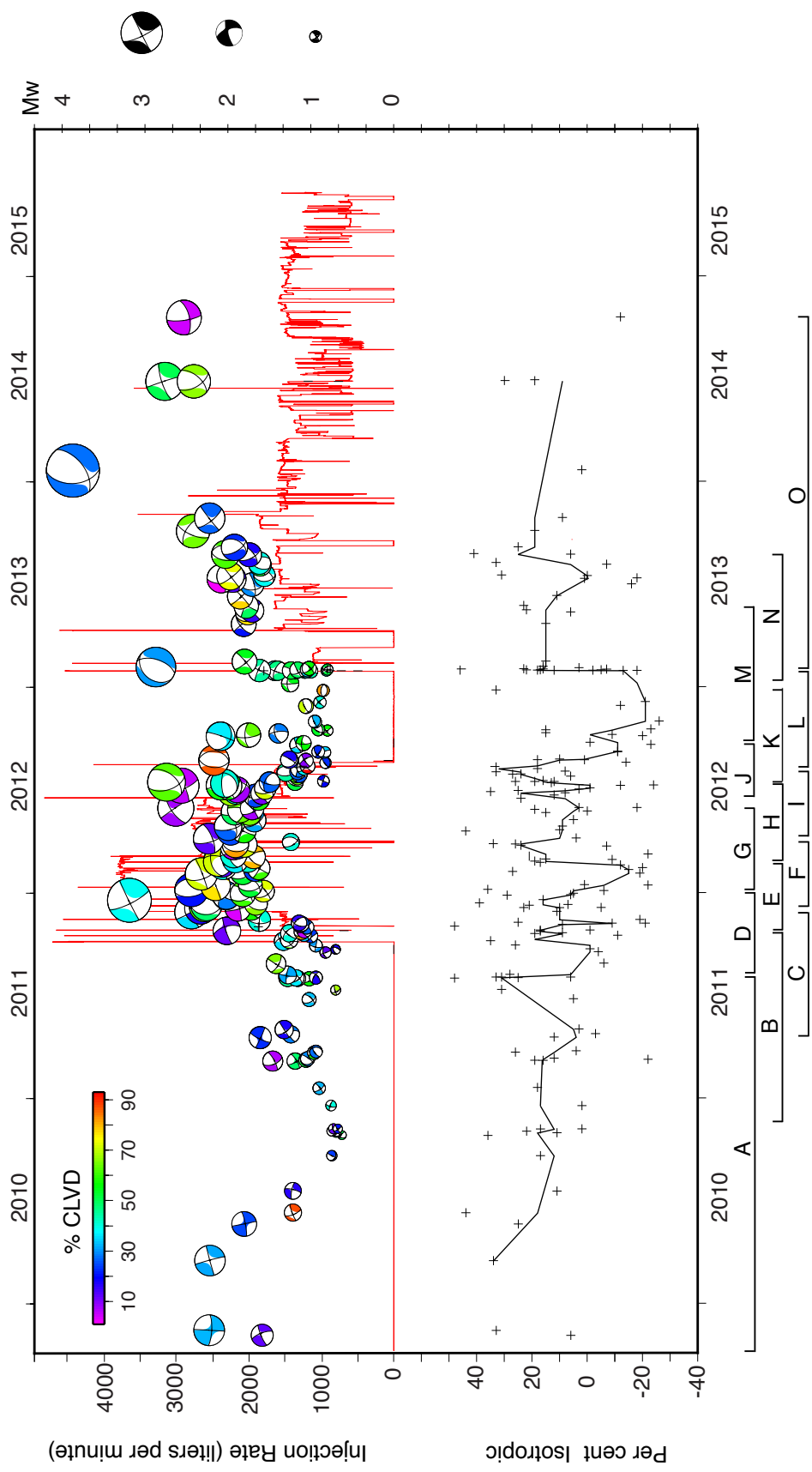

Figure 3.3. Time history of P-32 injection rate (red line) and deviatoric focal mechanisms shaded by per cent compensated linear vector dipole (CLVD) component. Injection rate in litres per minute is shown on the upper left vertical axis. Focal mechanism size is scaled by computed moment magnitude, M_w. The per cent isotropic component of corresponding full moment tensor solutions is marked with plus symbols. The median of the per cent isotropic component is delineated with the thin black line. Moment magnitude, M_w, and per cent isotropic scales are shown on the right and lower left vertical axes, respectively. Fifteen overlapping time windows for inversion of deviatoric focal mechanisms are labeled A - O below the horizontal time axis. No injection data available after 2015 May 30.

3.3.1.1 Case Studies of Selected Events

In this section, we focus on selected events to show examples of our processing methodology. The first example, an event with M_W 1.91 on 2012 March 27 occurs during injection with a rate of ~2574 lpm (680 gpm). The second event, M_W 2.44 2012 January 6, occurs during injection at a rate of ~3785 lpm (1000 gpm) and provides an opportunity to compare our results with those from investigations by Guilhem *et al*. (2014) and Johnson (2014a). Our third example, M_W 3.87 2014 January 21, is the largest magnitude event thus far in the EGS study area and occurs during injection at a rate of ~1514 lpm (400 gpm).

3.3.1.1.1 M_W 1.91 2012 March 27

Waveform fits and *P*-wave radiation patterns of the deviatoric moment tensor (a) and full solution (b) are shown in Fig. 3.4. The deviatoric moment tensor solution has a large 81 per cent CLVD component while the full moment tensor solution has a 35 per cent isotropic component. The improvement in fit from the extra degree of freedom is evaluated using the *F*-test. The *F*-test evaluates the improved ability to fit data with additional degrees of freedom against what could be expected due to random fluctuations in the data. The *F*-statistic is the ratio of the variances between models with different degrees of freedom. If the ratio is sufficiently large compared to the expectation of the *F*-distribution the improved fit of the higher degree of freedom model is deemed significant. Dreger *et al*. (2000) applied the *F*-test to evaluate the isotropic component of the moment tensor from a full moment tensor inversion compared to deviatoric solutions. The improvement in fit for this earthquake for the (6-element) full moment tensor compared to a (5-element) deviatoric moment tensor is 2 per cent and not statistically significant as determined by the *F*-test (level of significance is only 74 per cent).

In this example, we use the source-type inversion methodology of Nayak & Dreger (2015) shown in Figs 3.5(a)−(c) to explore the source-type-specific space of various data sets including (a) first motion, (b) waveform and (c) combined first-motion and waveform data and find the best-fitting region varies depending on the data set. The first-motions are inconsistent with the large CLVD mechanisms of the deviatoric solution, and the combination of waveforms and first-motions appears to require a small volume increase component. The combined first-motion and waveform data full moment tensor inversion results in a decomposition of 15 per cent DC, 59 per cent CLVD, and 26 per cent isotropic components. The interpretation for this normal focal mechanism event is that its full moment tensor mechanism is largely a CLVD with a small positive volumetric component. For the purpose of the subsequent stress inversion, however, the deviatoric waveform solution presented in Fig. 3.4(a) is used. It is noted that the DC component used in the stress inversion is the same for the deviatoric, full moment tensor, and the combined waveform and first-motion moment tensor solutions.

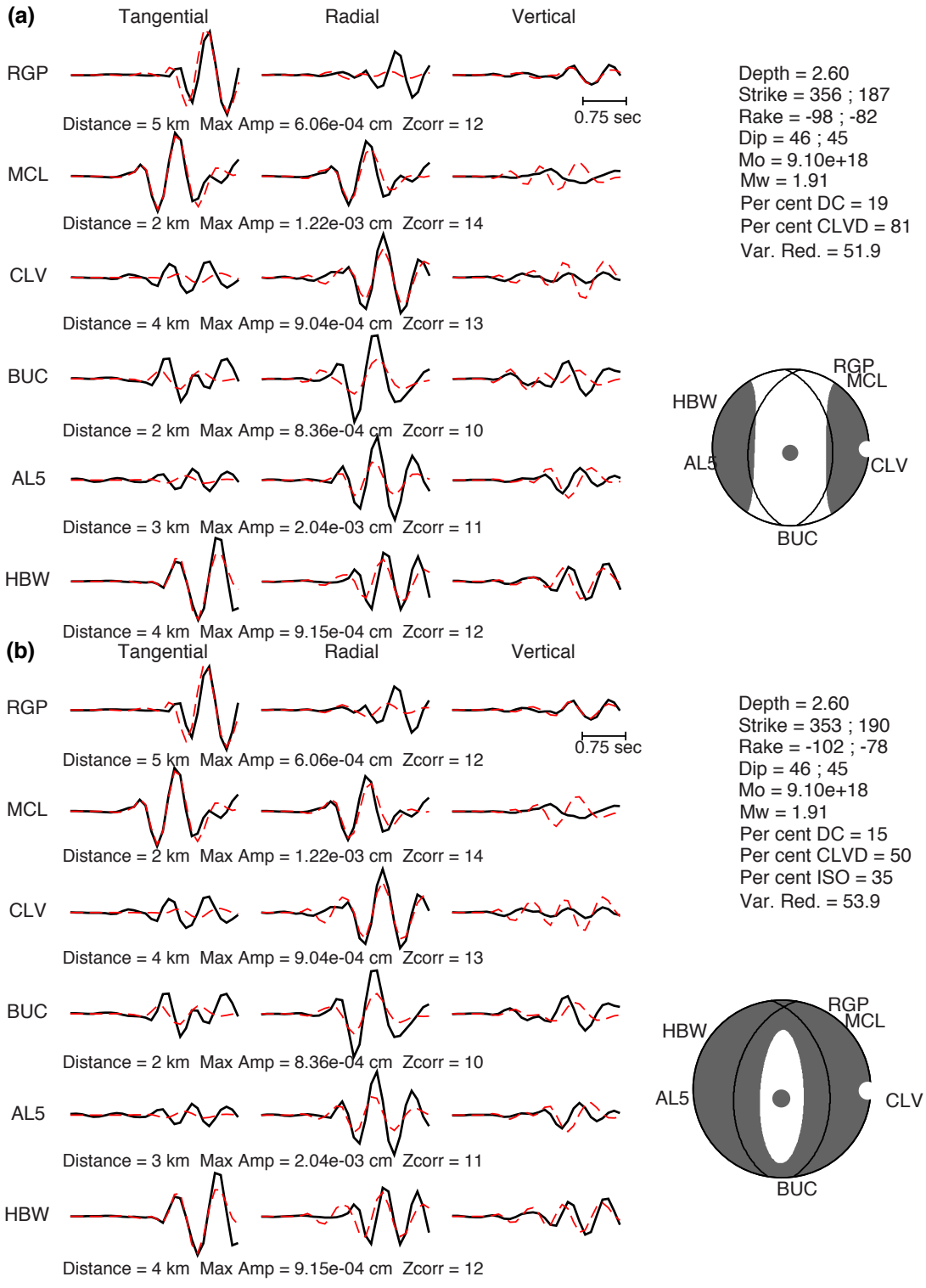

Figure 3.4. Comparison of filtered (0.7−1.7 Hz) observed velocity data (black) and synthetics (red) waveform fits and *P*-wave radiation pattern of the deviatoric moment tensor solution (a) and full moment tensor solution (b) for the M_W 1.91 2012 March 27 event. The improvement in fit of the full moment tensor solution is 2 per cent and is too small to be significant.

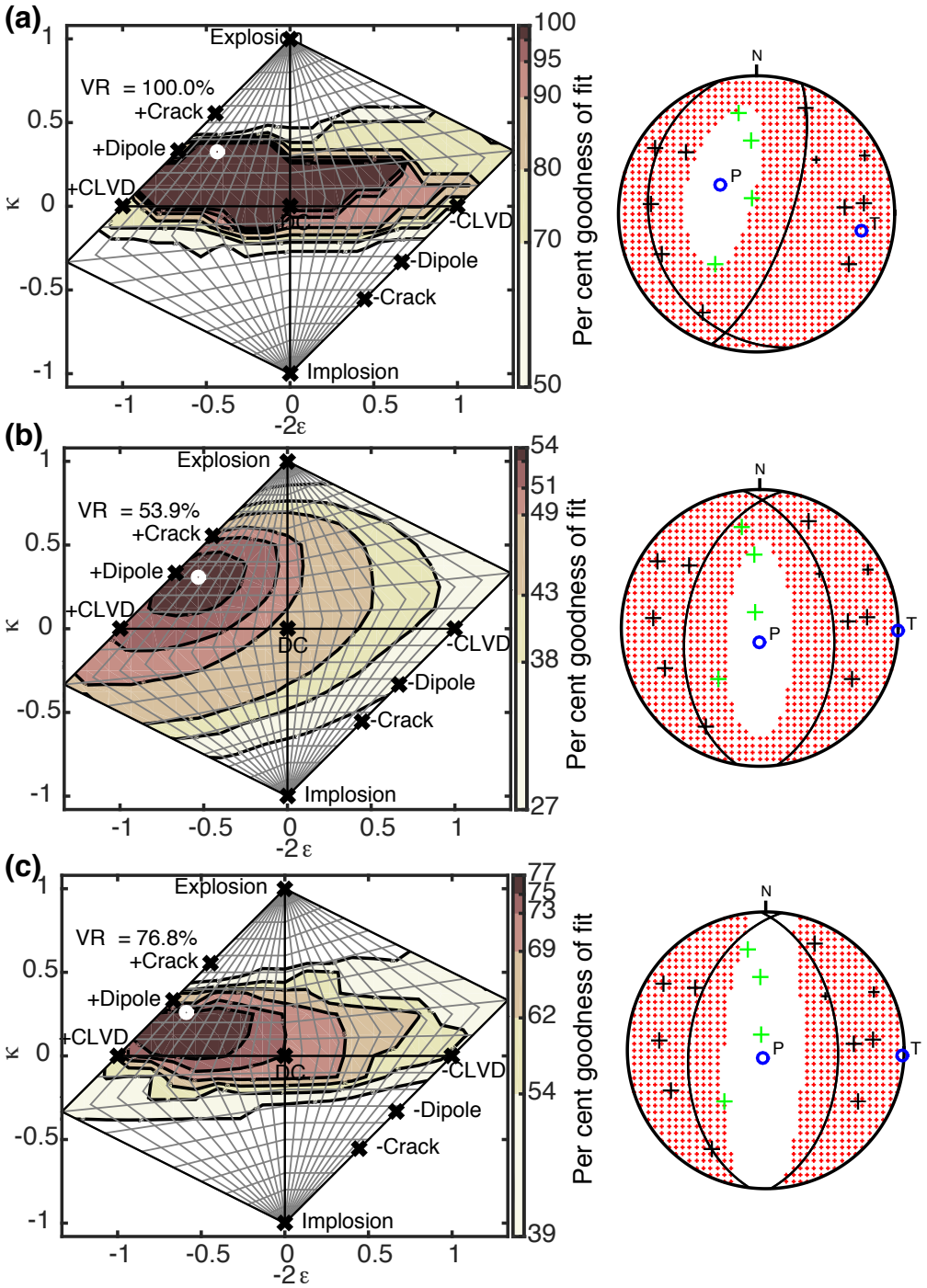

Figure 3.5. Network Sensitivity Solutions (NSS) of (a) first motion, (b) waveform and (c) combined first motion and waveform data using the methodology of Nayak & Dreger (2015) for the M_W 1.91 2012 March 27 event. The best-fitting solution for each data set is marked with the white circle on the source-type plots. The shading shows the per cent variance reduction goodness of fit parameter. Variability in source-type is evident amongst the various data sets. Corresponding best-fitting NSS focal mechanisms are shown to the right. First-motion polarity data are plotted with plus symbols, up first motions (black), down first motions (green).

3.3.1.1.2 M_W 2.44 2012 January 6

The earthquake on 2012 January 6 occurs during Prati 32 injection at a rate of ~3785 lpm (1000 gpm) and is included in the catalogs of Johnson (2014a) and Guilhem *et al*. (2014) and provides an opportunity to compare moment tensor solutions using the various methodologies. Waveform fits and *P*-wave radiation patterns of the deviatoric moment tensor (a) and full solution (b) from this study are shown in Fig. 3.6. The deviatoric moment tensor solution has a large 80 per cent DC component and the full moment tensor solution has a somewhat large 37 per cent isotropic component. The improvement in fit from the extra degree of freedom in the full moment tensor solution is 2 per cent and not statistically significant as determined by the *F*-test. The *F*-test level of significance is only 74 per cent.

Figs 3.7(a)−(c) explore the source-type-specific space of various data sets including (a) first motion, (b) waveform and (c) combined first-motion and waveform data and find the best-fitting region varies depending on the data set. The first-motions are somewhat inconsistent with the large DC mechanisms of the deviatoric solution, and the combination of waveforms and first-motions appears to require a volume increase component in which the best-fitting solutions are essentially represented by DC mechanisms with a volume-increase component. The combined first-motion and waveform data full moment tensor inversion results in a decomposition of 75 per cent DC, 3 per cent CLVD and 22 per cent isotropic components. The interpretation for this event with a normal focal mechanism is that its full moment tensor mechanism is largely a DC with a small positive volumetric component. For the purpose of the subsequent stress inversion, however, the deviatoric waveform solution presented in Fig. 3.6(a) is used. It is noted that the DC component, used in the stress inversion, is similar for the deviatoric, full moment tensor and the combined waveform and first-motion moment tensor solutions.

Guilhem *et al*. (2014) and this study use the same time-domain moment tensor inversion TDMT_INV (Dreger 2003) methodology and velocity model while Johnson (2014a) uses a frequency-domain approach and 1-D velocity model developed by O'Connell & Johnson (1991). Takeoff angles of first-motion polarity data in Guilhem *et al*. (2014) are calculated using 3-D velocity models and earthquake locations obtained from inversions using SimulPS (Thurber 1983). Consistency in the focal mechanisms is evident, however, the small differences in focal mechanisms from this study and Guilhem *et al*. (2014), (Figs 3.8c and d), respectively, may be due to differences in seismic waveform data, Green's functions, and event location used in the moment tensor inversion. Our solution fits the waveform and first-motion data well (Fig. 3.7c) and compares well with the solution obtained by Johnson (2014a).

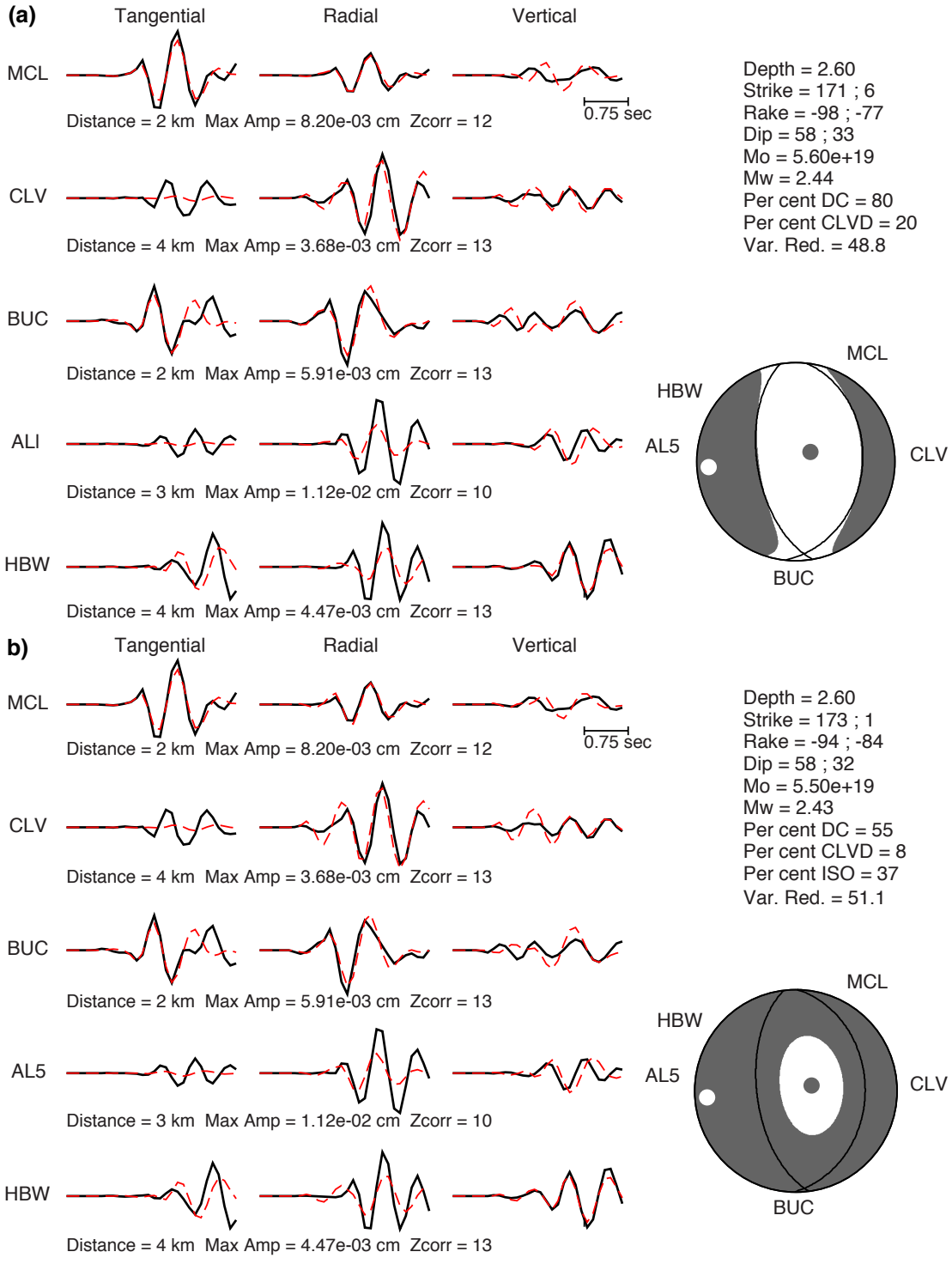

Figure 3.6. Comparison of filtered (0.7−1.7 Hz) observed velocity data (black) and synthetics (red) waveform fits and *P*-wave radiation pattern of the deviatoric moment tensor solution (a) and full moment tensor solution (b) for the M_W 2.44 2012 January 6 event. The improvement in fit of the full moment tensor solution is 2.3 per cent and is too small to be statistically significant as measured by the *F*-test. The *F*-test level of significance is only 74 per cent.

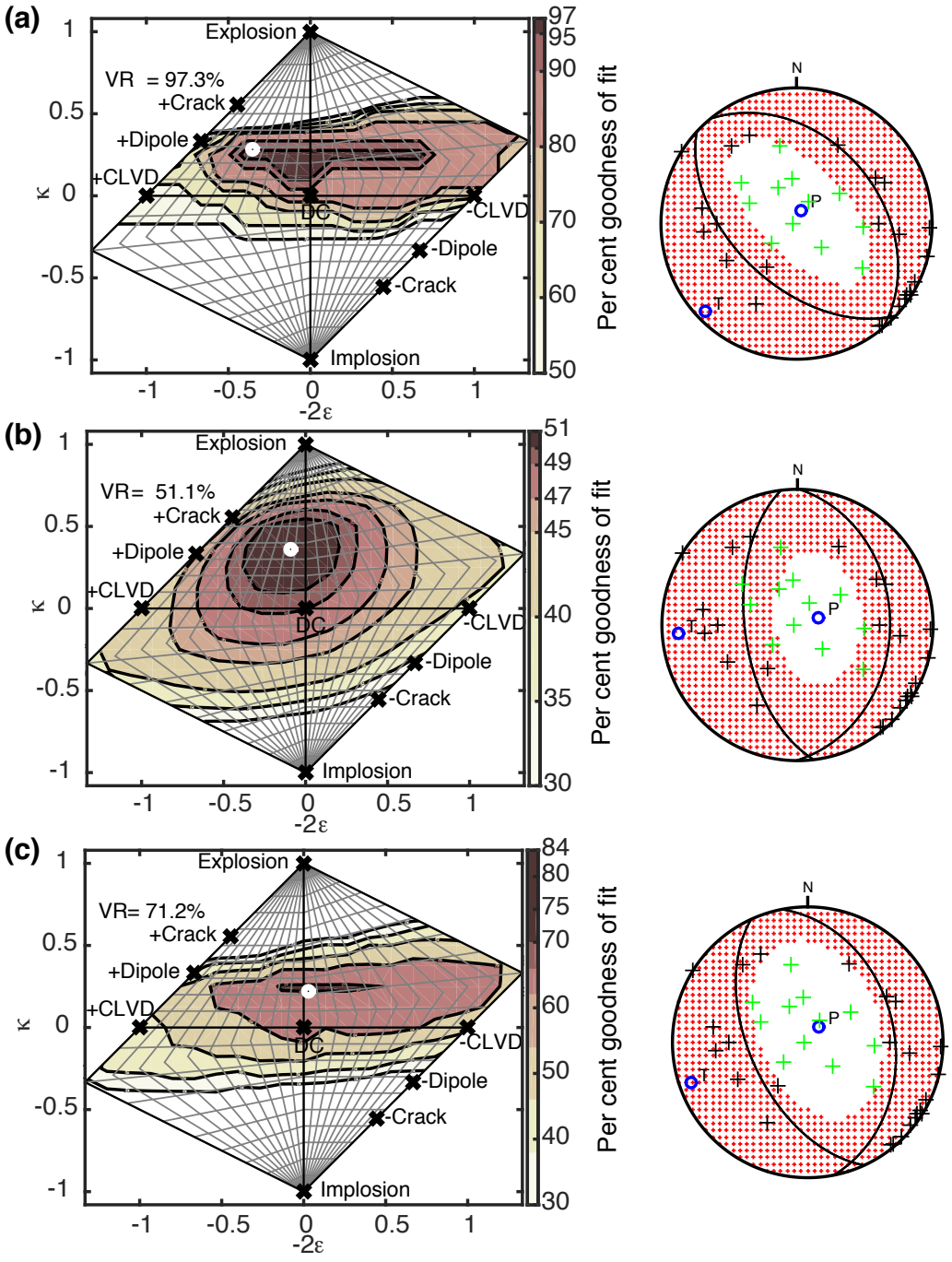

Figure 3.7. Network Sensitivity Solutions (NSS) of (a) first motion, (b) waveform and (c) combined first motion and waveform data using methodology of Nayak & Dreger (2015) for M_W 2.44 2012 January 6 event. The best-fitting solution for each data set is marked with the white circle on the source-type plots. The shading shows the per cent variance reduction goodness of fit parameter. Variability in source-type is evident amongst the various data sets. Corresponding best-fitting NSS focal mechanisms are shown to the right. First-motion polarity data are plotted with plus symbols, up first motions (black), down first motions (green).

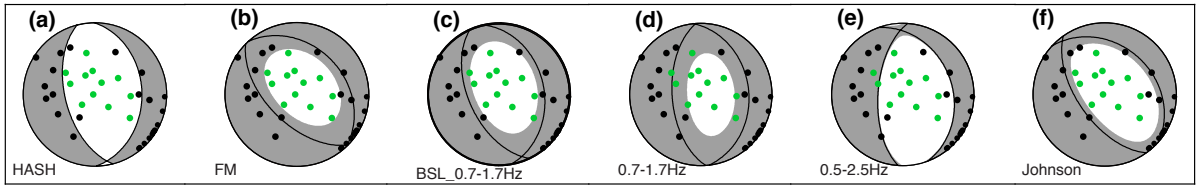

Figure 3.8. Focal mechanisms of the M_W 2.44 2012 January 6 event from multiple studies, adapted from fig.4 of Guilhem *et al*. (2014). Focal mechanisms determined from left to right as follows: (a) Guilhem *et al*. (2014) using HASH (Hardebeck & Shearer 2002). (b) Guilhem *et al*. (2014) NSS best-fitting solution using first motion data. (c) NSS solution using first motion and waveform data in the 0.7−1.7 Hz passband, this study. (d) Full moment tensor solution using 0.7−1.7 Hz filtered data, (Guilhem *et al*. 2014). (e) Full moment tensor solution using 0.5−2.5 Hz filtered data, (Guilhem *et al*. 2014). (f) Johnson (2014a) static moment tensor estimated from the low frequency level of the dynamic moment tensor. First-motion polarity data from Guilhem *et al*. (2014) plotted with up first motions (black) and down first motions (green).

3.3.1.1.3 M_W 3.87 2014 January 21

More than two years after the start of injection, the maximum magnitude event thus far occurs in the center of the study area at a catalog depth of 1.7 km following an extended shut-in period when the Prati 32 injection rate is ~1514 lpm (400 gpm). For this event the moment tensor solutions in Fig. 3.9 are computed using broadband data from regional stations in the Berkeley Digital Seismic Network (BDSN) and the routine moment tensor analysis software. Waveform fits and *P*-wave radiation patterns of the deviatoric moment tensor (a) and full solution (b) computed at a depth of 3.5 km are shown in Fig. 3.9. The deviatoric moment tensor solution has a large 73 per cent DC component and the full moment tensor solution has a small 3 per cent isotropic component. The improvement in fit from the extra degree of freedom in the full moment tensor solution is 0.1 per cent and not statistically significant as determined by the *F*-test.

3.3.1.2 Depth Distribution of Fault Mechanisms

The depth range of Prati 32 injection into the high temperature reservoir is from 2.6 to 3.4 km depth. Depths of the studied events range from 0.7 to 5.5 km with most between depths of 1.5 to 3.5 km. The most common faulting style is strike-slip (69 per cent), followed by normal (27 per cent), with 3 per cent thrust fault events, Fig. 3.10. Normal events are defined as having rake between −45° and −135°, reverse between 45° and 135°, and strike-slip otherwise. The strike-slip events are observed to occur at all depths, whereas the majority of normal and reverse events tend to occur above and within the high temperature reservoir in agreement with Kwiatek *et al*. (2015). There is an increase in normal fault mechanisms from 2.4 to 2.7 km while most strike-slip mechanisms occur at depths from 2.4 to 3.3 km.

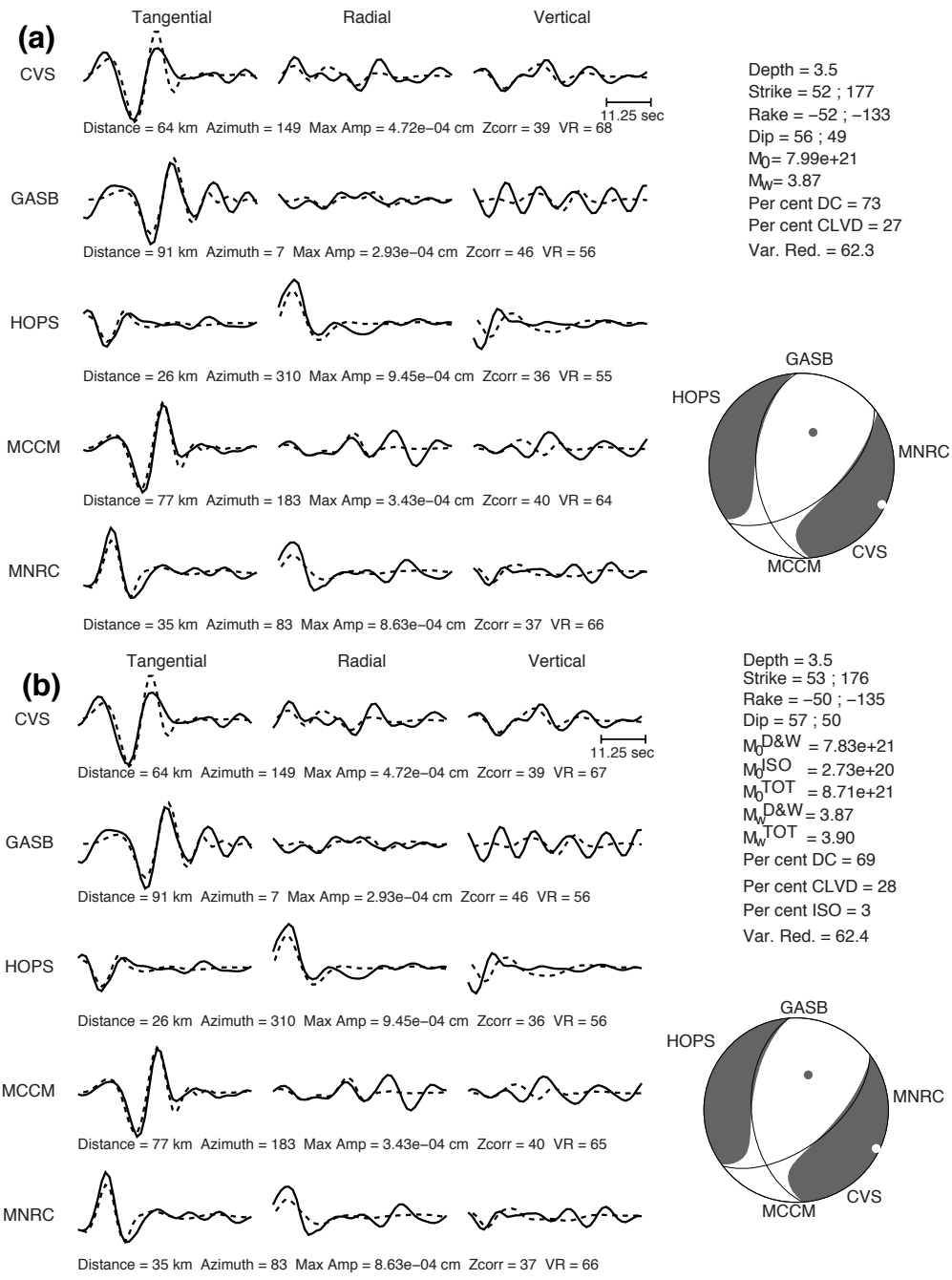

Figure 3.9. Comparison of filtered (0.02−0.10 Hz) observed displacement data (solid) and synthetics (dashed) waveform fits and *P*-wave radiation pattern of the deviatoric moment tensor solution (a) and full moment tensor solution (b) for the M_W 3.87 2014 January 21 event. The improvement in fit of the full moment tensor solution is 0.1 per cent and is too small to be statistically significant as measured by the *F*-test. These solutions were obtained using the routine BSL moment tensor software utilizing acausal Butterworth filtering, the GIL7 velocity model (Stidham *et al*. 1999), and FK-integration Green's functions computed using FKRPROG (written by Chandan Saikia) based on the method of Wang & Herrmann (1980).

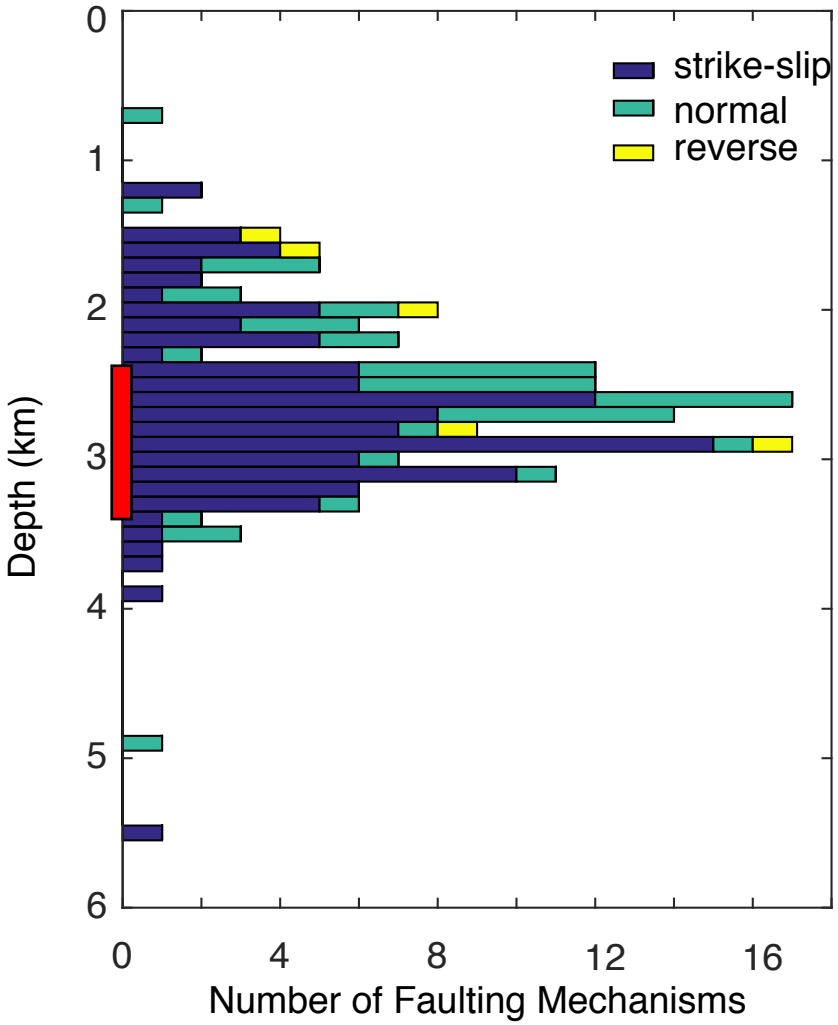

Figure 3.10. Histogram plot of faulting mechanism and depth. Strike-slip mechanisms (blue) account for 69 per cent of the fault mechanisms, followed by 28 per cent normal mechanisms (green), and 3 per cent reverse mechanisms (yellow). The red bar delineates the approximate extent of Prati 32 injection.

3.3.2 *In Situ* Stress Analysis

We present an analysis of the evolution of the state of stress with time and injection rate by performing stress inversions on 15 overlapping time windows, each with 30 moment tensor solutions, except for the last window containing 27 solutions. We use the STRESSINVERSE software package developed by Vavryčuk (2014) to invert the strike, rake and dip from our moment tensor catalog for the *in situ* state of stress during each sliding time window. Because it is not known which of the two possible nodal planes is the actual earthquake rupture plane, this iterative method finds the nodal planes most consistent with the stress field given fault frictional properties.

Previous studies have shown that 15 (Hardebeck & Michael (2006), 25 (Boyle & Zoback 2014) events per bin produced stable stress inversions, and Vavryčuk (2014) tested both the Michael (1984) and his methods synthetically and found that both produced satisfactory results with at least 20 noisy mechanisms per bin. In this analysis, we choose a sliding window containing 30 focal mechanisms, with a 20-event overlap between time windows to smooth the temporal variation. The 15 time windows are labeled A−O below the time axis in Fig. 3.3. Note that the duration of the time windows varies from 4 months to slightly less than 2 years depending on the frequency of studied events. The first and longest time window from 2009 November 16 to 2011 August 3 is prior to Prati 32 injection when seismicity is less frequent. Figs 3.11(a)-(o) contain location maps of focal mechanisms shaded by hypocenter depth for corresponding overlapping time windows A−O. Two-thirds of the focal mechanisms repeat in adjacent maps due to the 20-event overlap in the sliding time windows.

3.3.2.1 Spatial-Temporal Trends in Seismicity

Despite the repetition of overlapping events in adjacent maps, spatial-temporal patterns in seismicity are evident. Before injection begins, the eastern portion of the study area appears to be seismically active with shallow strike-slip faulting mechanisms throughout the study area (Fig. 3.11a, 2009 November 16 – 2011 August 3). It is of interest to note that other injection and production operations are in close proximity. Two other production wells Prati 25 (P-25) and Prati 38 are within the boundary of the EGS study area, and two other injection wells Prati State 29 (1 km) and Prati 9 (0.4 km) are to the east near faults known to intersect the study area. Injection at Prati 9 starts in 2010. Several studies have investigated the seismic response to injection in the area NE of the study area (e.g. Martínez-Garzón *et al*. 2013; Kwiatek *et al*. 2015; Martínez-Garzón *et al*. 2016).

3.3.2.2 Temporal Trends in Stress

The stress inversion results show an interesting change in the orientation of the principal stress axes during injection operations. Stereonet plots of the orientation of principal stress axes σ_1 (red), σ_2 (green), and σ_3 (blue) for each time window are shown in Figs 3.12(a)−(o). The colored regions show the 95 per cent confidence region from applying 100 random noise realizations assuming a mean mechanism uncertainty of 5°, and rerunning the inversion for each set of perturbed data. Initially, there is an east-southeast orientation of the minimum compressive stress σ_3 (blue) and south-southwest maximum compressive stress σ_1 (red) in a predominantly strike-slip faulting environment. Gradually with time during injection there is an approximately 15-degree counter-clockwise rotation of σ_3 until time window J ending 2012 September 20. Then, during time window K beginning in July 2012 there is a marked rotation of σ_1 towards a more vertical orientation. This time window from 2012 July 14 to 2012 December 26 corresponds to a period when injection operations temporarily cease at Prati 32 from 2012 August 20 for a period of approximately 160 days until 2013 January 29. Subsequent time windows L (2012 August 8 − 2013 January 31) and M (2012 September 24 − 2013 May 25) also show a similar rotation in orientation that corresponds to further changes in injection operations. Prati 32 injection resumes in early February 2013 until 2013 March 12. Prati State 31 continues to produce steam from 2012

December 5 until production stops due to a leak caused by corroded well casing. In mid-February 2013 injection shifts to Prati State 31 at a rate of 1135 lpm (300 gpm) resulting in a migration of seismicity to the south in the vicinity of Prati State 31. Injection continues in Prati State 31 until 2013 March 21 when the well is repaired. Injection in Prati 32 resumes 2013 April 9 (Garcia *et al*. 2016).

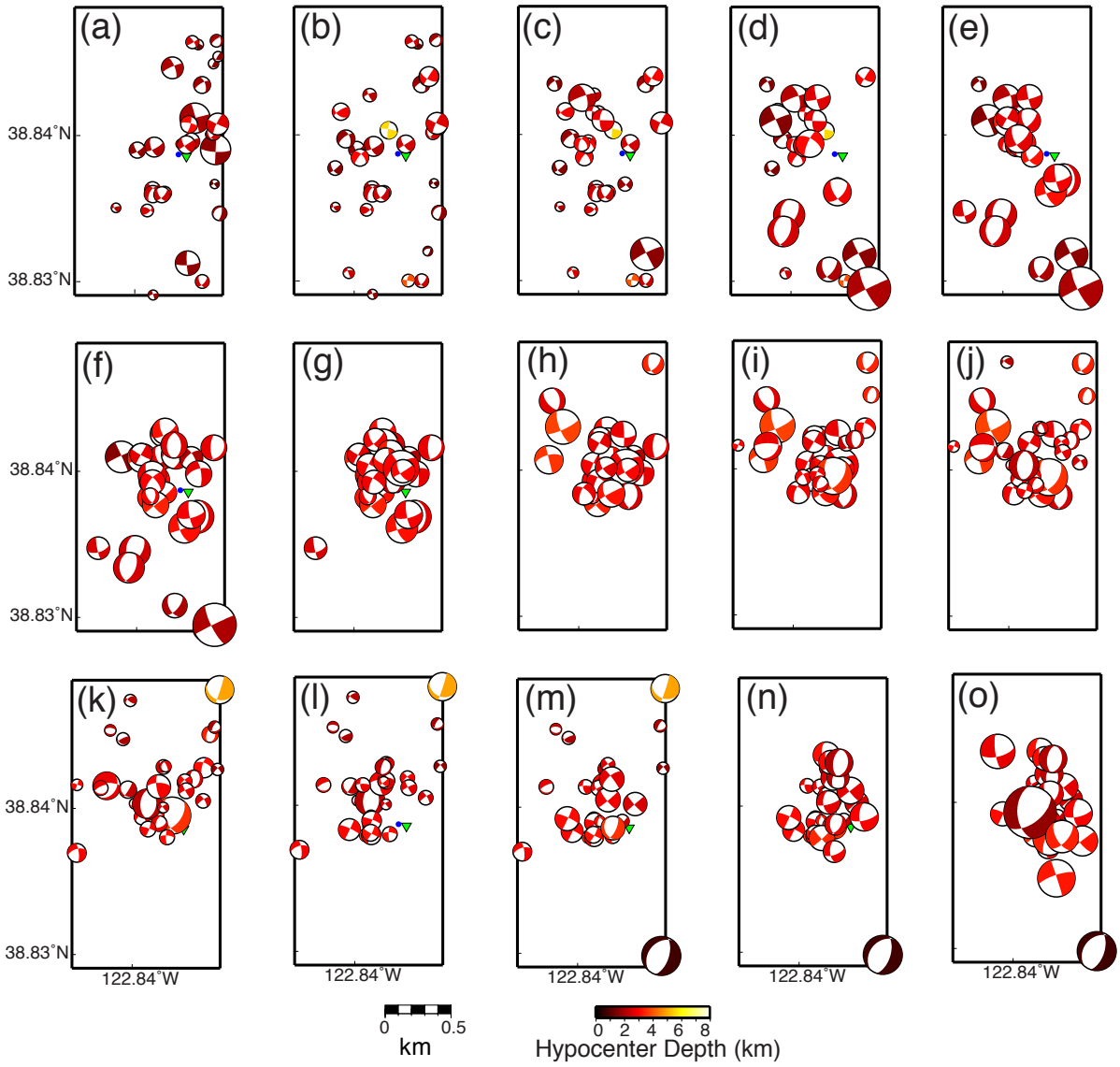

Figure 3.11. Location maps each with 30 focal mechanisms shaded by hypocenter depth during corresponding overlapping time windows A−O. Two-thirds of the focal mechanisms repeat in adjacent maps due to the 20-event overlap of the sliding time windows. Note that location map (o) contains 27 focal mechanisms.

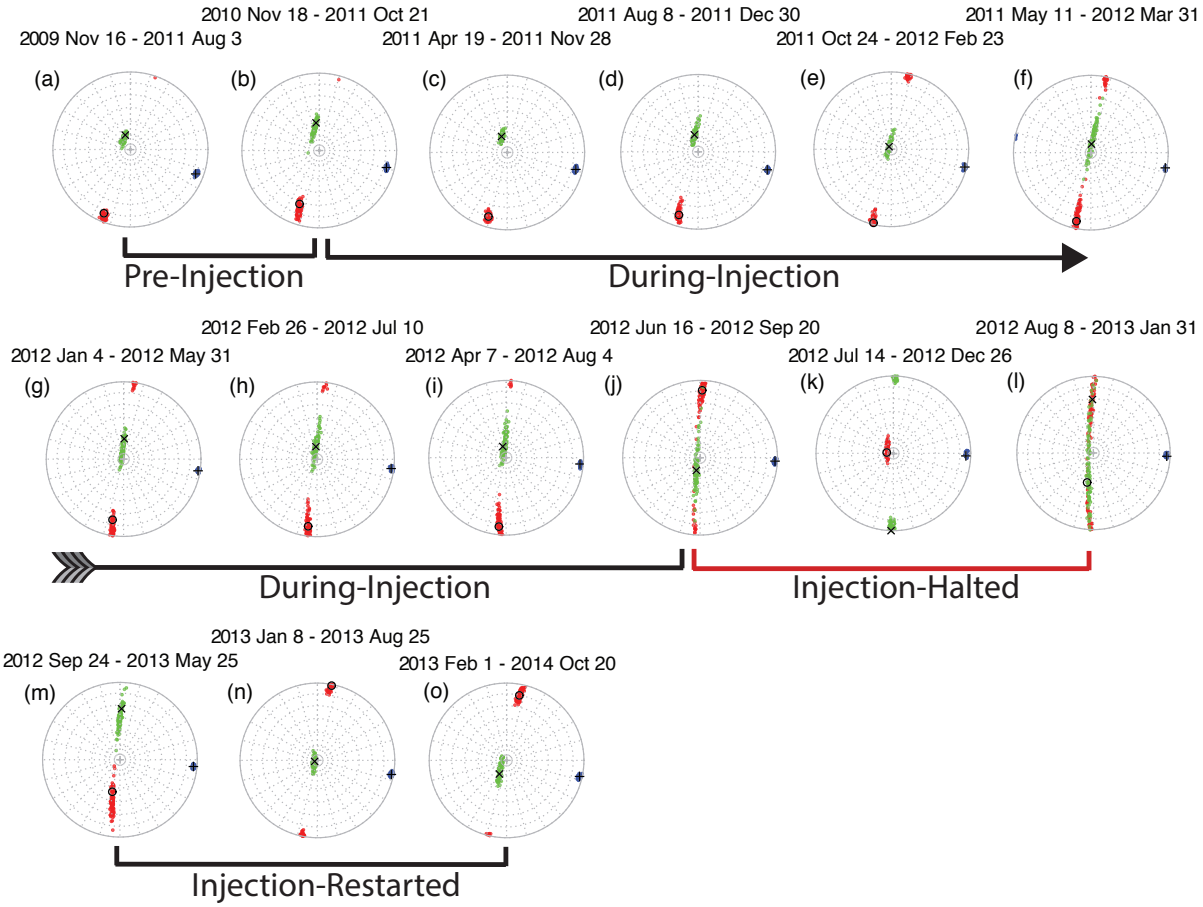

Figure 3.12. Stereonet plots labeled (a)-(o) of principal stress orientations obtained using STRESSINVERSE (Vavryčuk 2014) during 15 overlapping time periods. There are 30 focal mechanisms for each time period, except for the last time window with 27 focal mechanisms, with 66 per cent overlap. The orientations of the maximum compressive stress σ1 (red), intermediate stress σ2 (green) and minimum compressive stress σ3 (blue) are well constrained. The colored regions show the 95 per cent confidence region from applying 100 random noise realizations assuming a mean mechanism uncertainty of 5°, and rerunning the inversion for each set of perturbed data. Within each 95 per cent confidence region the best orientation of the principal stress axis is marked with a circle for σ1, a cross for σ2, and a plus symbol for σ3.

During this period the magnitude of σ_1 and σ_2 also begin to equalize (Fig. 3.13) indicating that the system is evolving to a more transtensional environment in which the mechanisms are comprised of both strike-slip and normal types. STRESSINVERSE (Vavryčuk, 2014) iteratively solves for an optimal friction parameter in evaluating the fault instability to find optimal fault planes. Vavryčuk (2014) states that numerical tests show that inversion results are insensitive to the friction parameter, and it is sufficient to assign a reasonable value for all inversions. We elected to allow the friction parameter to change and found it to not substantially change with values of 0.7 ± 0.2, which is consistent with laboratory estimates for

graywacke and other rocks at the confining pressures of the studied earthquakes (e.g. Byerlee 1978; Lockner *et al*. 1982).

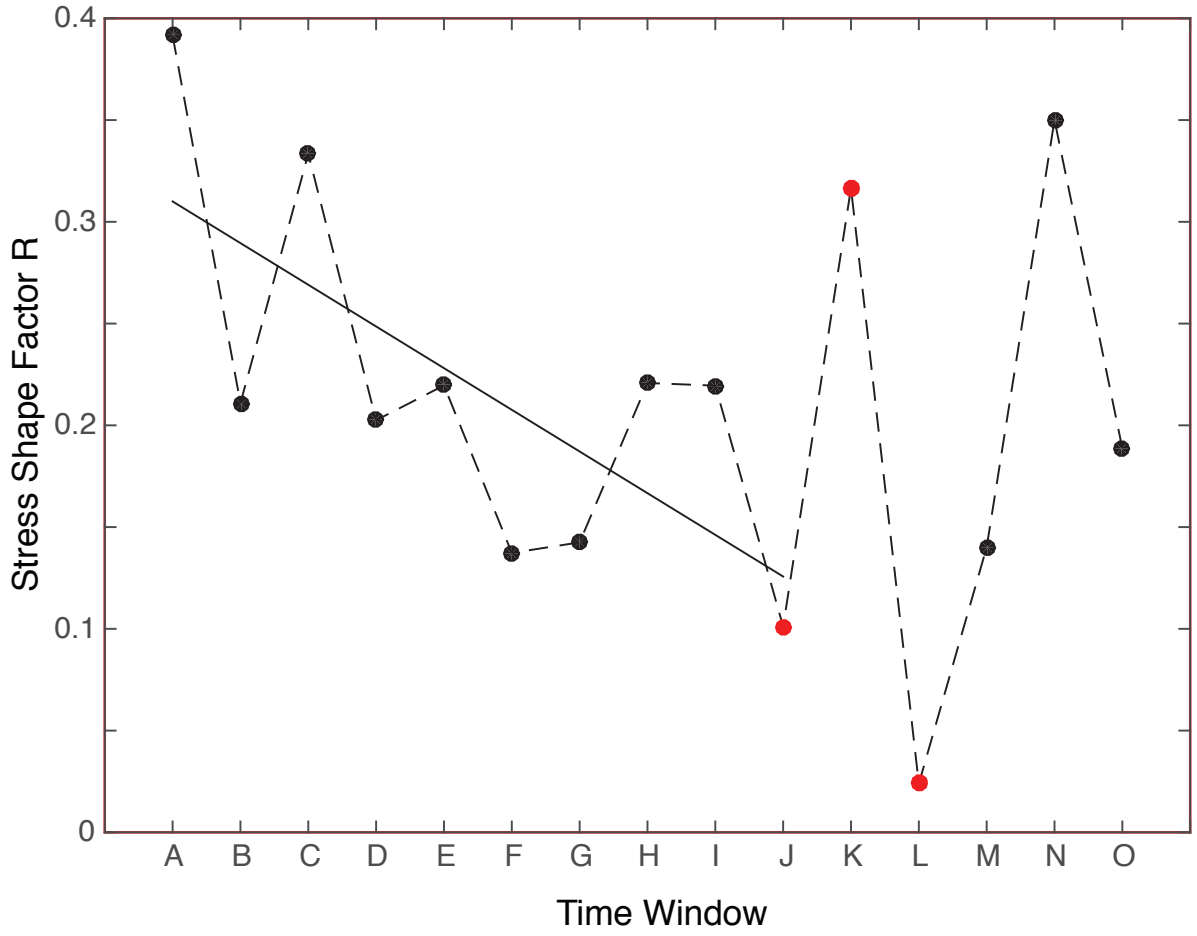

Figure 3.13. Plot of stress shape factor *R* for each moving time window. The solid line fitted to the *R* data has a negative slope that is statistically significant considering the 95 per cent confidence in the estimate of the slope up to time window J (R^2 = 0.5 and *p*-value = 0.02). *R* data points shaded red occur during windows J, K and L that sample periods of time when injection halted.

Examining the relative magnitude of the stress components, it is seen that as the orientation of the stress tensor is changing so too is the stress shape factor, *R* (Gephart & Forsyth 1984). *R* is defined as

$$R = \frac{\sigma_1 - \sigma_2}{\sigma_1 - \sigma_3} \tag{3.1}$$

where σ_1 is the maximum compressive stress and σ_3 is the least compressive stress. As can be seen in Fig. 3.13, *R* decreases systematically as injection rate and total volume of injected

water increases. The reduction in R is due to both a decrease in the relative magnitude of σ_3 and an increase in the relative magnitude of σ_2 indicating that the stress is evolving to a more transtensional environment, which can also be seen directly from examination of the focal mechanisms (Fig. 3.11). We find in fitting a line to the R data that the negative slope is statistically significant considering the 95 per cent confidence in the estimate of the slope up to time window J ($R^2 = 0.5$ and p-value = 0.02). At later times the large oscillations still lead to a negative slope, but the uncertainty indicates that it cannot be considered statistically significant at the 95 per cent confidence level.

3.4 Discussion

3.4.1 Moment Tensor Analysis

The results from the moment tensor analysis indicate that seismicity in the vicinity of The Geysers EGS demonstration area evolves in space and time as water injection operations progress. Based on our analysis, most of the events are likely the result of shear failure due to both tectonic shear stress and tensile stress induced by the injection of water. The observed rotation of the stress tensor does indicate the system is responding to tensile stress induced by fluid injection, however we cannot state whether the change in the stress tensor is due to thermal or other processes. In the thermo-hydromechanical modeling of Jeanne *et al*. (2015) and Ziegler *et al*. (2017) there is disagreement in the importance of the thermally induced tensile stress. Even though the moment tensor catalog is limited to 167 events with $M_W > 0.6$, patterns in earthquake source parameters emerge before and during multiple stages of injection and shut-in. Moment tensors of pre-injection events have a greater per cent DC component indicated by the cooler colors in Fig. 3.3. Similarly, the three largest magnitude events have a higher percentage DC component. Larger magnitude events are more frequent during periods of injection. Strike-slip events are most common prior to and during the initial injection phase with a gradual transition to more normal faulting mechanisms as injection progresses. In the adjacent Prati 9 and Prati State 29 region to the NE of the study area Kwiatek *et al*. (2015) report a slight increase in strike-slip events as injection proceeds. Bursts of increased earthquake rate occur 2011 August 2−3 with five studied events. The most notable burst with 12 studied events during a 3-day interval is from 2013 January 30 to February 1 when injection resumes after an extended shut-in period lasting 160 days. These events exhibit similar strike-slip faulting mechanisms with larger CLVD component (~40 per cent) indicated by shades of green (Fig. 3.3). Even though the statistical significance of the isotropic components (plus symbols) of the full moment tensor solutions for the entire catalog are not analyzed by this study, the selected cases previously presented indicate that based on simultaneous inversion of waveforms and first-motions the small isotropic components may be real. The variation of the isotropic median line with respect to injection rates is interesting and should be further investigated.

On 2014 January 21, more than two years after the start of injection, the M_W 3.87 maximum magnitude event occurs in the center of the study area at depth 1.7 km following an extended shut-in period when the injection rate is ~1514 lpm (400 gpm). It has been observed

at The Geysers that the month of May is when the largest number of $M \geq 4$ events have occurred. Because the water injection volume is highest in the months of February and March, due to an increase in the availability of run-off water from nearby communities, creek water and condensate (Hartline 2012), it is hypothesized that the time lag is associated with water percolating to deeper sections of the reservoir. At these deeper levels, as elevated temperatures convert water to steam, existing high stresses may be sufficiently increased that larger earthquakes may be sustained on fractures with suitable dimensions. The process of water flashing to steam withdraws a significant amount of heat from the rocks and in fact cools the rocks resulting in thermal contraction that produces additional thermal tensile stress that may give rise to larger magnitude events (Mossop 2001; Majer *et al*. 2007; Beall & Wright 2010; Kwiatek *et al.* 2015). Beall & Wright (2010) show a sharp boundary where most of the $M \geq 3$ events are located to the northwest in the region of the high temperature reservoir. It is believed that the small magnitude seismicity typically results from thermal cracks created when fluids cool the rock in the vicinity of the injection well (Stark 1990, 2003; Mossop 2001; Majer & Peterson 2007; Gritto *et al*. 2013; Rutqvist *et al*. 2013; Jeanne *et al*. 2014; Martínez-Garzón *et al*. 2014; Hartline *et al*. 2015).

Our waveform moment tensor based M_W is systematically lower than reported in the NCEDC EGS catalog by as much as 0.5 magnitude units. LBNL computes M_W by averaging the instrument corrected *P*-wave displacement spectrum from 1 Hz to the corner frequency for $M < 3.5$ events, and applying the whole space Green's function equation for direct *P* waves. Thus, even though both measures are effectively M_W one is computed using the complete waveform including *P*, *S* and surface waves (this study) and the other only the *P*-wave displacement spectrum. We have found that correcting the M_W in the NCEDC EGS catalog by a factor of $\log_{10}(2/8)$-0.03 (-0.63 magnitude units) accounts for the difference in M_W. The 2/8 factor accounts for the difference between theoretical half-space Green's functions and the semi-empirical half-space model that was used by LBNL in estimating M_W. The -0.03 factor accounts for differences between the specific moment magnitude relationships used. See Section 3.7 Appendix 3.A.2 for details. Following correction, a regression of the M_W data recovers a nearly 1:1 slope and a zero intercept with $R^2 = 0.95$ and *p*-value = 1.31e-23 (Fig. 3.14).

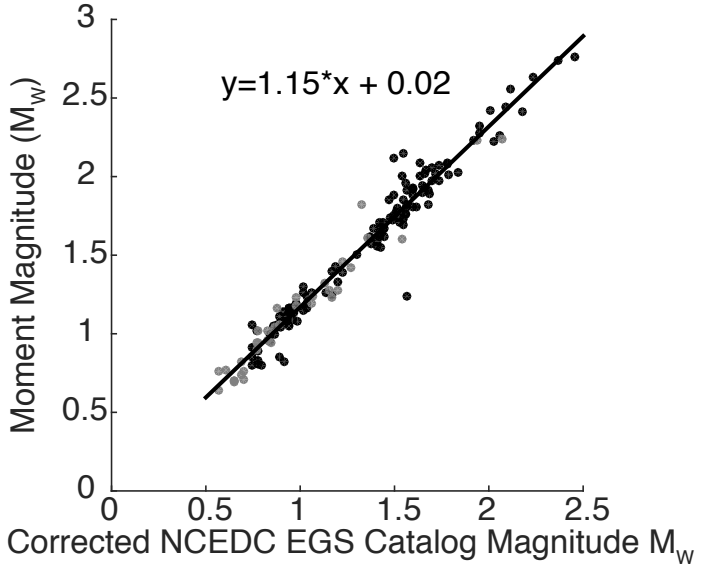

Figure 3.14. Comparison of waveform moment tensor M_W (this study) with corrected NCEDC EGS catalog M_W. Gray and black circles differentiate pre-injection from injection events, respectively. The solid line fits the data with $R^2 = 0.95$ and p-value = 1.31e-23.

3.4.2 Stress Analysis from Inversion of Focal Mechanisms

The Geysers and Clear Lake area are in a transtensional tectonic regime (Oppenheimer 1986; Donnelly-Nolan *et al*. 1993; Allis & Shook 1999; Boyle & Zoback 2014). The Clear Lake basin is assumed to be a pull-apart basin within the San Andreas Fault system (Hearn *et al*. 1988). The regional stress field based on the World Stress Map database release 2008 (Heidbach *et al*. 2010) shows a mean orientation of the maximum horizontal stress SHmax of 33° ± 28° based on 20 data records. Within The Geysers the mean SHmax orientation is 27° ± 20° based on 37 earthquake focal mechanism solutions from the period 1992 to 2011 (Gritto *et al*. 2014). This observation is consistent with results of Boyle & Zoback (2014). From their stress inversion of more than 6147 well-constrained earthquake focal mechanism solutions of events with $M > 1.5$ from 2005 to 2012 they obtained a mean SHmax orientation of 26°. SHmax inferred from our analysis for the localized study area indicates that it trends 10−15°. We note that the Northwest Geysers represents an area with complex fault bounded regions (e.g. Fig. 3.1) in which each could have slightly different stress orientation.

We observe a 15° counter-clockwise rotation of σ_3 during the study period, and during the period of time when injection temporarily ceased (windows K, L and M, Fig. 3.3) there is a marked rotation of σ_1 towards a more vertical orientation, which subsequently recovers when injection operations recommenced. This demonstrates that fluid injection operations have a substantial impact on the state of stress and the fractures that become activated. The magnitude of the stress rotations we observed is consistent with other nearby empirical observations (Martínez-Garzón *et al*. 2013) and thermo-hydromechanical simulation results (Jeanne *et al*. 2015; Ziegler *et al*. 2017).

Martínez-Garzón *et al*. (2013) studied the stress tensor using catalog first-motion focal mechanisms for a region just east of our study area finding a correlation between observed rotation in the stress tensor and multiple periods of high injection rate. The magnitude and direction of the rotation we observe for σ_3 is consistent with their findings. However, in their study area they found the plunge of σ_1 to decrease, whereas we observed it to increase. We see the change in plunge associated with the cessation of injection, whereas Martínez-Garzón *et al*. (2013) observed it during the injection phase, and this may be a reason for the difference in sign. It is possible there are different orientations of the initial stress tensor in the localized fault-bounded blocks, and thus the initial stress orientation and the directions of the perturbations could also differ at local scales affecting the direction of rotation. It is noted however that as injection resumes in windows L−O we find that the plunge of σ_1 decreases as pore pressure increases, which is consistent with what Martínez-Garzón *et al*. (2013) found. Jeanne *et al*. (2015) carried out numerical studies of a 9-year period spanning the Prati 9 injection and found rotations of σ_1 and σ_2 with respect to the vertical of 10 to 60 degrees depending on position above, below or adjacent to the well. In addition, they found rotations of SHmax between 5 and 15 degrees clockwise. Their results are based on an assumed normal faulting initial condition with σ_1 vertically oriented. While the initial stress state in our 1 x 2 km^2 area is strike-slip (σ_1 horizontal and σ_2 vertical) the amount of observed rotation of σ_1 and σ_2 with the vertical is comparable, as is the horizontal rotation of the stress tensor.

Results from Kwiatek *et al*. (2015) show a long-term temporal decrease in R in an observed normal stress regime, assuming $\sigma_V = \sigma_1$ is constant. As pore pressure increases over time there is a reduction in all effective stresses while there is an increase in horizontal stresses due to poroelastic effects (Shoenball *et al.* 2010; Altmann *et al*. 2014) such that the increase in σ_2 leads to decrease in R. We find that there is a systematic reduction in the stress shape factor, R, as injected volume increases, indicating an evolution towards a more transtensional stress state (Fig. 3.13), however after the cessation and resumption of injection the estimated stress shape factor becomes oscillatory indicating a significant change in the response of the system due to the interruption and restart of the injection operations. Such a reduction in R with increasing injection and pore pressure has been observed NE of the study area (Kwiatek *et al*. 2015; Martínez-Garzón *et al*. 2016), and Kwiatek *et al*. (2015) also note that the reduction of R slows as injection is ceased.

3.5 Conclusions

We have developed a semi-automated approach to estimate seismic moment tensors of micro-earthquakes utilizing three-component seismic waveforms in the 0.7 and 1.7 Hz frequency range for $M < 2.8$ events and in the 0.2 and 1.0 Hz frequency range for $M \geq 2.8$ events. The result of our effort has been the compilation of a 167-event waveform-based seismic moment tensor catalog for events ranging in moment magnitude from 0.6 to 3.9. We subsequently have utilized the moment tensor catalog for the Prati 32 study area to invert for the stress tensor and to investigate possible temporal changes resulting from the fluid injection. We have applied the approach of Vavryčuk (2014) to invert the focal mechanism

catalog for the stress tensor. We find that there is an approximate 15-degree counter-clockwise rotation of σ_3 during injection, and a relatively rapid rotation of σ_1 towards the vertical as the injection temporarily ceased. The magnitude of these rotations is consistent with other nearby empirical observations (Martínez-Garzón *et al*. 2013) and thermo-hydromechanical simulation results (Jeanne *et al*. 2015; Ziegler *et al*. 2017). We find that there is a systematic reduction in the stress shape factor, *R*, as injected volume increases, indicating an evolution towards a more transtensional stress state that may be the result of cooling of host rock and the tensile stress that results.

3.6 Acknowledgements

We are grateful for the technical support from Aurélie Guilhem, Andrea Chiang and Avinash Nayak and helpful discussions with Craig Hartline, Pierre Jeanne, Ramsey Haught, Steve Jarpe, Lawrence Hutchings, and Corinne Layland-Bachmann. We thank Editor Martin Mai, reviewer Grzegorz Kwiatek and an anonymous reviewer for helpful comments and suggestions that improved this manuscript. Seismic data for this study come from the Berkeley Geysers Seismic Network (BG), operated by Lawrence Berkeley National Laboratory, and from the Berkeley Digital Seismic Network (BDSN), doi:10.7932/BDSN, operated by the UC Berkeley Seismological Laboratory, which are archived at the Northern California Earthquake Data Center (NCEDC), doi:10.7932/NCEDC. Seismic waveform data were processed using Seismic Analysis Code (SAC), (Goldstein *et al*. 2003). Monthly injection data were acquired from the Online Geothermal Well Data Query for State of California, Department of Conservation, Division of Oil, Gas, and Geothermal Resources. Maps were made using the Generic Mapping Tools version 4.5.9 (www.soest.hawaii.edu/gmt: Wessel & Smith 1998). This research is funded by the Assistant Secretary for Energy Efficiency and Renewable Energy, Office of Geothermal Technologies of the U.S. Department of Energy under Contract No. DE-EE0006766.

3.7 Appendix

Table 3.A.1. Studied events: Event number, date, time, moment magnitude (M_W) this study, moment (dyne-cm), deviatoric moment tensor components M_{xx}, M_{xy}, M_{xz}, M_{yy}, M_{yz}, M_{zz} (dyne-cm), per cent double-couple (DC), per cent compensated linear vector dipole (C) and per cent variance reduction (VR).

No.	Date	Time	Mw	Mo dyne-cm	Mxx dyne-cm	Mxy dyne-cm	Mxz dyne-cm	Myy dyne-cm	Myz dyne-cm	Mzz dyne-cm	DC %	C %	VR %
1	11/16/09	22:50:37	1.6	3.18E+18	-1.85E+18	-2.16E+18	9.67E+17	2.33E+18	5.18E+16	-4.79E+17	88	12	54
2	11/25/09	16:21:40	2.24	2.86E+19	8.22E+17	-2.77E+19	-1.12E+18	-5.46E+18	-6.48E+18	4.64E+18	68	32	48
3	3/29/10	16:35:05	2.23	2.79E+19	-1.16E+19	-2.41E+19	1.19E+18	1.63E+19	6.76E+16	-4.70E+18	69	31	55
4	6/2/10	22:59:37	1.82	6.40E+18	-2.82E+18	-5.85E+18	-4.26E+17	2.05E+18	-8.35E+17	7.63E+17	76	24	80
5	6/22/10	23:20:13	1.23	8.63E+17	-3.69E+17	-5.70E+17	-2.26E+17	6.63E+17	4.57E+17	-2.94E+17	13	87	52
6	7/31/10	11:40:43	1.23	8.84E+17	4.26E+17	-7.68E+17	1.17E+17	-2.75E+17	2.03E+17	-1.51E+17	84	16	54
7	10/2/10	9:01:42	0.76	1.71E+17	-7.90E+16	4.65E+16	-5.06E+16	4.81E+16	1.42E+17	3.09E+16	77	23	69
8	11/7/10	7:51:48	0.64	1.13E+17	-3.98E+16	5.39E+16	5.40E+16	8.65E+16	4.70E+16	-4.67E+16	50	50	30
9	11/12/10	1:25:57	0.71	1.42E+17	6.54E+15	-7.54E+16	-5.94E+16	8.56E+16	6.42E+16	-9.22E+16	55	45	31
10	11/14/10	20:55:34	0.76	1.70E+17	-8.56E+16	5.21E+16	-6.40E+16	3.57E+16	1.29E+17	5.00E+16	95	5	56
11	11/18/10	20:21:49	0.74	1.62E+17	-8.97E+16	-1.27E+17	9.33E+15	9.95E+16	3.07E+16	-9.82E+15	89	11	40
12	11/19/10	0:26:54	0.69	1.33E+17	-1.16E+17	-4.98E+16	-1.06E+16	1.19E+17	3.84E+16	-2.97E+15	80	20	46
13	12/30/10	5:04:04	0.77	1.81E+17	6.59E+16	-1.39E+17	-4.85E+16	-1.27E+17	7.40E+15	6.12E+16	60	40	42
14	1/19/11	16:46:30	0.9	2.80E+17	-2.13E+17	-7.95E+16	-8.05E+16	2.85E+17	3.56E+16	-7.22E+16	68	32	37
15	3/8/11	21:22:23	1.46	1.94E+18	-1.04E+18	-1.09E+18	-8.96E+17	1.49E+18	9.03E+16	-4.49E+17	94	6	51
16	3/9/11	3:04:19	1.19	7.51E+17	-6.55E+17	-3.27E+17	-3.18E+17	5.67E+17	-8.63E+16	8.87E+16	52	48	48
17	3/10/11	18:19:23	1.06	4.89E+17	-4.41E+16	-2.43E+17	-7.28E+16	3.03E+17	3.32E+17	-2.59E+17	49	51	60
18	3/12/11	18:38:10	1.04	4.46E+17	-1.18E+17	-6.85E+16	-2.17E+17	2.60E+17	3.15E+17	-1.43E+17	71	29	52
19	3/23/11	12:04:44	0.96	3.48E+17	-2.47E+17	-1.57E+17	5.19E+16	3.26E+17	-1.34E+17	-7.88E+16	42	58	37
20	3/25/11	22:00:59	0.94	3.15E+17	2.68E+12	-1.03E+17	2.19E+17	1.96E+17	-6.16E+16	-1.96E+17	73	27	43
21	4/19/11	8:03:39	1.61	3.20E+18	-2.64E+18	2.00E+18	4.74E+17	2.24E+18	2.74E+17	4.01E+17	78	22	65
22	4/25/11	8:31:02	1.24	9.00E+17	-3.67E+17	-5.31E+17	3.78E+17	7.28E+17	-3.15E+16	-3.61E+17	72	28	57
23	5/3/11	14:02:32	1.32	1.21E+18	-9.78E+17	-4.64E+17	-3.52E+17	1.04E+18	3.20E+17	-6.21E+16	83	17	47
24	6/26/11	11:10:31	1.02	4.20E+17	-2.04E+17	-9.54E+16	-1.60E+17	4.38E+17	3.17E+16	-2.35E+17	67	33	36
25	7/12/11	22:08:32	0.7	1.41E+17	-6.89E+16	-8.20E+16	-6.03E+16	5.81E+16	8.92E+16	1.08E+16	32	68	31
26	8/2/11	1:29:03	1.02	4.21E+17	-2.74E+17	-9.69E+16	-9.98E+16	4.77E+17	-5.87E+15	-2.04E+17	44	56	43
27	8/2/11	23:14:12	1.16	6.78E+17	-5.86E+17	-2.04E+17	5.87E+16	6.68E+17	1.55E+17	-8.18E+16	74	26	55
28	8/3/11	21:54:53	1.28	1.02E+18	-4.33E+17	1.85E+16	2.85E+17	1.15E+18	-5.57E+16	-7.13E+17	55	45	45
29	8/3/11	23:45:47	1.18	7.34E+17	-4.54E+17	-1.06E+17	-2.59E+17	7.89E+17	7.61E+16	-3.35E+17	64	36	49
30	8/3/11	23:50:58	0.94	3.24E+17	-3.04E+17	4.63E+16	-2.74E+16	1.68E+17	-1.81E+17	1.36E+17	83	17	59
31	8/8/11	18:50:35	1.28	1.03E+18	2.10E+17	-9.55E+17	-1.40E+17	-4.25E+17	1.14E+17	2.14E+17	69	31	39
32	8/28/11	17:08:43	1.42	1.67E+18	-1.17E+18	6.31E+17	2.38E+15	1.62E+18	7.80E+17	-4.49E+17	35	65	54
33	9/18/11	0:26:05	0.82	2.11E+17	-1.05E+17	-1.24E+17	2.83E+16	9.18E+16	1.36E+17	1.28E+16	88	12	44
34	9/23/11	3:40:12	0.7	1.38E+17	5.72E+16	-7.80E+16	3.11E+16	4.50E+16	6.40E+16	-1.02E+17	83	17	62
35	9/29/11	21:30:11	0.94	3.15E+17	-9.39E+16	2.75E+17	9.65E+16	1.33E+17	5.02E+16	-3.95E+16	70	30	40
36	10/7/11	11:48:51	1.33	1.23E+18	-4.39E+17	-6.29E+17	5.18E+17	1.07E+18	-1.24E+17	-6.34E+17	65	35	47
37	10/10/11	7:09:03	1.26	9.53E+17	-6.98E+17	-1.69E+17	-3.01E+17	3.54E+17	7.18E+17	3.44E+17	38	62	22
38	10/17/11	8:23:21	1	3.93E+17	-2.79E+17	-2.37E+17	-3.71E+16	2.62E+17	1.59E+17	1.70E+16	77	23	61
39	10/20/11	9:51:25	1.08	5.14E+17	-3.75E+17	-1.03E+17	-3.08E+17	4.20E+17	8.14E+16	-4.55E+16	67	33	47
40	10/21/11	16:06:55	1.26	9.52E+17	-6.47E+17	4.81E+16	2.92E+17	1.01E+18	-2.66E+17	-3.59E+17	60	40	52
41	10/24/11	14:10:52	1.11	5.84E+17	-3.10E+17	-5.07E+16	-5.65E+16	7.12E+17	1.30E+17	-4.02E+17	20	80	56
42	10/26/11	13:55:34	2.01	1.27E+19	-6.02E+18	-9.08E+18	5.98E+18	7.08E+18	-7.25E+16	-1.06E+18	89	11	52
43	10/26/11	14:03:36	1.08	5.22E+17	-2.87E+17	-2.52E+17	2.10E+17	4.49E+17	9.90E+16	-1.62E+17	95	5	41
44	11/2/11	12:24:22	1.05	4.65E+17	-4.80E+17	-5.61E+16	-8.39E+16	4.22E+17	-5.81E+16	5.76E+16	74	26	44
45	11/5/11	18:10:49	1.13	6.11E+17	-3.45E+17	2.01E+17	2.35E+17	5.33E+17	-2.44E+17	-1.88E+17	91	9	48
46	11/7/11	17:56:26	1.13	6.23E+17	-7.87E+16	-4.61E+17	-3.17E+17	2.61E+17	-1.61E+17	-1.82E+17	77	23	63
47	11/7/11	17:56:40	1.11	5.70E+17	1.45E+17	-4.81E+17	-2.09E+17	-1.88E+17	1.62E+17	4.34E+16	74	26	67
48	11/9/11	8:20:40	1.14	6.32E+17	-2.17E+17	1.68E+17	2.47E+17	6.18E+17	-1.29E+17	-4.02E+17	85	15	52
49	11/14/11	6:30:51	1.62	3.34E+18	6.03E+17	-3.00E+18	-1.46E+18	-8.40E+16	3.99E+17	-5.19E+17	60	40	56
50	11/28/11	19:02:31	2.44	5.65E+19	-3.98E+19	-3.34E+19	5.36E+16	4.96E+19	9.73E+18	-9.84E+18	65	35	52
51	12/5/11	8:24:33	1.72	4.70E+18	-3.44E+18	-1.78E+18	4.31E+17	5.12E+18	4.77E+17	-1.68E+18	43	57	66
52	12/5/11	12:04:12	2.33	3.88E+19	-3.03E+19	-2.56E+19	3.41E+18	2.73E+19	3.21E+18	3.01E+18	83	17	61
53	12/5/11	15:14:35	1.88	8.24E+18	-3.56E+18	-7.10E+18	-1.33E+18	4.03E+18	-1.08E+18	-4.72E+17	97	3	59
54	12/9/11	13:41:48	2.28	3.26E+19	-1.00E+19	-1.50E+19	-3.31E+18	3.30E+19	-8.39E+18	-2.30E+19	38	62	49
55	12/10/11	22:17:03	2.26	3.06E+19	-7.86E+18	-7.87E+18	-5.56E+18	3.21E+19	7.70E+18	-2.43E+19	52	48	55
56	12/13/11	16:20:31	1.66	3.81E+18	-1.68E+18	-3.69E+17	5.13E+17	4.55E+18	-8.66E+16	-2.86E+18	34	66	52

No.	Date	Time	Mw	Mo dyne-cm	Mxx dyne-cm	Mxy dyne-cm	Mxz dyne-cm	Myy dyne-cm	Myz dyne-cm	Mzz dyne-cm	DC %	C %	VR %
57	12/19/11	14:09:38	3.19	7.52E+20	-5.12E+20	-4.50E+20	-1.19E+20	6.42E+20	1.49E+20	-1.31E+20	62	38	56
58	12/27/11	12:16:09	2.02	1.35E+19	-7.62E+18	-2.69E+18	-4.77E+18	1.40E+19	-2.83E+18	-6.42E+18	70	30	53
59	12/28/11	6:25:39	2.02	1.33E+19	-7.63E+18	6.07E+18	3.70E+18	1.21E+19	-4.07E+18	-4.45E+18	72	28	65
60	12/30/11	22:35:40	1.82	6.71E+18	-3.26E+18	-1.77E+18	-1.82E+18	7.31E+18	1.62E+18	-4.04E+18	40	60	43
61	1/4/12	19:34:47	1.57	2.78E+18	-1.59E+18	-1.07E+18	-7.54E+17	2.75E+18	1.20E+18	-1.16E+18	28	72	68
62	1/6/12	20:55:40	2.44	5.62E+19	-6.61E+18	2.35E+18	-6.96E+18	5.39E+19	-2.30E+19	-4.73E+19	80	20	49
63	1/14/12	14:32:44	2.15	2.05E+19	-7.51E+18	-1.41E+19	8.07E+18	1.25E+19	-1.05E+19	-4.98E+18	24	76	57
64	1/15/12	3:54:25	1.73	4.90E+18	-1.47E+18	-1.72E+18	-9.21E+17	5.21E+18	-3.60E+17	-3.75E+18	48	52	53
65	2/4/12	17:23:37	2.32	3.81E+19	-1.38E+19	-2.79E+19	-1.21E+19	2.75E+19	1.30E+19	-1.37E+19	29	71	74
66	2/7/12	14:14:37	1.82	6.75E+18	-3.42E+18	-2.05E+18	-2.09E+18	7.22E+18	9.65E+17	-3.80E+18	48	52	57
67	2/11/12	0:53:21	1.67	3.91E+18	-1.33E+18	-2.93E+18	-1.24E+18	1.68E+18	-1.74E+18	-3.54E+17	77	23	53
68	2/14/12	12:58:04	1.63	3.52E+18	-2.36E+18	1.85E+18	3.14E+16	3.56E+18	5.03E+17	-1.20E+18	40	60	31
69	2/19/12	6:48:19	2.06	1.51E+19	-3.73E+18	-1.30E+19	-2.03E+18	8.31E+18	-3.46E+18	-4.58E+18	61	39	58
70	2/23/12	17:22:08	2.07	1.56E+19	-8.21E+18	-5.78E+18	-6.90E+18	1.48E+19	-6.84E+17	-6.55E+18	87	13	63
71	2/26/12	0:29:56	2.12	1.90E+19	6.60E+18	-8.54E+18	9.45E+18	5.86E+18	1.15E+19	-1.25E+19	29	71	45
72	2/29/12	0:07:31	1.76	5.44E+18	-4.29E+18	5.40E+17	1.19E+18	5.76E+18	-1.47E+18	-1.48E+18	59	41	54
73	2/29/12	17:30:54	1.91	9.09E+18	-4.94E+18	-4.82E+18	-2.85E+18	8.41E+18	-3.30E+17	-3.47E+18	64	36	54
74	3/5/12	20:40:17	1.69	4.26E+18	-2.62E+18	-1.31E+18	4.21E+17	5.05E+18	6.52E+17	-2.43E+18	21	79	42
75	3/9/12	19:29:09	1.93	9.67E+18	-1.88E+18	-7.52E+18	1.11E+18	5.51E+18	3.94E+18	-3.63E+18	60	40	33
76	3/23/12	21:04:46	1.93	9.69E+18	-9.29E+18	-2.06E+18	-2.02E+18	8.88E+18	1.74E+18	4.03E+17	94	6	64
77	3/25/12	4:25:16	1.88	8.16E+18	-6.60E+17	-1.75E+18	-4.16E+17	5.59E+18	-5.98E+18	-4.93E+18	83	17	51
78	3/27/12	10:09:06	1.8	6.33E+18	-4.31E+18	5.06E+17	1.01E+18	7.66E+18	-2.73E+17	-3.35E+18	29	71	55
79	3/27/12	22:33:45	1.91	9.14E+18	-4.64E+18	-3.63E+17	2.19E+17	1.14E+19	1.84E+17	-6.80E+18	19	81	52
80	3/31/12	20:29:35	1.24	9.02E+17	-2.48E+17	2.33E+17	-2.72E+17	9.08E+17	-2.32E+17	-6.61E+17	60	40	33
81	4/7/12	2:48:10	2.23	2.73E+19	-1.17E+19	-1.95E+19	-9.29E+18	1.86E+19	-3.90E+18	-6.90E+18	88	12	65
82	4/19/12	12:02:38	1.97	1.14E+19	-1.74E+18	-4.21E+16	1.56E+18	1.18E+19	-2.54E+18	-1.01E+19	76	24	41
83	4/21/12	18:47:08	1.81	6.37E+18	-3.80E+18	3.98E+18	4.09E+17	6.02E+18	-4.24E+17	-2.22E+18	43	57	57
84	4/28/12	5:12:48	2	1.25E+19	-3.27E+18	-6.64E+18	-2.75E+18	9.24E+18	-6.37E+18	-5.97E+18	74	26	53
85	5/9/12	20:28:23	1.68	4.12E+18	-2.80E+18	-8.93E+17	-1.49E+18	4.24E+18	6.72E+17	-1.44E+18	69	31	46
86	5/22/12	9:55:28	1.74	5.07E+18	-2.92E+18	2.60E+18	8.71E+17	5.27E+18	-1.34E+17	-2.35E+18	36	64	56
87	5/25/12	1:30:26	1.92	9.37E+18	-2.41E+18	-8.16E+18	-2.72E+18	4.15E+18	2.44E+18	-1.74E+18	51	49	65
88	5/27/12	22:59:01	1.85	7.36E+18	-1.53E+18	6.10E+18	-2.76E+17	4.76E+18	2.19E+18	-3.23E+18	37	63	53
89	5/31/12	5:31:24	2.63	1.11E+20	-9.28E+19	-3.78E+19	2.37E+19	9.89E+19	3.30E+19	-6.11E+18	93	7	75
90	5/31/12	5:54:35	1.71	4.57E+18	-3.59E+18	-1.78E+18	-1.94E+18	3.68E+18	8.76E+17	-9.26E+16	93	7	64
91	6/16/12	14:17:52	1.63	3.48E+18	-2.41E+18	1.76E+18	-8.99E+16	3.59E+18	-8.79E+16	-1.18E+18	42	58	64
92	6/22/12	11:31:33	1.67	4.05E+18	-1.82E+18	1.60E+18	1.52E+18	3.88E+18	-6.19E+17	-2.06E+18	76	24	54
93	6/26/12	12:16:24	1.59	3.07E+18	-2.79E+18	-1.13E+18	-8.53E+17	2.29E+18	8.97E+17	5.00E+17	90	10	60
94	6/28/12	12:49:06	1.96	1.07E+19	-4.46E+18	-3.98E+17	-8.12E+17	1.23E+19	-3.15E+18	-7.86E+18	33	67	52
95	6/30/12	15:30:40	1.9	8.95E+18	2.50E+16	-7.98E+18	1.81E+18	7.89E+17	-3.97E+18	-8.14E+17	59	41	53
96	7/3/12	3:36:37	1.89	8.40E+18	-6.22E+16	3.28E+18	-3.38E+18	6.90E+18	-1.11E+18	-6.84E+18	93	7	53
97	7/5/12	6:36:27	1.55	2.60E+18	-1.06E+18	-1.17E+18	-4.78E+17	2.82E+18	1.50E+17	-1.76E+18	29	71	58
98	7/9/12	17:49:40	2	1.26E+19	-7.22E+18	-5.69E+18	-5.65E+18	7.39E+18	7.27E+18	-1.67E+17	44	56	48
99	7/10/12	9:18:31	2.56	8.50E+19	-5.19E+19	-5.43E+19	-2.80E+19	6.41E+19	-4.07E+18	-1.22E+19	95	5	70
100	7/10/12	23:06:41	2.09	1.68E+19	-6.10E+18	-1.25E+19	-1.33E+18	9.96E+18	8.41E+18	-3.86E+18	43	57	69
101	7/14/12	7:10:32	2.04	1.45E+19	6.04E+18	-5.31E+18	1.09E+19	2.40E+18	3.58E+18	-8.44E+18	60	40	45
102	7/16/12	11:41:38	2.74	1.60E+20	-7.13E+19	-4.57E+19	-2.99E+19	1.81E+20	-1.96E+19	-1.10E+20	38	62	55
103	7/16/12	13:41:14	1.5	2.25E+18	-5.78E+17	1.32E+18	9.98E+17	1.32E+18	-1.04E+18	-7.41E+17	74	26	58
104	7/16/12	14:17:27	1.19	7.54E+17	-1.81E+17	-2.13E+17	9.68E+16	7.89E+17	-1.94E+17	-6.08E+17	49	51	54
105	7/18/12	5:18:11	0.85	2.35E+17	-1.48E+17	1.72E+17	-5.98E+14	1.70E+17	-2.51E+16	-2.21E+16	81	19	53
106	7/26/12	1:18:23	1.16	6.92E+17	-4.28E+17	-2.48E+17	9.82E+16	7.48E+17	1.94E+17	-3.20E+17	36	64	59
107	7/29/12	15:43:16	1.17	7.05E+17	-3.94E+17	3.72E+16	-1.70E+17	8.08E+17	-1.60E+17	-4.14E+17	40	60	47
108	7/30/12	0:27:24	1.14	6.47E+17	-2.86E+17	4.34E+17	1.41E+17	4.68E+17	-2.21E+17	-1.82E+17	75	25	64
109	8/2/12	17:56:51	1.3	1.12E+18	-2.87E+17	-1.58E+16	-8.02E+16	1.14E+18	-4.88E+17	-8.55E+17	56	44	47
110	8/4/12	0:10:21	1.16	6.91E+17	1.89E+17	-4.72E+17	-1.23E+17	3.22E+17	-2.13E+17	-5.11E+17	74	26	48
111	8/8/12	9:49:58	1.15	6.55E+17	-3.55E+17	5.07E+17	-8.69E+16	4.21E+17	-1.31E+17	-6.52E+16	73	27	41
112	8/11/12	7:57:55	1.08	5.13E+17	-2.23E+17	4.51E+16	-1.93E+17	4.81E+17	-2.42E+17	-2.58E+17	63	37	43

No.	Date	Time	Mw	Mo dyne-cm	Mxx dyne-cm	Mxy dyne-cm	Mxz dyne-cm	Myy dyne-cm	Myz dyne-cm	Mzz dyne-cm	DC %	C %	VR %
113	8/13/12	17:25:20	1.04	4.55E+17	-3.11E+17	-5.82E+16	5.22E+15	5.85E+17	6.60E+16	-2.73E+17	7	93	55
114	8/19/12	18:24:37	0.82	2.14E+17	-1.25E+17	5.98E+16	-1.30E+17	1.98E+16	1.12E+17	1.05E+17	78	22	43
115	8/24/12	3:38:28	1.06	4.84E+17	-3.93E+17	-1.78E+17	1.75E+17	4.34E+17	6.34E+15	-4.06E+16	91	9	55
116	8/24/12	5:46:08	2.17	2.28E+19	-1.23E+19	-3.02E+18	3.99E+17	2.83E+19	-4.52E+18	-1.60E+19	14	86	46
117	8/25/12	8:59:21	1.26	9.73E+17	-3.19E+17	2.84E+16	-4.49E+17	5.34E+17	7.30E+17	-2.15E+17	83	17	51
118	9/7/12	8:26:03	0.83	2.15E+17	-6.41E+16	6.89E+15	6.94E+16	1.63E+17	1.50E+17	-9.90E+16	66	34	37
119	9/8/12	8:14:08	0.91	2.91E+17	-2.87E+17	3.46E+15	9.34E+16	1.64E+17	1.21E+17	1.23E+17	78	22	46
120	9/20/12	9:00:50	1.16	6.77E+17	-4.88E+17	-3.85E+17	-5.51E+16	5.76E+17	1.77E+17	-8.87E+16	65	35	59
121	9/24/12	5:09:27	1.09	5.44E+17	-5.11E+16	4.71E+17	2.08E+17	1.48E+16	-2.27E+17	3.63E+16	44	56	64
122	10/5/12	19:48:56	2.09	1.71E+19	-2.76E+18	7.08E+18	-7.22E+18	5.16E+18	1.34E+19	-2.40E+18	64	36	67
123	10/8/12	5:06:46	1.75	5.30E+18	-7.68E+17	-4.17E+18	-2.07E+18	7.06E+17	2.97E+18	6.20E+16	37	63	63
124	10/11/12	7:08:07	1.39	1.53E+18	-2.76E+17	-1.17E+18	2.68E+17	8.36E+17	6.37E+17	-5.60E+17	72	28	55
125	10/16/12	10:43:05	0.8	1.97E+17	-1.57E+17	-3.86E+16	1.19E+16	2.00E+17	8.35E+16	-4.35E+16	44	56	51
126	10/18/12	0:33:16	0.91	2.91E+17	1.10E+17	-1.99E+17	7.59E+16	6.32E+16	-1.48E+17	-1.73E+17	47	53	54
127	11/1/12	0:05:20	0.95	3.33E+17	-2.22E+17	-2.70E+15	-2.50E+17	1.09E+17	1.17E+17	1.12E+17	68	32	48
128	11/28/12	19:21:45	1.06	4.80E+17	3.45E+17	-1.61E+17	3.55E+17	-1.67E+17	-1.46E+17	-1.78E+17	30	70	35
129	12/5/12	15:59:05	0.89	2.66E+17	-2.66E+17	-1.74E+16	9.74E+16	2.36E+17	-4.69E+14	2.97E+16	60	40	37
130	12/26/12	7:36:30	0.85	2.36E+17	2.76E+17	3.27E+16	8.70E+16	-1.17E+17	6.83E+15	-1.59E+17	19	81	45
131	1/8/13	8:28:41	1.25	9.40E+17	-2.17E+16	-7.89E+17	-2.65E+17	9.69E+16	4.99E+17	-7.51E+16	46	54	63
132	1/30/13	0:47:44	1.07	5.03E+17	-5.03E+16	-3.97E+17	-2.74E+17	6.56E+15	1.74E+17	4.37E+16	55	45	64
133	1/30/13	1:38:45	1	3.96E+17	-2.36E+17	2.72E+17	4.99E+14	3.25E+17	-7.26E+16	-8.89E+16	57	43	53
134	1/30/13	6:35:23	1.05	4.69E+17	-2.24E+17	2.96E+17	1.14E+17	3.83E+17	-1.14E+17	-1.59E+17	68	32	54
135	1/30/13	7:33:43	1.43	1.74E+18	-9.92E+17	1.27E+18	-2.09E+16	1.32E+18	-3.42E+17	-3.27E+17	62	38	66
136	1/30/13	10:30:33	1.4	1.56E+18	-7.52E+17	1.01E+18	2.15E+17	1.29E+18	-4.92E+17	-5.34E+17	54	46	64
137	1/30/13	13:31:32	1.19	7.63E+17	1.35E+17	-1.95E+17	9.40E+16	3.66E+17	-5.79E+17	-5.01E+17	86	14	39
138	1/30/13	19:07:18	0.81	2.04E+17	-1.49E+17	-5.36E+16	-6.72E+16	1.88E+17	7.71E+16	-3.96E+16	61	39	34
139	1/31/13	0:14:11	1.62	3.33E+18	-2.13E+18	2.12E+18	-3.48E+16	2.90E+18	-5.72E+17	-7.67E+17	56	44	66
140	1/31/13	0:23:36	1.24	9.15E+17	-6.14E+17	4.99E+17	-1.12E+17	8.93E+17	-5.37E+16	-2.79E+17	49	51	61
141	2/1/13	6:15:39	1.16	6.74E+17	-4.43E+17	-3.06E+17	-2.42E+17	4.82E+17	3.39E+17	-3.86E+16	51	49	57
142	2/1/13	13:13:20	0.8	1.97E+17	-8.39E+16	3.52E+16	4.56E+16	2.18E+17	-3.89E+16	-1.34E+17	49	51	44
143	2/1/13	20:09:54	1.04	4.49E+17	-3.76E+17	-1.52E+17	2.61E+16	4.66E+17	2.24E+16	-9.03E+16	64	36	59
144	2/3/13	19:49:34	1.02	4.28E+17	-4.00E+17	-4.45E+16	-2.29E+17	3.54E+17	8.30E+15	4.60E+16	44	56	29
145	2/6/13	4:05:31	2.87	2.53E+20	1.88E+19	-1.23E+20	-2.02E+19	1.83E+20	1.13E+20	-2.02E+20	70	30	67
146	2/15/13	11:38:56	1.8	6.34E+18	-5.10E+18	-1.15E+18	-7.38E+17	7.17E+18	6.42E+17	-2.06E+18	46	54	59
147	4/23/13	8:34:16	1.81	6.56E+18	-5.34E+18	-1.32E+18	1.69E+18	6.39E+18	1.90E+18	-1.05E+18	80	20	53
148	5/13/13	21:15:30	1.76	5.48E+18	-2.60E+18	-1.11E+18	-1.02E+18	5.30E+18	3.41E+18	-2.70E+18	24	76	61
149	5/17/13	15:42:58	1.71	4.56E+18	-4.32E+18	-6.00E+17	-3.40E+17	4.62E+18	6.24E+17	-3.01E+17	85	15	57
150	5/25/13	7:55:28	1.78	5.75E+18	-3.59E+18	3.66E+18	-1.65E+17	5.04E+18	-1.15E+18	-1.44E+18	51	49	64
151	6/12/13	3:47:40	1.85	7.34E+18	-5.54E+18	-5.30E+17	-3.35E+17	9.05E+18	3.00E+17	-3.52E+18	23	77	61
152	7/2/13	17:34:30	1.71	4.59E+18	-1.35E+17	-3.52E+18	-2.43E+18	1.81E+18	2.50E+17	-1.68E+18	71	29	59
153	7/12/13	14:46:52	1.94	1.03E+19	-2.01E+18	-6.77E+18	-4.03E+18	7.02E+18	-2.23E+18	-5.01E+18	87	13	62
154	7/13/13	8:30:46	2.08	1.63E+19	-7.22E+17	-1.29E+19	-7.19E+18	6.44E+18	-3.44E+18	-5.72E+18	99	1	68
155	7/17/13	14:48:51	1.97	1.12E+19	-8.24E+18	-2.95E+18	-6.84E+17	1.30E+19	1.87E+18	-4.80E+18	27	73	66
156	7/18/13	11:45:39	1.56	2.75E+18	-4.95E+17	-9.54E+17	-5.90E+17	2.77E+18	1.26E+17	-2.28E+18	62	38	42
157	8/6/13	13:46:48	1.61	3.18E+18	-1.82E+17	-2.54E+18	-9.99E+17	1.91E+18	-8.66E+16	-1.73E+18	48	52	68
158	8/9/13	16:33:49	1.62	3.31E+18	-1.11E+18	-2.32E+17	8.63E+17	3.65E+18	-1.71E+17	-2.54E+18	61	39	41
159	8/24/13	11:29:01	1.74	5.02E+18	-2.74E+18	-1.63E+18	-2.08E+18	4.91E+18	-4.51E+17	-2.17E+18	83	17	54
160	8/25/13	14:06:47	2.03	1.36E+19	-4.47E+18	-2.95E+18	5.00E+17	1.50E+19	-4.01E+18	-1.05E+19	39	61	39
161	9/6/13	16:39:32	1.92	9.49E+18	-3.48E+18	-6.76E+17	-3.53E+18	9.53E+18	-2.89E+18	-6.05E+18	78	22	48
162	10/5/13	16:50:12	2.42	5.29E+19	-2.83E+19	2.24E+19	7.89E+18	5.59E+19	-1.43E+19	-2.76E+19	36	64	66
163	10/28/13	16:47:26	2.22	2.62E+19	-2.30E+19	-6.13E+18	-4.40E+18	2.54E+19	7.07E+18	-2.42E+18	74	26	55
164	1/21/14	11:11:12	3.87	8.01E+21	-8.39E+20	-4.32E+21	-2.93E+21	6.54E+21	-2.70E+20	-5.70E+21	73	27	62
165	6/28/14	16:05:11	2.76	1.70E+20	-7.70E+19	-1.31E+20	1.49E+18	1.25E+20	3.87E+19	-4.77E+19	50	50	65
166	6/29/14	3:30:11	2.41	5.13E+19	-3.03E+19	-8.15E+18	-1.04E+19	6.08E+19	-2.36E+17	-3.05E+19	34	66	52
167	10/20/14	4:25:16	2.53	7.65E+19	-1.84E+19	-6.20E+19	-2.07E+19	3.25E+19	-2.78E+19	-1.41E+19	96	4	59

3.A.2: Derivation of the difference between NCEDC EGS catalog M_W and waveform M_W estimates from this study.

The whole-space Green's function for a far-field P-wave is:

$$u(\omega) = \frac{M_0}{4\pi\rho\alpha^3 r} s(\omega),$$

while for a half-space it is approximately:

$$u(\omega) = \frac{2M_0}{4\pi\rho\alpha^3 r} s(\omega),$$

where u is the displacement spectrum, s is the unit source spectrum, Mo is the scalar moment, ρ is source density, α is *P*-wave velocity and r is distance. Thus, solving for the scalar moment we have.

$$M_0 = 2\pi\rho\alpha^3 r \cdot u(\omega = 0)$$

In LBNL's notation this should be written as follows, which assumes that the products of ρ and ρ', and c and c' have the theoretical powers of 1 (for density) and 3 (for alpha).

$$M_0 = 2\pi\rho'\rho c'cd \cdot D,$$

where d is the distance and D is the frequency averaged estimate of the low frequency asymptote.

The equation used by LBNL is:

$M_0 = 8\pi\acute{\rho}\rho\acute{c}cdD$
Where:
$\acute{\rho}$ *is* $(source\ density)^{0.5}$
ρ *is* $(surface\ density)^{0.5}$
$\acute{c}$ *is* $(source\ Vp)^{2.5}$
c *is* $(surface\ Vp)^{0.5}$

Thus, we found that the difference between NCEDC EGS catalog M_W and our waveform M_W estimates is shifted by the factor of log10(2/8). The -0.03 factor is simply the difference between using the 9.1 versus 9.05 definition for the moment magnitude relationship intercept. The regression in Figure 3.14 is after the NCEDC EGS M_W has been corrected and it shows that the theoretical correction is good. The details of this correction are needed for others to be

able to apply the correction. It should be noted that LBNL has changed their relationship from 2015 onward.

Chapter 4

Stress Drop and Scaling of Earthquakes at The Geysers Geothermal Field, California

4.1 Chapter Abstract

Seismicity from the Enhanced Geothermal System (EGS) demonstration project at The Geysers, California Prati 32 injection well has been investigated for the seismic moment tensor, *in situ* stress, and the scaling of micro-earthquake source parameters. One objective is to develop an approach for estimating a statistical representation of the fracture network generated from the injection of fluids into hot dry rock. This can be accomplished by utilizing a relationship between scalar seismic moment and fault dimension, in which catalog events with a reported M_W can be converted to a source dimension, and then knowledge of the state of stress can be used to randomly assign the orientation of the rupture fault consistent with the known state of stress. In order to attempt this it is first necessary to investigate the finite-source properties of the micro-earthquakes and evaluate their rupture dimension, slip and stress drop scaling. Towards this end, we have performed finite-source inversions of seismic moment rate functions obtained for earthquakes spanning the magnitude range of M_W 1.0 to 5.0 at or near the EGS demonstration site. We find that micro-earthquakes are not simple ruptures and can have strong directivity effects, with multiple patches of slip. Rupture area is found to be consistent with the Wells and Coppersmith (1994) and Leonard (2010) scaling laws developed for much larger ($M_W \geq 5.5$) globally-occurring earthquakes. Owing to the complex nature of the kinematic finite-source models we use the method of Ripperger and Mai (2004) to compute the static stress change. We find that peak stress drops can be large, however on average they are consistent with the aforementioned source scaling laws.

4.2 Introduction

Identifying, creating, and managing fractures and flow paths are essential tasks during EGS resource development. The successful generation of a fracture network requires a priori knowledge of *in situ* stress and natural fracture orientation, spacing, and the scaling of dimension with magnitude. To obtain this information requires continuous monitoring of seismic activity prior to and during fluid injection stimulation. As high rates of fluid injection may disturb the natural stress state (Kwiatek *et al*., 2015; Martínez-Garzón *et al*., 2013, 2014; Boyd *et al*., 2018; Chapter 3), it is advantageous to continuously monitor induced seismicity and in addition to locating events and estimating magnitudes monitor the *in situ* stress and how it evolves during the injection process. Such monitoring is demonstrated in Chapter 3.

Knowing the stress evolution, the size and spatial distribution of the fractures, and the nature of the rupture process can be utilized together to help inform on the activated fracture network and fluid flow pathways.

In this chapter our focus is a finite-source analysis of seismicity in and around the Prati 32 EGS study area to better understand the source characteristics of the micro-earthquakes and to develop scaling laws to relate derived scalar seismic moment to rupture dimension for induced earthquakes resulting from EGS resource development, building on the research presented in Chapters 2 and 3. The first step in the finite-source analysis we use is finding highly correlated pairs of events to determine the seismic moment rate function (MRF) at a recording station using the method of waveform deconvolution of a small magnitude earthquake. Given two nearly collocated earthquakes with a magnitude difference of more than one magnitude unit, and the same or similar focal mechanism, it is possible to deconvolve the signal of the smaller event from the larger event recovering the seismic moment rate function (e.g. Mori and Hartzell, 1990). We use the spectral domain method of deconvolution using a 'water level' to avoid difficulties due to spectral nulls in the smaller earthquake spectrum (Clayton and Wiggens, 1976). The water level is set as low as possible. Ideally the magnitude difference is greater than 1.0 unit in moment magnitude to ensure that the small earthquake source corner frequency is well above that of the larger target event. A smaller magnitude earthquake that satisfies these conditions is known as an empirical Green's function (eGf) event (Hartzell, 1978; Wu, 1978; Mueller, 1985; Hough and Seeber, 1991). The empirical Green's function deconvolution essentially removes the effects of earthquake radiation pattern, wave propagation, attenuation and site response, leaving the moment rate function, which can vary in duration and amplitude due to the finite extent of the earthquake rupture, and the rupture kinematics. The empirical Green's function approach has proven useful for the study of micro-earthquakes (Bakun and Bufe, 1975; Mori and Hartzell, 1990; Mori, 1993; Hutchings and Wu, 1990), moderate earthquakes (Ide, 2001; Uchide and Ide, 2010) and to large and great earthquakes (Antolik *et al*., 1996, 1999; Kaverina *et al*., 1998; Ide *et al*., 2011).

The deconvolved moment rate functions are then inverted for slip (Mori and Hartzell, 1990; Dreger, 1994, 1997; Dreger *et al*., 2007), testing the two possible double-couple nodal planes from the seismic moment tensor analyses presented in Chapters 2 and 3, thereby also finding the causative rupture plane of the earthquake. In this study spatio-temporal source properties (source dimension (length and area), slip distribution, and rupture speed) are determined for ten M_W 1.0 to 5.0 events using moment-rate time histories of the source from empirical Green's function deconvolution.

With estimates of moment magnitudes, rupture area, and slip we investigate scaling relationships for the purpose of estimating the coseismic fracture area associated with Prati 32 injection. Wells and Coppersmith (1994) present empirical relationships between various source parameters from a database of over 250 worldwide $M > 4.7$ events occurring in various tectonic regimes excluding subduction zones, within oceanic slabs, and at both plate interfaces. The majority of events in that study have magnitudes greater than M 6. Leonard (2010) presents self-consistent fault scaling relationships between seismic moment, rupture area, and displacement that can be applied to all types of faults and includes the datasets of

Wells and Coppersmith (1994) along with several others. As these relationships are constrained by data from mostly $M_W > 6.0$ earthquakes it is not clear whether the scaling relationships of these larger tectonic earthquakes would extend to micro-earthquakes located in an induced seismicity environment, and therefore it is necessary to evaluate them, and possibly estimate independent scaling relationships if necessary.

The stress drops of earthquakes are largely constant over the complete magnitude range (e.g. Ide and Beroza, 2001), however there can be variations between different environments (Choy and Boatwright, 1995; Viegas *et al*., 2010). Furthermore stress drop is typically determined from measurements of the corner frequency and then related to a mechanical model relating corner frequency to the rupture dimensions (e.g. Brune, 1970, 1971; Madariaga, 1976; Sato and Hirasawa, 1973). These are very common methods, now routinely applied (Hough and Dreger, 1995; Abercrombie 1995, 2014; Shearer *et al*., 2006; Mayeda *et al*., 2007; Ruhl *et al*., 2017), however the estimated corner frequency is subjected to cube scaling to get to rupture dimension and therefore errors in the estimate can lead to large uncertainty in the rupture parameters. Finite-source analysis offers an independent approach in that the moment rate functions, their duration and shape, are inverted for the distribution of fault slip, which is often found to be complex (e.g. Mori and Hartzell, 1990). The slip distribution can then be used to map to the coseismic stress change using the methodology of Ripperger and Mai, 2004. This formulation considers simplified fault geometries consisting of a single fault segment on a single 2-D fault plane in a homogeneous medium defined in a whole space. While Okada's (1992) half-space approach accommodates complex fault geometries and the effect of a free surface in a half-space, the approach of Ripperger and Mai (2004) is an efficient initial estimate of static stress change for this study of $M_W < 5$ events. The stress change estimated in this way is itself complex, where areas that slipped see a stress relaxation, and adjacent portions of the fault see stress increases. From these stress change maps it is possible to determine the average stress drop, which is most consistent with the corner frequency estimates and a peak stress drop that is difficult to estimate in any other way (e.g. Dreger *et al*., 2007).

The outcome of the finite-source, seismic moment tensor and stress tensor analyses can lead to a more detailed mapping of the fracture network inferred from the induced seismicity (Dreger *et al*., 2018a,b; Gritto *et al*., 2018; Boyd *et al*., 2017), which in turn can inform on possible fluid pathways due to the stimulation.

4.3 Data and Methodology

Finite Source Rupture Estimation

For large earthquakes finite-source inversion commonly uses theoretical Green's functions (e.g. Hartzell and Heaton, 1983), however for small events related to the EGS stimulation project it is necessary to consider frequencies higher than those that can be adequately predicted from the simple plane layered velocity models used to calculate

theoretical Green's functions. Therefore as discussed above, empirical Green's functions are employed, utilizing the waveforms of nearly collocated smaller events to correct for path, site and common elements in the source (focal mechanism) and recover an estimate of the seismic moment rate function (MRF). As shown in Mori and Hartzell (1990) these MRF vary with azimuth from the source and carry information about the earthquake rupture directivity and the finite-extent of the rupture.

In our application for The Geysers we first utilized event locations from the Northern California Earthquake Data Center (NCEDC) Northern California Seismic Network (NCSS) catalog to identify possible empirical Green's function events that could be used for the eGf deconvolution to obtain the needed seismic moment rate functions. This proved to be difficult, and the strategy was adjusted to utilize double-difference relative earthquake locations. With the high-resolution double-difference earthquake catalog from Waldhauser and Schaff (2008) a search was performed to find events that are at least 1.0 magnitude unit smaller and horizontally located within 200 m from the larger target event. No constraint was imposed on the allowable depth of the eGf events since depth is less well resolved. From these search results several eGfs were found for a number of the target events. For $M < 4$ target earthquakes in the EGS demonstration site centered on the Prati 32 injection well, we added additional constraints on the event origin time to reduce the total number of nearby earthquakes. For these smaller magnitude target earthquakes we incorporated the Northern California Earthquake Data Center Enhanced Geothermal System (NCEDC EGS) earthquake catalog to identify additional potential eGf events occurring within a month or more of the target event. The target event and eGf waveforms were instrument-corrected, and high-pass filtered at 0.1 Hz to remove low frequency noise. The eGf records were then deconvolved from the target event waveforms using a frequency-domain approach with an applied (0.1 %) water level (Clayton and Wiggins, 1976) to identify those events that produced pulse-like MRF with the highest signal to noise to be used to invert for finite-source parameters and to test for the causative fault plane orientation. Recovery of a pulse-like signal from the convolution process verifies the empirical Green's function assumptions of 1) co-location, 2) common radiation pattern and 3) sufficient difference in magnitude to resolve the source corner frequency. In cases where any of these assumptions do not hold pulses are not recovered.

As done in Dreger (1997) and Dreger *et al*. (2007) the MRF are interpreted by cutting the pulses at the zero crossings. These functions are then normalized such that their area is equal to the scalar seismic moment of the target event. Since there is a single scalar seismic moment for a given earthquake the moment rate functions observed at any azimuth carrying information about the rupture directivity (narrow in rupture direction, wider opposite to it) must integrate to the same scalar seismic moment. In the analysis we use this as a constraint on the obtained moment rate functions. The method used to invert the MRF for slip distribution is based on the methods of Mori and Hartzell (1990), Mori (1993), Dreger (1997) and Dreger *et al*. (2007). The relationship between the observed MRF and the moment distribution on a discretized fault is presented in equation (4.1) below

$$MRF_i(t, R_i) = \sum_j^N w_j B\left[T_R;\ t - t_t\left(R_{ij}, V_R\right)\right] \tag{4.1}$$

where i denotes a station index, R is the distance of the station to each of the discretized subfaults, j is the subfault index and B is a boxcar time function that depends on rise time (T_R) and the subfault trigger time (t_t), which depends on the distance between the station and traveltime, as well as on the rupture velocity (V_R). The subfault weight, w, is proportional to the moment rate and is determined by inversion. Inversions are performed for a suite of rise time and rupture velocity to find a best-fitting solution. The inversion is performed using a non-negative least-squares algorithm (Lawson and Hansen, 1974). The inversion is further regularized by a first derivative smoothing constraint. The smoothing weight is found by trial and error, in which the smoothest model that still retains a high level of fit to the data is found by means of a tradeoff curve. Inversions are performed for the two possible nodal planes from the double-couple portion of the moment tensor solution to find the causative fault geometry.

One complication in the finite-source work is that The Geysers earthquakes are sometimes found to have isotropic or volumetric components to the source process (Julian *et al*., 1993; Kirkpatrick *et al*., 1996; Guilhem *et al*., 2014; Johnson, 2014a; Boyd *et al*., 2015; Martínez-Garzón *et al*., 2017). This could pose a problem when there may be a difference in the isotropic component of the target and eGf events. None of the events for which we have been able to determine finite-source parameters have non-deviatoric, isotropic, components of the moment tensor that we would argue are statistically significant. Four of the largest studied events have positive isotropic components as evident from the moment tensor catalog presented in Chapter 2. For smaller magnitude events in the EGS demonstration site, our moment tensor analysis suggests the existence of both volume-increase and volume-decrease sources. The possible mixture of shear and tensile source components poses an interesting problem for finite-source analysis since one of the initial assumptions is that the mechanism of the target and smaller eGf events are the same. The proportionality of an isotropic component with respect to shear-slip would not necessarily remain fixed as a function of magnitude. Johnson (2014a,b) investigated small event moment tensors using a spectral approach that allows for time dependent moment tensor solutions. The results indicate that many of the small events have volumetric terms. Johnson 2014b developed a wing-crack model to explain the proportionality of the double-couple and wing-tensile-crack components. One result of Johnson's (2014a,b) analysis and model indicates, as found by Boyd *et al*. (2015), that it is possible that some events initiate as a shear dislocation progressing to a tensile-dominated mechanism, while other events start as a tensile process leading to shear dislocation. In order to account for the possibility of tensile failure in the finite-source process would require the use of theoretical Green's functions, which is not presently possible at the high frequencies needed to study these smaller events. Furthermore in Guilhem *et al*. (2014) and Boyd *et al*. (2015) the proportionality of the isotropic terms is relatively small and the waveforms are dominated by the shear dislocation term. Thus we limit the analysis to the eGf finite-source approach, and consider the recovery of MRF pulses from the deconvolution process as evidence for justification in assuming the mechanisms of the eGf and target events are the same (or very similar).

4.4 Results

The results for each of the following events are discussed in the order of increasing magnitude.

4.4.1 Event 1 M_W 1.05 January 30, 2013

The target and eGf events are centrally located in the EGS demonstration site, Figure 4.1, and differ in catalog magnitude (NCEDC EGS M_W) by 1.11 units, Table 4.1. The target event is included in a seismic sequence that initiated when Prati 32 injection operations resumed after a 160-day injection hiatus discussed in Chapter 3. The studied events in this sequence exhibit strike-slip faulting mechanisms with a high percentage compensated-linear-vector-dipole (CLVD) component, ~ 40 %.

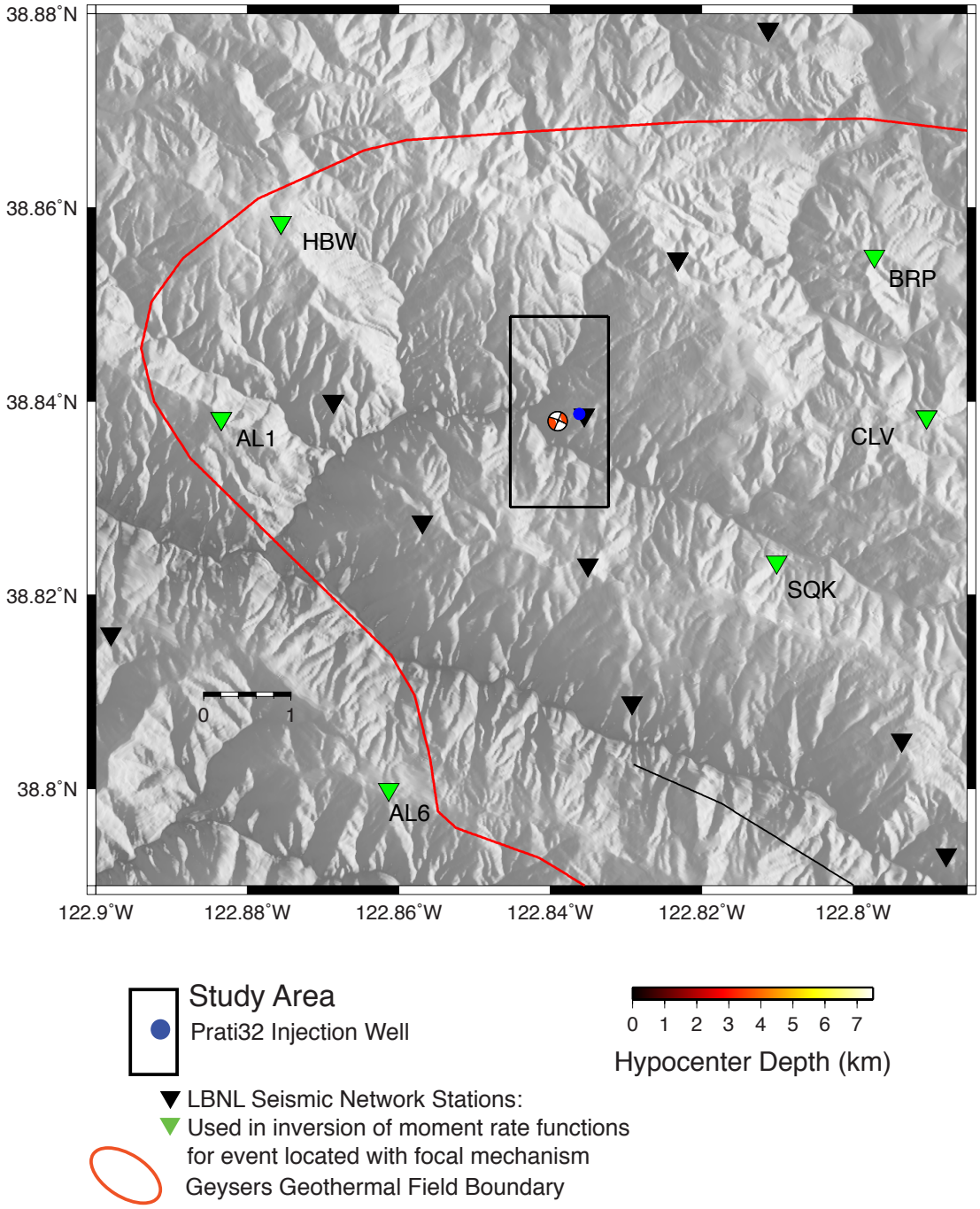

Figure 4.1. Map of the Northwest Geysers geothermal field. The EGS study area is a 1 x 2 km^2 rectangle centered on the EGS production well Prati State 31 (PS-31) and EGS injection well Prati 32 (P-32), blue dot. The location of the M_W 1.05 target event is shown with its deviatoric focal mechanism shaded by hypocenter depth. The locations of short-period seismic stations operated by Lawrence Berkeley National Laboratory (LBNL) used in this study are indicated by triangles (data from stations marked by green triangles were used to invert for moment rate functions. The approximate boundary of The Geysers steam field and selected faults are delineated with red and black lines, respectively.

Table 4.1. Target and empirical Green's function event information from the NCEDC EGS catalog for event 1, January 30, 2013: moment magnitude, date, time, latitude, longitude, and depth.

Event	Mw	Date	Time	Latitude	Longitude	Depth (km)
Target	1.47	2013/01/30	01:38:44.64	38.83797	-122.83900	3.57
eGf	0.36	2013/05/09	14:29:05.71	38.83612	-122.83943	3.47

The moment tensor of the target event is investigated using data filtered in passband 0.7 to 1.7 Hz. Waveform data downloaded from the NCEDC for stations in the LBNL Berkeley Geysers (BG) seismic network, event times, and locations as specified in the NCEDC EGS catalog are used. The focal mechanism in Figure 4.2 is strike-slip and is composed of 57% double-couple (DC) and 43% CLVD components.

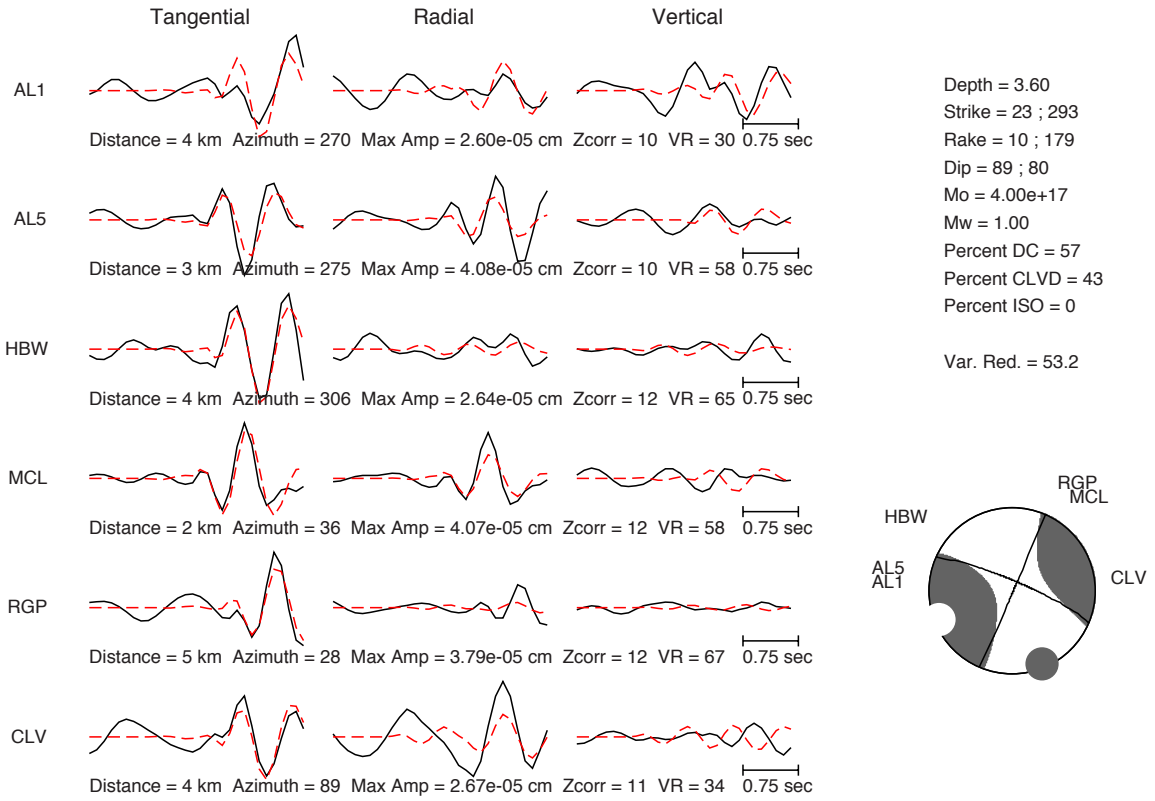

Figure 4.2. Comparison of filtered (0.7 to 1.7 Hz) observed velocity data (black) and synthetics (red) waveform fits and P-wave radiation pattern of the deviatoric moment tensor solution for target event 1, January 30, 2013.

The full moment tensor solution is composed of 51% DC, 37% CLVD, and 12% isotropic components, Figure 4.3. The improvement in fit of the full moment tensor solution compared with the deviatoric moment tensor solution is only 0.1% and is not statistically significant as measured by the *F*-test.

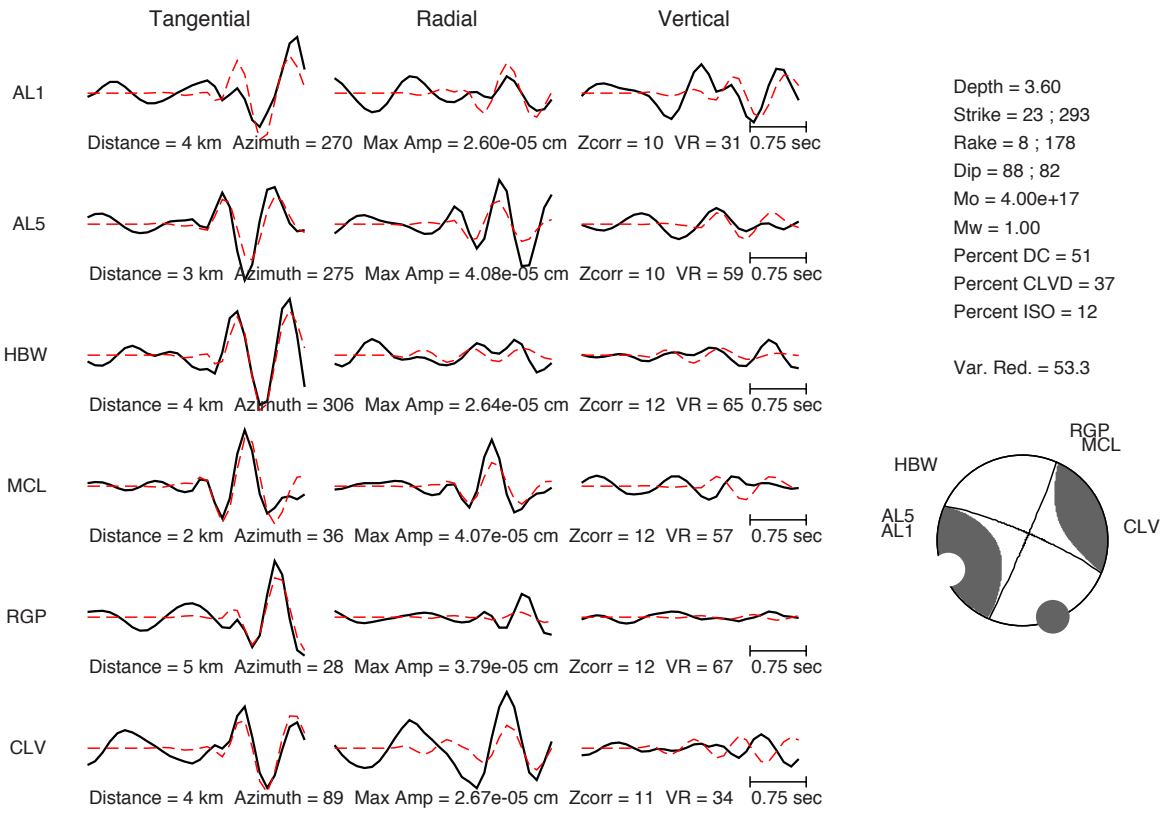

Figure 4.3. Comparison of filtered (0.7 to 1.7 Hz) observed velocity data (black) and synthetics (red) waveform fits and *P*-wave radiation pattern of the full moment tensor solution for target event 1, January 30, 2013. The improvement in fit of the full moment tensor solution is 0.1% and is too small to be significant.

To constrain the full moment tensor we used the source-type inversion methodology of Nayak and Dreger (2015) to explore the source-type-specific space of combined first-motion and waveform data. The combined first-motion and waveform data full moment tensor inversion results in a decomposition of 47% DC, 36% CLVD, and 17% isotropic components, Figure 4.4. The interpretation for this oblique strike-slip event is that its full moment tensor mechanism is composed of mostly DC with a negative volumetric component, Table 4.2. The percent double-couple component of the solutions presented in Figures 4.2 to 4.4 is very similar with a northeast striking, steeply dipping left-lateral fault, and a west-northwest striking right-lateral fault.

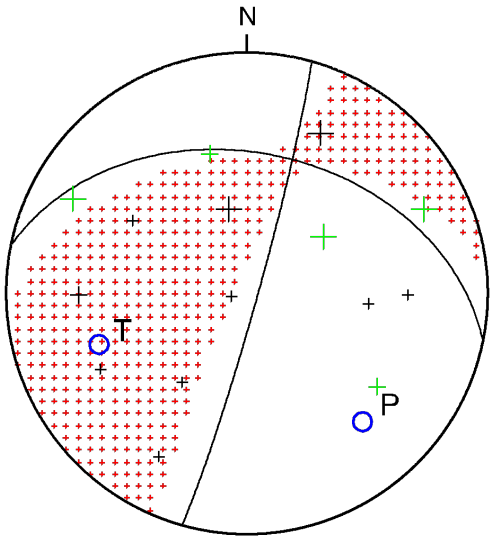

Figure 4.4. Constrained waveform and first motion mechanism for target event 1, M_W 1.05 January 30, 2013 using the source-type inversion methodology of Nayak and Dreger (2015). Shaded quadrants are compressional. First-motions are shown with plus symbols, up first motions (black), down first motions (green). The negative isotropic component evidenced by the lack of shading in the compressional quadrants indicates a volume-decrease component. Compression (P) and tension (T) axes are marked with open blue circles.

Table 4.2. Combined waveform and first motion full moment tensor parameters for target event 1, M_W 1.05 January 30, 2013. Strike, dip, and rake for both nodal planes.

Bowers Moment (dyne-cm)	Mw	Strike	Dip	Rake	% DC	% CLVD	% ISO
4.653E+17	1.05	281/16	41/86	174/49	47	36	17

The empirical Green's function approach assumes that the target and eGf pair are co-located events having a similar source mechanism with a difference in magnitude of at least one unit. Suitable eGf events horizontally located within 200 m from larger target events were found in the NCEDC EGS catalog. The eGf waveforms were then deconvolved from the target waveforms to identify those that produced pulse-like moment rate functions (MRF) with the highest signal to noise ratio. The pulse widths of the resulting MRFs range from 0.08 s at station AL6 in the south to a narrow width of 0.04 s at station HBW in the north, suggestive of a south to north rupture, Figure 4.5.

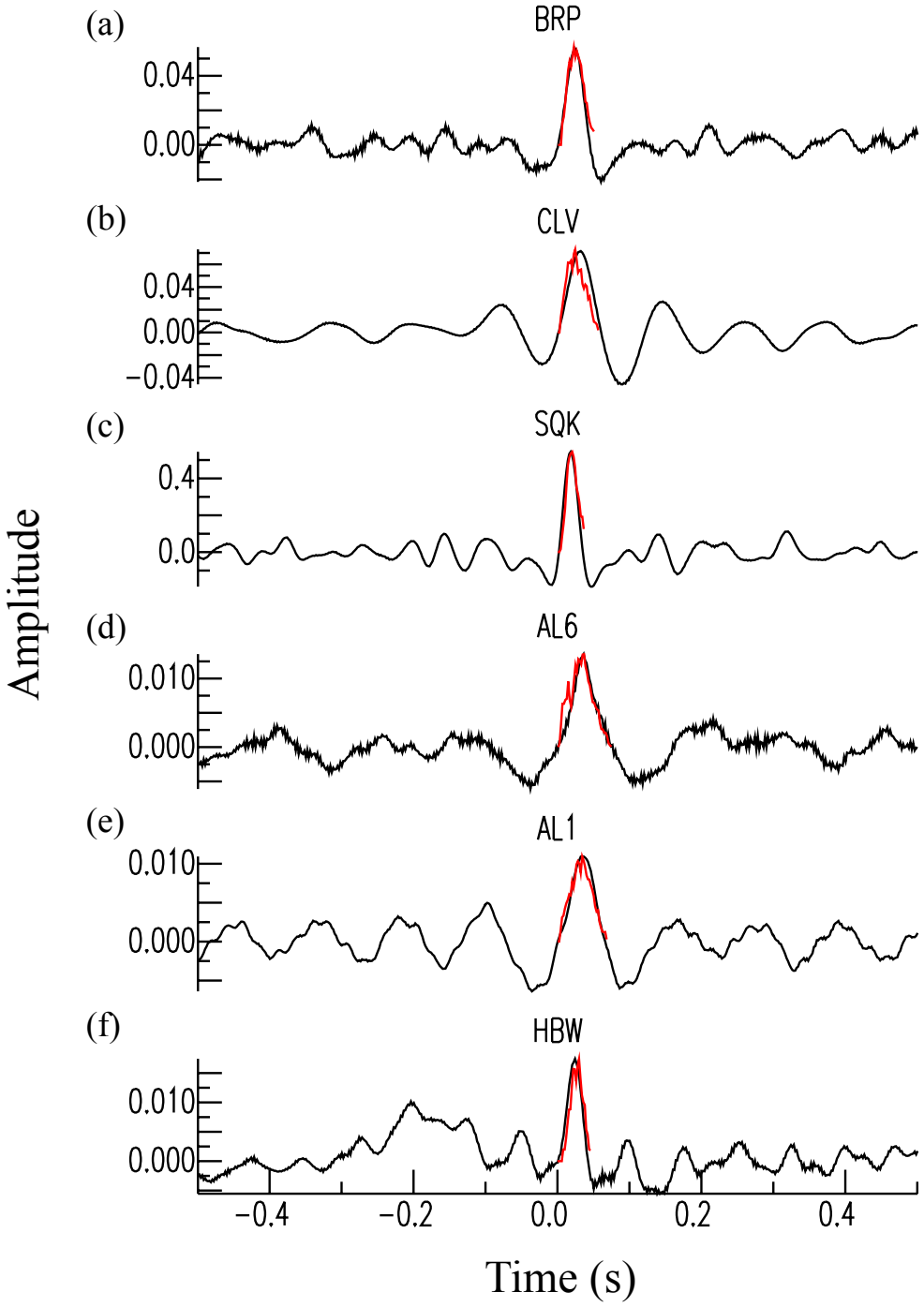

Figure 4.5. Stacked moment rate function (MRF) pulse trains (black), synthetic pulses (red) ordered by increasing azimuth for stations (a) BRP (b) CLV (c) SQK (d) AL6 (e) AL1 and (f) HBW for target event 1, M_W 1.05 January 30, 2013.

To invert the MRF for the slip distribution (Mori and Hartzell, 1990; Mori, 1993; Dreger, 1997; Dreger *et al*., 2007) we used a 1 km^2 fault model discretized by 61 x 61 giving a subfault size of 16.4 m. The fault is centered on the NCEDC EGS catalog location and depth. The model assumes a constant rupture velocity of initially 0.8 times the shear wave speed at the source depth. The slip at each patch on the fault is assumed to occur with the duration of a fixed-width boxcar function ranging from 0.01 – 0.02 s. The total allowable slip duration is 1 s. The subfault dimension is consistent with the 12.4 m wavelength for shear (*S*) waves with velocity Vs = 3.1 km/s at 3.6 km depth and 250 Hz bandwidth using the Nyquist frequency. The inversion uses a slip positivity constraint and a smoothing constraint to minimize the spatial derivative of the slip. The smoothing weight is investigated by searching for the smallest value that produces a smoothed model with a fit close to the maximum fit to the data as measured by the variance reduction. The rupture area is determined by the number of subfaults with slip greater than 10% of the maximum slip and varies with smoothing parameter. This threshold is used to ignore small amplitude patches of slip that are poorly constrained by the inversion. Smoothing parameters ranging from 2 to 2000 were investigated for variance reduction and area ranging from 0.01 – 0.07 km^2, Figures 4.6a and 4.6b, respectively.

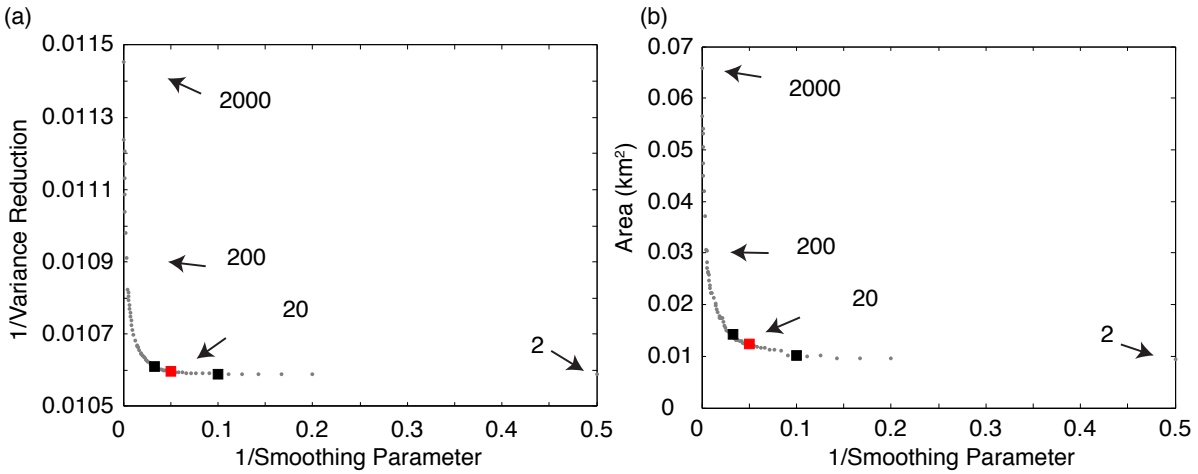

Figure 4.6**.** Investigation of 1/smoothing parameter ranging from 2 to 2000 with 1/variance reduction (a) and area (b) for target event 1, M_W 1.05 January 30, 2013. A preferred smoothing parameter of 20 is marked with a red square. The percent change in variance reduction for smoothing parameters of 20 ± 50 percent (black squares) is negligible.

The ability to fit the data well trades off with the smoothing parameter where large values of smoothing result in the poorest fits as shown in Figure 4.6a. Of course smoothing also affects the overall rupture area (Figure 4.6b). Results for smoothing parameters 2, 20, 200, and 200 are tabulated in Table 4.3. The west-northwest fault plane (strike 281°, dip 41°, rake 174°) is preferred with a higher goodness of fit, 94 percent compared to 91 percent for the east-northeast fault plane (strike 16°, dip 86°, rake 49°). For this event the peak stress drop is < 0.6 MPa for smoothing parameter 20, rise time 0.01 s, strike 281°, dip 41°, and rake 174°.

Table 4.3. Finite-source model smoothing parameter, slip area, average slip, and goodness of fit for rise time 0.01 s for target event 1, January 30, 3013.

Smoothing	Slip Area (km^2)	Ave Slip (cm)	Goodness of Fit %
2	0.009	0.008	94.43
20	0.012	0.015	94.37
200	0.031	0.006	92.38
2000	0.066	0.003	87.31

The slip distribution and stress change maps from the inversion of moment rate functions at six nearby stations for rupture velocity 80% of the local shear wave velocity and smoothing parameters 2, 20, 200, and 2000 are shown in Figures 4.7(a−d) and Figures 4.8(a−d), respectively.

Based on the goodness of fit level the preferred model has a smoothing of 20. For higher smoothing values the fit degrades rapidly. For a smoothing of 20 the dimensions of the slip and the subevents within the slip model are approximately ¼ wavelength for a central frequency of 16.6 Hz (0.06 second MRF duration). Smaller values of smoothing introduce smaller scale subevents, which are too small to be reliably imaged given the bandwidth of the MRF data.

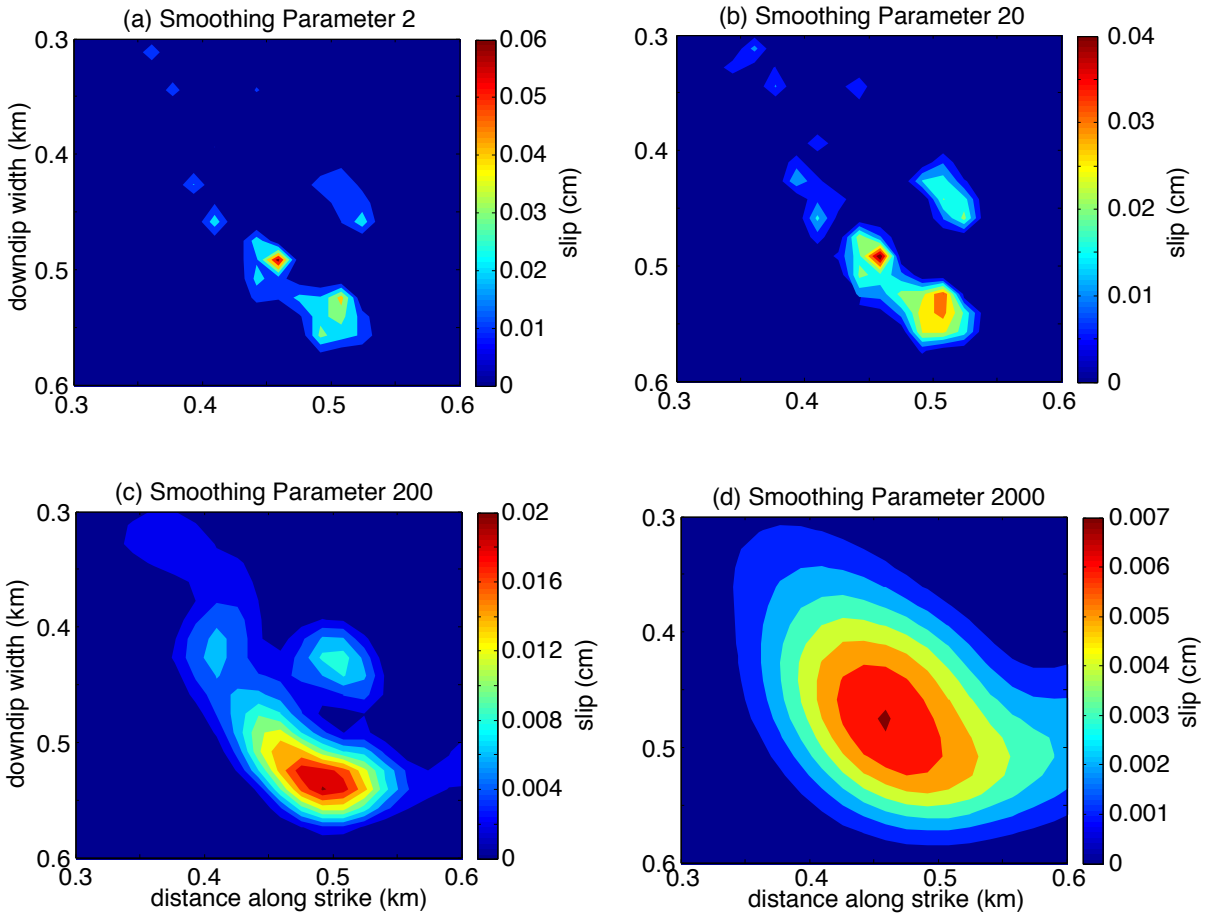

Figure 4.7. Target event 1, M_W 1.05 January 30, 2013, slip distribution maps from inversion of moment rate functions with smoothing parameters 2 (a) 20 (b) 200 (c) and 2000 (d), rise time 0.01 s, strike 281°, dip 41°, and rake 174°. The preferred model with smoothing parameter 20 has a peak slip of 0.04 cm. The hypocenter is located at the center of the each plot.

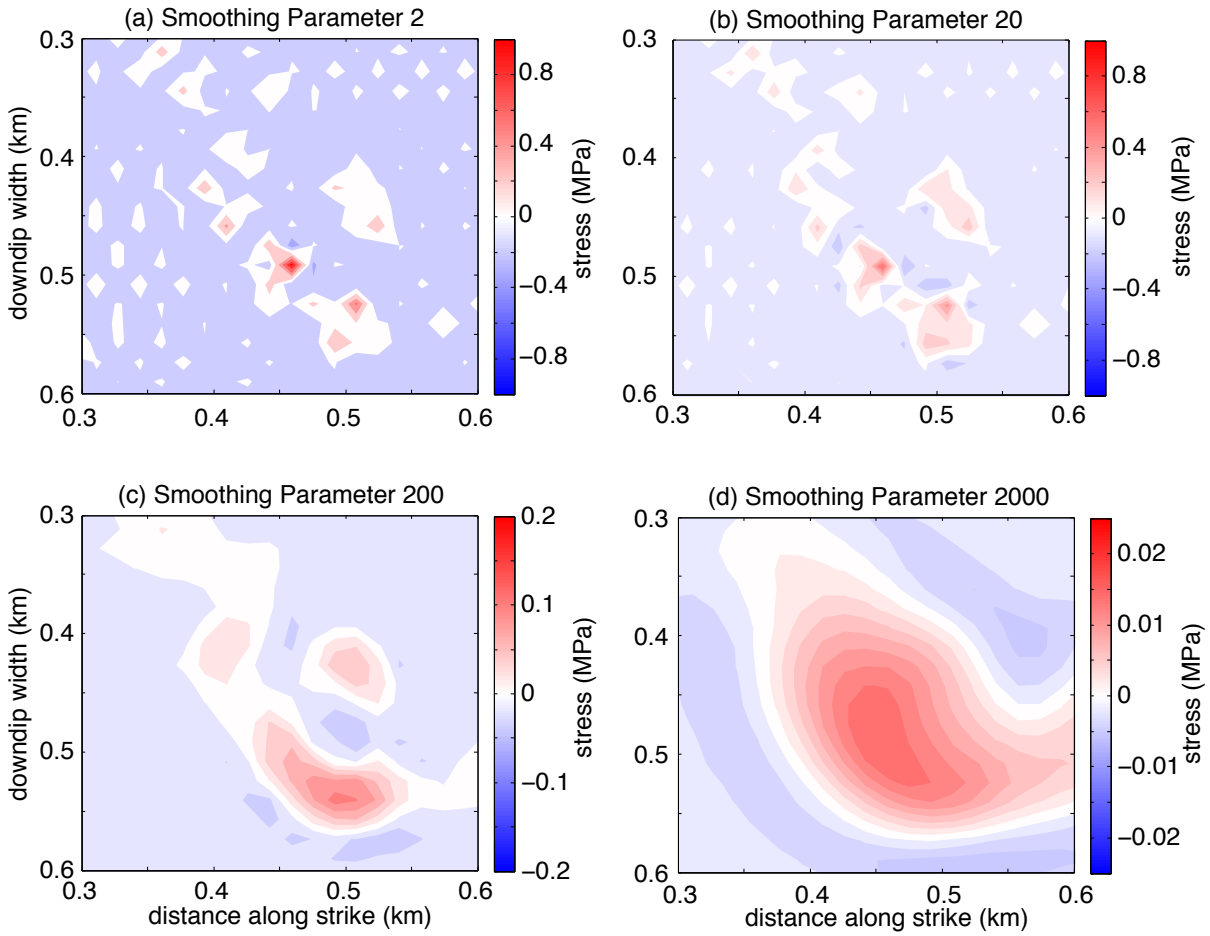

Figure 4.8. Target event 1, M_W 1.05 January 30, 2013, stress change maps from inversion of moment rate functions with smoothing parameters 2 (a) 20 (b) 200 (c) and 2000 (d), rise time 0.01 s, strike 281°, dip 41°, and rake 174°. The preferred model with smoothing parameter 20 has a peak stress drop of 0.61 MPa. Stress change on the fault surface is shaded red as stress drop and blue as stress increase. The hypocenter is located at the center of each plot.

4.4.2 Event 2 M_W 1.48 January 30, 2013

The target and eGf events are centrally located in the EGS demonstration site, Figure 4.9, and differ in catalog magnitude (NCEDC EGS M_W) by 1.15 units, Table 4.4. The target and eGf events occur during the above-mentioned seismic sequence that initiated when Prati 32 injection operations resumed after a 160-day injection hiatus. The strike-slip focal mechanism with a high 46% CLVD component is consistent with the other studied events in the seismic sequence.

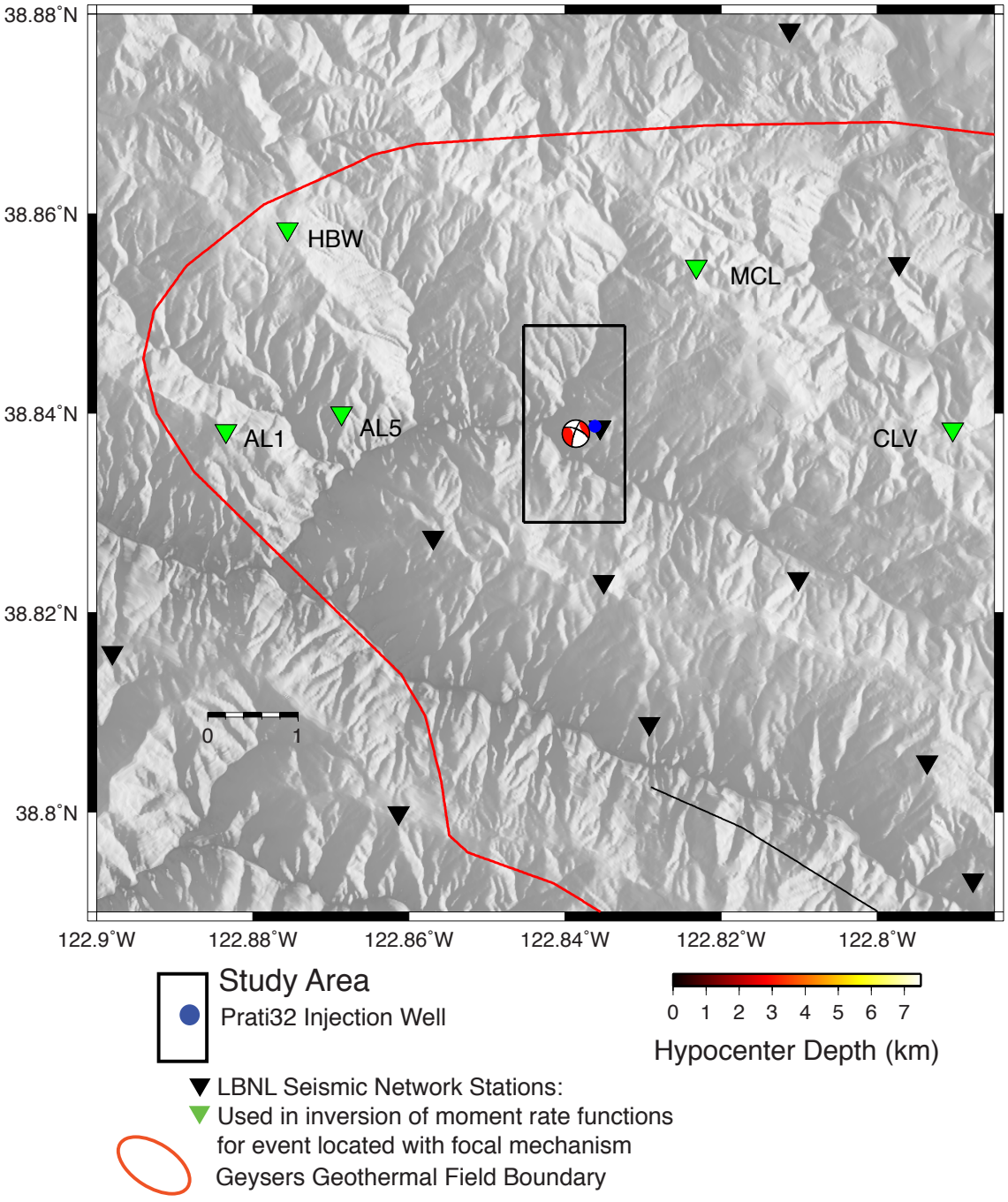

Figure 4.9. Map of the Northwest Geysers geothermal field. The EGS study area is a 1 x 2 km^2 rectangle centered on the EGS production well Prati State 31 (PS-31) and EGS injection well Prati 32 (P-32), blue dot. The location of the M_W 1.48 target event is shown with its deviatoric focal mechanism shaded by hypocenter depth. The locations of short-period seismic stations operated by Lawrence Berkeley National Laboratory (LBNL) used in this study are indicated by triangles (data from stations marked by green triangles were used to invert for moment rate functions. The approximate boundary of The Geysers steam field and selected faults are delineated with red and black lines, respectively.

Table 4.4. Target and empirical Green's function event information from the NCEDC EGS catalog for event 2, January 30, 2013: moment magnitude, date, time, latitude, longitude, and depth.

Event	Mw	Date	Time	Latitude	Longitude	Depth (km)
Target	1.80	2013/01/30	10:30:33.46	38.83797	-122.83855	2.97
eGf	0.65	2013/01/30	14:17:54.63	38.83555	-122.83727	3.14

We investigated the moment tensor of the target event using data filtered in passband 0.7 to 1.7 Hz. Waveform data were downloaded from the NCEDC for stations in the LBNL Berkeley Geysers (BG) seismic network. We used event times and locations as specified in the NCEDC EGS catalog. The focal mechanism in Figure 4.10 is strike-slip and is composed of 54% DC and 46% CLVD components.

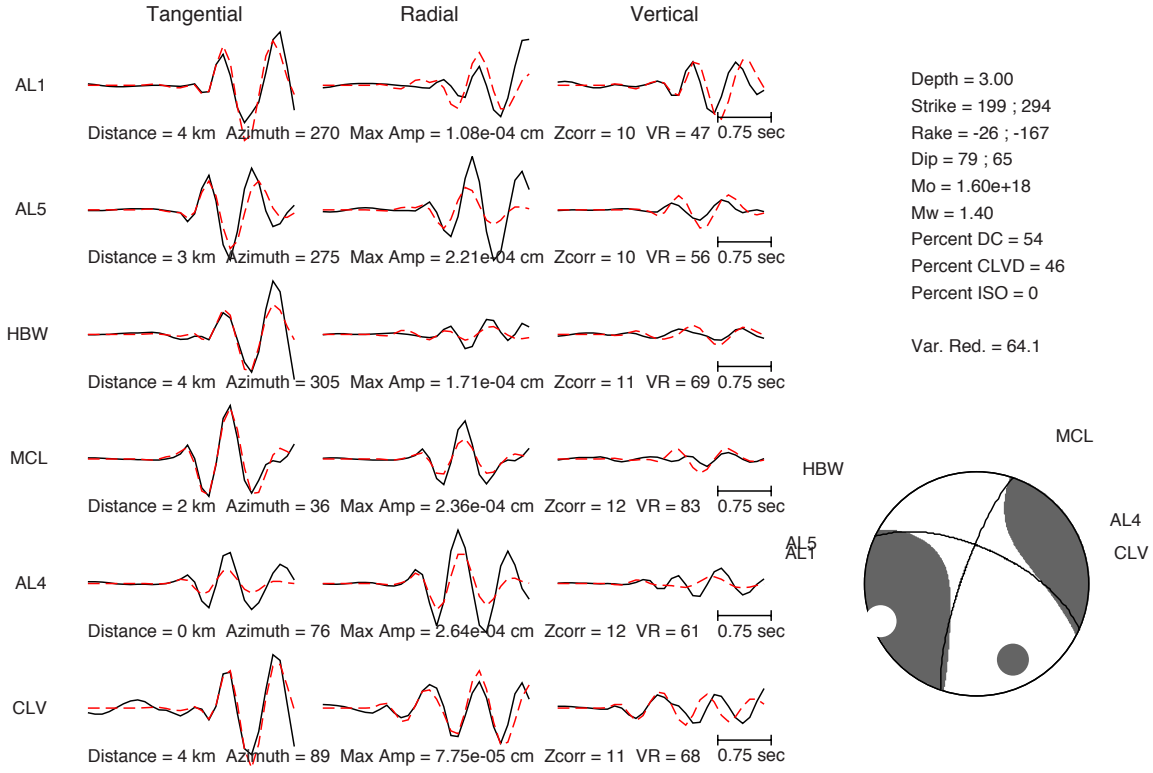

Figure 4.10. Comparison of filtered (0.7 to 1.7 Hz) observed velocity data (black) and synthetics (red) waveform fits and *P*-wave radiation pattern of the deviatoric moment tensor solution for target event 2, January 30, 2013.

The full moment tensor solution is composed of 46% DC, 35% CLVD, and 19% isotropic components, Figure 4.11. The improvement in fit of the full moment tensor solution compared with the deviatoric moment tensor solution is only 0.2% and is not statistically significant as measured by the *F*-test.

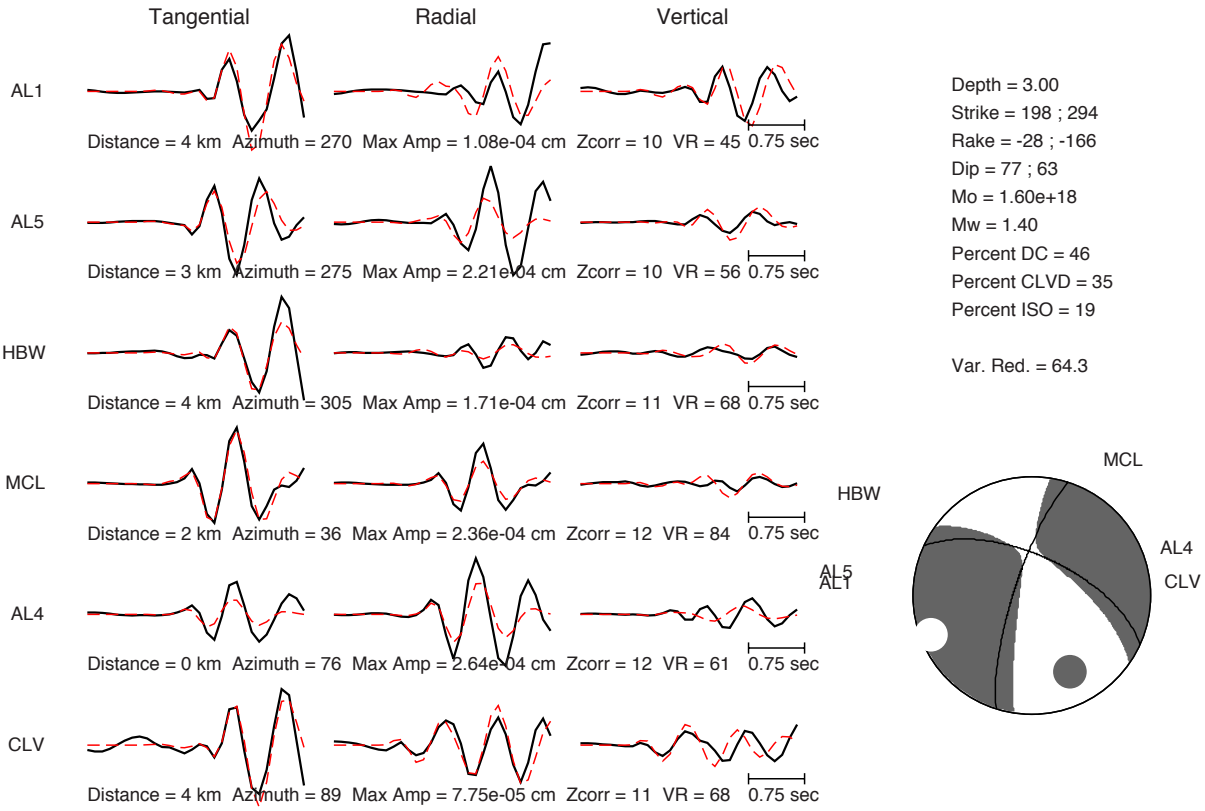

Figure 4.11. Comparison of filtered (0.7 to1.7 Hz) observed velocity data (black) and synthetics (red) waveform fits and *P*-wave radiation pattern of the full moment tensor solution for target event 2, January 30, 2013. The improvement in fit of the full moment tensor solution is 0.2% and is too small to be significant.

To constrain the full moment tensor we used the source-type inversion methodology of Nayak and Dreger (2015) to explore the source-type-specific space of combined first-motion and waveform data. The combined first-motion and waveform data full moment tensor inversion results in a decomposition of 52% DC, 31% CLVD, and 17% isotropic components, Figure 4.12. The interpretation for this oblique strike-slip event is that its full moment tensor mechanism is composed of mostly DC with a small volumetric increase component, Table 4.5.

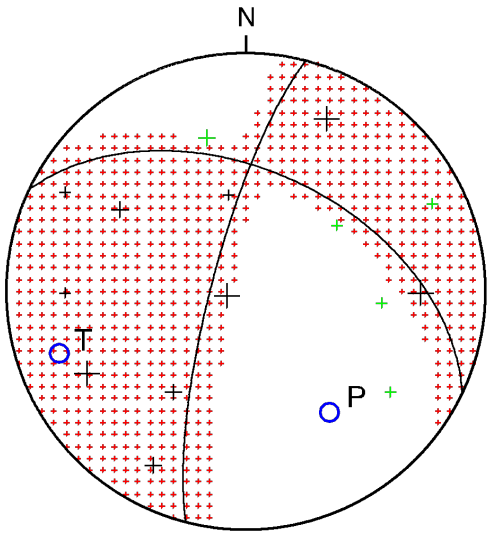

Figure 4.12. Constrained waveform and first motion mechanism for target event 2, M_W 1.48 January 30, 2013 using the source-type inversion methodology of Nayak and Dreger (2015). Shaded quadrants are compressional. First-motions are shown with plus symbols, up first motions (black), down first motions (green). The positive isotropic component evidenced by shading in the tensional quadrants indicates a volume-increase component. Compression (P) and tension (T) axes marked with open blue circles.

Table 4.5. Combined waveform and first motion full moment tensor parameters for target event 2, M_W 1.48 January 30, 3013. Strike, dip, and rake for both nodal planes.

Bowers Moment (dyne-cm)	Mw	Strike	Dip	Rake	%DC	%CLVD	%ISO
2.093E+18	1.48	295/195	48/78	-164/-43	52	31	17

The eGf waveforms were deconvolved from the target waveforms to identify those that produced pulse-like moment rate functions (MRF) with the highest signal to noise ratio. The pulse widths of the resulting MRFs range from 0.06 s at station AL1 to a narrow width of 0.04 s at station HBW in the north, suggestive of a south to north rupture. The MRFs for the target event are presented in Figure 4.13.

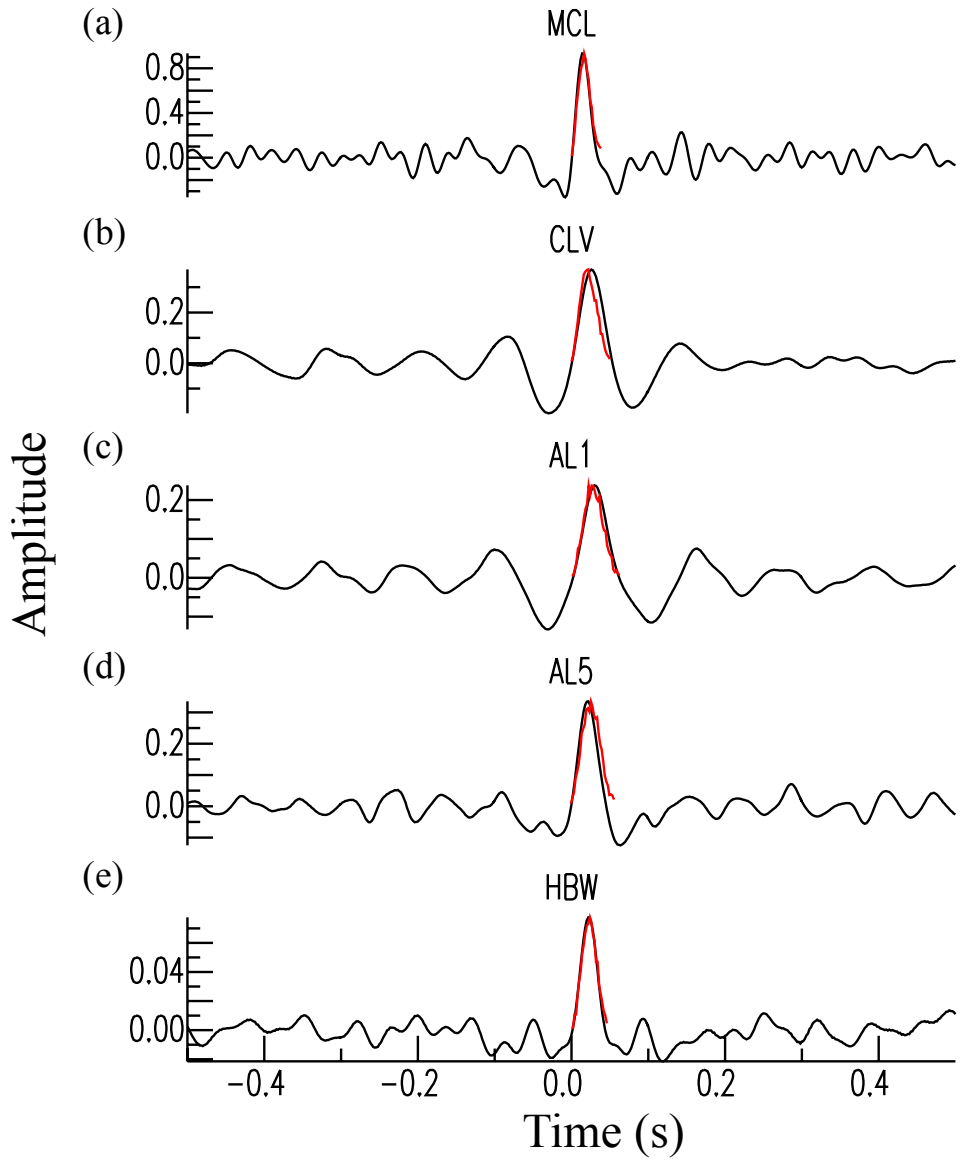

Figure 4.13. Stacked MRF pulse trains (black), synthetic pulses (red) ordered by increasing azimuth for stations (a) MCL (b) CLV (c) AL1 (d) AL5 and (e) HBW for event 2, M_W 1.48 January 30, 2013.

The parameterization of the finite-source model (overall dimension, subfault dimension, minimum rise time, and overall slip duration) is the same as for event 1, above. At the depth of this event subfault dimension of 16.4 m is consistent with the 12.0 m wavelength for *S* waves with Vs = 3.0 km/s at 3.0 km depth and 250 Hz bandwidth. The inversion uses a slip positivity constraint and a smoothing constraint to minimize the spatial derivative of the slip. The smoothing weight is investigated by searching for the smallest value that produces a smoothed model with a fit close to the maximum fit to the data as measured by the variance reduction. The rupture area is determined by the number of subfaults with slip greater than 10% of the maximum slip and varies with smoothing parameter. This threshold is used to

ignore small amplitude patches of slip that are poorly constrained by the inversion. Smoothing parameters of 2, 20, and 200 resulted in areas ranging from 0.006 – 0.016 km^2, Table 4.6.

Table 4.6. Finite-source model smoothing parameter, slip area, average slip, and goodness of fit for rise time 0.02 s for target event 2, M_W 1.48 January 30, 3013.

Smoothing	Slip Area (km^2)	Ave Slip (cm)	Goodness of Fit %
2	0.006	0.117	96.85
20	0.012	0.088	96.64
200	0.016	0.060	95.77

For the preferred smoothing parameter of 20, the east-northeast fault plane (strike 195°, dip 78°, rake −43°) is preferred with a higher goodness of fit, 97 percent compared to 93 percent for the west-northwest fault plane (strike 295°, dip 48°, rake −164°). The model for a smoothing of 20 is preferred because it is close to the maximum goodness of fit, and for values larger than 20 the fit begins to degrade. In addition, the overall slip model is about 1 wavelength, and the peak in slip is about ¼ of the wavelength for the band of the MRF data. Thus these features are well imaged by the model. Maps of slip distribution and stress change for smoothing parameter 20, rise time 0.02 s, strike 195°, dip 78°, rake −43° are shown in Figures 4.14a and 4.14b, respectively. For this event the peak stress drop is < 1.8 MPa.

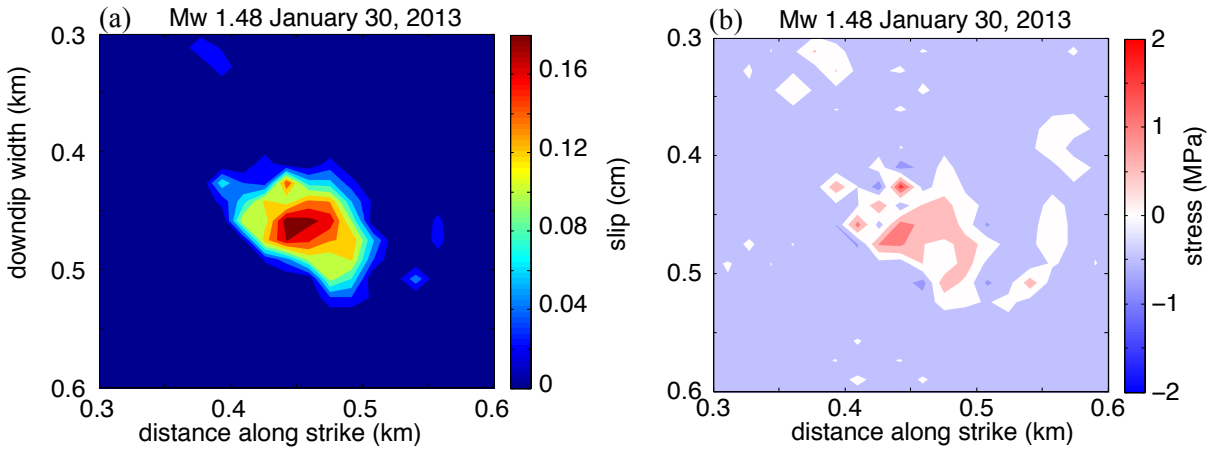

Figure 4.14. Target event 2, M_W 1.48 maps of slip distribution (a) and stress change (b) from inversion of moment rate functions with smoothing parameter 20, rise time 0.02 s, strike 195°, dip 78°, rake −43°. The hypocenter is located at the center of each plot. The peak slip is 0.2 cm and the peak stress drop is 1.77 MPa. Stress change on the fault surface with red as stress drop and blue as stress increase.

4.4.3 Event 3 M_W 2.09 August 25, 2013

The target and eGf events are located in the EGS demonstration site approximately 0.5 km north of Prati 32 injection well, Figure 4.15.

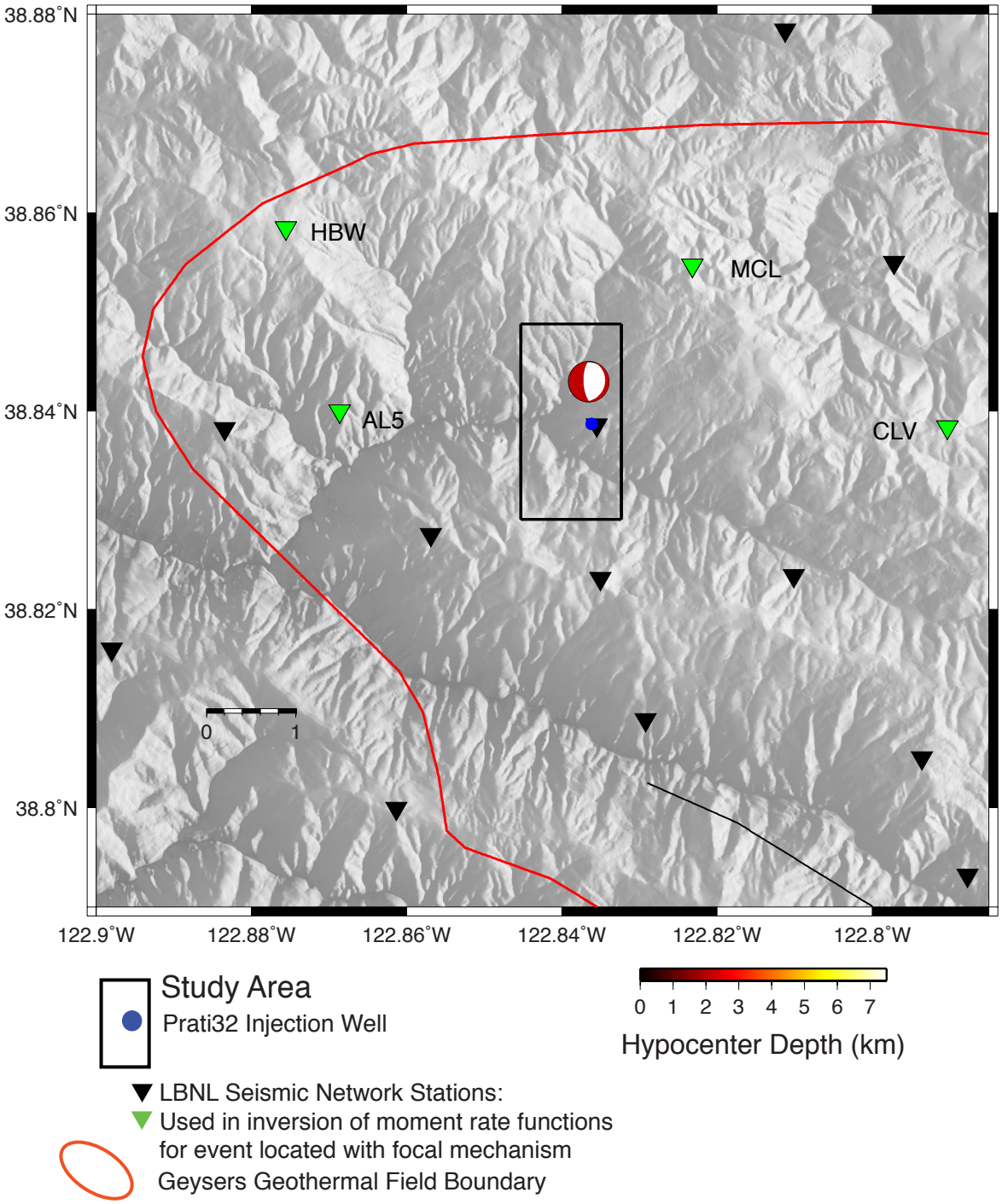

Figure 4.15. Map of the Northwest Geysers geothermal field. The EGS study area is a 1 x 2 km^2 rectangle centered on the EGS production well Prati State 31 (PS-31) and EGS injection well Prati 32 (P-32), blue dot. The location of the M_W 2.09 target event is shown with its

deviatoric focal mechanism shaded by hypocenter depth. The locations of short-period seismic stations operated by Lawrence Berkeley National Laboratory (LBNL) used in this study are indicated by triangles (data from stations marked by green triangles were used to invert for moment rate functions. The approximate boundary of The Geysers steam field and selected faults are delineated with red and black lines, respectively.

The catalog magnitudes (NCEDC EGS M_W) differ by 1.34 units, Table 4.7. The target event occurred in late August 2013 when Prati 32 injection was stable at 425 gallons per minute (gpm) (27 kilograms/second (kg/s)). The eGf event occurred mid-September 2013 when Prati 32 injection was halted from September 9 to 18, 2013.

Table 4.7. Target and empirical Green's function event information from the NCEDC EGS catalog for event 3, August 25, 2013: moment magnitude, date, time, latitude, longitude, and depth.

Event	Mw	Date	Time	Latitude	Longitude	Depth (km)
Target	2.47	2013/08/25	14:06:47.39	38.84297	-122.83650	2.10
eGf	1.13	2013/09/14	11:40:40.15	38.84298	-122.83900	2.14

We investigated the moment tensor of the target event using data filtered in passband 0.7 to 1.7 Hz. Waveform data were downloaded from the NCEDC for stations in the LBNL Berkeley Geysers (BG) seismic network. We used event times and locations as specified in the NCEDC EGS catalog. The focal mechanism is normal and the deviatoric moment tensor is composed of 39% DC and 61% CLVD components, Figure 4.16.

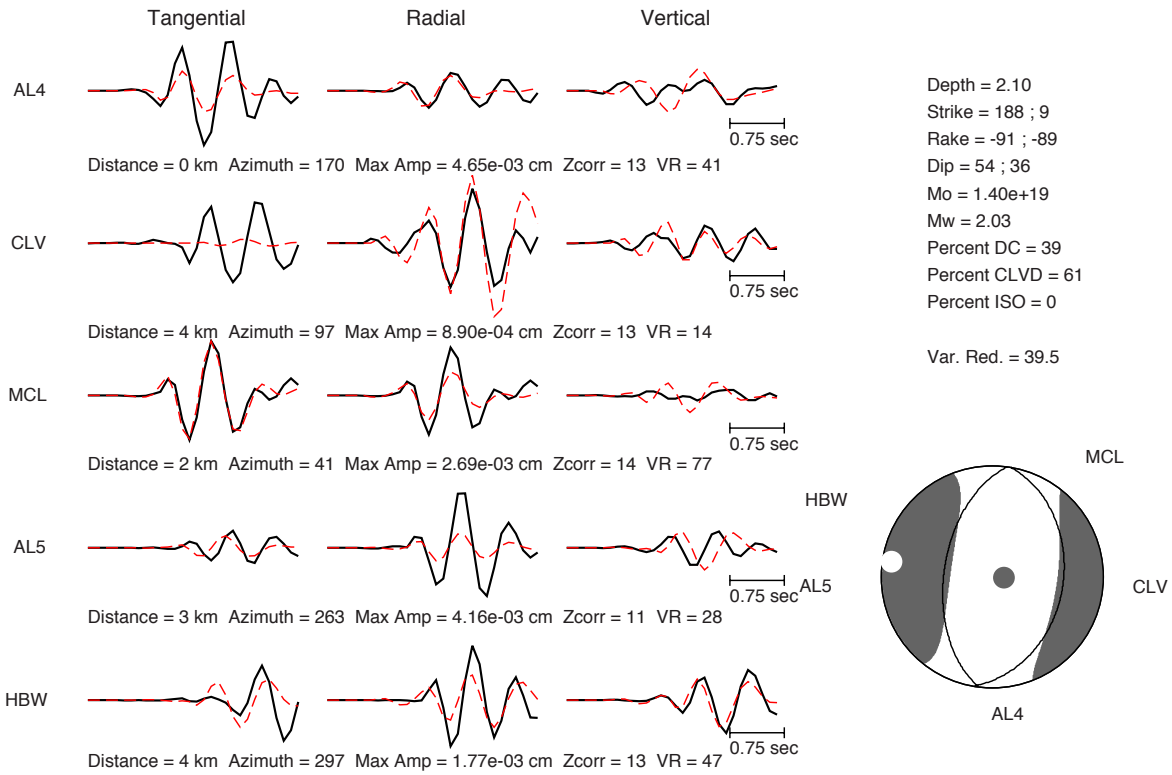

Figure 4.16. Comparison of filtered (0.7 to 1.7 Hz) observed velocity data (black) and synthetics (red) waveform fits and *P*-wave radiation pattern of the deviatoric moment tensor solution for target event 3, August 25, 2013.

The full moment tensor solution is composed of 26% DC, 32% CLVD, and 42% isotropic components, Figure 4.17. The improvement in fit of the full moment tensor solution compared with the deviatoric moment tensor solution is 2.0% and is not statistically significant as measured by the *F*-test.

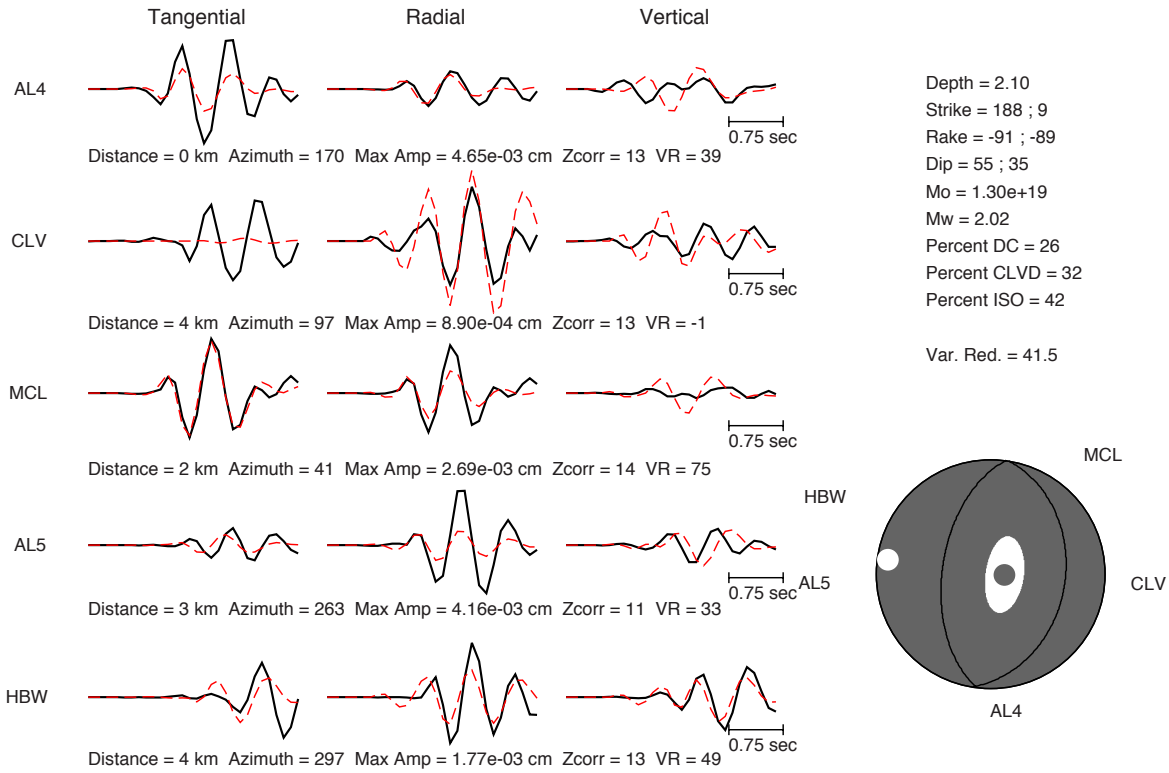

Figure 4.17. Comparison of filtered (0.7 to 1.7 Hz) observed velocity data (black) and synthetics (red) waveform fits and *P*-wave radiation pattern of the full moment tensor solution for target event 3, August 25, 2013. The improvement in fit of the full moment tensor solution is 2% and is too small to be significant.

To constrain the moment tensor we used the source-type inversion methodology of Nayak and Dreger (2015) to explore the source-type-specific space of combined first-motion and waveform data. The combined first-motion and waveform data full moment tensor inversion results in a decomposition of 41% double-couple (DC), 37% CLVD, and 22% ISO components (Figure 4.18), where the isotropic moment volume decreases in contrast to what was shown in Figure 4.17 using only the waveforms. The fit to the combined first-motion waveform data set has a variance reduction (VR) of 63%. This illustrates how the combined use of first-motions can either help to constrain the volumetric component of a moment tensor, or as in this case that the volume increase found from the waveform inversion is unreliable. What is important is that the double-couple portion of the moment tensor solution is found to be similar in all three moment tensor inversions.

.

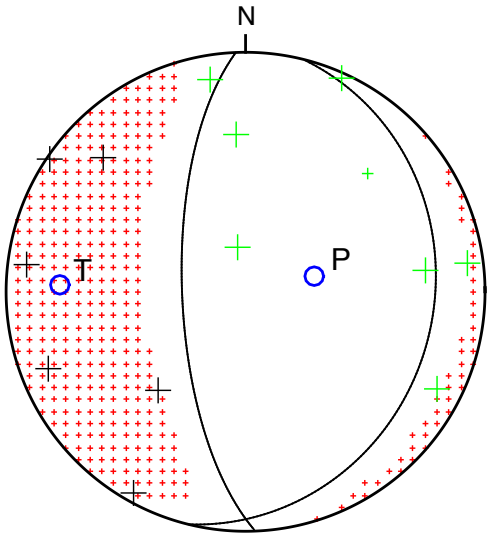

Figure 4.18. Constrained waveform and first motion mechanism for target event 3, M_W 2.09 August 25, 2013 using the source-type inversion methodology of Nayak and Dreger (2015). Shaded quadrants are compressional. First-motions are shown with plus symbols, up first motions (black), down first motions (green). The negative isotropic component evidenced by the lack of shading in the compressive quadrants indicates a volume-decrease component. Compression (P) and tension (T) axes marked with open blue circles.

The interpretation for this oblique normal event is that its full moment tensor mechanism is composed of roughly equal parts DC-CLVD, Table 4.8.

Table 4.8. Combined waveform and first motion full moment tensor parameters for target event 3, M_W 2.09 August 25, 2013. Strike, dip and rake for both nodal planes.

Bowers Moment (dyne-cm)	Mw	Strike	Dip	Rake	%DC	%CLVD	%ISO
1.7E+19	2.09	14/178	22/68	-75/-96	41	37	22

Suitable eGf events horizontally located within 200 m from larger target events were found in the DOE EGS LBNL catalog. The eGf waveforms were then deconvolved from the target waveforms to identify those that produced pulse-like moment rate functions (MRF) with the highest signal to noise ratio. The pulse widths of the resulting MRFs range from 0.11 s at station HBW in the north to a narrow width of 0.07 s at station CLV in the south, suggestive of a north to south rupture. The MRFs for the target event are presented in Figure 4.19.

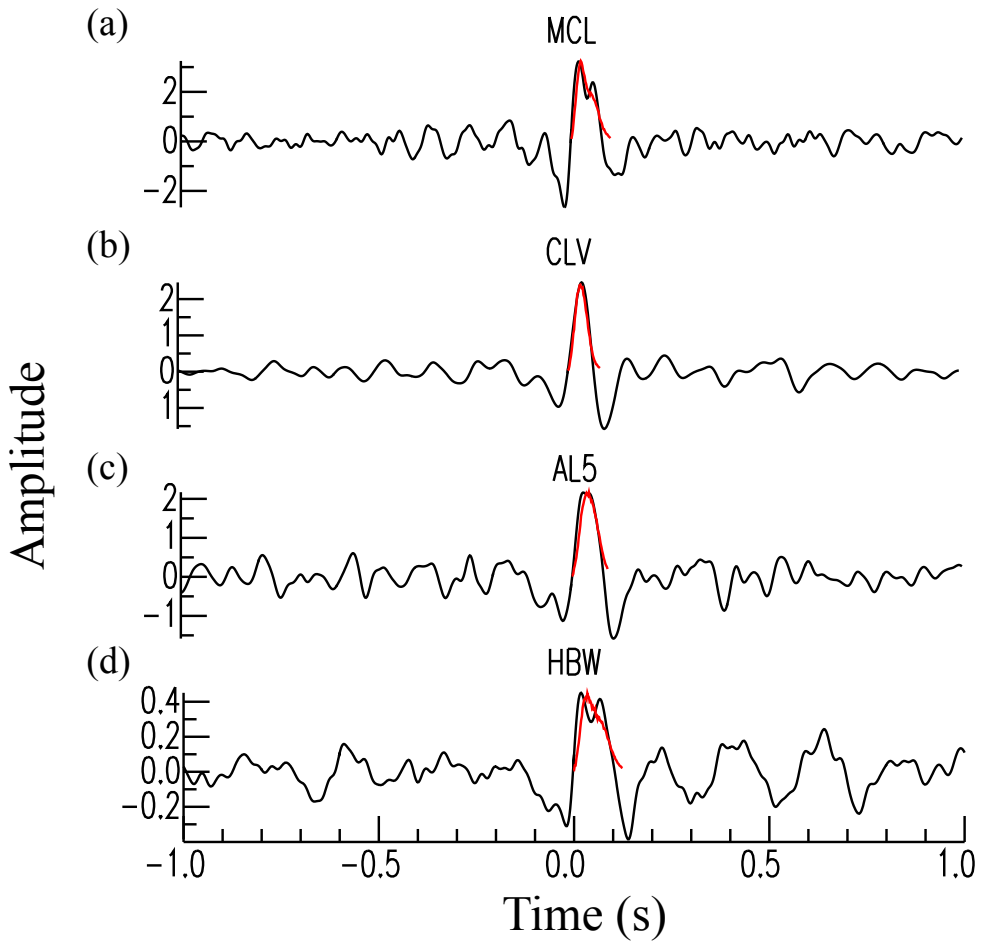

Figure 4.19. Target event 3, M_W 2.09 August 25, 2013, stacked MRF pulse trains (black), synthetic pulses (red) ordered by azimuth for stations (a) MCL (b) CLV (c) AL5 and (d) HBW.

The finite-source model has the same fault dimensions, number of grid points, subfault size, and a constant rupture velocity as described for target events 1 and 2, above. The slip at each patch on the fault occurs with a rise time of a 0.02 s fixed-width boxcar. The total allowable slip duration is 1 s. The subfault dimension of 16.4 m is consistent with the 11.8 m wavelength for *S* waves with Vs = 2.94 km/s at 2.1 km depth and 250 Hz bandwidth. As before the smoothing weight was tested by searching for the smallest value that produces a smoothed model with a fit close to the maximum fit to the data as measured by the variance reduction. The rupture area is determined by the number of subfaults with slip greater than 10% of the maximum slip and varies with smoothing parameter. This threshold is used to ignore small amplitude patches of slip that are poorly constrained by the inversion. Smoothing parameters of 2, 20, 200, and 2000 were investigated for an area ranging from 0.01 – 0.08 km^2, Table 4.9. The goodness of fit between the observed and synthetic MRFs is comparable for the strike, rake, and dip of both nodal planes yet one nodal plane with strike 14°, dip 22°, and rake −75° has a smoothed and somewhat simpler slip distribution. Based on this modeling a smoothing parameter of 200 is preferred. The overall dimension of slip model is about 1

wavelength, and the two major slip patches are approximately ½ wavelength of the MRF data band indicating the slip model is well imaged.

Table 4.9. Finite-source model smoothing parameter, slip area, and goodness of fit with rise time 0.02 s for target event 3, M_W 2.09 August 25, 3013.

Smoothing	Slip Area (km^2)	Goodness of Fit %
2	0.015	99.4
20	0.022	99.3
200	0.035	99.0
2000	0.076	95.6

The slip distribution and stress change maps from the inversion of moment rate functions at four nearby stations for rupture velocity 80% of the local shear wave velocity are shown in Figures 4.20a and 4.20b, respectively. For this event the peak stress drop is somewhat low < 2 MPa.

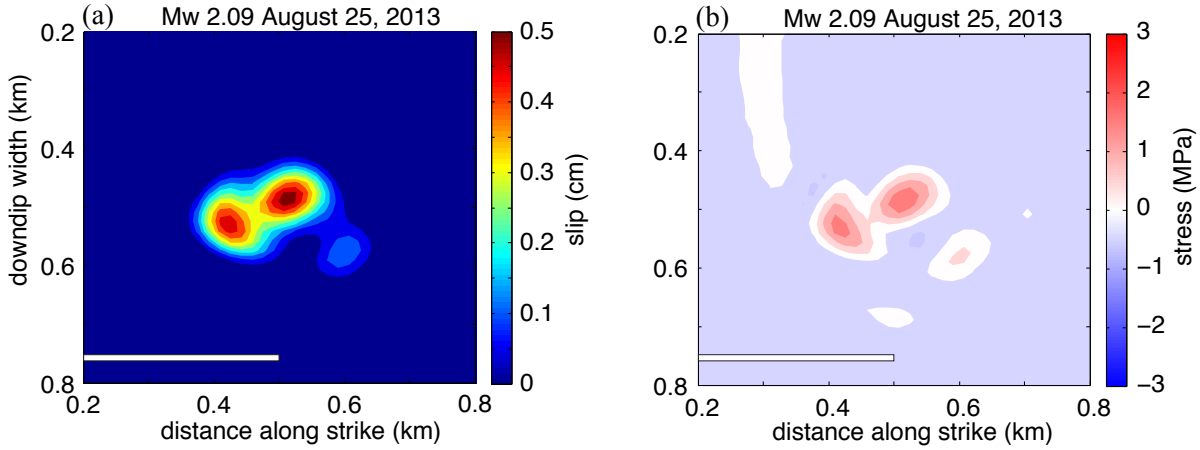

Figure 4.20. Target event 3, M_W 2.09 August 25, 2013, maps of slip distribution (a) and stress change (b) from inversion of moment rate functions with smoothing parameter 200, rise time 0.02 s, strike 14°, dip 22°, rake −75°. The hypocenter is located at the center of each plot. The peak slip is 0.5 cm and the peak stress drop is 1.95 MPa. Stress change on the fault surface with red as stress drop and blue as stress increase. The horizontal bar represents the dimension in kilometers of target events 1 and 2, with M_W 1.05 and M_W 1.48, respectively.

4.4.4 Event 4 M_W 2.87 February 6, 2013

The target and eGf events are located in the southeast corner of the EGS demonstration site, Figure 4.21.

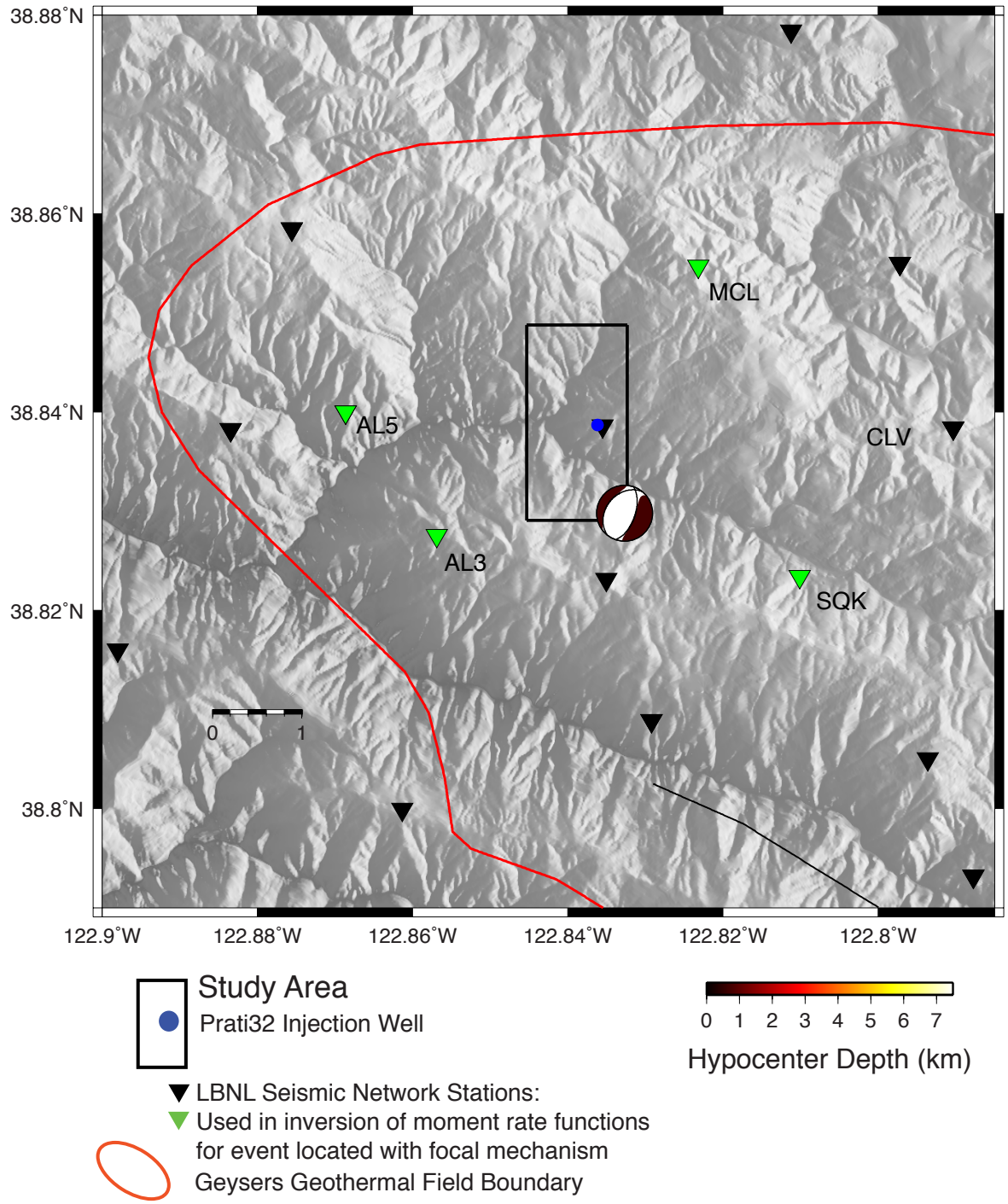

Figure 4.21. Map of the Northwest Geysers geothermal field. The EGS study area is a 1 x 2 km^2 rectangle centered on the EGS production well Prati State 31 (PS-31) and EGS injection well Prati 32 (P-32), blue dot. The location of the M_W 2.87 target event is shown with its deviatoric focal mechanism shaded by hypocenter depth. The locations of short-period

seismic stations operated by Lawrence Berkeley National Laboratory (LBNL) used in this study are indicated by triangles (data from stations marked by green triangles were used to invert for moment rate functions. The approximate boundary of The Geysers steam field and selected faults are delineated with red and black lines, respectively.

The locations of both events are from the NCEDC Double-Difference (DD) catalog. The event separation is 0.12 km in horizontal and 0.26 km in depth. The catalog magnitudes (duration magnitude, Md) differ by 1.44 units, Table 4.10. The target event occurred February 6, 2013 a week after injection resumed at Prati 32 following a 160-day hiatus. The injection rate was stable at 388 gpm (24 kilograms/second (kg/s)). The eGf event occurred a year and a half earlier on August 24, 2011 before injection commenced at Prati 32.

Table 4.10. Target and empirical Green's function event information from the NCEDC Double-Difference catalog for event 4, February 6, 2013: duration magnitude, date, time, latitude, longitude, and depth.

Event	Md	Date	Time	Latitude	Longitude	Depth (km)
Target	2.84	2013/02/06	04:05:30.89	38.83026	-122.83313	1.28
eGf	1.40	2011/08/24	09:33:47.61	38.83060	-122.83445	1.54

We investigated the moment tensor of the target event using data filtered in passband 0.2 to 1.0 Hz. Waveform data were downloaded from the NCEDC for stations in the LBNL Berkeley Geysers (BG) seismic network. We used event times and locations as specified in the NCEDC NCSN catalog. The focal mechanism is normal and the deviatoric moment tensor is composed of 70% DC and 30% CLVD components, Figure 4.22.

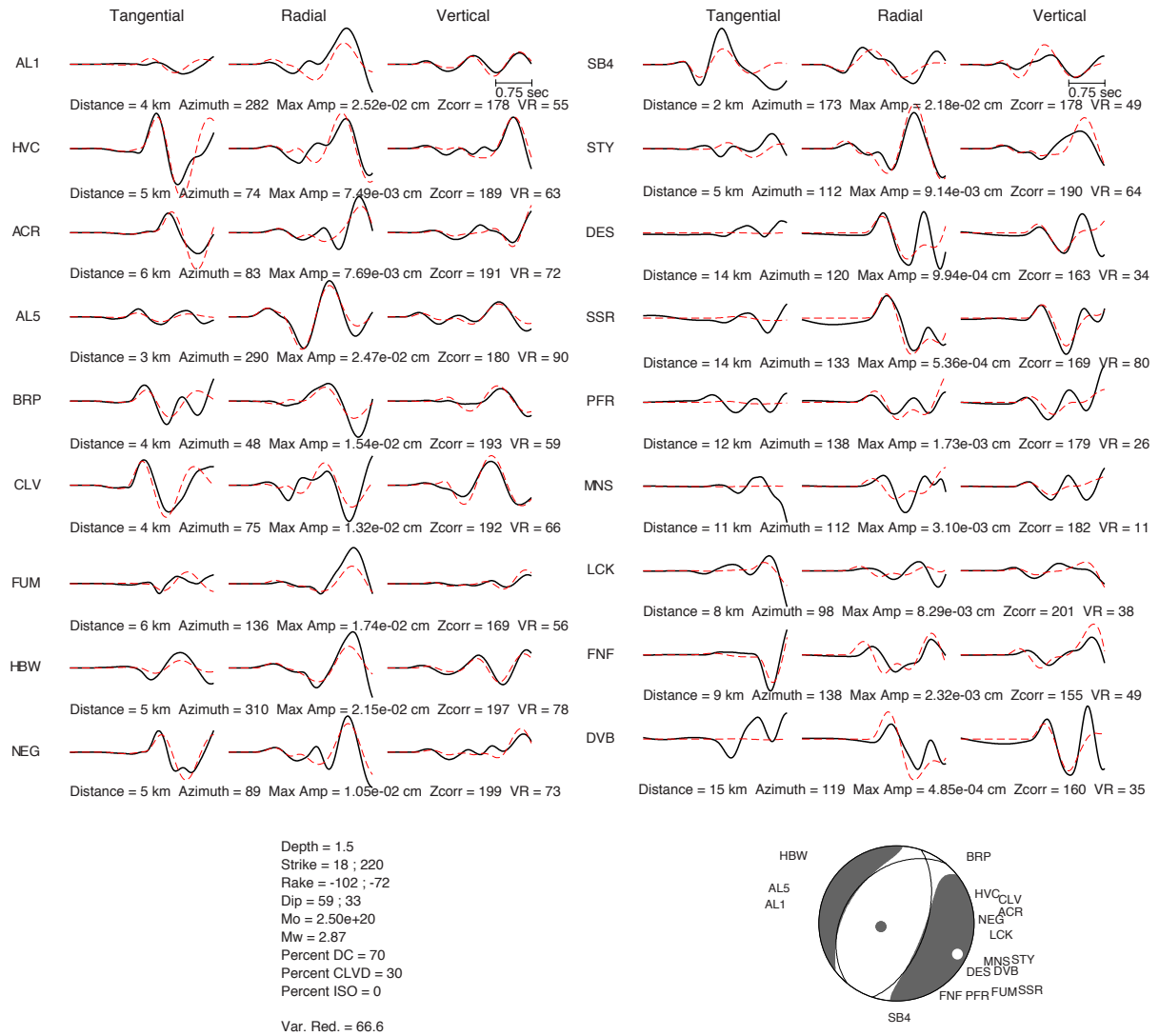

Figure 4.22. Comparison of filtered (0.2 to 1.0 Hz) observed velocity data (black) and synthetics (red) waveform fits and *P*-wave radiation pattern of the deviatoric moment tensor solution for target event 4, M_W 2.87 February 6, 2013. Gray and white dots represent pressure and tension axes, respectively.

The full moment tensor solution is largely a double-couple with a 17% isotropic component, Figure 4.23. The improvement in fit compared to the deviatoric solution is 0.3% and is not statistically significant as measured by the *F*-test.

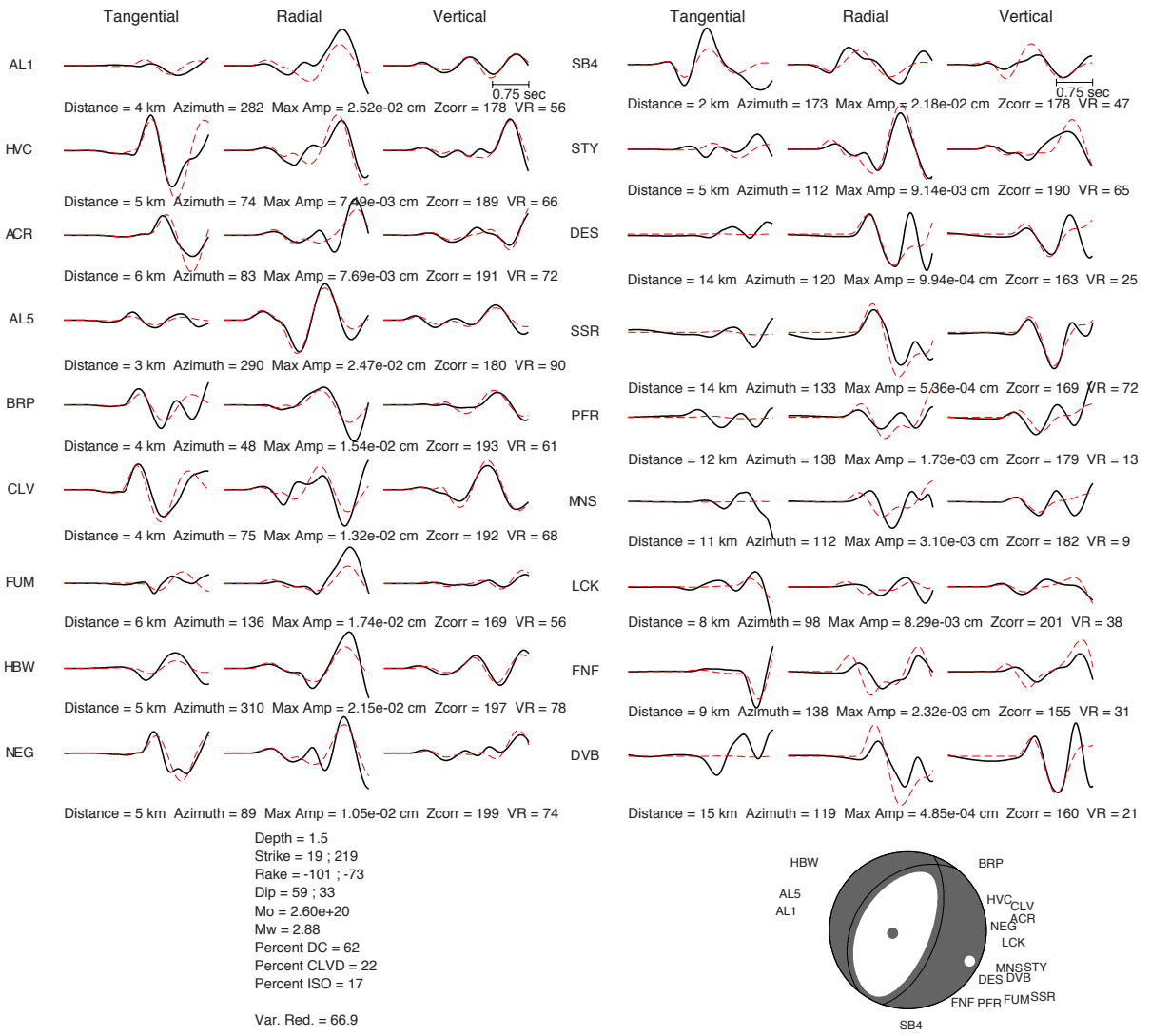

Figure 23. Comparison of filtered (0.2 to 1.0 Hz) observed velocity data (black) and synthetics (red) waveform fits and *P*-wave radiation pattern of the full moment tensor solution for target event 4, M_W 2.87 February 6, 2013. The improvement in fit of the full moment tensor solution is 0.3% and is too small to be statistically significant. Gray and white dots represent pressure and tension axes, respectively.

To further constrain the moment tensor we used the source-type inversion methodology of Nayak and Dreger (2015) to explore the source-type-specific space of combined first-motion and waveform data. The combined first-motion and waveform data full moment tensor inversion results in a decomposition of 41% DC, 37% CLVD, and 22% volume-decrease ISO components. There is good agreement between the double-couple portions of all three solutions. For the purpose of the finite-source analysis the robust 18-station deviatoric moment tensor solution is used.

Suitable eGf events horizontally located within 200 m from larger target event were found in the NCEDC DD catalog. The eGf waveforms were then deconvolved from the target

waveforms to identify those that produced pulse-like moment rate functions (MRF) with the highest signal to noise ratio. The pulse widths of the resulting MRFs range from 0.24 s at station AL3 in the southwest to a narrow width of 0.15 s at station SQK in the southeast. The MRFs for the target event are presented in Figure 4.24.

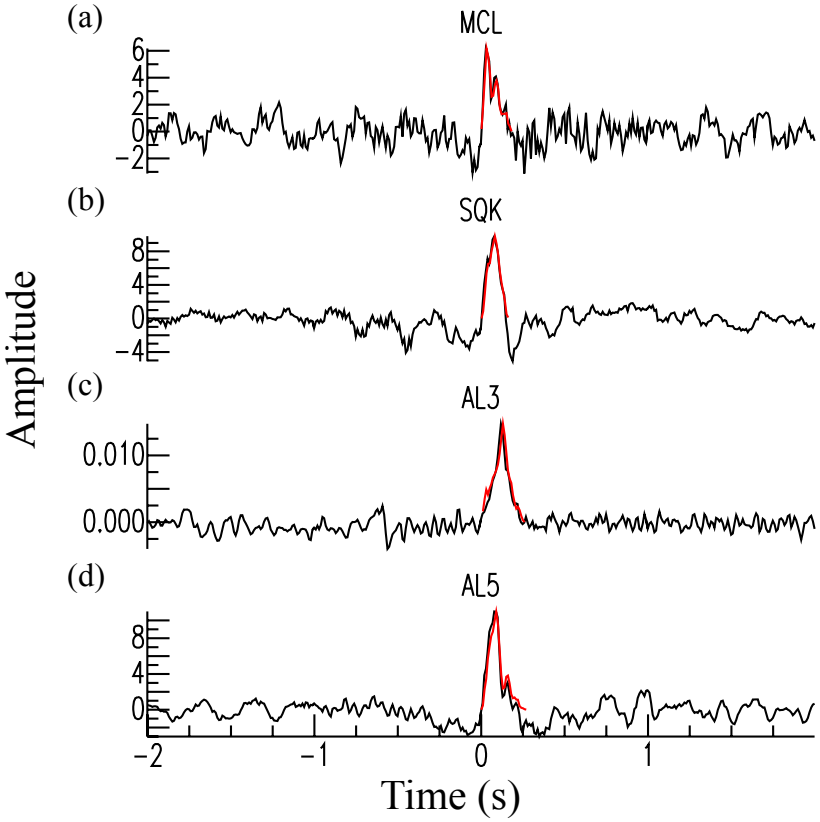

Figure 4.24. Target event 4, M_W 2.87 February 6, 2013, stacked MRF pulse trains (black), synthetic pulses (red) ordered by azimuth for stations (a) MCL (b) SQK (c) AL3 and (d) AL5.

The finite-source model has the same fault dimensions, number of grid points, subfault size, and a constant rupture velocity as described for target events 1− 3, above. The model assumes a constant rupture velocity of 0.9 times the shear wave speed at the source depth. The slip at each patch on the fault occurs with a rise time of a 0.02 s fixed-width boxcar. The total allowable slip duration is 1 s. The subfault dimension of 16.4 m is consistent with the 9.3 m wavelength for *S* waves with Vs = 2.34 km/s at 0.7 km depth and 250 Hz bandwidth. The inversion uses a slip positivity constraint and a smoothing constraint to minimize the spatial derivative of the slip. The smoothing weight is investigated by searching for the smallest value that produces a smoothed model with a fit close to the maximum fit to the data as measured by the variance reduction. The rupture area is determined by the number of subfaults with slip greater than 10% of the maximum slip and varies with smoothing parameter. This threshold is used to ignore small amplitude patches of slip that are poorly constrained by the inversion. Smoothing parameters of 2, 20, 200, and 2000 were investigated. The goodness of fit between the observed and synthetic MRFs is comparable for the strike, rake, and dip of both nodal planes yet one nodal plane with strike 18°, dip 59°, and rake −102° has a higher goodness of fit. The slip distribution and stress change maps from the

inversion of moment rate functions at four nearby stations for rupture velocity 90% of the local shear wave velocity are shown Figures 4.25a and 4.25b, respectively. The overall dimension of slip model is about 1 wavelength, and the little slip patches are approximately ⅕ wavelength of the MRF data band indicating the slip model is well imaged.

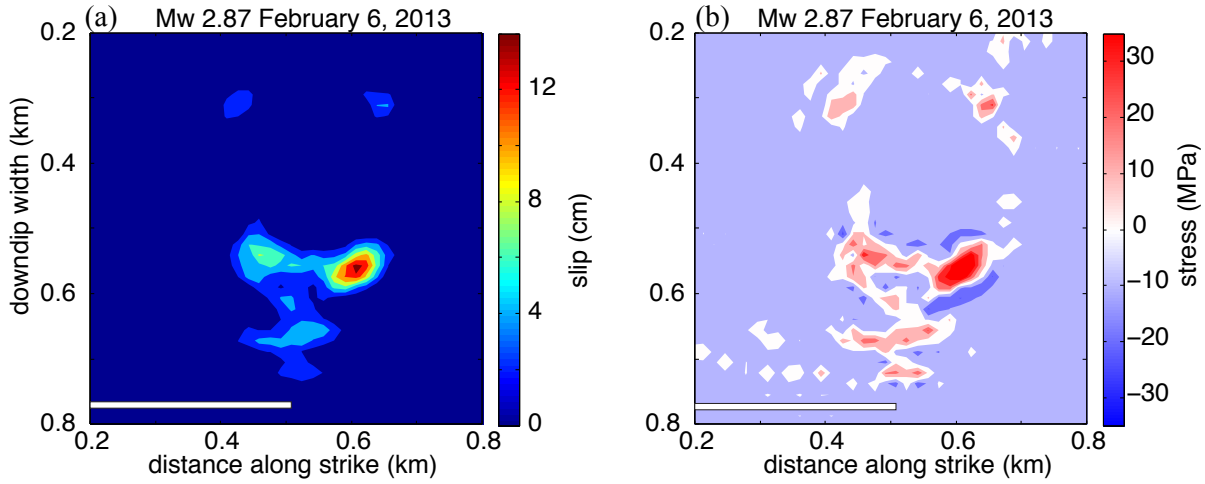

Figure 4.25. Target event 4, M_W 2.87 February 6, 2013, maps of slip (a) and stress change (b) distributions from inversion of moment rate functions with smoothing parameter 20, rise time 0.02 s, strike 18°, dip 59°, rake −102°. The hypocenter is located at the center of each plot. The peak slip is 15 cm and the peak stress drop is 69 MPa. Stress change on the fault surface with red as stress drop and blue as stress increase. The horizontal bar represents the dimension in kilometers of target events 1 and 2, with M_W 1.05 and M_W 1.48, respectively.

4.4.5 Event 5 M_W 3.19 May 8, 2016

A search of the NCEDC Double-Difference (DD) Catalog indicated multiple potential eGfs for the chosen target event on May 8, 2016 located on the east side of the EGS study area, Figure 4.26.

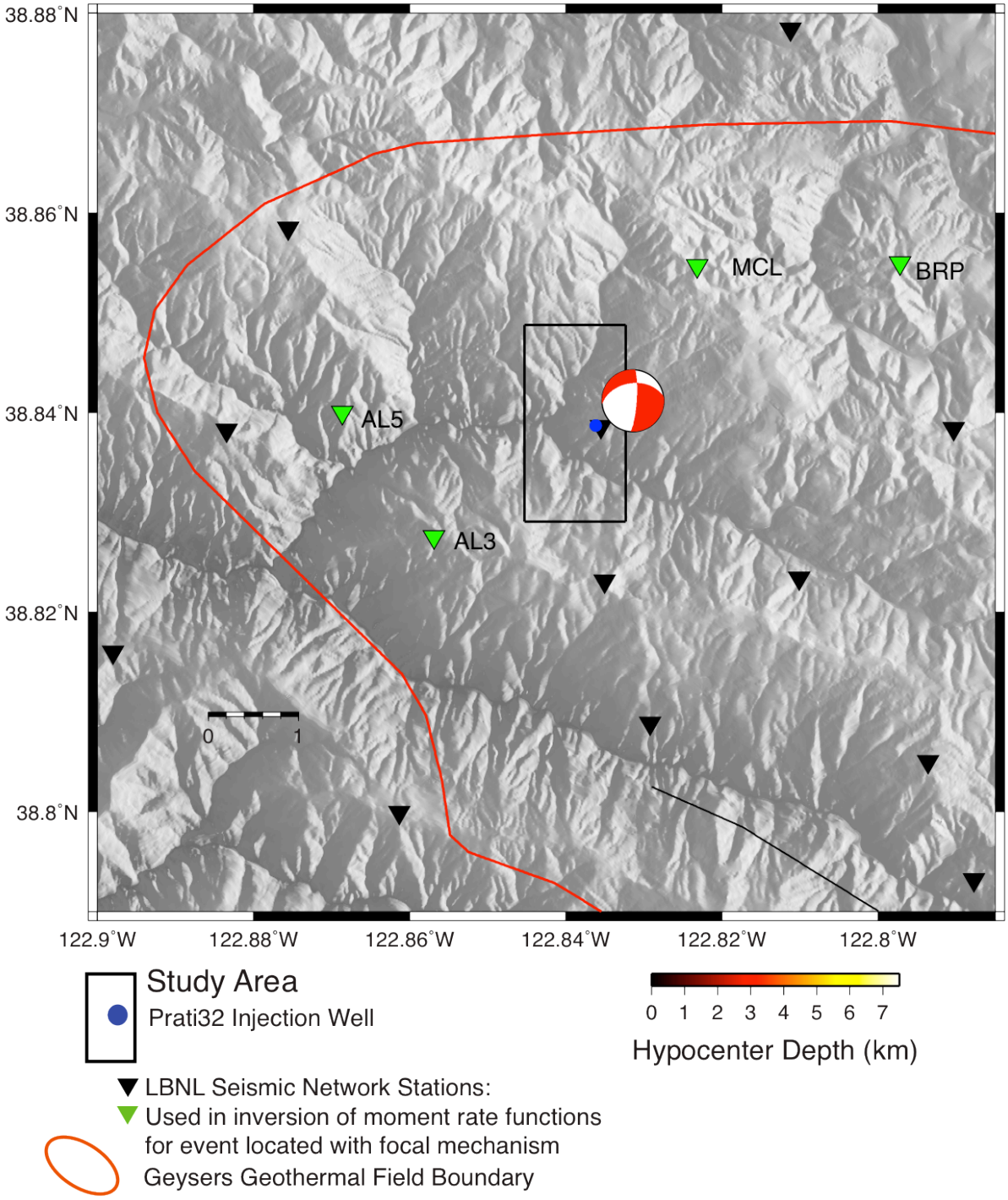

Figure 4.26. Map of the Northwest Geysers geothermal field. The EGS study area is a 1 x 2 km^2 rectangle centered on the EGS production well Prati State 31 (PS-31) and EGS injection well Prati 32 (P-32), blue dot. The location of the M_W 3.19 target event is shown with its double-couple focal mechanism from the combined waveform and first-motion solution and shaded by hypocenter depth. The locations of short-period seismic stations operated by Lawrence Berkeley National Laboratory (LBNL) used in this study are indicated by triangles (data from stations marked by green triangles were used to invert for moment rate functions. The approximate boundary of The Geysers steam field and selected faults are delineated with red and black lines, respectively.

The locations of both events are from NCEDC Double-Difference (DD) catalog. The target event occurred May 8, 2016 and the eGf event occurred about five and a half years earlier on December 5, 2010 before injection commenced at Prati 32, Table 4.11. The target-eGf event separation is 0.06 km in horizontal distance and 0.02 km in depth. The catalog magnitudes (duration magnitude, Md) differ by 1.26 units.

Table 4.11. Target and empirical Green's function event information from the NCEDC Double-Difference catalog for event 5, May 8, 2016: duration magnitude (Md), date, time, latitude, longitude, and depth.

Event	Magnitude	Date	Time	Latitude	Longitude	Depth
Target	2.79	2016/05/08	19:25:30.78	38.8416	-122.8327	1.96
eGf	1.53	2010/12/05	18:42:34.72	38.8420	-122.8322	1.98

Waveform data were downloaded from the NCEDC for stations in the LBNL seismic network. Event times and locations as specified in the NCEDC EGS catalog were used with data filtered in passband 0.2 to 1.0 Hz to investigate the moment tensor of the target event. Waveform fits and *P*-wave radiation patterns of the deviatoric moment tensor and full solution are shown in Figures 4.27 and 4.28, respectively. The deviatoric moment tensor solution has a large 75% CLVD component.

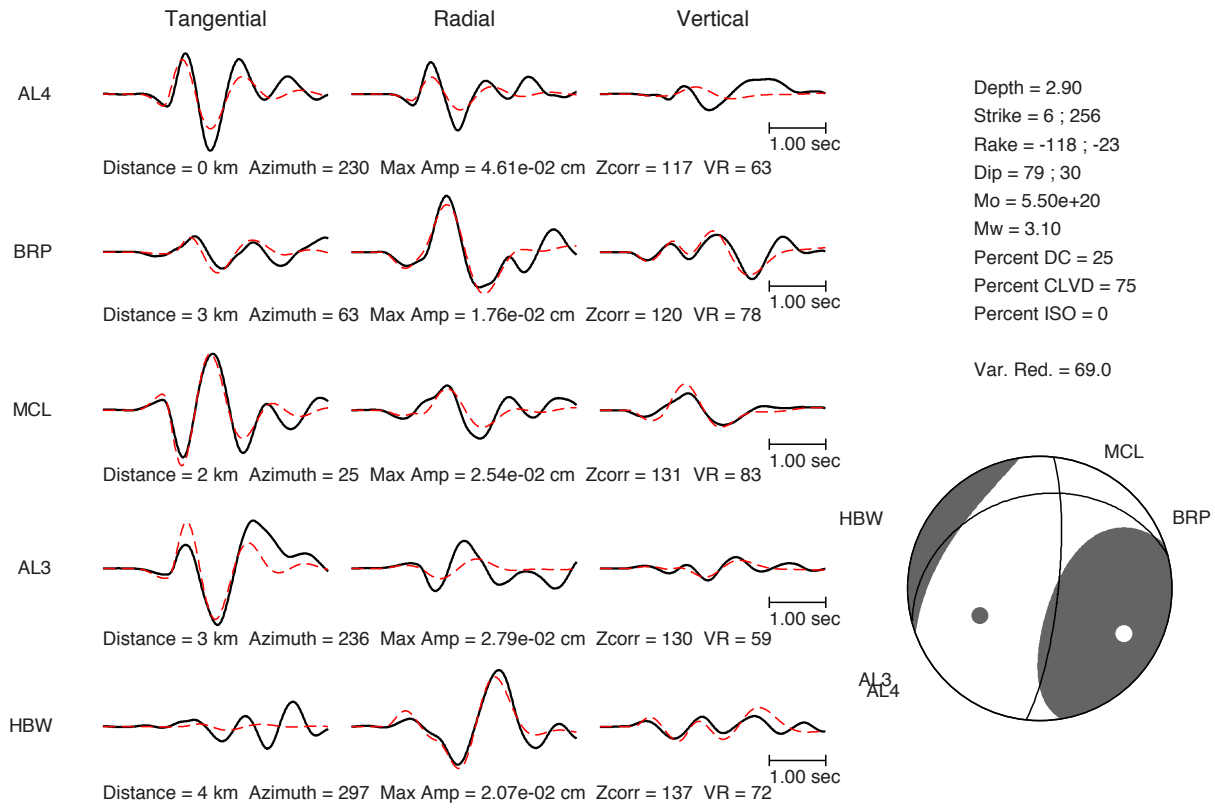

Figure 4.27. Comparison of filtered (0.2 to 1.0 Hz) observed velocity data (black) and synthetics (red) waveform fits and *P*-wave radiation pattern of the deviatoric moment tensor solution for target event 5, May 8, 2016.

The full moment tensor solution has a small 1% isotropic component. The improvement in fit from the extra degree of freedom in the full moment tensor solution is negligible, Figure 4.28.

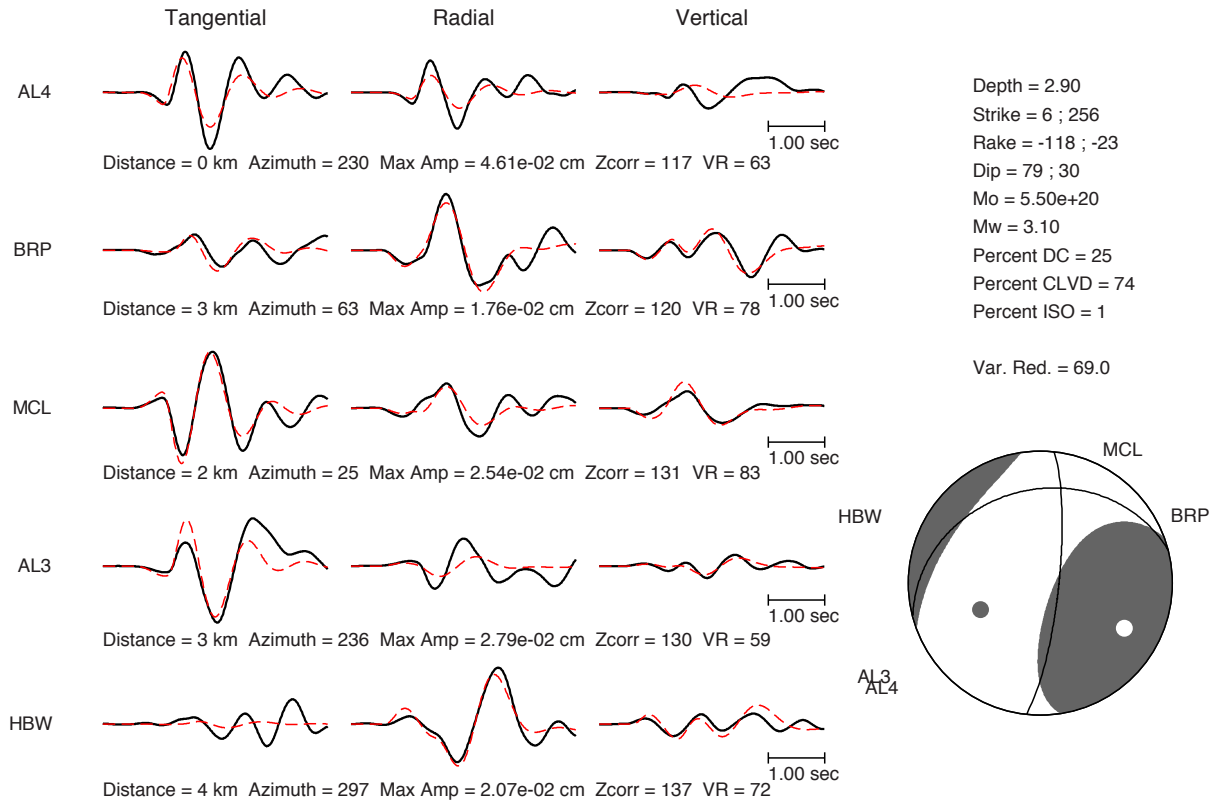

Figure 4.28. Comparison of filtered (0.2 to 1.0 Hz) observed velocity data (black) and synthetics (red) waveform fits and *P*-wave radiation pattern of the full moment tensor solution for target event 5, May 8, 2016. The improvement in fit of the full moment tensor solution is negligible.

To constrain the moment tensor we used the source-type inversion methodology of Nayak and Dreger (2015) to explore the source-type-specific space of combined first-motion and waveform data filtered in the 0.2 to 1.0 Hz passband. The combined first-motion and waveform data full moment tensor inversion results in a decomposition of 45% DC, 44% CLVD, and 11% isotropic components, Figure 4.29. The interpretation for this oblique normal event is that its full moment tensor mechanism is a mixture of DC and CLVD with a small positive volumetric component. As before the strike, rake and dip of the double-couple portion of the solution are very similar between all three moment tensor inversions.

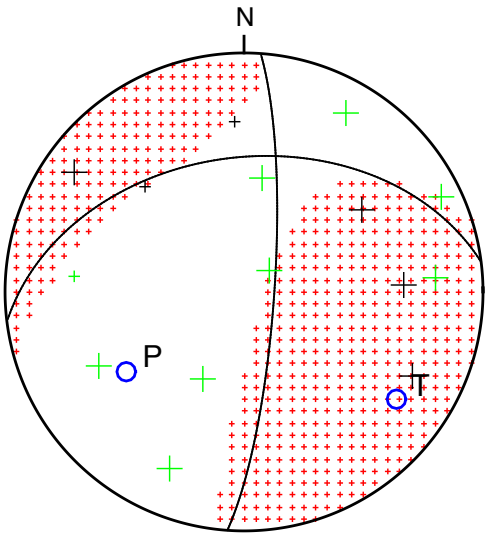

Figure 4.29. Constrained waveform and first motion mechanism for target event 5, M_W 3.19 May 8, 2016, using the source-type inversion methodology of Nayak and Dreger (2015). Shaded quadrants are compressional. First-motions are shown with plus symbols, up first motions (black), down first motions (green). The positive isotropic component evidenced by shading in the tensile quadrants indicates a volume-increase component. Compression (P) and tension (T) axes marked with open blue circles.

For the purpose of the subsequent finite-source inversion, we use the source parameters of the combined first-motion and waveform moment tensor solution, Table 4.12.

Table 4.12. Combined waveform and first motion full moment tensor parameters for target event 5, M_W 3.19 May 8, 2016. Strike, dip and rake for both nodal planes.

Moment (dyne-cm)	Mw	Strike	Rake	Dip	%DC	%CLVD	%ISO
7.582E+20	3.19	4/263	-132/-15	80/43	45	44	11

Suitable eGf events horizontally located within 200 m from larger target event were found in the NCEDC DD catalog. The eGf waveforms were then deconvolved from the target waveforms to identify those that produced pulse-like moment rate functions (MRF) with the highest signal to noise ratio. The pulse widths of the resulting MRFs range from 0.18 s at station MCL in the northeast to a narrow width of 0.12 s at station BRP further east, Figure 4.30.

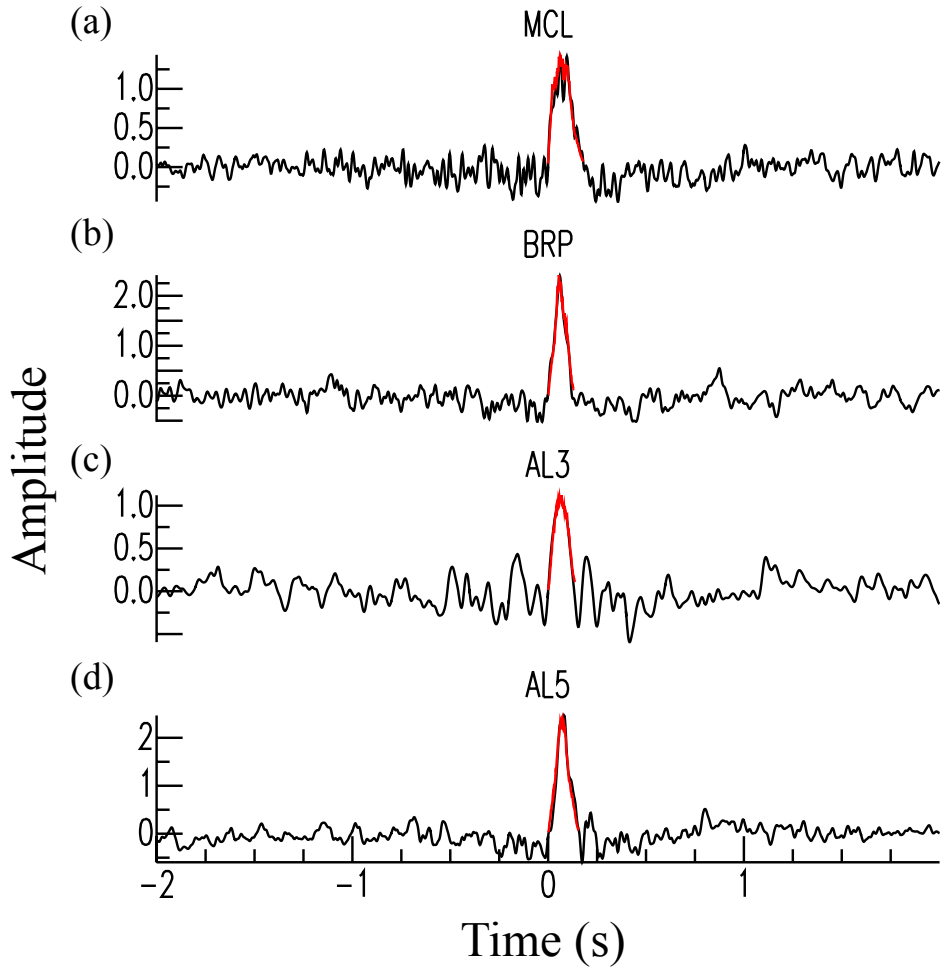

Figure 4.30. Target event 5, M_W 3.19 May 8, 2016, stacked MRF pulse trains (black), synthetic pulses (red) ordered by azimuth for stations (a) MCL (b) BRP (c) AL3 and (d) AL5.

The finite-source model has the same fault dimensions, number of grid points, subfault size, and a constant rupture velocity as described for target events 1-4, above. The subfault size of 16.4 m dimension is consistent with the 10.4 m wavelength for *S* waves with Vs = 2.59 km/s at 1.96 km depth and 250 Hz bandwidth. The inversion uses a slip positivity constraint and a smoothing constraint to minimize the spatial derivative of the slip. The smoothing weight is investigated by searching for a the smallest value that produces a smoothed model with a fit close to the maximum fit to the data as measured by the variance reduction. The rupture area is determined by the number of subfaults with slip greater than 10% of the maximum slip and varies with smoothing parameter. For smoothing parameters between 80 and 200, the area stays constant at approximately 0.07 km^2.

The goodness of fit between the observed and synthetic MRFs is comparable for the strike, rake, and dip of both nodal planes yet one nodal plane with strike 4°, dip 80°, and rake −132° has a smoothed and somewhat simpler slip distribution. The slip and stress distributions from inversion of moment rate functions at four nearby stations for rupture velocity 90% of the

local shear wave velocity and smoothing parameter 200 are shown in Figures 4.31a and 4.31b, respectively. For this model the overall dimension of the slip is about 1 wavelength, and the peak slip is between ¼–½ wavelength of the MRF data band.

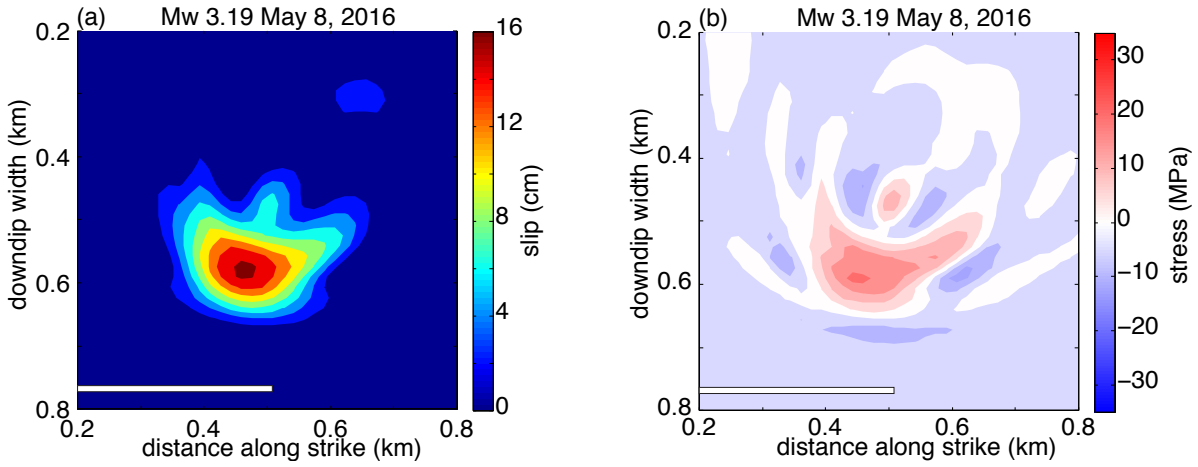

Figure 4.31. Target event 5, M_W 3.19 May 8, 2016 maps of slip distribution (a) and stress change (b) from inversion of moment rate functions with smoothing parameter 200, rise time 0.02 s, strike 4°, dip 80°, rake −132°. The hypocenter is located at the center of each plot. The peak slip is 15 cm and the peak stress drop is 23 MPa. Stress change on the fault surface with red as stress drop and blue as stress increase. The horizontal bar represents the dimension in kilometers of target events 1 and 2, with M_W 1.05 and M_W 1.48, respectively.

4.4.6 Event 6 *M*w 3.73 January 21, 2014

Target event 6, M_W 3.73 January 21, 2014, occurs more than two years after injection initiates at Prati 32 and is located in the center of the study area, Figure 4.32. This event is the maximum magnitude event thus far in the Prati 32 study area, Chapter 3.

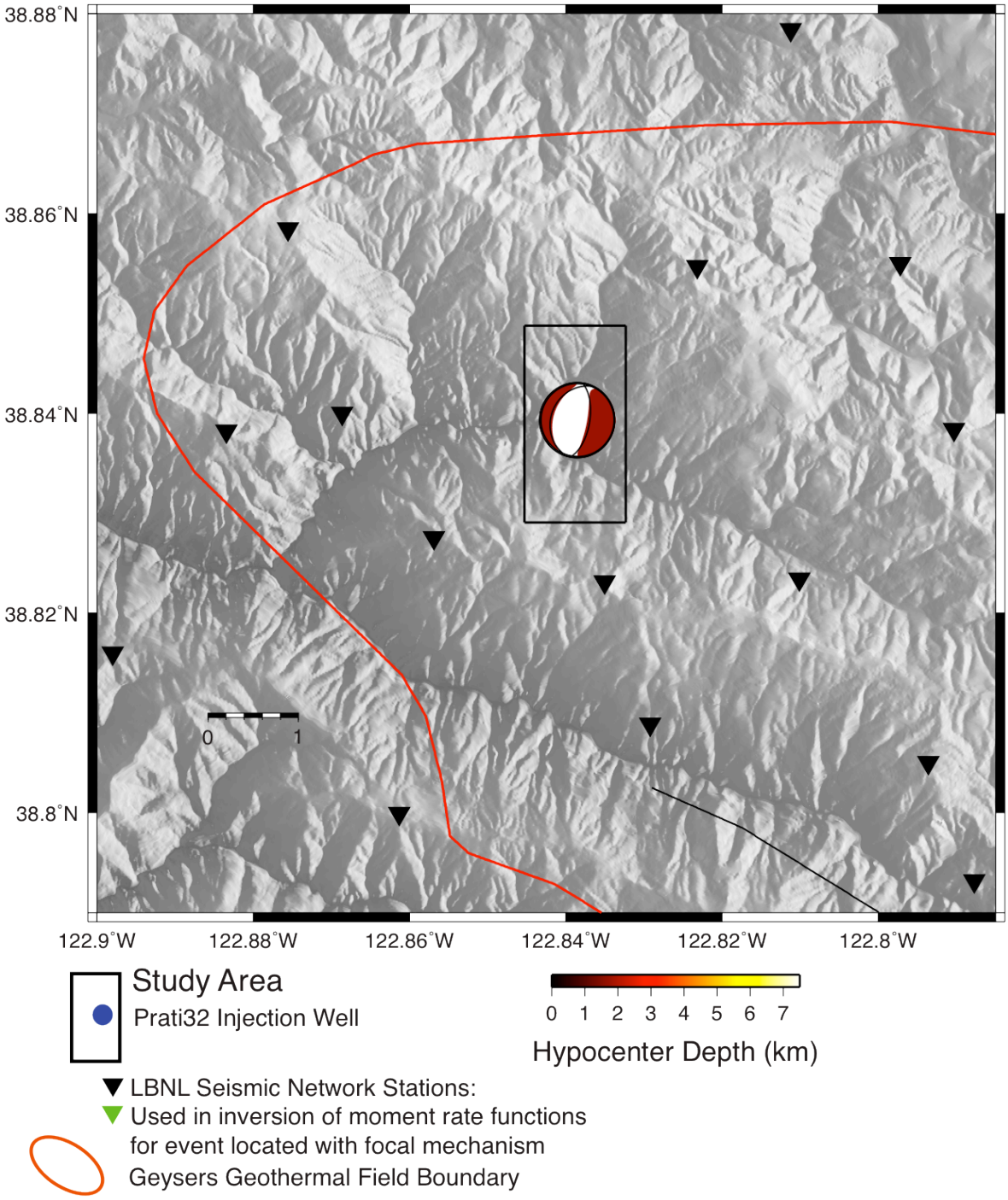

Figure 4.32. Map of the Northwest Geysers geothermal field. The EGS study area is a 1 x 2 km^2 rectangle centered on the EGS production well Prati State 31 (PS-31) and EGS injection well Prati 32 (P-32), blue dot. The location of the M_W 3.73 target event is shown with its double-couple focal mechanism from the combined waveform and first-motion solution and shaded by hypocenter depth. The locations of short-period seismic stations operated by Lawrence Berkeley National Laboratory (LBNL) used in this study are indicated by triangles (data from stations marked by green triangles were used to invert for moment rate functions. The approximate boundary of The Geysers steam field and selected faults are delineated with red and black lines, respectively.

The locations of the target and eGf events are from NCEDC NCSN catalog. The target event occurred January 21, 2014 and the eGf event occurred about six and a half years earlier on July 31, 2007 before injection commenced at Prati 32, Table 4.13. The target-eGf event separation is 0.38 km in horizontal distance and 1.07 km in depth. The catalog magnitudes differ by 1.32 units.

Table 4.13. Target and empirical Green's function event information from the NCEDC NCSN catalog for event 6, January 21, 2014: moment magnitude (M_W) or duration magnitude (Md), date, time, latitude, longitude, and depth.

Event	M_W /Md	Date	Time	Latitude	Longitude	Depth (km)
Target	3.87 Mw	2014/01/21	11:11:11.64	38.83933	-122.83850	1.73
eGf	2.55 Md	2007/07/31	13:25:22.78	38.83750	-122.84216	0.66

The seismic waveform data were processed by removing the instrument response to ground velocity, followed by bandpass filtering of the waveforms with a causal 4^{th}-order Butterworth filter with corners at 0.2 and 1.0 Hz. To constrain the moment tensor the source-type inversion methodology of Nayak and Dreger (2015) was used to explore the source-type-specific space of combined first-motion and waveform data filtered in the 0.2 to1.0 Hz passband. The combined first-motion and waveform data full moment tensor inversion results in a decomposition of 58% DC, 31% CLVD, and 11% isotropic components, Figure 4.33. The interpretation for this oblique normal event is that its full moment tensor mechanism is primarily a mixture of compensated linear vector dipole (CLVD) and double-couple components with a small statistically insignificant volume increase component.

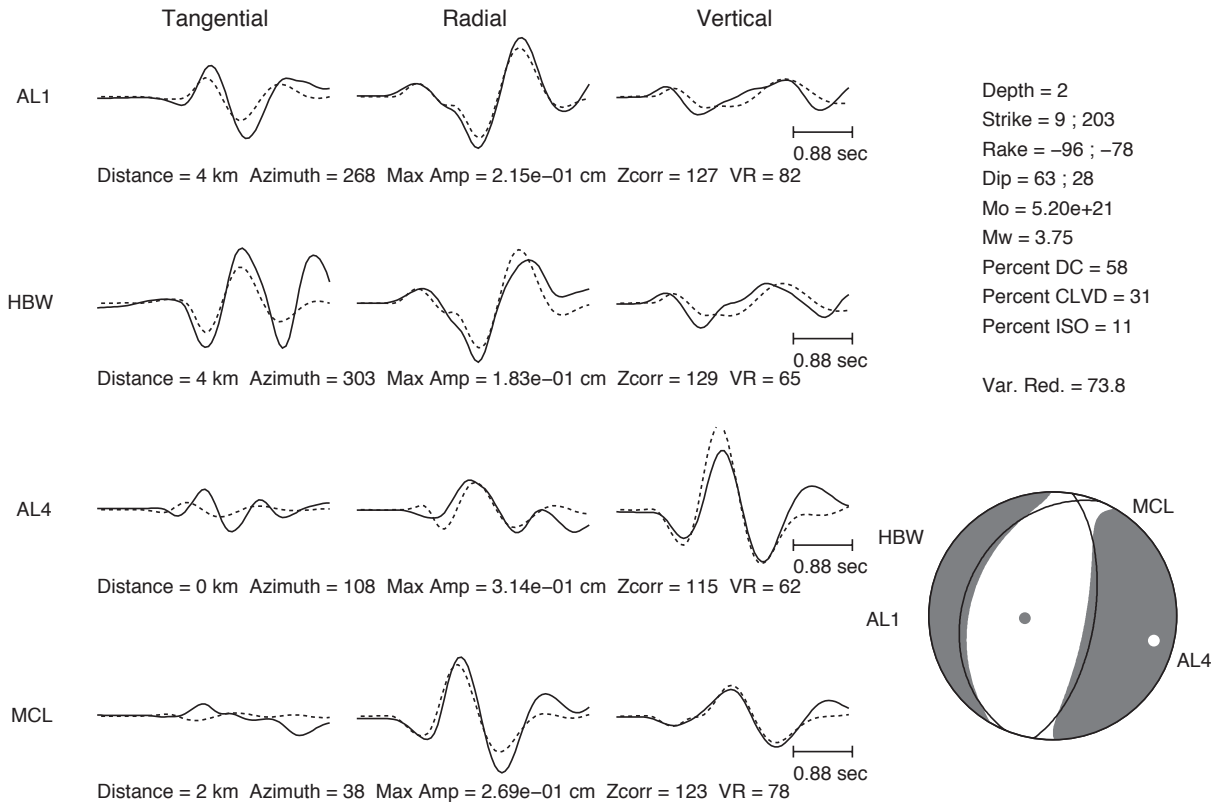

Figure 4.33. Comparison of filtered (0.2 to 1.0 Hz) observed velocity data (solid) and synthetic (dashed) waveform fits and *P*-wave radiation pattern of the constrained first-motion and waveform full moment tensor solution for target event 6, January 21, 2014.

A source-type network sensitivity solution (NSS; Ford *et al*., 2010; Nayak and Dreger, 2015) obtained by simultaneously inverting the waveforms and first-motion observations from geophone stations indicates that the mechanism is deviatoric and that acceptable solutions include a pure-double-couple. The best fitting solution is shown is Figure 4.34.

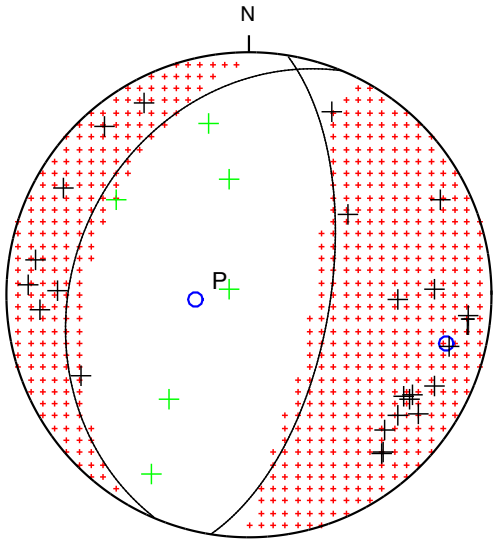

Figure 4.34. Constrained waveform and first motion mechanism for target event 6, M_W 3.73 January 21, 2014 using the source-type inversion methodology of Nayak and Dreger (2015). Shaded quadrants are compressional. First-motions are shown with plus symbols, up first motions (black), down first motions (green). The positive isotropic component evidenced by shading in the tensile quadrants indicates a volume-increase component. Compression (P) and tension (T) axes marked with open blue circles.

The eGf waveforms were then deconvolved from the target waveforms at broadband stations in the regional Berkeley Digital Seismic Network (BDSN), Figure 35a to identify those that produced pulse-like moment rate functions (MRF) with the highest signal to noise ratio. The pulse widths of the resulting MRFs range from approximately 0.48 to 0.51 s, Figure 4.35b. This duration is unusually long for an event of this magnitude.

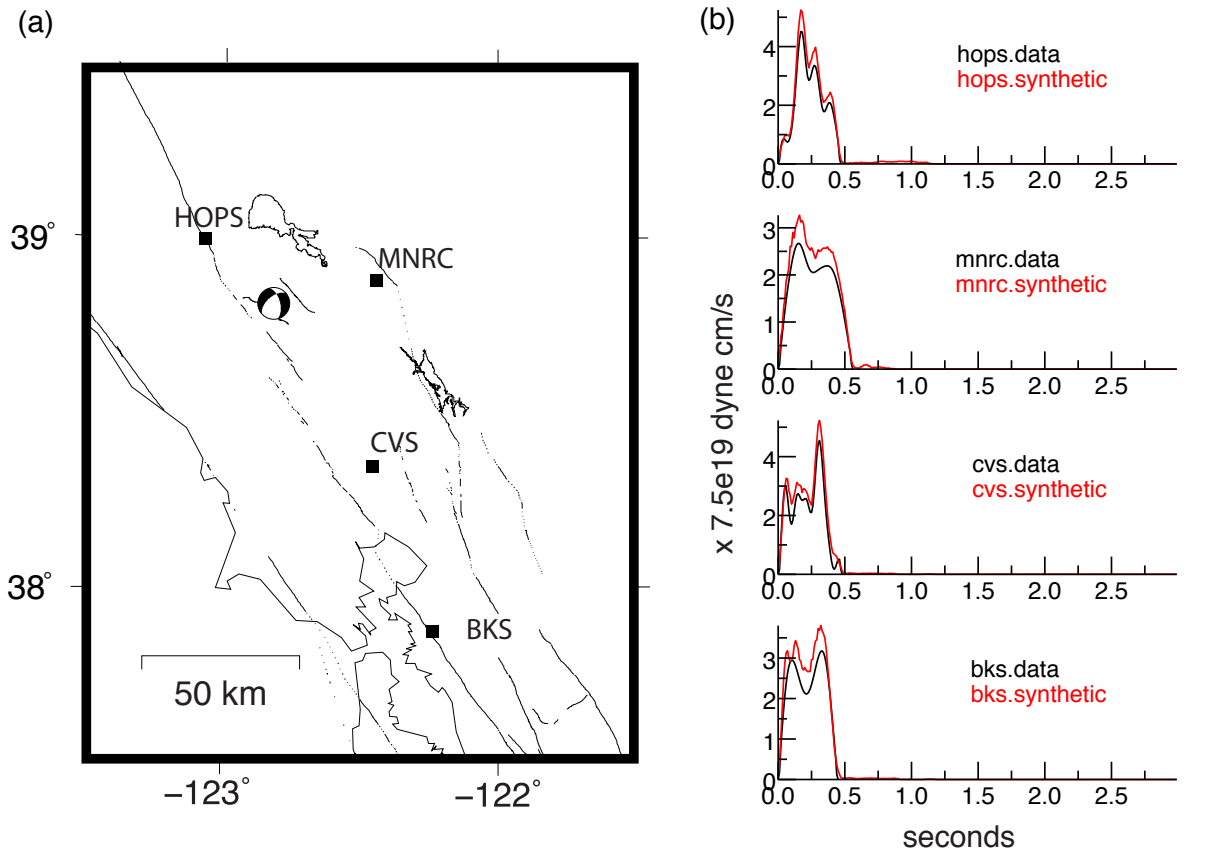

4.35. Map showing the location of target event 6, oblique-normal M_W 3.7 January 21, 2014, and the four regional broadband stations used to determine source moment rate functions. The eGf waveforms were deconvolved from the target waveforms at broadband stations HOPS, MNRC, CVS, and BKS in the regional Berkeley Digital Seismic Network (BDSN) (a) to identify pulse-like moment rate functions with the highest signal to noise ratio. Observed moment rate functions (black) are compared to synthetics (red) (b). The amplitudes of the MRFs are proportional to 7.5e19 dyne cm/s.

The finite-source model for target event 6 has a larger fault dimension 2 km than models for previous events, using the same number of grid points (61 x 61), resulting in a larger subfault size of 32.8 m. The model assumes a constant rupture velocity of 0.9 times the shear wave speed at a source depth. The slip at each patch on the fault occurs with a rise time of a 0.05 s fixed-width boxcar. The total allowable slip duration is 3 s. The subfault dimension is consistent with the 38 m wavelength for *S* waves with Vs = 1.9 km/s at 2 km depth and 50 Hz bandwidth. The smoothing weight is investigated by searching for a the smallest value that produces a smoothed model with a fit close to the maximum fit to the data as measured by the variance reduction. The rupture area is determined by the number of subfaults with slip greater than 10% of the maximum slip and varies with smoothing parameter.

Figure 4.36 shows the slip distribution of the M_W 3.7 event obtained by deconvolving the records of a nearby Md 2.5 eGf earthquake. The slip distribution is complex, with 3 or 4 asperities being well resolved, Figure 4.36a. The moment rate functions, Figure 4.35b show

multiple pulses of moment release that give rise to the observed slip patches. The overall slip model is a little more than 1 wavelength in dimension for a central wavelength of the MRF data band. The subevents are about ¼ wavelength. The average and peak slips are 7.9 and 26.5 cm, respectively. Using the method of Ripperger and Mai (2004) the slip distribution can be mapped into stress change, Figure 4.36b. The average stress drop over the fault rupture is 12 MPa, with a peak stress drop of 66 MPa. These high stress drops result from the compact nature of the individual slip patches in the rupture model, and demonstrate that the field is under high stress.

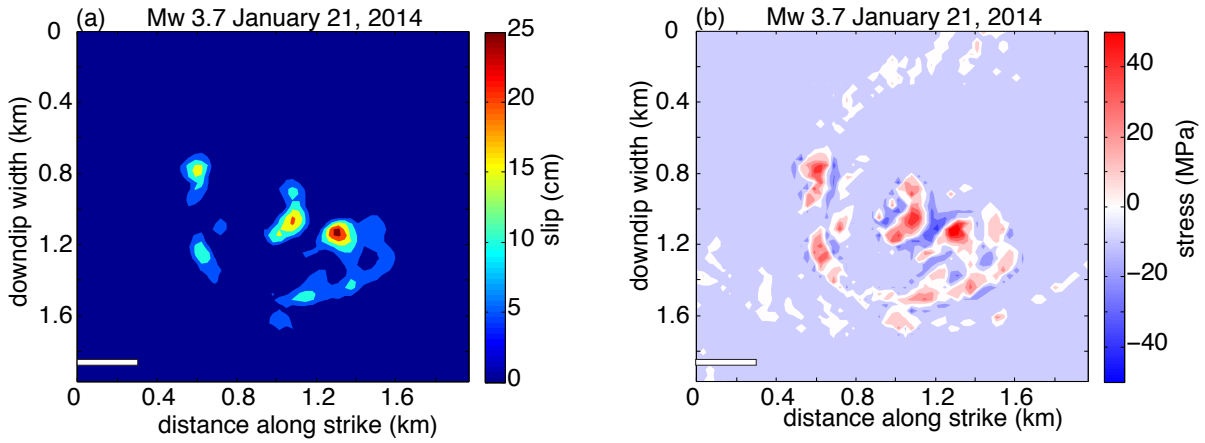

4.36. Target event 6, M_W 3.7 January 21, 2014 maps of slip distribution (a) and stress change (b) from inversion of moment rate functions with smoothing parameter 10, rise time 0.05 s, strike 200°, dip 30°, rake −82°. A rupture velocity of 90% of the shear wave velocity was assumed. The hypocenter is located at the center of each plot. The peak slip is 26.5 cm and the peak stress drop is 66 MPa. Stress change on the fault surface with red as stress drop and blue as stress increase. The horizontal bar represents the dimension in kilometers of target events 1 and 2, with M_W 1.05 and M_W 1.48, respectively.

Finite-source results of events with $M_W > 4$

Four larger earthquakes (M_W > 4.0) located in Figure 4.37 were found with closely located smaller events that proved to be suitable for empirical Green's function (eGf) analysis as evidenced by the recovery of moment rate function (MRF) pulses describing the source time history of the events. For the four events the MRF recorded at four regional broadband stations with good azimuthal coverage were inverted for finite-source parameters, which included the spatial distribution of fault slip, rupture velocity, and the orientation of the causative plane. In every case the preferred fault plane (testing the two possible double-couple nodal planes from the moment tensor analysis) was the N-NW striking plane, which is consistent with the overall trend of major fault structures near the Geysers (McLaughlin, 1981). The results show complexity in the MRF and resulting slip models in which there are multiple sub-events or patches of slip for a given earthquake. The slip distribution models were used to determine the co-seismic stress change, which yielded high average stress drops

on the order of 10 MPa, with peak values of 50−100 MPa, indicating regions within the field with locally high strength and stress. One event was found to have a low average stress drop of 1.6 MPa with a very complex slip distribution extending over 7 km, which is extremely large for a M_W 4.5 event. The other $M_W > 4$ events are modeled similarly in terms of number of subfaults, overall fault dimension, and subfault dimension and will be described below for each event.

The deviatoric moment tensor solutions were determined in Chapter 2 using filtered (0.02 to 0.05 Hz) observed displacement data and synthetics. To explore the stability of the finite-source solutions, we tested various groups of stations, several different rupture velocities and subfault sizes. The fits in all cases were stable for both fault plane solutions with the north-northwest striking fault plane marginally better. The maximum fit for all four events resulted from using the three closest stations CVS, HOPS, and MNRC and a rupture velocity of 90% of the shear wave velocity. The May 5, 2012 and March 14, 2013 events had the largest difference in fit for the two fault plane solutions for the 3-station group BKS, HOPS and MNRC and may be due to the southward directivity of those ruptures.

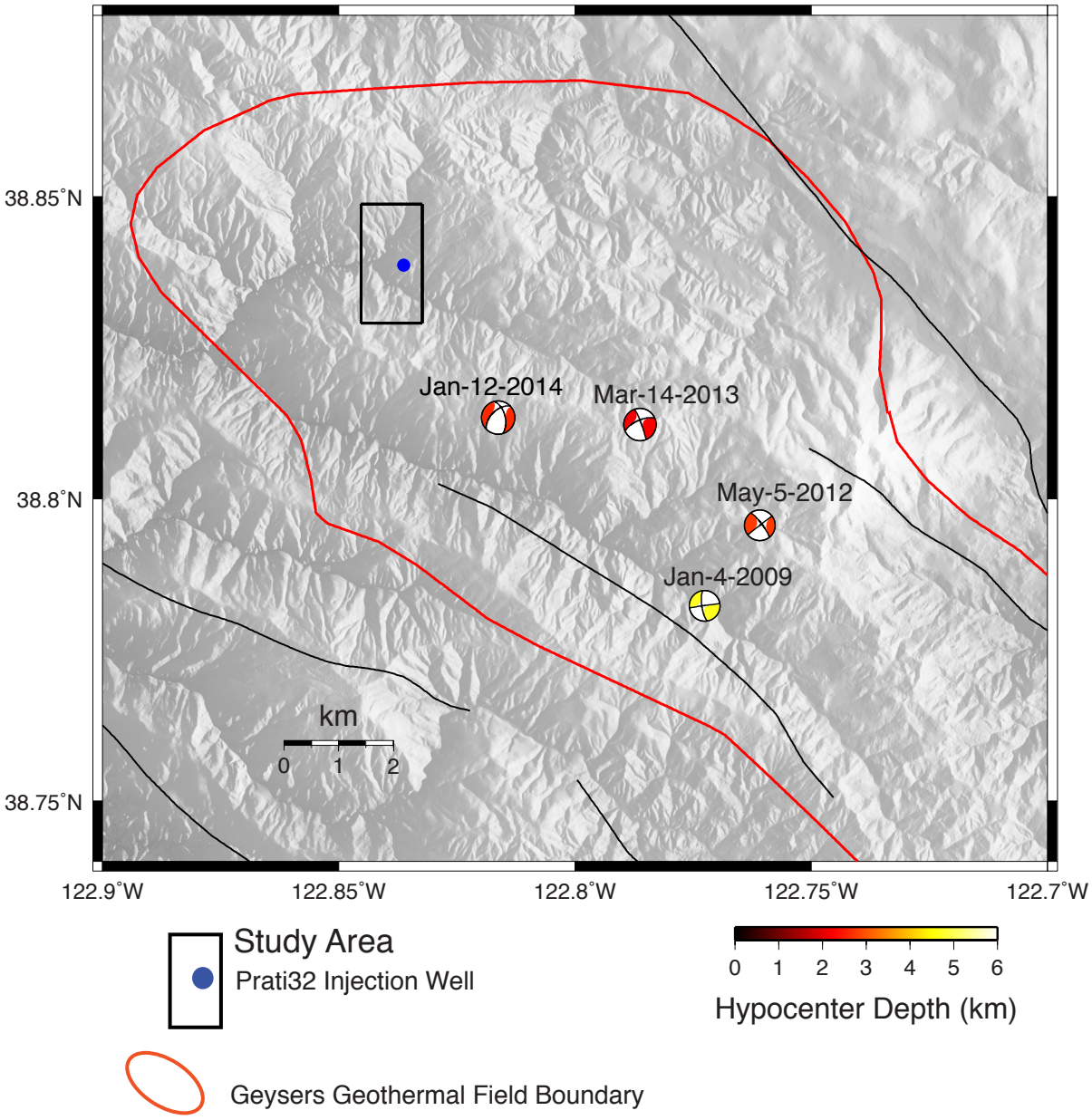

Figure 4.37. Location map showing deviatoric focal mechanisms of $M_W > 4$ studied events shaded by hypocenter depth. These events occur southeast of the Prati 32 study area (black rectangle) in the central portion of the geothermal field where many of the larger magnitude events occur.

4.4.7 Event 7 M_W 4.25 May 5, 2012

Target event 7 is located in the central portion of geothermal field with its deviatoric focal mechanism shaded by hypocentral depth, Figure 4.37.

The locations of the target and eGf events are from NCEDC NCSN catalog. The target event occurred May 5, 2012 and the eGf event occurred about four and a half years earlier on January 12, 2008, Table 4.14. The target-eGf event separation is 0.26 km in horizontal distance and 0.71 km in depth. The catalog magnitudes differ by 1.56 units.

Table 4.14. Target and empirical Green's function event information from the NCEDC NCSN catalog for event 7 May 5, 2012: moment magnitude (M_W) or duration magnitude (Md), date, time, latitude, longitude, and depth.

Event	M_W /Md	Date	Time	Latitude	Longitude	Depth (km)
Target	4.25 M_W	2012/05/05	09:23:23.06	38.79567	-122.76083	1.83
eGf	2.69 Md	2008/01/12	03:08:30.62	38.79367	-122.76234	1.12

Waveform data were downloaded from the NCEDC for broadband stations in the BDSN. Event times and locations as specified in the NCSN catalog were used with data filtered in passband 0.02 to 0.05 Hz to investigate the moment tensor of the target event. Waveform fits and *P*-wave radiation pattern of the deviatoric moment tensor solution are shown in Figure 4.38. The deviatoric moment tensor is composed of roughly equal percentages of DC and CLVD components.

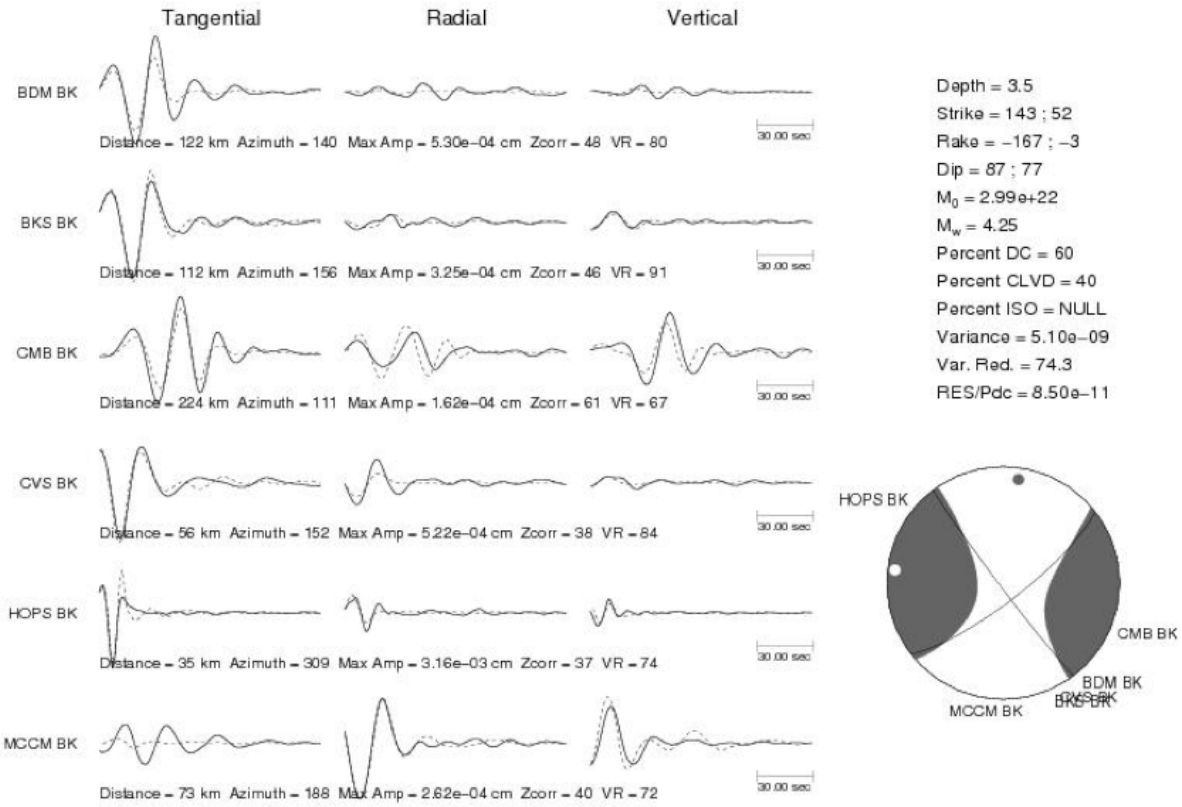

Figure 4.38. Comparison of filtered (0.02 to 0.05 Hz) observed velocity data (solid) and synthetics (dashed) waveform fits and *P*-wave radiation pattern of the deviatoric moment tensor solution for target event 7, M_W 4.25 May 5, 2012.

The eGf waveforms were then deconvolved from the target waveforms at four broadband stations in the regional BDSN to identify those that produced pulse-like moment rate functions (MRF) with the highest signal to noise ratio. The pulse widths of the resulting MRFs range from approximately 0.5 s in the south at station BKS to 0.8 s in the north at station HOPS, suggestive of a north to south rupture, Figure 4.39.

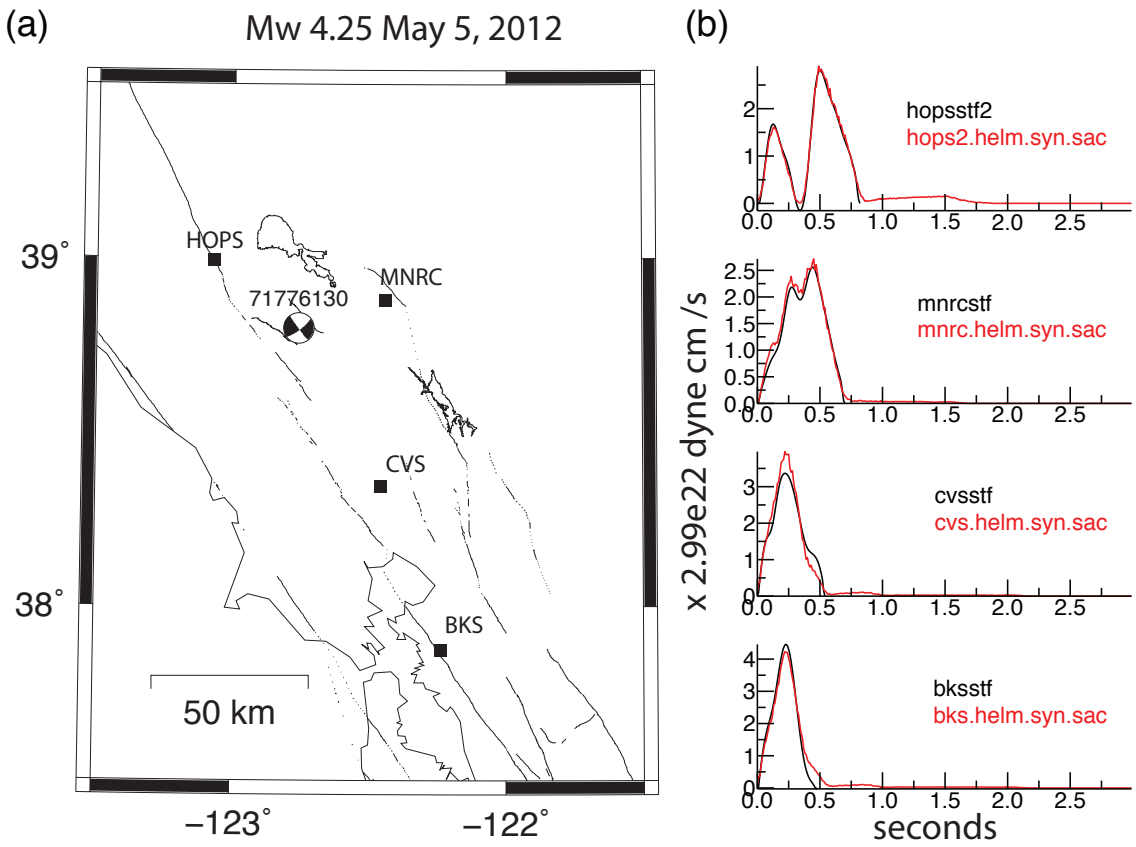

Figure 4.39. Map showing the location of target event 7, strike-slip M_W 4.25 May 5, 2012, and four regional broadband stations used to determine source moment rate functions. The eGf waveforms were deconvolved from the target waveforms at broadband stations HOPS, MNRC, CVS, and BKS in the regional Berkeley Digital Seismic Network (BDSN) (a) to identify pulse-like moment rate functions with the highest signal to noise ratio. Observed moment rate functions (black) are compared to synthetics (red) (b). The low pass filtered deconvolutions show clear source pulses at the four stations and a very good level of fit is obtained. The amplitudes of the MRFs are proportional to 2.99e22 dyne cm/s.

The finite-source model has larger fault dimensions 4 km than previous models, same number of grid points (61 x 61), with a larger subfault size of 65.6 m, and a constant rupture velocity of 0.9 times the shear wave speed at a source depth. The slip at each patch on the fault occurs with a rise time of a 0.1 s fixed-width boxcar. The total allowable slip duration is 3 s. The subfault dimension is consistent with the 48 m wavelength for *S* waves with Vs = 2.4 km/s at 3 km depth and 50 Hz bandwidth. The inversion uses a slip positivity constraint and a smoothing constraint to minimize the spatial derivative of the slip. The smoothing weight is investigated by searching for a the smallest value that produces a smoothed model with a fit close to the maximum fit to the data as measured by the variance reduction. The rupture area is determined by the number of subfaults with slip greater than 10% of the maximum slip and varies with smoothing parameter.

The goodness of fit between the observed and synthetic MRFs is comparable for the strike, rake, and dip of both nodal planes yet one nodal plane with strike 143°, dip 87°, and rake −167 has a smoothed and somewhat simpler slip distribution. The slip and stress distributions from inversion of moment rate functions at four nearby stations for rupture velocity 90% of the local shear wave velocity and smoothing parameter 10 are shown in Figures 4.40a and 4.40b, respectively. The overall dimension of slip model is about 2.5 wavelengths, and the major slip patch is approximately ⅓ wavelength of the MRF data band indicating the slip model is well imaged.

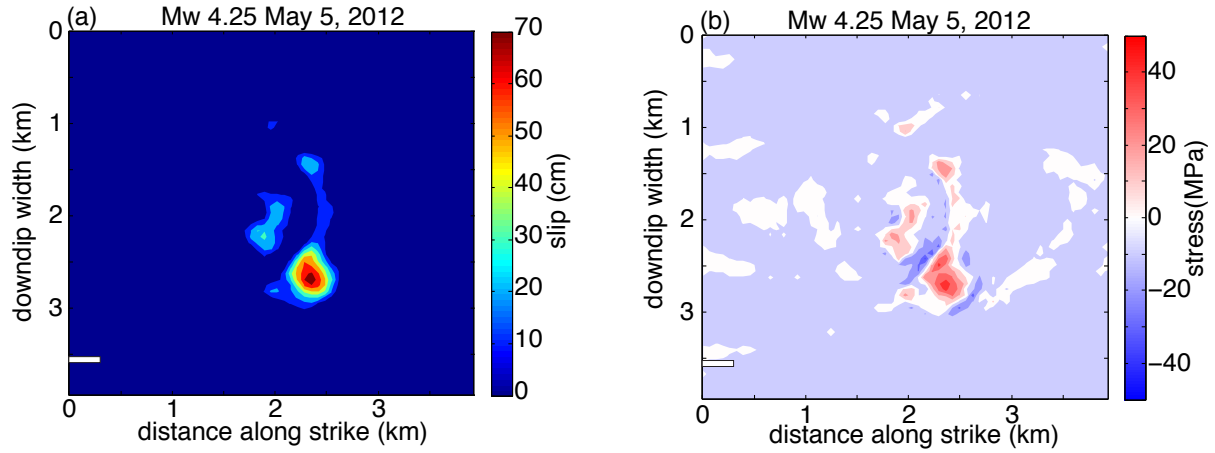

Figure 4.40. Target event 7, M_W 4.25 May 5, 2012 maps of slip distribution (a) and stress change (b) from inversion of moment rate functions at four regional broadband stations with smoothing parameter 10, rise time 0.1 s, strike 143°, dip 87°, rake −167°. A rupture velocity of 90% of the shear wave velocity was assumed. The hypocenter is located at the center of each plot. The peak slip is 76.5 cm and the peak stress drop is 45 MPa. Stress change on the fault surface with red as stress drop and blue as stress increase. The horizontal bar represents the dimension in kilometers of target events 1 and 2, with M_W 1.05 and M_W 1.48, respectively.

4.4.8 Event 8 M_W 4.27 January 4, 2009

Target event 8 is located in the central portion of geothermal field with its deviatoric focal mechanism shaded by hypocentral depth, Figure 4.37. The locations of the target and eGf events are from NCEDC NCSN catalog. The target event occurred January 4, 2009 and the eGf event occurred more than two and a half years later on September 22, 2011, Table 4.15. The target-eGf event separation is 0.88 km in horizontal distance and 1.17 km in depth. The catalog magnitudes differ by 1.34 units.

Table 4.15. Target and empirical Green's function event information from the NCEDC NCSN catalog for event 8 January 4, 2009: moment magnitude (M_W) or local magnitude (Ml), date, time, latitude, longitude, and depth.

Event	M_W /Ml	Date	Time	Latitude	Longitude	Depth (km)
Target	4.27 M_W	2009/01/04	17:27:10.48	38.78233	-122.77250	3.82
eGf	2.93 Ml	2011/09/22	19:34:17.48	38.78933	-122.77734	2.65

Waveform data were downloaded from the NCEDC for broadband stations in the BDSN. Event times and locations as specified in the NCSN catalog were used with data filtered in passband 0.02 to 0.05 Hz to investigate the moment tensor of the target event. Waveform fits and *P*-wave radiation pattern of the deviatoric moment tensor solution are shown in Figure 4.41. The deviatoric moment tensor has a large 77 percent DC component.

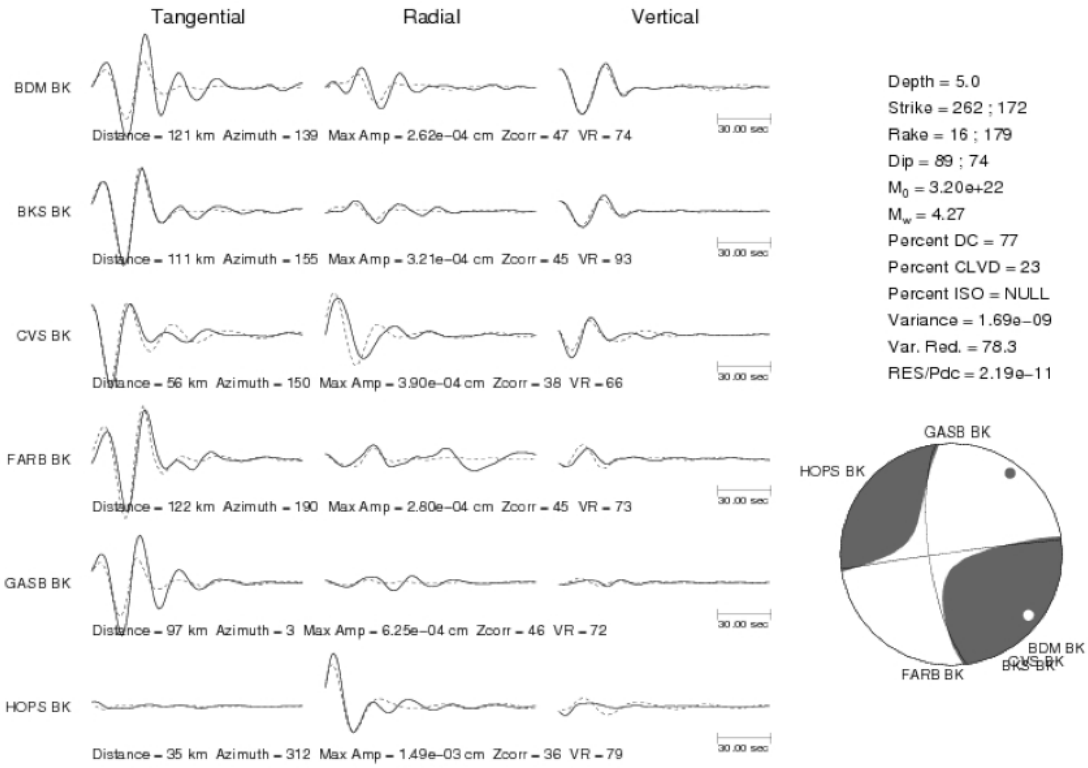

Figure 4.41. Comparison of filtered (0.02 to 0.05 Hz) observed velocity data (solid) and synthetics (dashed) waveform fits and *P*-wave radiation pattern of the deviatoric moment tensor solution for target event 8, M_W 4.27 January 4, 2009.

The eGf waveforms were then deconvolved from the target waveforms at four broadband stations in the regional BDSN to identify those that produced pulse-like moment rate functions (MRF) with the highest signal to noise ratio. The pulse widths of the resulting MRFs range from approximately 0.49 s in the south at station BKS to 0.6 s in the northeast at station MNRC, Figure 4.42. The map (a) shows the location of the strike-slip January 4, 2009 M_W 4.27 event and the four regional broadband stations used to determine source moment rate functions. The observed (black) and predicted (red) moment rate functions are compared in (b).

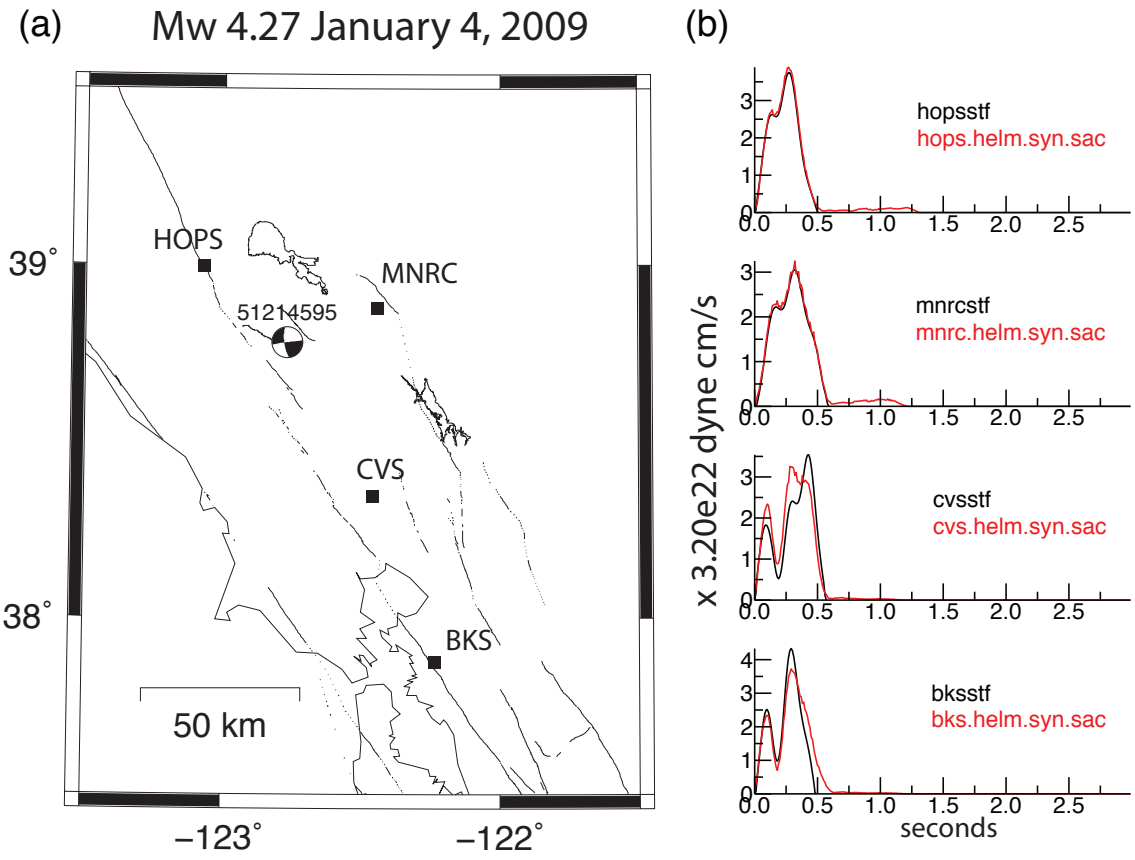

Figure 42. Map showing the location of target event 8, strike-slip M_W 4.27 January 4, 2009, and four regional broadband stations used to determine source moment rate functions. The eGf waveforms were deconvolved from the target waveforms at broadband stations HOPS, MNRC, CVS, and BKS in the regional Berkeley Digital Seismic Network (BDSN) (a) to identify pulse-like moment rate functions with the highest signal to noise ratio. Observed moment rate functions (black) are compared to synthetics (red) (b). The low pass filtered deconvolutions show clear source pulses at the four stations and a very good level of fit is obtained. The amplitudes of the MRFs are proportional to 3.20e22 dyne cm/s.

The finite-source model has fault dimensions 3 km, same number of grid points (61 x 61), with a subfault size of 49.2 m, and a constant rupture velocity of 0.9 times the shear wave speed at a source depth. The slip at each patch on the fault occurs with a rise time of a 0.1 s fixed-width boxcar. The total allowable slip duration is 3 s. The subfault dimension is consistent with the 48 m wavelength for *S* waves with Vs = 2.4 km/s at 3 km depth and 50 Hz bandwidth. The inversion uses a slip positivity constraint and a smoothing constraint to minimize the spatial derivative of the slip. The smoothing weight is investigated by searching for a the smallest value that produces a smoothed model with a fit close to the maximum fit to the data as measured by the variance reduction. The rupture area is determined by the number of subfaults with slip greater than 10% of the maximum slip and varies with smoothing parameter.

The goodness of fit between the observed and synthetic MRFs is comparable for the strike, rake, and dip of both nodal planes yet one nodal plane with strike 172°, dip 74°, and rake 179° is preferred. The slip and stress distributions from inversion of moment rate functions at four nearby stations for rupture velocity 90% of the local shear wave velocity and smoothing parameter 10 are shown in Figures 4.43a and 4.43b, respectively. The overall dimension of slip model is about 2 wavelengths, and the major slip patch is approximately ¼ wavelength of the MRF data band indicating the slip model is well imaged.

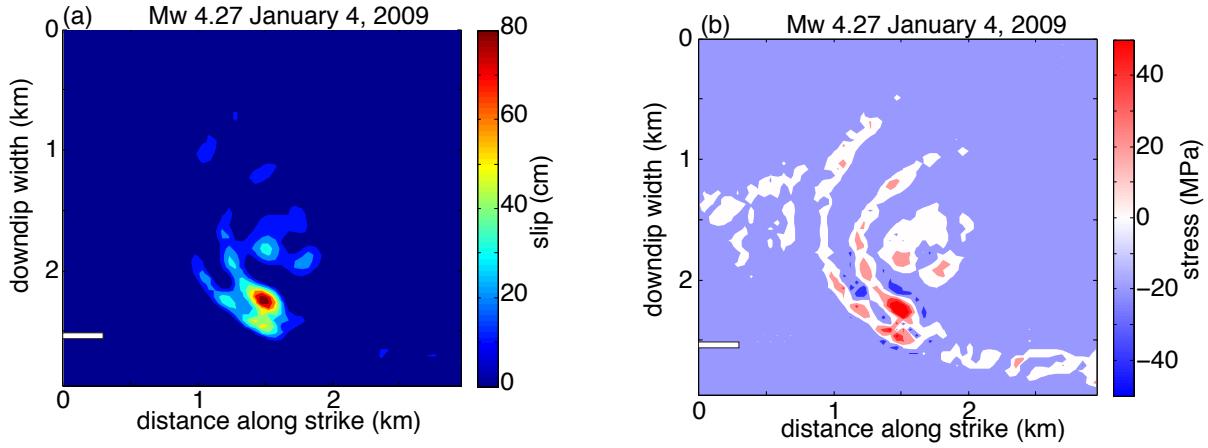

Figure 4.43. Target event 8, M_W 4.27 January 4, 2009 maps of slip distribution (a) and stress change (b) from inversion of moment rate functions at four regional broadband stations with smoothing parameter 10, rise time 0.1 s, strike 172°, dip 74°, rake 179°. A constant rupture velocity of 2.3 km/s was assumed. The hypocenter is located at the center of each plot. The peak slip is 88.3 cm and the peak stress drop is 102 MPa. Stress change on the fault surface with red as stress drop and blue as stress increase. The horizontal bar represents the dimension in kilometers of target events 1 and 2, with M_W 1.05 and M_W 1.48.

4.4.9 Event 9 M_W 4.44 March 14, 2013

Target event 9 is located in the central portion of geothermal field with its deviatoric focal mechanism shaded by hypocentral depth, Figure 4.37. The locations of the target and eGf events are from NCEDC NCSN catalog. The target event occurred March 14, 2013 and the eGf event occurred seven years earlier on February 2, 2006, Table 4.16. The target-eGf event separation is 0.39 km in horizontal distance and 1.09 km in depth. The catalog magnitudes differ by 1.58 units.

Table 4.16. Target and empirical Green's function event information from the NCEDC NCSN catalog for event 9 March 14, 2013: moment magnitude (M_W) or duration magnitude (Md), date, time, latitude, longitude, and depth.

Event	M_W /Md	Date	Time	Latitude	Longitude	Depth (km)
Target	4.44 M_W	2013/03/14	09:09:23.33	38.81233	-122.78616	1.34
eGf	2.86 Md	2006/02/02	19:39:23.52	38.81567	-122.78750	2.43

Waveform data were downloaded from the NCEDC for broadband stations in the BDSN. Event times and locations as specified in the NCSN catalog were used with data filtered in passband 0.02 to 0.05 Hz to investigate the moment tensor of the target event. Waveform fits and *P*-wave radiation pattern of the deviatoric moment tensor solution are shown in Figure 4.44. The deviatoric moment tensor has a large 73 percent DC component.

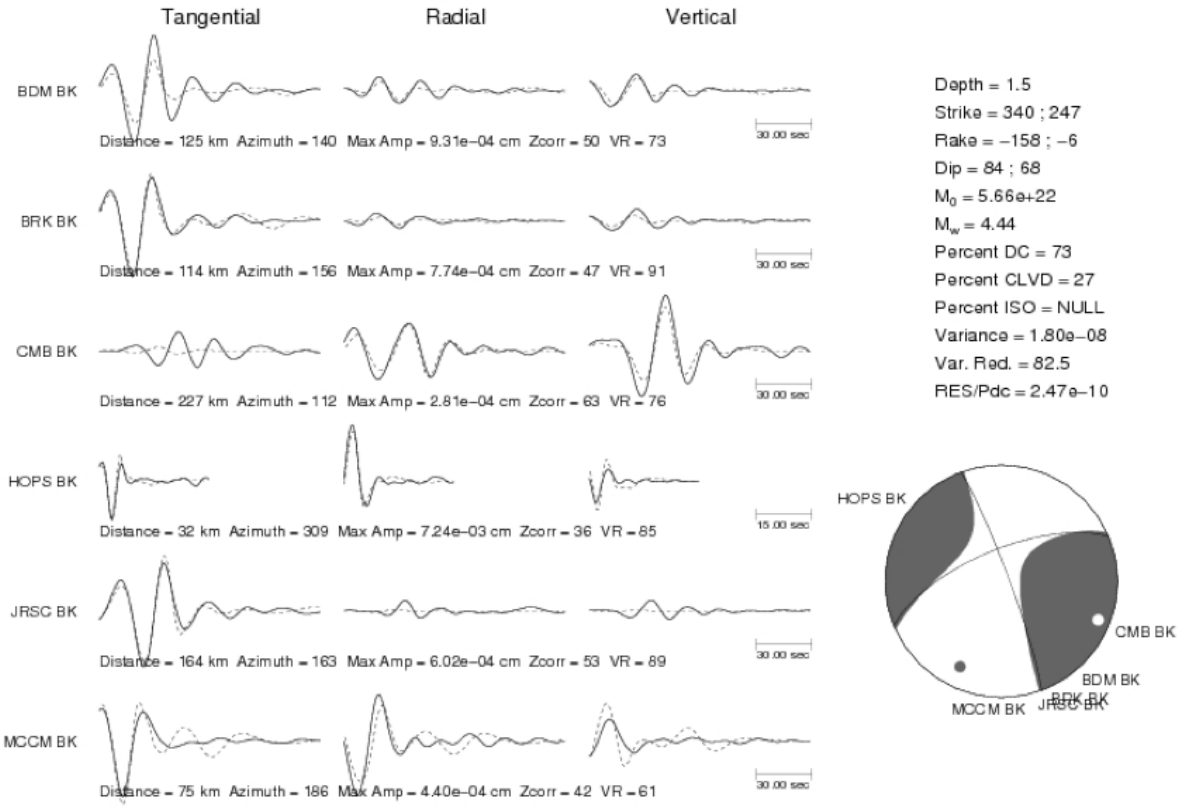

Figure 4.44. Comparison of filtered (0.02 to 0.05 Hz) observed velocity data (solid) and synthetics (dashed) waveform fits and *P*-wave radiation pattern of the deviatoric moment tensor solution for target event 9, Mw 4.44 March 14, 2013.

The eGf waveforms were then deconvolved from the target waveforms at four broadband stations of the BDSN to identify those that produced pulse-like moment rate functions (MRF) with the highest signal to noise ratio. The pulse widths of the resulting MRFs range from approximately 0.3 s in the south at station BKS to 0.7 s in the north at station HOPS suggestive of a north to south rupture, Figure 4.45. The map (a) shows the location of the strike-slip March 14, 2013 M_W 4.44 event and the four regional broadband stations used to determine source moment rate functions. The observed (black) and predicted (red) moment rate functions are compared in (b).

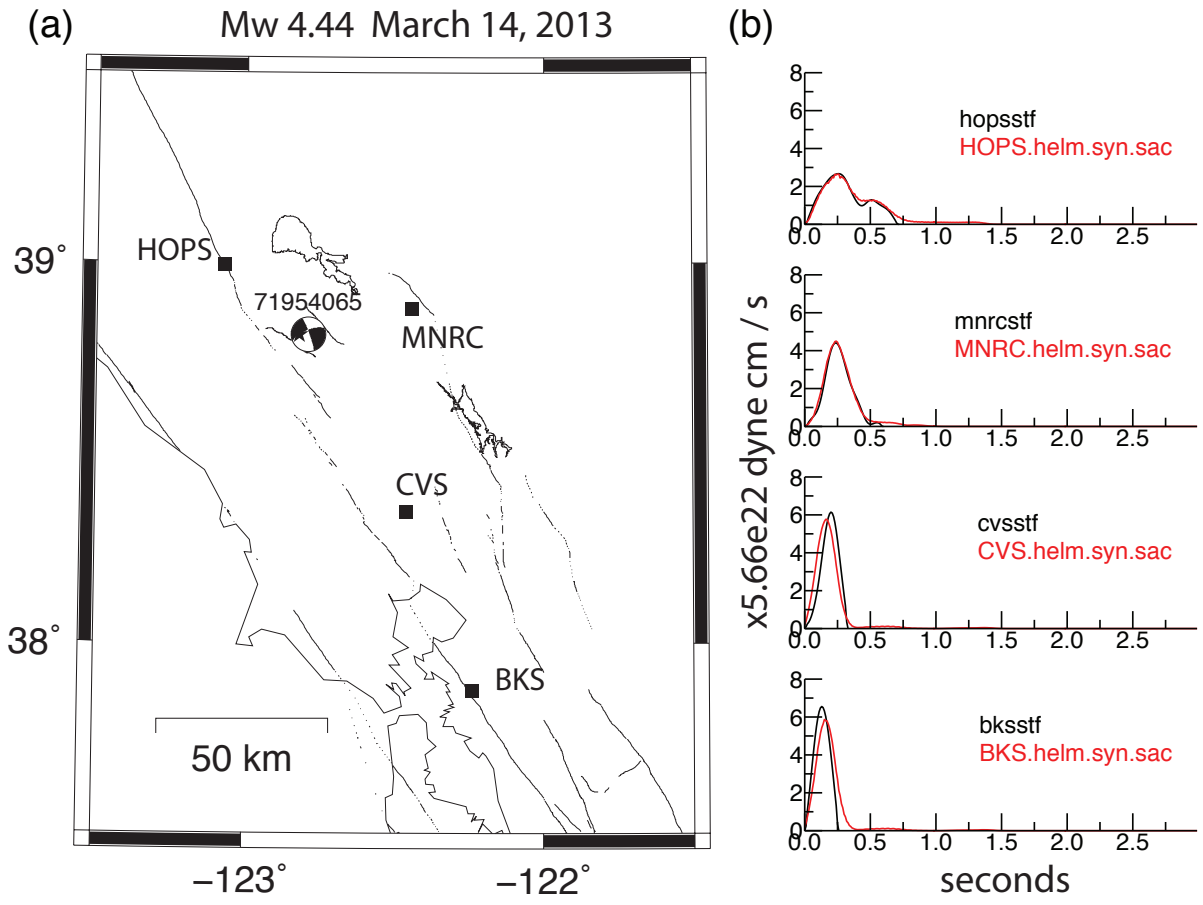

Figure 4.45. Map showing the location of target event 9, strike-slip M_W 4.44 March 14, 2013 and four regional broadband stations used to determine source moment rate functions. The eGf waveforms were deconvolved from the target waveforms at broadband stations HOPS, MNRC, CVS, and BKS in the regional Berkeley Digital Seismic Network (BDSN) (a) to identify pulse-like moment rate functions with the highest signal to noise ratio. Observed moment rate functions (black) are compared to synthetics (red) (b). The low pass filtered deconvolutions show clear source pulses at the four stations and a very good level of fit is obtained. The amplitudes of the MRFs are proportional to 5.66e22 dyne cm/s.

The finite-source model has fault dimension 3 km, same number of grid points (61 x 61), with a subfault size of 49.2 m, and a constant rupture velocity of 0.9 times the shear wave speed at a source depth. The slip at each patch on the fault occurs with a rise time of a 0.1 s fixed-width boxcar. The total allowable slip duration is 3 s. The subfault dimension is consistent with the 48 m wavelength for *S* waves with Vs = 2.4 km/s at 3 km depth and 50 Hz bandwidth. The inversion uses a slip positivity constraint and a smoothing constraint to minimize the spatial derivative of the slip. The smoothing weight is investigated by searching for a the smallest value that produces a smoothed model with a fit close to the maximum fit to the data as measured by the variance reduction. The rupture area is determined by the number of subfaults with slip greater than 10% of the maximum slip and varies with smoothing parameter.

The goodness of fit between the observed and synthetic MRFs is comparable for the strike, rake, and dip of both nodal planes yet one nodal plane with strike 340°, dip 84°, and rake −158° is preferred. The slip and stress distributions from inversion of moment rate functions at four nearby stations for rupture velocity 90% of the local shear wave velocity and smoothing parameter 100 are shown in Figures 4.46a and 4.46b, respectively. The overall dimension of slip model is about 2 wavelengths, and the two major slip patches are approximately ½ wavelength of the MRF data band indicating the slip model is well imaged.

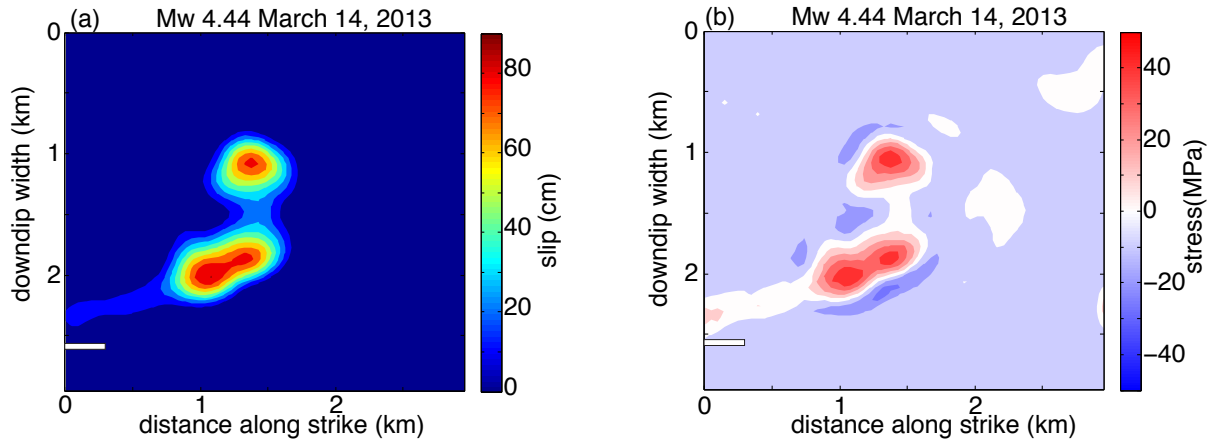

Figure 4.46. Target event 9, M_W 4.44 March 14, 2013, maps of slip distribution (a) and stress change (b) from inversion of moment rate functions at four regional broadband stations with smoothing parameter 100, rise time 0.1 s, strike 340°, dip 84°, rake −158°. A constant rupture velocity of 2.3 km/s was assumed. The hypocenter is located at the center of each plot. The peak slip is 88.3 cm and the peak stress drop is 102 MPa. Stress change on the fault surface with red as stress drop and blue as stress increase. The horizontal bar represents the dimension in kilometers of target events 1 and 2, with M_W 1.05 and M_W 1.48.

4.4.10 Event 10 M_W 4.53 January 12, 2014

Target event 10 is located in the central portion of geothermal field with its deviatoric focal mechanism shaded by hypocentral depth, Figure 4.37. The locations of the target and eGf events are from NCEDC NCSN catalog. The target event occurred January 12, 2014 and the eGf event occurred six months earlier on July 4, 2013, Table 4.17. The target-eGf event separation is 0.22 km in horizontal distance and 0.74 km in depth. The catalog magnitudes differ by 1.31 units.

Table 4.17. Target and empirical Green's function event information from the NCEDC NCSN catalog for event 10 January 12, 2014: moment magnitude (M_W) or local magnitude (Ml), date, time, latitude, longitude, and depth.

Event	M_W /Ml	Date	Time	Latitude	Longitude	Depth (km)
Target	4.53 M_W	2014/01/12	20:24:46.74	38.81350	-122.81617	1.900
eGf	3.22 Ml	2013/07/04	09:39:14.29	38.81183	-122.81483	2.640

Waveform data were downloaded from the NCEDC for broadband stations in the BDSN. Event times and locations as specified in the NCSN catalog were used with data filtered in passband 0.02 to 0.05 Hz to investigate the moment tensor of the target event. Waveform fits and *P*-wave radiation pattern of the deviatoric moment tensor solution are shown in Figure 4.47. The deviatoric moment tensor has a large 62 percent CLVD component

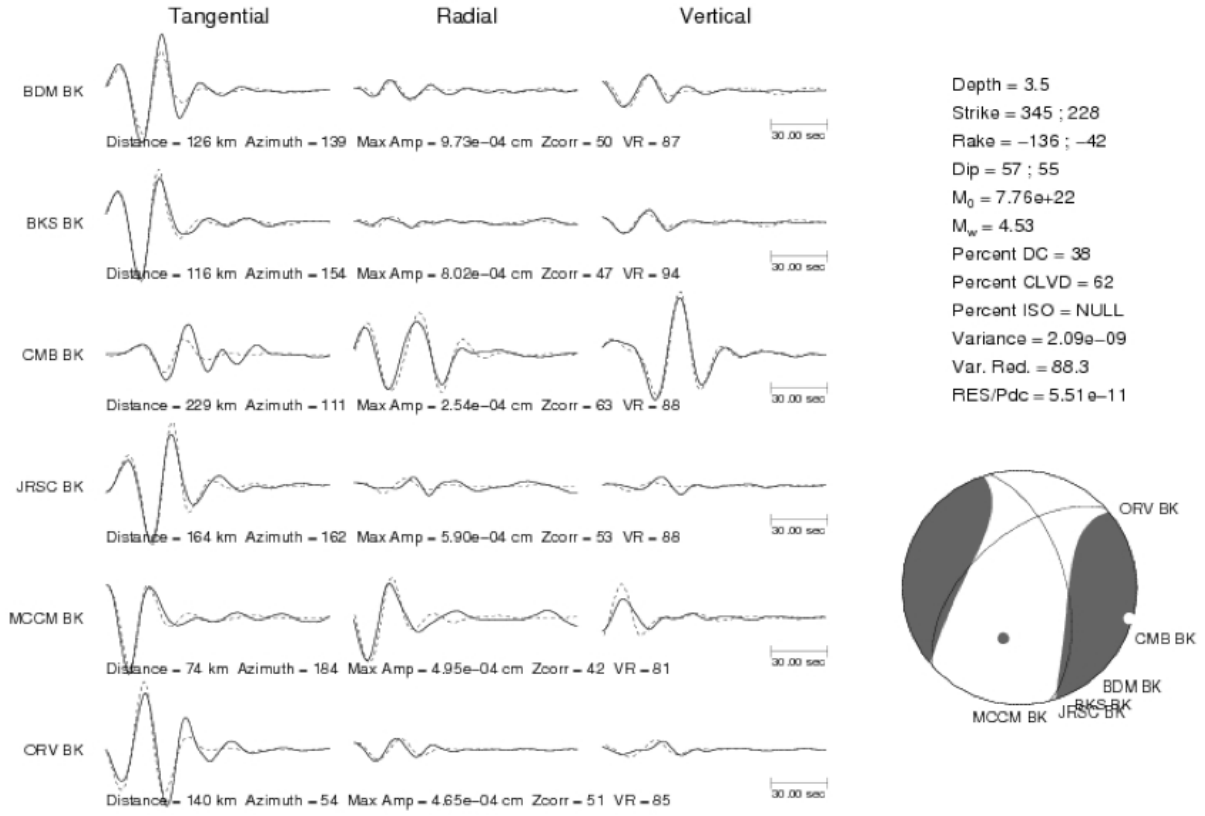

Figure 4.47. Comparison of filtered (0.02 to 0.05 Hz) observed velocity data (solid) and synthetics (dashed) waveform fits and *P*-wave radiation pattern of the deviatoric moment tensor solution for target event 10, M_W 4.53 January 12, 2014.

The eGf waveforms were then deconvolved from the target waveforms at four broadband stations in the regional BDSN to identify those that produced pulse-like moment rate functions (MRF) with the highest signal to noise ratio. The map Figure 4.48a shows the location of the oblique normal M_W 4.53 January 12, 2014 event and the four regional broadband stations used to determine source moment rate functions. The observed (black) and predicted (red) moment rate functions are compared in Figure 4.48b. This event is the noisiest of the four $M_W > 4$ presented here. What is interesting about this example is the relatively long source duration of 1 to 2 seconds, which is considerably longer than expected from standard scaling laws for a M_W 4.5 event. Secondly, the MRF indicate a complex source process with two or three episodes of moment release.

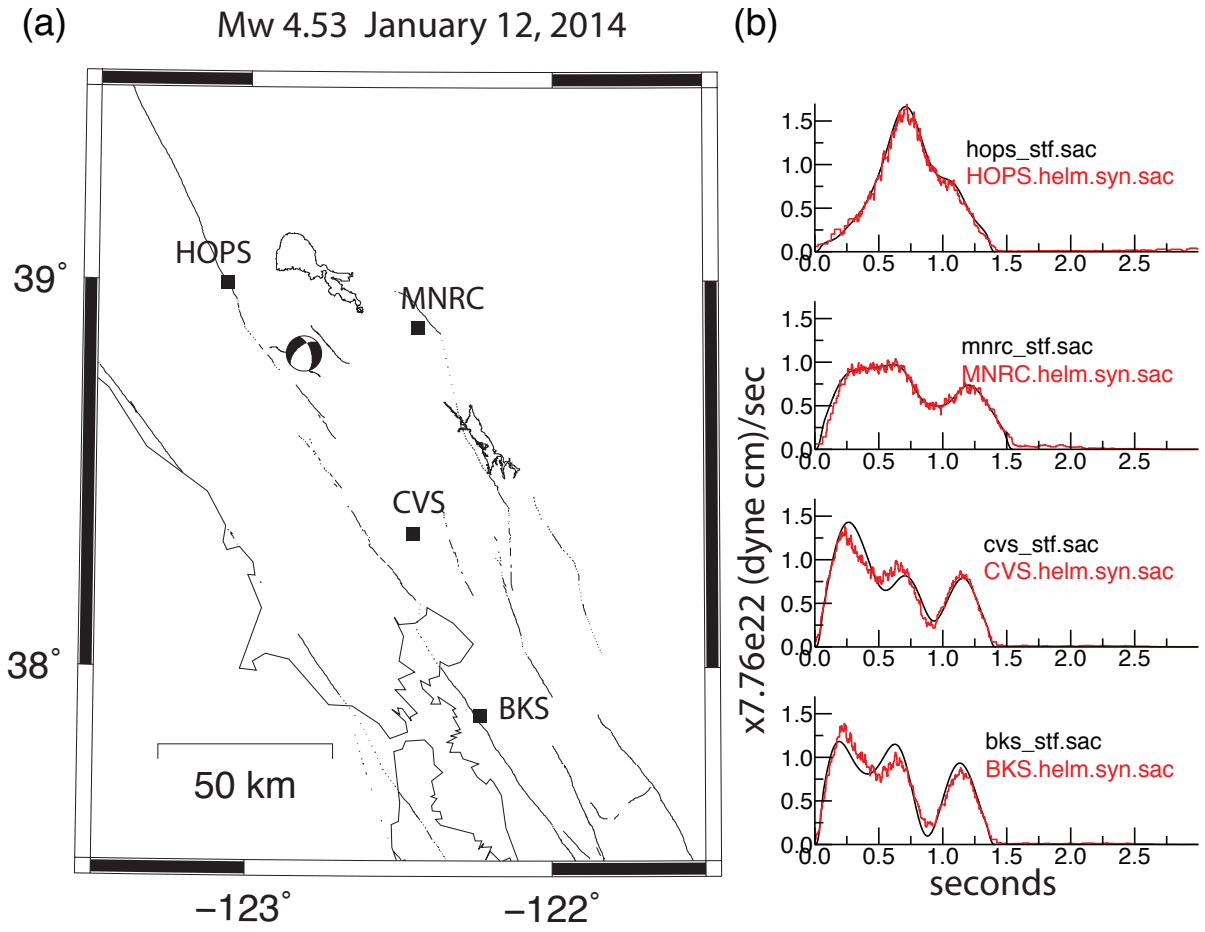

Figure 4.48. Map showing the location target event 10, oblique normal M_W 4.53 January 12, 2014 and the four regional broadband stations used to determine source moment rate functions. The eGf waveforms were deconvolved from the target waveforms at broadband stations HOPS, MNRC, CVS, and BKS in the regional Berkeley Digital Seismic Network

(BDSN) (a) to identify pulse-like moment rate functions with the highest signal to noise ratio. Observed moment rate functions (black) are compared to synthetics (red) (b). The low pass filtered deconvolutions show clear source pulses at the four stations and a very good level of fit is obtained. The amplitudes of the MRFs are proportional to 7.76e22 dyne cm/s.

The finite-source model has the largest fault dimension 7 km, and uses fewer grid points (31 x 31) corresponding to a subfault size of 225.8 m. The model has a constant rupture velocity of 0.9 times the shear wave speed at a source depth. The slip at each patch on the fault occurs with a rise time of a 0.2 s fixed-width boxcar. The total allowable slip duration is 3 s. The subfault dimension in this model is larger than the 55.6 m minimum wavelength for *S* waves with Vs = 2.78 km/s at 3 km depth and 50 Hz bandwidth to allow for the long duration of the MRF and the needed rupture extent of the overall fault model. The inversion uses a slip positivity constraint and a smoothing constraint to minimize the spatial derivative of the slip. The smoothing weight is investigated by searching for a the smallest value that produces a smoothed model with a fit close to the maximum fit to the data as measured by the variance reduction. The rupture area is determined by the number of subfaults with slip greater than 10% of the maximum slip and varies with smoothing parameter.

The goodness of fit between the observed and synthetic MRFs is comparable for the strike, rake, and dip of both nodal planes yet one nodal plane with strike 345°, dip 57°, and rake −136° is preferred. The slip and stress distributions from inversion of moment rate functions at four nearby stations for rupture velocity 90% of the local shear wave velocity and smoothing parameter 10 are shown in Figures 4.49a and 4.49b, respectively. Three primary slip patches are found with a peak slip of 14.2 cm and average of 5.2 cm (a). This level of complexity for a M_W 4.5 event is surprising. The rupture extends over 4 km in dimension with several discrete subevents. The dimensions of the subevents are about ¼ wavelength of the central MRF data band. The stress change is computed using the method of Ripperger and Mai (2004) with an average stress drop of 1.4 MPa. The peak stress change is approximately 6.4 MPa.

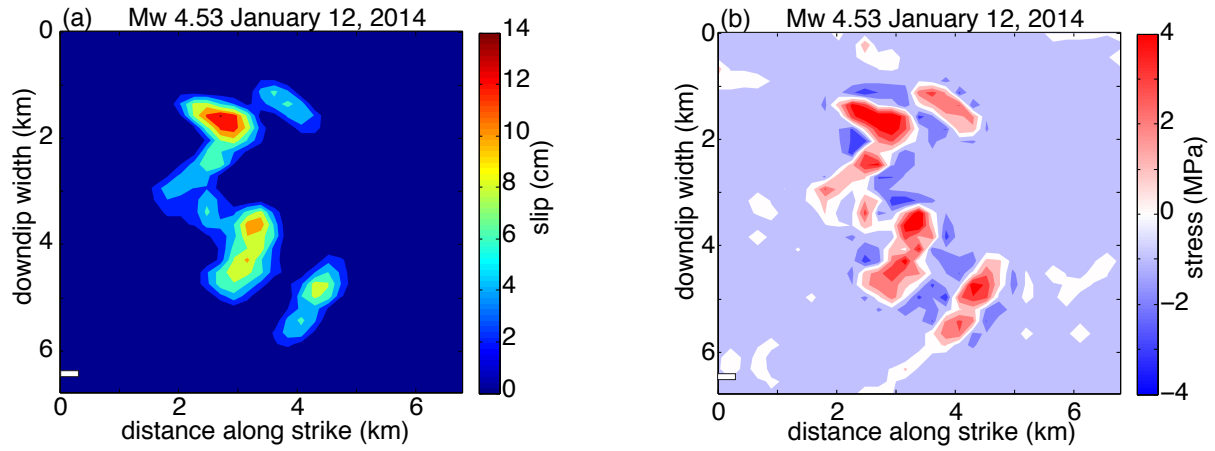

Figure 4.49. Target event 10, M_W 4.53 January 12, 2014 maps of slip distribution (a) and stress change (b) from inversion of moment rate functions at four regional broadband stations with smoothing parameter 10, rise time 0.2 s, strike 345°, dip 57°, rake −136°. A constant

rupture velocity of 2.5 km/s was assumed. The hypocenter is located at the center of each plot. The peak slip is 14.2 cm and the peak stress drop is 6.4 MPa. Stress change on the fault surface with red as stress drop and blue as stress increase. The horizontal bar represents the dimension in kilometers of target events 1 and 2, with M_W 1.05 and M_W 1.48.

The observed and fitted MRF for the January 4, 2009, May 5, 2012 and March 13, 2013 events have much shorter durations compared to the January 12, 2014 event. The May 5 and March 13 events indicate a southward directivity as evidenced by the narrowing of the MRF in that direction. The rupture speed for all events is between 80% to 90% of the local shear wave velocity. A rise time of 0.1 to 0.2 seconds was assumed in all cases. Interestingly for all of the events the best fitting nodal planes are the N-NW striking planes, which are consistent with the large scale faulting in the region, but are conjugate to the micro-fractures in the field.

4.5 Discussion

Finite-source models have been determined for ten earthquakes at The Geysers spanning the magnitude range from M_W 1.05 to 4.53. Kinematic parameters including rupture velocity, rise time, and slip distribution are estimated. The slip distributions were used to calculate the coseismic stress change (Ripperger and Mai, 2004) which is used to estimate the stress drop of the earthquakes. A smoothing constraint was applied to stabilize the inversion and to determine models that optimize fit without overfitting the data with respect to the wavelength of the MRF signal. It was found that the rupture velocity was not particularly well resolved, however values of between 0.8 to 0.9 times the shear velocity were found to fit well, and are consistent with what is typically found in kinematic source inversions. Generally, it was found that the small earthquakes display complexity in rupture, notably with non-uniform slip distributions, sometimes with several slip patches or asperities much like their larger counterparts. The heterogeneous slip distributions lead to heterogeneous stress change models in which the average values of stress drop are in line with the accepted range for earthquakes 0.1 to 10 MPa, with peak stress drops ranging from 0.61 to 101.77 MPa. The values for average stress drop are consistent with what others have found at The Geysers using more traditional spectral methods for estimating stress drop.

An early investigation of source parameters using Brune's (1970, 1971) source model was accomplished by Majer and McEvilly (1979) yielding low ~ 0.1 MPa stress drops using seismic data recorded on a temporary seismic network of thirteen short-period vertical seismographs installed across The Geysers geothermal field in 1976. Stark and Majer (1989) estimated stress drops in the Southeastern Geysers to be generally < 0.65 MPa with a maximum stress drop of 1.38 MPa also using Brune's (1970, 1971) source model and data recorded on a temporary seismic array consisting of ten stations, nine single-component vertical and one three-component, installed in the South Geysers area. Near real-time source and statistical parameters were computed using the Automated Seismic Processor (ASP) described in McEvilly and Majer (1982). More recently Viegas and Hutchings (2011) investigated source parameters in the Northwest Geysers near Prati 9 before and during water

injection between 2005 and 2010 using seismic data recorded with the LBNL seismic array of thirty three-component short period geophones. They fit empirical Green's functions spectral ratios following Abercrombie and Rice (2005). Assuming Madariaga's (1976) dynamic source rupture model to relate the diameter of a circular fault with corner frequency, they find on average stress drops of 11 MPa using Eshelby's (1957) circular static crack solution. They find similarity in rupture process for small induced and nearby tectonic earthquakes having stress drops of ~17 MPa. Martínez-Garzón *et al*. (2014) report variations in average static stress drops during two injection cycles at the Northwest Geysers near injection wells Prati 9 and Prati State 29. Static stress drops were computed using a modified spectral fitting methodology of Kwiatek *et al*. (2011, 2014) to invert for scalar seismic moment, corner frequency and attenuation and the Madariaga (1976) circular source model to calculate the source radius along with Eshelby's formula to calculate average static stress drops ranging from 4 to 200 MPa during Cycle 1 injection, the first substantial injection in the area, with higher values associated with events having normal faulting mechanisms. Average static stress drops ranged from 2 to 10 MPa during Cycle 2 injection. Kwiatek *et al*. (2015) investigate the seven-year spatial temporal evolution of seismic source parameters in the vicinity of Prati 9 and Prati State 29 injection wells located in the Northwest Geysers. Following the methodology described in Kwiatek *et al*. (2011, 2014) to initially estimate seismic source parameters, they obtained over 300 events with refined source characteristics by combining many spectral ratios to constrain the source parameters of a single event. In this approach seismic moments and corner frequencies are computed as an average model from marginal distributions, and those having marginal distributions with a non-Gaussian shape are rejected. The refined corner frequencies were used to find the source radius assuming the circular source model of Madariaga (1976) and static stress drops were computed following Eshelby (1957). Their results suggest constant static stress drop scaling with an average static stress drop of 7 MPa assuming the Madariaga source model. Furthermore Convertito *et al*. (2015) determine seismic source parameters following the approach of Zollo *et al*. (2014) using a combined parametric model with a multi-step non-linear inversion strategy to jointly invert source and attenuation parameters. The results of their analysis show self-similar constant stress drop source parameter scaling suggesting that micro-earthquake ruptures are consistent with the Madariaga (1976) circular shear crack model expanding with a constant rupture velocity. They determine a low value of the median static stress drop to be 1.7 MPa.

With the finite-source models spanning the magnitude range from 1.0 to 4.5 we can investigate the scaling of average slip, rupture area (and dimension). At the outset of the work it was considered that it might be necessary to develop a scaling law specifically for The Geysers due to the induced nature of the seismicity. However, Figure 4.50 shows that the estimated rupture area is consistent with the extrapolation of both the Wells and Coppersmith (1994) and the Leonard (2000) scaling laws. This is remarkable as those relationships were developed for events with M_W larger than 5.5, with the great majority of events in those studies having magnitudes larger than M_W 6.0. Figure 4.50 demonstrates that The Geysers earthquakes follow the self-similar scaling laws determined for the global seismicity catalog, but events may be on average slightly more compact, or higher stress drop as they generally plot below the Wells and Coppersmith (1994) and Leonard (2000) curves. However, The Geysers events are still well within the typical stress drop range from the literature (e.g. Kanamori and Anderson, 1975).

The Geysers events are found to lie within the 2-sigma curves for the Leonard (2000) relationship (gray dashed lines) and the 0.1 and 100 MPa Brune stress drops (black dashed lines). The minimum moment rate function resolution is approximately 0.015 s and may be a reason that the smallest magnitude event M_W 1.05 is slightly outside the 2-sigma range. It is expected that there will be a minimum magnitude below which the pulse widths will not get smaller due to limitations in the bandwidth of the data. The M_W 1.05 event may be at that point.

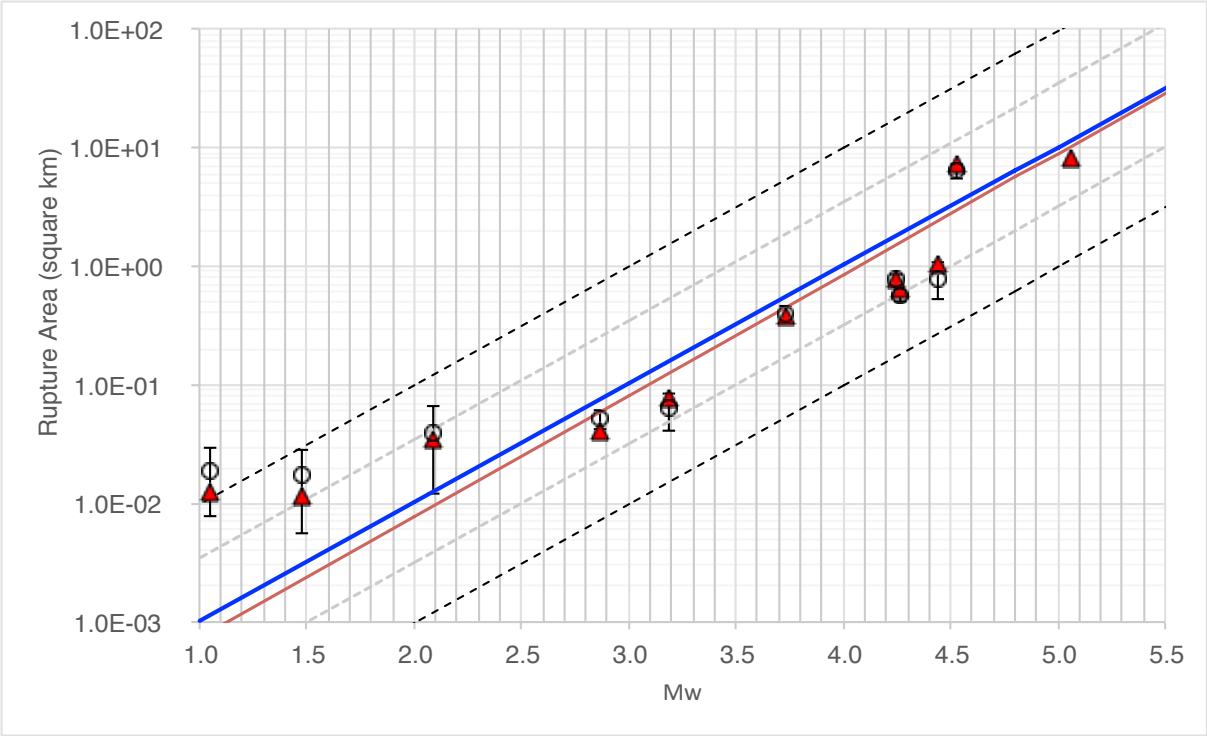

Figure 4.50. The Leonard (2010) (blue) and Wells and Coppersmith (1994) (red) rupture area vs. M_W scaling laws are compared to area estimates for Geysers earthquakes obtained from finite-source inversion. The gray lines show the two-sigma errors for the Leonard (2010) relationship and the black dashed lines represent 0.1 MPa (upper) and 100 MPa (lower) Brune stress drops. The red triangles represent preferred solutions with error estimates (mean rupture area marked with circle and standard deviation with error bars). The result of the finite-source inversion for the December 14, 2016 M_W 5.01 event is shown for comparison but is not included in this investigation.

The average slip of the studied events is also found to follow the Leonard (2000) self-similar scaling law shown in Figure 4.51. For most events the average slip is between the 1-sigma curves for the Leonard (2000) relationship (short dashed gray lines). The 2-sigma curves are shown with dark gray dashed lines.

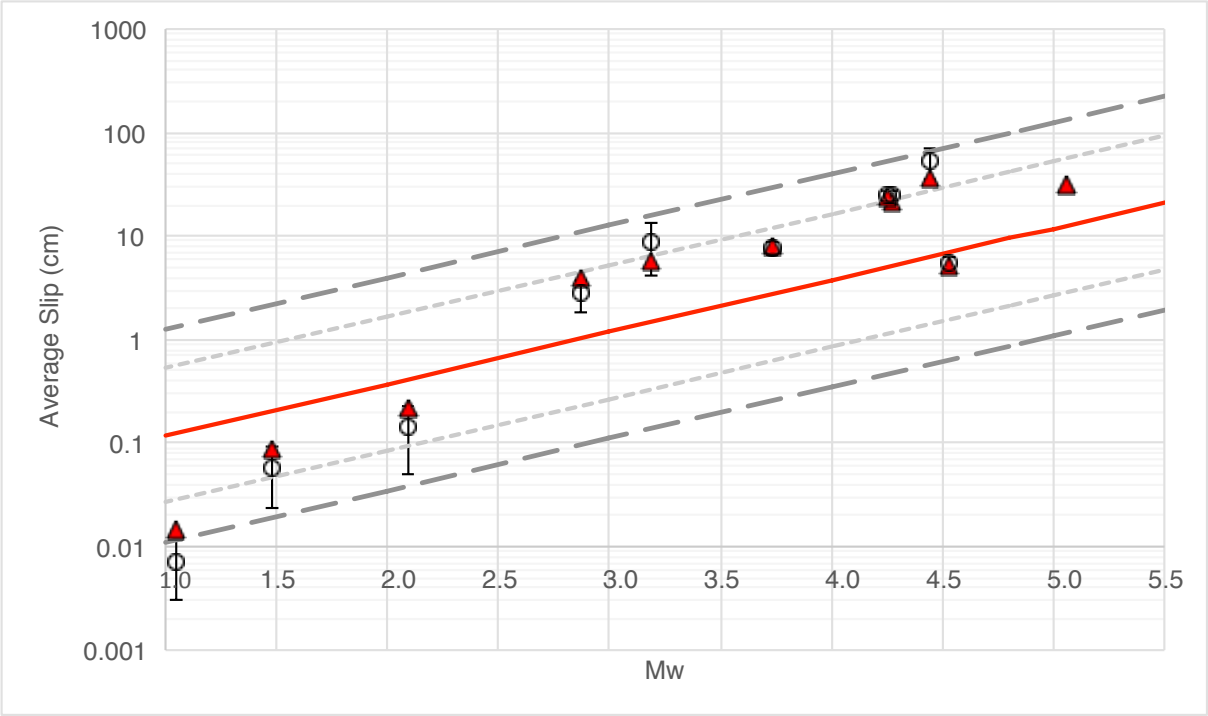

Figure 4.51. The Leonard (2010) (red) average slip vs. M_W scaling law is compared to average slip estimates for Geysers earthquakes obtained from finite-source inversion. The light gray dashed lines show the one-sigma errors for the Leonard (2010) relationship and the dark gray dashed lines show the two-sigma errors. The red triangles represent preferred solutions with error estimates (mean average slip marked with circle and standard deviation with error bars). The result of the finite-source inversion for the December 14, 2016 M_W 5.01 event is shown for comparison but is not included in this investigation.

The results are interesting because while the studied seismicity is a direct result of the injection of fluids into hot rock the induced micro-earthquakes display magnitude-area and magnitude-slip scaling consistent with tectonic earthquakes. The consistency of the finite-source results from this study with extrapolations of the Wells and Coppersmith (1994) and Leonard (2010) scaling laws indicates that there is no break in scaling to $M1$ at the Geysers. It is therefore reasonable to use the published global scaling laws at The Geysers in order to map the source dimensions of the micro-earthquakes induced by the stimulation.

Returning to how the source modeling presented here might be used to evaluate operations of an EGS operation by mapping the activated fracture network, the missing ingredient is the orientation of the individual ruptures. It is not possible to estimate focal parameters for the many thousands of $M < 1$ events that occur during EGS stimulation. An approximate method is proposed where random fault orientations can be selected by sampling a distribution of orientations with a mean oriented optimally with respect to the maximum compressive stress from the *in situ* stress tensor results as presented in Chapter 3. For example, fault orientation can be randomly sampled from a population of orientations

centered at the maximum compressive stress orientation, σ1=N20E, with an uncertainty of 10 degrees (two-sigma) and a dip of 80 degrees with the same uncertainty. Of course this is a significant approximation that would not be valid if there is a preferred fracture system in the rock units and if individual events are occurring on those pre-existing fractures under suboptimal stress conditions. However in the absence of direct sampling of the orientation of fractures at depth, sampling fracture orientation based on estimated stress orientations is a reasonable approach to the problem. With this assumption, it is then possible to take the catalog locations, estimated magnitudes, the rupture area scaling (verified from the finite-source analysis of this Chapter) to arrive at a plausible statistical representation of the seismically active fracture network (Figures 4.52a and 4.52b). The degree of overlap of the events could then be used to assess the fluid pathways in the medium. It must be noted that this method simply maps the seismically active fractures. Other fractures not exhibiting earthquakes, or fractures oriented suboptimally with the stress field exist and could also contribute to the fluid pathway system.

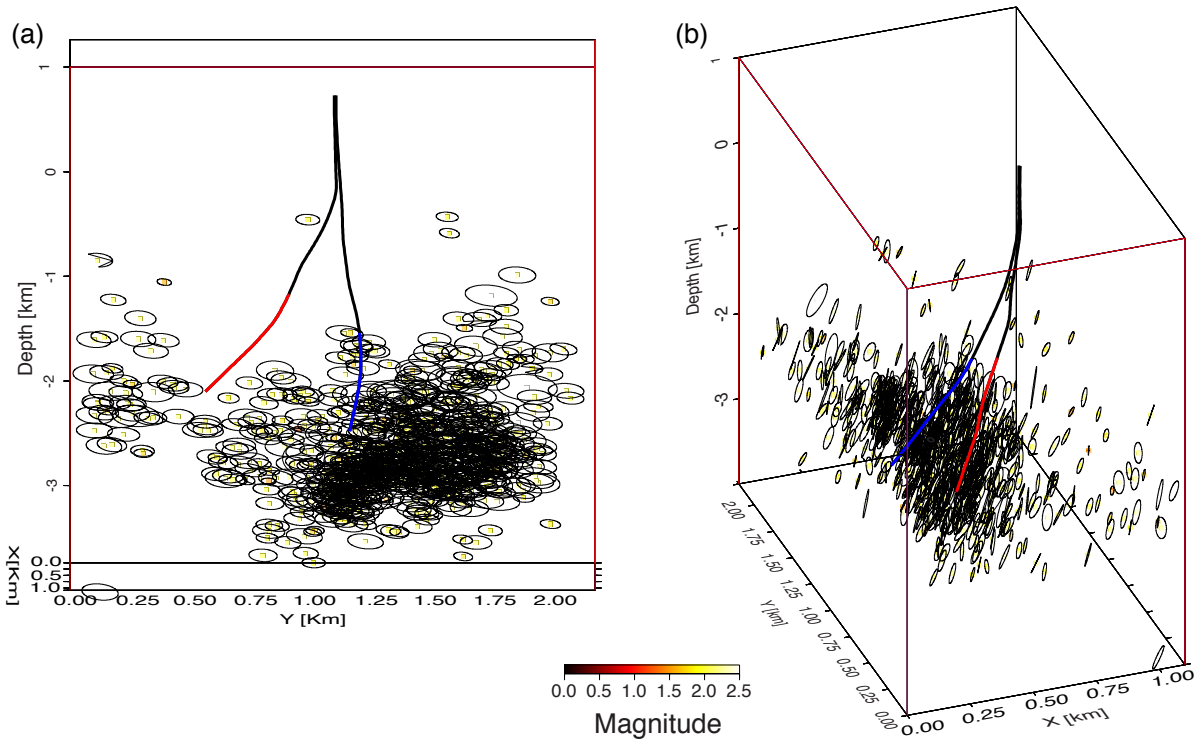

Figure 4.52. Statistical representation of the generated fracture network below production well Prati State 31 (red) and injection well Prati 32 (blue). The circle diameters represent the rupture area determined by the rupture-area scaling relationship while the strike and dip were determined using statistics with a Gaussian distribution based on the results of the stress inversions that indicated a σ1 orientation N20E with an uncertainty of 10 degrees (two-sigma) and a dip of 80 degrees with the same uncertainty. The colored dots at the hypocenters denote moment magnitude. The shape of the circles is deformed to ellipses due to compression of the vertical axis (1:2) and fracture dip. View is from east to west (a) and rotated (b).

4.6 Conclusions

It has been shown that it is possible to obtain seismic waveform-based moment tensor solutions for Geysers events to M_W 0.6, and to estimate kinematic rupture models for micro-earthquakes at The Geysers to approximately M_W 1.0. The empirical Green's function deconvolution method is effective at removing the effects of path, site and common source terms recovering seismic MRF. The MRF functions for the small earthquakes are seen to be as complex as those for larger events displaying evidence of strong directivity (directional narrowing of pulses due to rupture propagation), as well as complexity with multiple pulses of moment release indicating slip complexity. Inverting the MRF for each event for kinematic finite-source models reveals spatially heterogeneous slip that can extend bilaterally, along strike and up or down dip from the earthquake hypocenter that is sometimes comprised of multiple patches of slip during rupture. These are features that are commonly observed in finite-source models for larger earthquakes (e.g. Ye *et al*., 2016). When the rupture area and average slip parameters from the finite-source models are compared with global large-earthquake catalog scaling relationships, it is observed that The Geysers events agree well with extrapolations of those relationships to low magnitude. Thus Geysers seismicity displays self-similar scaling characteristics consistent with extrapolations of commonly used global scaling laws (Wells and Coppersmith, 1994; Leonard, 2010).

On average the finite-source models show average static stress drop ranging between 0.13 to 14.55 MPa over a magnitude range from $1.05 < M_W < 4.53$. Events with $M_W < 2.1$ have average static stress drop < 1MPa. Events with $M_W < 4$ occurred within the Prati 32 EGS study area in the Northwest Geysers during injection operations. The average static stress drops for the four $M_W > 4$ events are 14.5, 11.4, 11.7 and 1.4 MPa for the January 04, 2009, May 05, 2012, March 14, 2013 and January 12, 2014 events, respectively. These larger magnitude events are located outside the Prati 32 EGS study area to the southeast. The low static stress drop of the January 12, 2014 event compared to the other larger magnitude events is intriguing with its complex slip distribution extending over 7 km, an extremely large area for a M_W 4.5 event. This event may have occurred in the vicinity of several injection wells. These results indicate that there is strong variability in the stress drop of events at The Geysers and that stress drop can be quite high on average. The stress change models indicate there can be small localized regions in which the stress drop can be very high, approaching 50-100 MPa indicating that there are regions that have locally high strength, possibly resulting from fracture of intact rock. Error estimates derived for $M > 4$ events using various groups of stations and several different rupture velocities and subfault sizes have consistent fits. Other studies of Geysers seismicity show stress drops < 200 MPa with low average static stress drops < 2 MPa determined from both the early investigations (Majer and McEvilly 1979; Stark and Majer, 1989) using Brune's (1970, 1971) source model and the recent investigation by Convertito *et al*. (2015) using the Madariaga (1976) source model. The highest average static stress drops are reported by Martínez-Garzón *et al*. (2014) for events having normal faulting mechanisms during Prati 9 injection from 2008 to 2009 in the Northwest Geysers. Average static stress drops decreased during the second cycle of injection at Prati 9 from 2010 to 2011 and are comparable to values of stress drop reported by Viegas and Hutchings (2011) and Kwiatek *et al*. (2015) who also investigated stress drop of events

associated with Prati 9 injection over a longer time periods of five and seven years, respectively.

Owing to the difficulty of directly sampling of the orientation of fractures within the geothermal field, and the limited scope that direct borehole measurements provide, using seismicity to map the fracture network is a simpler alternative that may provide better spatial characterization of the fractures. However, the difficulty of precisely determining the focal mechanisms and rupture characteristics of many thousands of micro-earthquakes, most of which are below *M* 1.0, precludes a deterministic approach. Rather it has been demonstrated here that seismic moment tensor analysis may be used to estimate the *in situ* state of stress and in fact monitor its evolution during stimulation activities. The stress tensors may then be used to constrain the distribution of likely induced earthquake orientations. Together with the mapping of the rupture dimensions from finite-source inversion rupture area and slip scaling results enables the development of inferred fracture network maps. While these are themselves approximate it is possible to use them to assess the density and interconnectivity of fractures that were seismically activated through the fluid injection process.

Future work should focus on the further development of methods for estimation of seismic moment tensor solutions for micro-earthquakes so that more of the activated seismic cloud may be characterized. Work is also needed to refine methods for the estimation of finite-source models of micro-earthquakes, and to develop stimulation specific rupture area scaling laws for the induced earthquakes. The four $M_W > 4$ earthquake slip models display vertical distributions in slip as well as some horizontal directivity. While the station geometry is good with stations in the strike and anti-strike directions as well as perpendicular, it would be worthwhile in future work to try to include more local stations and those from temporary broadband networks to try to better constrain the vertical distribution of slip as well as the preferred nodal plane. It is also possible that by using a waveform eGf inversion instead of the MRF inversion presented here, better constraints on the spatial distribution of slip may be obtained. Nevertheless the overall dimensions, average slip and stress change are well constrained. As shown in Dreger *et al*. (2007) peak values of slip and stress also tend to be well constrained.

4.7 Acknowledgments

Seismic data from the Berkeley Digital Seismic Network (BDSN), Lawrence Berkeley National Laboratory (LBNL), and the Northern California Seismic Network (NCSN) provided by the Northern California Earthquake Data Center (NCEDC), Berkeley Seismological Laboratory, University of California, Berkeley, and U.S. Geological Survey, Menlo Park. This research is supported by the Department of Energy Geothermal Technologies Program, Award Number DE-EE0002756. We thank Taka'aki Taira for providing a list of target and eGf events, Peggy Hellweg, Shan Dou, Mong-Han Huang, Andrea Chiang, Avinash Nayak, Katie Wooddell, and Qingkai Kong for their helpful discussions. Seismic data from the Berkeley Digital Seismic Network (BDSN) and the Northern California Seismic Network (NCSN) provided by the Northern California Earthquake Data Center (NCEDC), Berkeley

Seismological Laboratory, University of California, Berkeley, and U.S. Geological Survey, Menlo Park. Event relocations provided by Felix Waldhauser's Real Time Double Difference Catalog.

References

Abercrombie, R.E. (1995). Earthquake source scaling relationships from -1 to 5 M_L using seismograms recorded at 2.5-km depth, *J. Geophys. Res*., **100**, 24,015–24,036, doi:10.1029/95JB02397.

Abercrombie, R.E., and J.R. Rice (2005). Can observations of earthquake scaling constrain slip weakening?, *Geophys. J. Int*., **162**, 406-424, doi:10.1111/j.1365-246X.2005.02579.x.

Abercrombie, R.E. (2014). Stress drops of repeating earthquakes on the San Andreas Fault at Parkfield, *Geophys. Res. Lett*., **41**, 8784-8791, doi:10.1002/2014GL06207.

Allis, R., and G.M. Shook (1999). An alternative mechanism for the formation of The Geysers vapor-dominated reservoir, *Proceedings of the 24th Workshop on Geothermal Reservoir Engineering*, Stanford, California, SGP-TR-162.

Altmann, J.B., B.I.R. Müller, T.M. Müller, O. Heidbach, M.R.P. Tingay, and A. Weißhardt (2014). Pore pressure stress coupling in 3D and consequences for reservoir stress states and fault reactivation, *Geothermics*, **52**, 195-205.

Antolik, M., D. Dreger, and B. Romanowicz (1996). Finite fault source study of the great 1994 deep Bolivia earthquake, *Geophys. Res. Lett*., **23,** 1589-1592, doi:10.1029/96GL00968.

Antolik, M., D. Dreger, and B. Romanowicz (1999). Rupture processes of large deep-focus earthquakes from inversion of moment rate functions, *J. Geophys. Res*., **104**, 863–894, doi:10.1029/1998JB900042.

Ashby, M.F., and C.G. Sammis (1990). The Damage Mechanics of Brittle Solids in Compression, *Pure Appl. Geophys.* **133,** 489-521.

Baig, A., and T. Urbancic (2010). Microseismic moment tensors: A path to understanding frac growth, *The Leading Edge* **29** 320-324.

Bakun, W.H., and C.G. Bufe (1975). Shear-wave attenuation along the San Andreas fault zone in central California, *Bull. Seism. Soc. Am.,* **65**, 439-1459.

Barton, D.J., G.R. Foulger, J.R. Henderson, and B.R. Julian (1999). Frequency-magnitude statistics and spatial correlation dimensions of earthquakes at Long Valley caldera, California, *Geophys. J. Int.* **138** 563-570.

Beall, J.J., M.C. Wright, A.S. Pingol, and P. Atkinson (2010). Effect of High Rate Injection on Seismicity in The Geysers, *Trans. Geoth. Resour. Counc.* **34** 1205-1208.

Beall, J.J., and M. Wright, (2010). Southern extent of The Geysers high temperature reservoir based on seismic and geochemical evidence, *Trans. Geoth. Resour. Counc.,* **34**, 1199-1202.

Ben-Zion, Y., and J.-P. Ampuero (2009). Seismic radiation from regions sustaining material damage, *Geophys. J. Int.* **178** 1351-1356.

Bock, D.E., P.F. Velleman, and R.D. De Veaux (2010). *Stats Modeling the World*, 3rd ed., Pearson Education, Inc., Addison-Wesley.

Bowers, D., and J.A. Hudson (1999). Defining the scalar moment of a seismic source with a general moment tensor, *Bull. Seism. Soc. Am.* **89** 1390-1394.

Boyd, O.S., D.S. Dreger, V.H. Lai, and R. Gritto (2015). A systematic analysis of seismic moment tensor at The Geysers geothermal field, California, *Bull. Seism. Soc. Am*., **105,** 2969-2986, doi:10.1785/0120140285.

Boyd, O.S., D.S. Dreger, R. Gritto, and J. Garcia (2018). Analysis of seismic moment tensors and *in situ* stress during Enhanced Geothermal System development at The Geysers geothermal field, California, *Geophys. J. Int*., **215**, 1483-1500, doi:10.1093/gji/ggy326.

Boyd, O.S., D.S. Dreger, T.Taira, and R. Gritto (2017). Magnitude and rupture area scaling relationships of seismicity at The Northwest Geysers EGS Demonstration Project, Annual Meeting of the American Geophysical Union, New Orleans, LA, 11-15 Dec., S34B-02.

Boyle, K., and M. Zoback (2014). The stress state of the Northwest Geysers, California Geothermal Field, and implications for fault-controlled fluid flow, *Bull. Seism. Soc. Am*., **104,** 2303-2312, doi:10.1785/012013084.

Brune, J.N. (1970). Tectonic stress and the seismic shear waves from earthquakes, *J. Geophys. Res*., **75**, 4997–5009, doi:10.1029/JB075i026p04997.

Brune, J.N. (1971). Correction (to Brune (1970)), *J. Geophys. Res*, **76**, 5002.

Bufe, C.G., S.M. Marks, F.W. Lester, R.S. Ludwin, and M.C. Stickney (1981). Seismicity of the Geysers-Clear Lake Region in *Research in The Geysers-Clear Lake Geothermal Area, Northern California* Robert J. McLaughlin and Julie M. Donnelly-Nolan (Editors) Geological Survey Professional Paper 1141, United States Government Printing Office, Washington, D. C., 129-137.

Byerlee, J.D. (1978). Friction of rock, *Pure Appl. Geophys*., **116**, 615–626.

Chiang, A., D.S. Dreger, S.R. Ford, and W.R. Walter (2014). Source Characterization of Underground Explosions from Combined Regional Moment Tensor and First-Motion Analysis, *Bull. Seism. Soc. Am*. **104** 1587-1600, doi:10.1785/0120130228.

Choy, G.L., and J.L. Boatwright (1995). Global patterns of radiated seismic energy and apparent stress, *J. Geophys. Res*., **100**, 18,205–18,228.

Cladouhos, T., S. Petty, B. Larson, J. Iovenitti, B. Livesay, and R. Baria (2009). Toward More Efficient Heat Mining: A Planned Enhanced Geothermal System Demonstration Project, *Trans. Geoth. Resour. Counc.* **33** 165-170.

Clayton, R.W., and R.A. Wiggins (1976). Source shape estimation and deconvolution of teleseismic bodywaves, *Geophys. J. R. Astron. Soc.,* **47**, 151-177, doi:10.1111/j.1365-246X.1976.tb01267.x.

Convertito, V., A. Zollo, N. Shama, A. Orefice, and A. Emolo (2015). Earthquake source parameters and scaling relationships at The Geysers geothermal field, California, *Proceedings of AGIS Workshop on Inducced Seismicity*, 10-30 March 2015, Davos Schatzalp, Swiss Seismolog. Serv., Switzerland.

Cuenot, N., J. Charlety, L. Dorbath, and H. Haessler (2006). Faulting mechanisms and stress regime at the European HDR site of Soultz-sous-Forets, France, *Geothermics* **35** 561-575.

Deichmann, N., and D. Giardini (2009). Earthquakes induced by the stimulation of and enhanced geothermal system below Basel (Switzerland), *Seismol. Res. Lett*. **80** 784-798.

Donnelly-Nolan, J.M., M.G. Burns, F.E. Goff, E.K. Peters, and J.M. Thompson, (1993). The Geysers-Clear Lake area, California; thermal waters, mineralization, volcanism, and geothermal potential, *Economic Geology,* **88**, 301-316.

Dreger, D.S., H. Tkalčić, and M. Johnston (2000). Dilational Processes Accompanying Earthquakes in the Long Valley Caldera, *Science* **288** 122-125.

Dreger, D.S. (2003). TDMT_INV: Time Domain Seismic Moment Tensor INVersion, in *International Handbook of Earthquake and Engineering Seismology*, Vol. 81B, p. 1627, ed. Lee, W. H. K., Kanamori, H., Jennings, P. C. & Kisslinger C., Academic Press.

Dreger, D., R.M. Nadeau, and A. Chung (2007). Repeating earthquake finite source models: Strong asperities revealed on the San Andreas Fault, *Geophys. Res. Lett*., **34**, L23302, doi:10.1029/2007GL031353.

Dreger, D.S. (1997). The large aftershocks of the Northridge earthquake and their relationship to mainshock slip and fault-zone complexity, *Bull. Seism. Soc. Am.,* **87**, 1259-1266.

Dreger, D.S. (1994). Empirical Green's function study of the January 17, 1994 Northridge, California earthquake, *Geophys. Res. Lett*., **21**, 2633-2636, doi:10.1029/94GL02661.

Dreger, D.S., O.S. Boyd, and R. Gritto (2018a). Seismic analysis of spatio-temporal fracture generation at The Geysers EGS Demonstration Project, Proceedings, 42nd Workshop on Geothermal Reservoir Engineering, Stanford University, Stanford, California, February 12-14, 2018.

Dreger, D.S., O.S. Boyd, T. Taira, and R. Gritto (2018b). Stress drop and scaling of earthquakes at the Geysers Geothermal Field, *Seismol. Res. Lett*., **89**, 911.

Dufumier, H., and L. Rivera (1997). On the resolution of the isotropic component in moment tensor inversion, *Geophys. J. Int*. **131** 595-606.

Dziewonski, A.M., and J.H. Woodhouse (1983). An Experiment in Systematic Study of Global Seismicity – Centroid – Moment Tensor Solutions for 201 Moderate and Large Earthquakes of 1981, *J. Geophys. Res*. **88** 3247-3271.

Eberhart-Phillips, D., and D.H. Oppenheimer (1984). Induced seismicity in The Geysers geothermal area, California, *J. Geophys. Res*. **89** 1191-1207.

Enedy, S., K. Enedy, and J. Maney (1991). Reservoir response to injection in the Southeast Geysers, *Proc. Sixteenth Workshop on Geothermal Reservoir Engineering*, Stanford University, SGP-TR-134.

Eshelby, J.D. (1957). The determination of the elastic field of an ellipsoidal inclusion and related problems, *Proc. R. Soc. Lond*., A, **241**, 376-396.

Fichtner, A., and H. Tkalčić (2010). Insights into the kinematics of a volcanic caldera drop: Probabilistic finite-source inversion of the 1996 Bardarbunga, Iceland, earthquake, *Earth Planet. Sci. Lett*. **297** 607-615.

Ford, S.R., W.R. Walter, and D.S. Dreger (2012). Event discrimination using regional moment tensors with teleseismic-P constraints, *Bull. Seism. Soc. Am*. **102** 867-872.

Ford, S.R., D.S. Dreger, and W.R. Walter (2010). Network sensitivity solutions for regional moment tensor inversions, *Bull. Seism. Soc. Am*. **100** 1962-1970.

Ford, S.R., D.S. Dreger, and W.R. Walter (2009). Identifying isotropic events using a regional moment tensor inversion, *J. Geophys. Res*. **114**, no. B01306, doi:10.1029/2008JB005743.

Ford, S., D. Dreger, and W. Walter (2008). Source Characterization of the August 6, 2007 Crandall Canyon Mine Seismic Event in Central Utah, *Seismol. Res. Lett*. **79** 637-644.

Garcia, J., M. Walters, J. Beall, C. Hartline, A. Pingol, S. Pistone, and M. Wright (2012). Overview of the Northwest Geysers Demonstration Project, *Proceedings of the 37th Workshop on Geothermal Reservoir Engineering*, Stanford, California, SGP-TR-194.

Garcia, J., C. Hartline, M. Walters, M. Wright, J. Rutqvist, P.F. Dobson, and P. Jeanne (2016). The Northwest Geysers EGS Demonstration Project, California Part 1: Characterization and reservoir response to injection, *Geothermics*, **63**, 97-119.

Gee, L., D. Neuhauser, D. Dreger, R. Uhrhammer, M. Pasyanos, and B. Romanowicz (2003). The Rapid Earthquake Data Integration Project in *International Handbook of Earthquake and Engineering Seismology*, William H. K. Lee, Hiroo Kanamori, Paul C. Jennings, and Carl Kisslinger (Editors), Volume 81B, Academic Press, 1261-1273.

Gephart, J.W., and D.W. Forsyth (1984). An improved method for determining the regional stress tensor using earthquake focal mechanism data: Application to the San Fernando earthquake sequence, *J. Geophys. Res*., **89**, 9305-9320.

Godano, M., T. Bardainne, M. Regnier, and A. Deschamps (2011). Moment-tensor determination by nonlinear inversion of amplitudes, *Bull. Seism. Soc. Am*. **101** 366-378.

Goldstein, P., D. Dodge, M. Firpo, and L. Minner (2003). SAC2000: Signal Processing and Analysis Tools for Seismologists and Engineers in *International Handbook of Earthquake and Engineering Seismology*, William H. K. Lee, Hiroo Kanamori, Paul C. Jennings, and Carl Kisslinger (Editors), Volume 81B, Academic Press, 1613-1614.

Greensfelder, R.W. (1993). New Evidence of the causative relationship between well injection and microseismicity in The Geysers Geothermal Field, *Trans. Geoth. Resour. Counc*. **17** 243-247.

Gritto, R., S.H. Yoo, and S. Jarpe (2013). Three-dimensional seismic tomography at The Geysers geothermal field, CA, USA. 38th Workshop on Geothermal Reservoir Engineering, February 11–13, SGP-TR-198, Stanford University, Stanford, CA, pp. 1–12.

Gritto, R., D. Dreger, O. Heidbach, and L. Hutchings (2014). Towards the Understanding of Induced Seismicity in Enhanced Geothermal Systems, DOE Final Report, Performance Period January 29, 2010 through May 31, 2014, Award No. DE-EE0002756.

Gritto, R., D.S. Dreger, and O.S. Boyd (2018). Seismic analysis of spatio-temporal fracture generation during EGS resource development, *DOE GTP Final Report*, Performance Period October 1, 2014 – June 30, 2018.

Guilhem, A., L. Hutchings, D.S. Dreger, and L.R. Johnson (2014). Moment tensor inversions of M ~ 3 earthquakes in the Geysers geothermal fields, California, *J. Geophys. Res*. **119** 2121-2137, doi: 10.1002/2013JB010271.

Hamiel, Y., V. Lyakhovsky, and A. Agnon (2004). Coupled evolution of damage and porosity in poroelastic media: theory and applications to deformation of porous rocks, *Geophys. J. Int*. **156** 701-713.

Hamilton, R.M., and L.J.P. Muffler (1972). Microearthquakes at The Geysers geothermal Area, California, *J. Geophys. Res*. **77** 2081-2086.

Hardebeck, J.L., and E. Hauksson (2001). Crustal stress field in southern California and its implications for fault mechanics, *J. Geophys. Res*., **106**, 21859-21882.

Hardebeck, J.L., and A.J. Michael (2006). Damped regional-scale stress inversions: Methodology and examples for southern California and the Coalinga aftershock sequence, *J. Geophys. Res*., **111**, doi:10.1029/2005JB004144.

Hardebeck, J.L., and P.M. Shearer (2002). A new method for determining first-motion focal mechanisms, *Bull. Seism. Soc. Am*. **92** 2264-2276.

Hartline, C.S., M.A. Walters, and M.C. Wright (2015). Three-dimensional structural model building, induced seismicity analysis, drilling analysis, reservoir management at The Geysers geothermal field, northern California, *Trans. Geoth. Resour. Counc.,* **39**, 603-614.

Hartline, C.S. (2012). Seismic Monitoring Advisory Committee Review, May 14, 2012, www.geysers.com/media/SMAC_14May2012.pdf.

Hartzell, S.H. (1978). Earthquake aftershocks as Green's functions, *Geophys. Res. Lett*., **5**, 1-4.

Hartzell, S.H., and T.H. Heaton (1983). Inversion of strong ground motion and telseismic waveform data for the fault rupture history of the 1979 Imperial Valley, California, earthquake, *Bull. Seism. Soc. Am*., **73**, no. 6, 1553-1583.

Hearn, B.C., R.J. McLaughlin, and J.M. Donnelly-Nolan (1988). Tectonic framework of the Clear Lake basin, California, *GSA Special Papers,* doi: 10.1130/SPE214-p9, pp. 9-20.

Heidbach, O., M. Tingay, A. Barth, J. Reinecker, D. Kurfeß, and B. Müller (2010). Global crustal stress pattern based on the World Stress Map database release 2008, *Tectonophys.* **482**, 3-15, doi.org/10.1016/j.tecto.2009.07.023.

Herrmann, R.B. (2013). Computer programs in seismology: An evolving tool for instruction and research, *Seism. Res. Lett*., **84**, 1081-1088, doi:10.1785/022011096.

Horalek, J., Z. Jechumtalova, L. Dorbath, and J. Sileny (2010). Source mechanisms of micro-earthquakes induced in a fluid injection experiment at the HDR site Soultz-sous-Forets (Alsace) in 2003 and their temporal and spatial variations, *Geophys. J. Int*. **181** 1547-1565.

Hough, S.E., and L. Seeber (1991). Seismological constraints on source properties of the m_b = 4.0 Ardsley, New York earthquake: a characteristic rupture? *J. Geophys. Res*., **96**, 18,183–18,195, doi:10.1029/91JB1795.

Hough S.E., and D.S. Dreger (1995). Source parameters of the 23 April 1992 *M* 6.1 Joshua Tree, California, earthquake and its aftershocks: Empirical Green's function analysis of GEOS and TERRAscope data, *Bull. Seism. Soc. Am*., **85**, 1576-1590.

Hutchings, L., and F. Wu (1990). Empirical Green's funcions from small earthquakes: A waveform study of locally recorded aftershocks of the 1971 San Fernando earthquake, *J. Geophys. Res*., **95**, 1187–1214.

Hudson, J.A., R.G. Pearce, and R.M. Rogers (1989). Source type plot for inversion of the moment tensor, *J. Geophys. Res*. **94** 765-774.

Ide, S. (2001). Complex source processes and the interaction of moderate earthquakes during the earthquake swarm in the Hida-Mountains, Japan, 1998, *Tectonophysics*, 334, 35-54.

Ide, S., and G. Beroza (2001). Does apparent stress vary with earthquake size?, *Geophys. Res. Lett*., **28**, 3349-3352.

Ide. S., A. Baltay, and G.C. Beroza (2011). Shallow dynamic overshoot and energetic deep rupture in the 2011 M_W 9.0 Tohoku-Oki Earthquake, *Science*, 332, 1426-1429, doi:10.1126/science.1207020.

Jeanne, P., J. Rutqvist, P. Dobson, M. Walters, C. Hartline, and J. Garcia (2014). The impacts of mechanical stress transfers caused by hydromechanical and thermal processes on fault stability during hydraulic stimulation in a deep geothermal reservoir, *Int. J. Rock Mech. Min. Sci*., **72**, 149-163, doi:10.1016/j.ijrmms.2014.09.005.

Jeanne, P., J. Rutqvist, P.F. Dobson, J. Garcia, M. Walters, C. Hartline, and A. Borgia (2015). Geomechanical simulation of the stress tensor rotation caused by injection of cold water in a deep geothermal reservoir, *J. Geophys. Res*., **120**, doi:10.1002/2015JB012424.

Johnson, L.R., and C.G. Sammis (2001). Effects of Rock Damage on Seismic Waves Generated by Explosions, *Pure Appl. Geophys*. **158** 1869-1908.

Johnson, L.R. (2014a). Source Mechanisms of Induced Earthquakes at The Geysers Geothermal Reservoir, *Pure Appl. Geophys*., doi 10.1007/s00024-014-0795-x.

Johnson, L.R. (2014b). A Source Model for Induced Earthquakes at The Geysers Geothermal Reservoir, *Pure Appl. Geophys*., doi 10.1007/s00024-014-0798-7.

Julian, B.R., A.D. Miller, and G.R. Foulger (1993). Non-shear focal mechanisms of earthquakes at The Geysers, California, and Hengill, Iceland, Geothermal Areas, *Trans. Geoth. Resour. Counc*. **17** 123-128.

Julian, B.R., A. Ross, G.R. Foulger, and J.R. Evans (1996). Three-dimensional seismic image of a geothermal reservoir: The Geysers, California, *Geophys. Res. Lett*., **23**, 685-688.

Kanamori, H., and D.L. Anderson (1975). Theoretical basis of some empirical relations in seismology, *Bull. Seism. Soc. Am*., **65**, 1073-1095.

Kaverina, A., D. Dreger, and M. Antolik (1998). Source process of the 21 April, 1997 Santa Cruz Island earthquake (M_W 7.8), *Geophys. Res. Lett.*, **25**, 4027-4030, doi:10.1029/1998GL900017.

King, G.C.P., R.S. Stein, and J. Lin (1994). Static Stress Changes and the Triggering of Earthquakes, *Bull. Seism. Soc. Am*. **84** 935-953.

Kirkpatrick, A., J.E. Peterson, E.L. Majer, and R. Nadeau (1999). Characteristics of microseismicity in the DV11 injection area, southeast Geysers, California, *Proc. Twenty-Fourth Workshop on Geothermal Reservoir Engineering*, Stanford University, SGP-TR-162.

Kirkpatrick, A., J.E. Peterson, and E.L. Majer (1996). Source mechanisms of microearthquakes at the southeast Geysers Geothermal Field, California, *Proc. Twenty-First Workshop on Geothermal Reservoir Engineering,* Stanford University, SGP-T151, 359-366.

Kirkpatrick, A., A. Romero, J. Peterson, L. Johnson, and E. Majer (1996). Microearthquake source mechanism studies at The Geysers geothermal field, Lawrence Berkeley Laboratory Report LBL-38600, 1-13.

Knopoff, L., and M.J. Randall (1970). The compensated linear vector dipole: A possible mechanism for deep earthquakes, *J. Geophys. Res*. **75** 4957-4963.

Kwiatek, G., P. Martínez-Garzón, G. Dresen, M. Bohnhoff, H. Sone, and C. Hartline (2015). Effects of long-term fluid injection on induced seismicity parameters and maximum magnitude in northwestern part of The Geysers geothermal field, *J. Geophys. Res.,* **120,** 7085-7101, doi:10.1002/2015JB012362.

Kwiatek, G., P. Martínez-Garzón, and M. Bohnhoff (2016). HybridMT: A MATLAB/Shell environment package for seismic moment tensor inversion and refinement, *Seismol. Res. Lett.*, doi:10.1785/0220150251.

Kwiatek. G., K. Plenkers, and G. Dresen (2011). Source parameters of picoseismicity recorded at Mponeng deep gold mine, South Africa: Implications for scaling relations, *Bull. Seism. Soc. Am*., **101**, 2592-2608, doi:10.1785/0120110094.

Kwiatek, G., F. Bulut, M. Bohnhoff, and G. Dresen (2014). High-resolution analysis of

seismicity induced at Berlín geothermal field, El Salvador, *Geothermics*, **52**, 98-111, doi:10.1016/j.geothermics.2013.09.008.

Lange, A.L., and W.H. Westphal (1969). Microearthquakes near the Geysers, Sonoma County, California, *J. Geophys. Res*. **74** 4377-4378.

Lawson, C.L., and R.J. Hanson (1974). *Solving Least Squares Problems*, Prentice-Hall, Englewood Cliffs, New Jersey.

Leonard, M. (2010). Earthquake fault scaling: Self-consistent relating of rupture length, width, average displacement, and moment release, *Bull. Seism. Soc. Am*., **100**, no. 5A, 1971-1988, doi:10.1785/0120090189.

Leptokaropoulos, K., M. Staszek, S. Lasocki, P. Martínez-Garzón, and G. Kwiatek, (2018). Evolution of seismicity in relation to fluid injection in the North-Western part of The Geysers geothermal field, *Geophys. J. Int*., **212**, 1157-1166, doi:10.1093/gji/ggx481.

Lockner, D.A., R. Summers, D. Moore, and J.D. Byerlee (1982). Laboratory measurements of reservoir rock from the Geysers Geothermal Field, California, *Int. J. Rock Mech. Min. Sci. & Geomech. Abst*., **19**, 65-80.

Lutz, S.J., M. Walters, S. Pistone, and J.N. Moore (2012). New insights into the high-temperature reservoir, Northwest Geysers, *Trans. Geoth. Resour. Counc.,* **36**, 907-916.

Lyakhovsky, V., Y. Ben-Zion, and A. Agnon (1997). Distributed damage, faulting, and friction, *J. Geophys. Res*. **102** 27635-27649.

Madariaga, R. (1976). Dynamics of am expanding circular crack, *Bull. Seism. Soc. Am*., **66**, 639-666.

Majer, E.L., and T.V. McEvilly (1979). Seismological investigations at the Geysers Geothermal Field, *Geophysics* **44** 246-269, doi:10.1190/1.1440965.

Majer, E.L. and J.E. Peterson (2005). Application of microearthquake monitoring for evaluating and managing the effects of fluid injection at naturally fractured EGS sites, *Trans. Geoth. Resour. Counc*. **29** 103-107.

Majer, E.L., R. Baria, M. Stark, S. Oates, J. Bommer, and H. Asanuma (2007). Induced seismicity associated with Enhanced Geothermal Systems, *Geothermics* **36** 185-222.

Majer, E.L., and J.E. Peterson (2007). The impact of injection on seismicity at The Geysers, California Geothermal Field, *Int. J. Rock Mech. Min. Sci*., **44**, 1079-1090, doi:10.1016/j.ijrmms.2007.07.023.

Majer, E.L., R. Baria, M. Stark, S. Oates, J. Bommer, B. Smith, and H. Asanuma (2007). Induced seismicity associated with Enhanced Geothermal Systems, *Geothermics,* **36**, 185-222.

Martínez-Garzón, P., M. Bohnhoff, G. Kwiatek, and G. Dresen (2013). Stress tensor changes related to fluid injection at The Geysers geothermal field, California, *Geophys. Res. Lett*., **40**, 2596-2601, doi:10.1002/grl.50438.

Martínez-Garzón, P., G. Kwiatek, H. Sone, M. Bohnhoff, G. Dresen, and C. Hartline (2014). Spatiotemporal changes, faulting regimes, and source parameters of induced seismicity: A case study from The Geysers geothermal field, *J. Geophys. Res.,* **119**, 8378-8396, doi:10.1002/2014JB011385.

Martínez-Garzón, P., V. Vavryčuk, G. Kwiatek, and M. Bohnhoff (2016). Sensitivity of stress inversion of focal mechanisms to pore pressure changes, *Geophys. Res. Lett*., **43**, 8441–8450.

Martínez-Garzón, P., G. Kwiatek, M. Bohnhoff, and G. Dresen (2017). Volumetric components in the earthquake source related to fluid injection and stress state, *Geophys. Res. Lett*., **44**, 800-809, doi:10.1002/2016GL071963.

Mayeda, K., L. Malagnini, and W.R. Walter (2007). A new spectral ratio method using narrow band envelopes: Evidence for non-self-similarity in the Hector Mine sequence, *Geophys. Res. Lett.*, **34**, L11303, doi:10.1029/2007GL030041.

McEvilly, T.V., and E.L. Majer (1982). ASP: An automated seismic processor for micro-earthquake networks, *Bull. Seism. Soc. Am.,* **72**, 303-325.

McLaughlin, R.J. (1981). Tectonic Setting of Pre-Tertiary Rocks and Its Relation to Geothermal Resources in The Geysers-Clear Lake Area in *Research in The Geysers-Clear Lake Geothermal Area, Northern California*, Robert J. McLaughlin and Julie M. Donnelly-Nolan (Editors), Geological Survey Professional Paper 1141, United States Government Printing Office, Washington, D. C., 3-23.

Mendoza, C., and S.H. Hartzell (1988). Aftershock patterns and main shock faulting, *Bull. Seism. Soc. Am.,* **78**, 1438-1449.

Michael, A. (1984). Determination of stress from slip data: faults and folds, *J. Geophys. Res.,* **89**, 11,517-11,526.

Michael, A. (1987). Use of focal mechanisms to determine stress: A control study, *J. Geophys. Res*., **92**, 357-368.

Minson, S., and D. Dreger (2008). Stable Inversions for Complete Moment Tensors, *Geophys. J. Int*. **174** 585-592.

Minson, S., D. Dreger, R. Bürgmann, H. Kanamori, and K. Larsen (2007). Seismically and Geodetically Determined Non-Double-Couple Source Mechanisms From the 2000 Miyakejima Volcanic Earthquake Swarm, *J. Geophys. Res*. **112**, B10308, doi:10.1029/2006JB004847.

Moore, J.N., and R.P. Gunderson (1995). Fluid-inclusion and oxygen-isotopic systematics of an evolving magmatic-hydrothermal system, *Geochim. Cosmochim*. *Acta* **59** 3887-3907.

Mori, J. (1993). Fault plane determinations for three small earthquakes along the San Jacinto Fault, California: Search for cross faults, *J. Geophys. Res*., **98**, 17,711–17,722.

Mori, J., and S. Hartzell (1990). Source inversion of the 1988 Upland earthquake: determination of a fault plane for a small event, *Bull. Seism. Soc. Am.,* **80**, 507-518.

Mossop, A.P. (2001). *Seismicity, subsidence and strain at The Geysers geothermal field*, PhD thesis, Stanford University, Palo Alto, California.

Mueller, C.S. (1985). Source pulse enhancement by deconvolution of an empirical Green's function, *Geophys. Res. Lett.*, **12**, 33-36, doi:10.1029/GL012i001p00033.

Nayak, A., and D.S. Dreger (2014). Moment Tensor Inversion of Seismic Events Associated with the Sinkhole at Napoleonville Salt Done, Louisiana, *Bull. Seism. Soc. Am*. **104** 1763-1776, doi: 10.1785/0120130260.

Nayak, A., and D.S. Dreger (2015). Source-type-specific inversion of moment tensors, *Bull. Seism. Soc. Am*., **105**, 2987-3000, doi: 10.1785/0120140334.

NCEDC (2014). Northern California Earthquake Data Center, UC Berkeley Seismological Laboratory. Dataset, doi:10.7932/NCEDC.

Nielson, D., M. Walters, and J. Hulen (1991). Fracturing in the Northwest Geysers, Sonoma County, California, *Trans. Geoth. Resour. Counc.*, **15**, 27-33.

Nettles, M., and G. Ekstrom (1998). Faulting mechanism of anomalous earthquakes near Bardarbunga Volcano, Iceland, *J. Geophys. Res*. **103** 17973-17983.

O'Connell, D.R.H., and L.R. Johnson (1988). Second-order moment tensors of microearthquakes at The Geysers Geothermal Field, California, *Bull. Seism. Soc. Am*. **78** 1674-1692.

O'Connell, D.R.H., and L.R Johnson,. 1991. Progressive inversion for hypocenters and P wave and S wave velocity structure: Application to the Geysers, California, geothermal field, *J. Geophys. Res*., **96**, 6223–6236.

Okada, Y. (1992). Internal deformation due to shear and tensile faults in a half-space, *Bull. Seism. Soc. Am.,* **82**, 1018-1040.

Oppenheimer, D.H. (1986). Extensional tectonics at The Geysers Geothermal Area, California, *J. Geophys. Res*. **91** 11463-11476.

Pasyanos, M.E., D.S. Dreger, and B. Romanowicz (1996). Toward real-time estimation of regional moment tensors, *Bull. Seism. Soc. Am*. **86** 1255-1269.

Peppin W.A., and C.G. Bufe (1980). Induced versus natural earthquakes: search for a seismic discriminant, *Bull. Seism. Soc. Am*. **70** 269-281.

Reasenberg, P.A., and D. Oppenheimer (1985). FPFIT, FPPLOT, and FPPAGE: Fortran computer programs for calculating and displaying earthquake fault-plane solutions, U. S. Geol. Surv. Open-File Rep. 85-739.

Ripperger J., and P.M. Mai (2004). Fast computation of static stress changes on 2D faults from final slip distributions, *Geophys. Res. Lett.*, **31**, L18610, doi:10.1029/2004GL020594.

Romanowicz, B., D. Dreger, M. Pasyanos, and R. Urhammer (1993). Monitoring of Strain Release in Central and Northern California Using Broadband Data, *Geophys. Res. Lett*. **20** 1643-1646.

Ross, A., G.R. Foulger, and B.R. Julian (1996). Non-double-couple earthquake mechanisms at The Geysers geothermal area, California, *Geophys. Res. Lett*. **23** 877-880.

Ross, A., G.R. Foulger, and B.R. Julian (1999). Source processes of industrially-induced earthquakes at The Geysers geothermal area, California, *Geophysics* **64** 1877-1889.

Ruhl, C.J., R.E. Abercrombie, and K.D. Smith (2017). Spatiotemporal variation of stress drop during the 2008 Mogul, Nevada, earthquake swarm, *J. Geophys. Res*., **122**, 8163-8180, doi:10.1002/2017JB014601.

Rutqvist, J., P.F. Dobson, J. Garcia, C. Hartline, P. Jeanne, C.M. Oldenburg, D.W. Vasco, and M. Walters (2013). The Northwest Geysers EGS Demonstration Project, California: Pre-stimulation modeling and interpretation of the stimulation, *Math Geosci*., **47**, 3-29, doi:10.1007/s11004-013-9493-y.

Saikia, C.K. (1994). Modified frequency-wavenumber algorithm for regional seismograms using Filon's quadrature: modeling of Lg waves in eastern North America, *Geophys. J. Int*. **118** 142-158.

Sato, T., and T. Hirasawa (1973). Body wave spectra from propagating shear cracks, *J. Phys. Earth*, **21**, 415-431.

Schoenball, M., T.M. Müller, B.I.R. Müller, and O. Heidbach (2010). Fluid-induced microseismicity in pre-stressed rock masses, *Geophys. J. Int*., **180**, 813-819.

Scott, D.S., and H. Kanamori (1985). On the consistency of moment tensor source mechanisms with first-motion data, *Phys. Earth Planet. Int*. **37** 97-107.

Shearer, P.M., G.A. Prieto, and E. Hauksson (2006). Comprehensive analysis of earthquake source spectra in southern California, *J. Geophys. Res*., **111**, B06303, doi:10.1002/2005JB003979.

Shimizu, H., S. Ueki, and J. Koyama (1987). A tensile-shear crack model for the mechanism of volcanic earthquakes, *Tectonophysics* **144** 287-300.

Stark, M. (2003). Seismic Evidence for a Long-Lived Enhanced Geothermal System (EGS) in the Northern Geysers Reservoir, *Trans. Geoth. Resour. Counc.* **27** 727-731.

Stark, M.A. (1990). Imaging injected water in The Geysers reservoir using microearthquake data, *Trans. Geoth. Resour. Counc*. **14** 1697-1704.

Stark, C.L., and E.L. Majer (1989). Seismicity of the Southeastern Geysers, Lawrence Berkeley Laboratory Report LBL-26679, 1-109.

Stidham, C., M. Antolik, D. Dreger, S. Larsen, and B. Romanowicz (1999). Three-Dimensional Structure Influences on the Strong Motion Wavefield of the 1989 Loma Prieta Earthquake, *Bull. Seism. Soc. Am*., **89**, 1184-1202.

Templeton, D.C., and D.S. Dreger (2006). Non-double-couple earthquakes in the Long Valley volcanic region, *Bull. Seism. Soc. Am*. **96** 69-79.

Tkalčić, H., D.S. Dreger, G.R. Foulger, and B.R. Julian (2009). The puzzle of the 1996 Bardarbunga, Iceland, Earthquake: No volumetric component in the source mechanism, *Bull. Seism. Soc. Am*. **99** 3077-3085, doi:10.1785/0120080361.

Thurber, C.H. (1983). Earthquake locations and three-dimensional crustal structure in the Coyote Lake area, central California, *J. Geophys. Res*., **88**, 8226–8236.

Uchide, T. and S. Ide (2010). Scaling of earthquake rupture growth in the Parkfield area: Self-similar growth and suppression by the finite seismogenic layer, *J. Geophys. Res*., **115**, B11302, doi:10.1029/2009JB007122.

Vavryčuk, V. (2001). Inversion for parameters of tensile earthquakes, *J. Geophys. Res*. **106** 16339-16355.

Vavryčuk, V. (2011). Tensile earthquakes: theory, modeling, and inversion, *J. Geophys. Res*. **116**, no. B12, doi 10.1029/2011JB008770.

Vavryčuk, V. (2014). Iterative joint inversion for stress and fault orientations from focal mechanisms, *Geophys. J. Int*., **199**, 69-77, doi: 10.1093/gji/ggu224.

Viegas, G., R.E. Abercrombie, and W.-Y. Kim (2010). The 2002 M5 Au Sable Forks, NY, earthquake sequence: Source scaling relationships and energy budget, *J. Geophys. Res*., **115**, B07310, doi:10.1029/2009JB006799.

Viegas, G., and L. Hutchings (2011). Characterization of induced seismicity near an injection well at the Northwest Geysers geothermal field, California, *Trans. Geotherm. Resour. Counc*., **35,** 1773-1780.

Waldhauser, F., and D.P. Schaff (2008). Large-scale relocation of two decades of Northern California seismicity using cross-correlation and double-difference methods, *J. Geophys. Res*., **113**, B08311, doi:10.1029/2007JB005479.

Walters, M.A., J.N. Sternfeld, J.R. Haizlip, A.F. Drenick, and J. Combs (1992). A vapor-dominated high-temperature reservoir at The Geysers California, in Monograph on The Geysers Geothermal Field, Special Report No. 17, 77–87, ed. C. Stone, Geothermal Resources Council.

Walters, M., and J. Beall (2002). Influence of meteoric water flushing on noncondensible gas and whole-rock isotope distributions in the Northwest Geysers, *Trans. Geoth. Resour. Counc.,* **26**, 379–383.

Wang, C.Y., and R.B. Herrmann (1980). A numerical study of *P*-, *SV*-, and *SH*-wave generation in a plane layered medium, *Bull. Seism. Soc. Am*. **70** 1015-1036.

Wells, D.L., and K.L. Coppersmith (1994). New empirical relationships among magnitude, rupture length, rupture width, rupture area and surface displacement, *Bull. Seism. Soc. Am*., **84**, no. 4, 974-1002.

Wessel, P., and W.H.F. Smith (1998). New, improved version of Generic Mapping Tools released, *EOS Trans*. AGU **79**, 579.

Williams, C.F., S.P. Galanis, T.H. Moses, and F.V. Grubb (1993). Heat-flow studies in the Northwest Geysers Geothermal Field, *Trans. Geoth. Resour. Counc.,* **17**, 281-288.

Wu, F.T. (1978). Prediction of strong ground motion using small earthquakes, Proceedings of the Second International Conference on Microzonation for Safer Construction – Research and Application, Vol. II, 701-704, NSF, November 26-December 1, San Francisco, CA.

Ye, L., T. Lay, H. Kanamori, and L. Rivera (2016). Rupture characteristics of major and great ($M_W \geq 7.0$) megathrust earthquakes from 1990 to 2015: 2. Depth dependence, *J. Geophys. Res*. *Solid Earth*, **121**, 845-863, doi:10.1002/2015JB012427.

Ziegler, M.O., O. Heidbach, A. Zang, P. Martínez-Garzón, and M. Bohnhoff (2017). Estimation of the differential stress from the stress rotation angle in low permeable rock, *Geophys. Res. Lett*., **44**, 6761-6770, doi:10.1002/2017GL073598.

Zollo, A., A. Orefice, and V. Convertito (2014). Source parameter scaling and radiation efficiency of microearthquakes along the Irpinia fault zone in southern Apennines, Italy, *J. Geophys. Res*. *Solid Earth*, **119**, 3256-3275, doi:10.1002/2013JB010116.